MODIFICATION OF THE EARTH'S IONOSPHERE BY VERY-LOW-FREQUENCY TRANSMITTERS

A DISSERTATION

SUBMITTED TO THE DEPARTMENT OF ELECTRICAL ENGINEERING

AND THE COMMITTEE ON GRADUATE STUDIES

OF STANFORD UNIVERSITY

IN PARTIAL FULFILLMENT OF THE REQUIREMENTS

FOR THE DEGREE OF
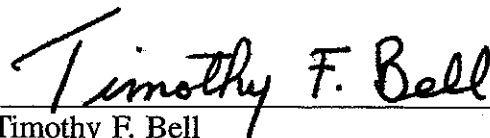
DOCTOR OF PHILOSOPHY

By

Juan Valentin Rodriguez

June, 1994

I certify that I have read this dissertation and that in my opinion it is fully adequate, in scope and quality, as a dissertation for the degree of Doctor of Philosophy.

_____
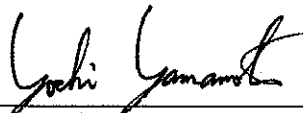Umran S. Inan   (Principal Advisor)

I certify that I have read this dissertation and that in my opinion it is fully adequate, in scope and quality, as a dissertation for the degree of Doctor of Philosophy.

_____
Timothy F. Bell

I certify that I have read this dissertation and that in my opinion it is fully adequate, in scope and quality, as a dissertation for the degree of Doctor of Philosophy.

_____
Yoshihisa Yamamoto

Approved for the University Committee on Graduate Studies:

_____

To my mother and father
Alicia and Juan
and to my wife
Paige

Abstract

It has been known since the 1930's that free electrons in the Earth's ionosphere are heated under the influence of electromagnetic waves from powerful radio transmitters. Until recently research focused on the effects of commercial broadcast and experimental high-frequency transmitters. In 1989, however, researchers at Stanford discovered that powerful, continuously operating U. S. Navy communications transmitters in the 20–30 kHz (very-low-frequency, VLF) range can substantially heat the D region of the Earth's ionosphere (50–90 km altitude).

This dissertation concerns the design and implementation of a controlled experiment aimed at determining the extent to which VLF transmitters operating worldwide modify the ionosphere. VLF signals propagating in the Earth-ionosphere waveguide are used to probe the heated nighttime D region over three U. S. Navy VLF transmitters. Ionospheric cooling and heating are observed when a transmitter turns OFF and ON in the course of normal operations. Heating by the NAA transmitter (1000 kW radiated power) was observed by this method in 41 of 52 ON/OFF episodes during December 1992, increasing the amplitude and retarding the phase of the 21.4 kHz NSS subionospheric probe wave measured at Gander, Newfoundland, by as much as 0.84 dB and 5.3°, respectively. Heating by the NSS (21.4 kHz, 265 kW) and NLK (24.8 kHz, 850 kW) transmitters was observed serendipitously in data from earlier observations of VLF signals propagating in the Earth-ionosphere waveguide.

A three-dimensional model of wave absorption and electron heating in a magnetized, weakly ionized plasma is used to calculate the extent and shape of the collision frequency (i.e., electron temperature) enhancement above a VLF transmitter. The heated patches

are annular with a geomagnetic north-south asymmetry and a radius at the outer half-maximum of the collision frequency enhancement of about 150 km. Increases up to a factor of 3 in the electron temperature are predicted to occur in the nighttime D region due to heating by the NAA transmitter. The calculated changes in the D region conductivity are used in a three-dimensional model of propagation in the Earth-ionosphere waveguide to predict the effect of the heated patch on a subionospheric VLF probe wave. The range of predicted scattered field amplitudes is in general consistent with the perturbations of NSS-Gander observed during December 1992.

In the light of the continuous operation of several powerful VLF transmitters around the world it is interesting to consider the consequences of electron heating on the state of the D region. One possible effect, the modification of the nighttime D region electron number density, is investigated theoretically using a four-species model of the ion chemistry. The effects of a 100 kW (NAU), a 265 kW (NSS), and a 1000 kW (NAA) VLF transmitter are calculated for different ambient electron density profiles. The dominant effect of the heating on electron number density is a reduction in the D region electron density due to an increase in the three-body attachment rate of electrons to O_2. Results indicate that the electron density is depleted by up to 26% at ~ 80 km altitude over a 1000 kW transmitter.

Preface

With the completion of this dissertation, I am rounding out eleven years of study at Stanford University, seven of which I have had the privilege to spend as a member of the VLF Group in the Space, Telecommunications and Radioscience (STAR) Laboratory. That I have come this far is due in large part to the unflagging encouragement and support of my advisor, Umran Inan. His dedication to both teaching and research, in particular to the research process as an integral part of teaching, has made it possible for me both to start and to complete my doctoral studies. My associate advisor, Tim Bell, has provided sage advice and reassurance as well as illuminating insight into the physics behind intricate theories. Bob Helliwell sparked my interest in ionospheric physics when he played a recording of a whistler in my introductory circuits class my sophomore year. His enthusiasm for the past, present, and future of ionospheric studies is infectious. I have enjoyed many conversations with Don Carpenter, Martin Walt, and Vikas Sonwalkar. Don and Martin took time from their busy schedules to comment on my dissertation, and Vikas graciously shared the Quadra with me during the last furious month of dissertation writing. Jerry Yarbrough and Bill Trabucco provided many a lively lunchtime conversation in ERL 224 as well as a wealth of information about VLF research. June Wang and Jenny Xu have gone out of their way to help me with numerous administrative tasks. I enjoyed Tony Fraser-Smith's light-hearted banter in the halls and appreciated his many words of support. My thanks go to Tony for serving on and to Professor Clayton Bates for being the chairman of my oral defense committee, and to Professor Yoshihisa Yamamoto for cheerfully reading my dissertation on short notice. In addition, I am deeply grateful to Dr. Tom Chang of M. I. T. for allowing me to use a guest account on his group's computer to connect to the STAR Laboratory computers while I have been living in Cambridge.

The successful installation and operation of the Gander system would not have been

possible without the efforts of many people, especially Steve Reising, Bill Trabucco, and Dave Shafer at Stanford, and CWO Bert Corbin, Cpl. Shawn North, and Cpl. Tim Moss of the Canadian Forces 770 Communications Research Squadron in Gander. I am indebted to the members of the Squadron for their hospitality and their conscientious and expert operation of our system.

During the period of data analysis and interpretation that followed, several fellow students were particularly helpful. The instruction of Sean Lev-Tov and Steve Cummer made it easier for me to learn the waveguide propagation model. I had the opportunity to direct Matt Bradford in a data analysis project that benefited both of us. My conversations with Victor Pasko on his model of the nighttime D region chemistry were thoroughly enjoyable. Bill Burgess' MacTrimpi analysis program and thesis typesetting macros for TEX have been invaluable. Dave Shafer provided encouragement at crucial moments during our simultanous preparations for our oral dissertation defenses.

It has been a privilege to work with the fine group of students that the VLF group has attracted through the years. In addition to those already mentioned, I would like to thank Sasha Draganov, Tom Mielke, Lee Poulsen, Jasna Ristić-Djurović, Yuri Taranenko, and Tom Wolf for their advice, encouragement, and friendship.

None of my work here would have been possible without the constant love and support of my parents, Juan and Alicia, my sister, Silvia, my brothers, Diego and Carlos, and my wife, Paige. It has meant very much to me to have Diego and Silvia follow me to Stanford as undergraduates. Meeting Paige was the most important event in my life at Stanford (followed closely by the wedding!). In spirit, this dissertation is as much hers as it is mine.

JUAN V. RODRIGUEZ

Stanford, California
May 31, 1994

Contents

Tables

Illustrations

1

Introduction

This dissertation is concerned with the effect of powerful electromagnetic waves from very-low-frequency transmitters on the temperature and number density of free electrons in the Earth's upper atmosphere. The partially ionized atmospheric region of interest here lies between 50 and 100 km altitude, forming the lowest portion of the Earth's ionosphere, "that part of a planetary atmosphere where ions and electrons are present in quantities sufficient to affect the propagation of radio waves" [*Wave Propagation Standards Committee*, 1977]. The transmitters in question operate at frequencies between 20 and 30 kHz, the upper end of the very-low-frequency, or VLF (3-30 kHz), portion of the radio spectrum.

The region of the ionosphere between 50 and 100 km, known as the D region, is a good reflector for radio waves at very low frequencies. The surface of the Earth and the D region form a concentric spherical waveguide that permits long distance propagation at these frequencies. The D region altitude at which VLF waves incident from below reflect depends on the distribution of ionization with altitude, which is a function of the time of day, the season, and the level of solar activity, among other influences. In the D region, the important ionizing radiations from the Sun are the discrete Lyman α line at 1216 Å in the ultraviolet, and hard X-rays of wavelength < 10 Å [*Davies*, 1990, p. 33]. The diurnal variation in the amount of these fluxes striking the atmosphere is generally the cause of the largest fluctuation in the ionization content of the D region (2–3 orders of magnitude).

The field strengths and phases of VLF waves propagating in the Earth-ionosphere waveguide are sensitive to relatively small (~ 10 %) fluctuations in the number density of free electrons in the D region. Changes in the temperature of D region electrons

also affect the propagation of VLF waves by altering the frequency of collisions between electrons and neutral particles and hence the absorption rate of waves in the D region. The specific question addressed by this dissertation is the extent to which powerful VLF transmitters can modify both the number density and temperature of free electrons in the D region. This introduction places the contributions of this dissertation in the context of past radio studies of the lower ionosphere, especially investigations at very low frequencies.

1.1   HISTORY OF THE DISCOVERY OF THE IONOSPHERE

As the aurora borealis gradually passed from being an object of fear and portent to the subject of study by the new brand of natural philosophers, its presence suggested to astute observers the existence of ionization and currents in the upper atmosphere of the Earth. Some eighteenth-century scientists such as Benjamin Franklin and Mikhail Vasil'evich Lomonosov, inspired by the growing experimental knowledge of electrical discharges, proposed that aurora was an electrical phenomenon [*Eather*, 1980, pp. ix, 70]. Others such as Edmund Halley and John Dalton, observing movements of compass needles at the time of auroral disturbances, deduced that the phenomenon was related to the magnetic field of the Earth [*Eather*, 1980, pp. 52, 61]. Karl Friedrich Gauss speculated in 1839 that fluctuations in the Earth's magnetic field were due to currents in the upper atmosphere, citing the aurora as evidence that electricity in motion could exist at high altitudes; this idea was put forward again in 1882 by Balfour Stewart and developed into a mathematical theory by Arthur Schuster in 1889 [*Green*, 1946; *Bates*, 1993].

The first successful trans-Atlantic radio transmission by Guglielmo Marconi in 1901, over a 3500-km path from Poldhu, Cornwall, to St. Johns, Newfoundland, stimulated much speculation about the physical process that had bent the signal over a 240-km-high "wall of ocean" [*Ratcliffe*, 1974]. Unaware of the work of the geomagneticians and independently of each other, Oliver Heaviside, Arthur E. Kennelly, and Oliver Lodge proposed in 1902 the existence of an electrically conducting layer in the upper atmosphere [*Bates*, 1993]. Alone of the three, *Lodge* [1902] suggested that the conductivity was due to solar ultraviolet radiation ionizing the neutral constituents. However, based on his very brief note, Lodge seems to have viewed this conducting layer more as a cause of attenuation than as a good reflector, attributing most if not all of the guiding of the wave to the ocean. Despite these early surmises, it would be over twenty years before the

existence of the ionosphere would be proven to the satisfaction of essentially all members of the community of radio scientists and engineers (see *Green* [1946] for a detailed and fascinating discussion of this long process).

1.1.1 Early Theoretical Work on Long-Distance Propagation

The first attempts to explain Marconi's observations quantitatively by solving Maxwell's equations assumed that diffraction of the signal along the surface of the Earth could account for the observed signal strengths. The problem attracted some of the finest mathematical physicists of the day, including Rayleigh and Poincaré [*Bates*, 1993]. Essentially, the solution to the problem of radiation from a vertical dipole at the surface of a conducting sphere was, in spherical coordinates, a series of spherical harmonics whose coefficients depended on the boundary conditions of the problem. Unfortunately, this series converged very slowly, and many attempts were made in the years prior to the First World War to compute the field approximately yet accurately, with varying degrees of success [*Love*, 1915].

After almost two decades of scientific controversy, *Watson* [1918, 1919] conclusively demonstrated in a pair of important papers that diffraction could not explain the signal strengths commonly observed at great distances ever since Marconi's initial discovery. Instead, a concentric conducting layer in the upper atmosphere resulted in the prediction of signal strengths comparable with those observed. His conclusive demonstration was made possible by a transformation in the complex plane of the original poorly-converging series of zonal harmonics to a convergent "residue" series that is essentially a sum of waveguide modes. The "Watson transformation" is still of great interest in the understanding of diffraction around a blunt obstacle [*Booker*, 1975]. Although the highly-conducting upper boundary postulated by *Watson* [1919] results in inaccurate predictions of radio wave reflection from the lower ionosphere* the basic concept of a residue series or waveguide modes is fundamental to most modern theories and models of propagation in the Earth-ionosphere waveguide [*Budden*, 1961, 1962; *Wait*, 1962; *Pappert et al.*, 1967; *Galejs*, 1972a].

---

* *Wait* [1962, p. 133] points out that the lower ionosphere acts more like a magnetic reflector (tangential $H \simeq 0$) rather than an electric reflector (tangential $E \simeq 0$).

1.1.2 Communications and Experiments at Frequencies below 100 kHz before 1920

While the theoreticians were wrestling with the mathematics of diffraction theory, the Marconi company and others proceeded with the construction and operation of long-distance wireless communications transmitters. Marconi's first successful transatlantic transmission in 1901 probably occurred not at 820 kHz, the fundamental frequency of his spark gap transmitter, but at one of its harmonics such as 2460 kHz [*Ratcliffe*, 1974; *Belrose*, 1993]. The first successful transatlantic transmissions below 100 kHz were accomplished by R. A. Fessenden in 1906 between Brant Rock, Massachusetts, and Machrihamish, Scotland, first with a spark transmitter and antenna tuned to 88 kHz, and later with a continuous wave transmitter at 80 kHz [*Belrose*, 1993]. The first commercial transatlantic wireless service was established by Marconi in 1907 between Clifden, Ireland, and Glace Bay, Nova Scotia, at 82 kHz; by 1912, frequencies of operation had moved down into the 12-30 kHz range, the region of minimum attenuation [*Watt*, 1967, p. 120]. Numerous transmitting antennas were built for commercial transoceanic communications, communications among far-flung parts of empires, and naval communications. The development of commercial high-power radio stations was interrupted by the onset of World War I, but powerful military facilities were built in the United States and Europe, some of which were later used for commercial purposes [*Carter and Beverage*, 1962].

During these years many radio engineers, aware of the shortcomings of the diffraction theory, speculated about the existence of conducting layers in the upper atmosphere. Early observations of wave interference probably due to reflection from the ionosphere came about through the use of Poulsen arc transmitters for wireless telegraphy, in which the "marking" (dot or dash) and "spacing" (no character) waves were radiated continuously at closely adjacent frequencies [*Green*, 1946]. For example, *De Forest* [1913] reported that for several hours following sunset the 92 kHz marking wave from the Los Angeles station of the Federal Telegraph Company would fade to near or total inaudibility at San Francisco while the field strength of the 97 kHz spacing wave would stay the same or increase. He attributed this effect to reflection from "partially ionized masses of air" in the upper atmosphere. In more extensive tests using the Federal Telegraph Company transmitters in Honolulu and San Francisco, *Fuller* [1915] observed fading on signals propagating over the 3880-km distance between the two cities during the day and especially at night by sweeping in frequency from 25.4 kHz to 100 kHz. Furthermore, *Fuller* [1915] also observed that a signal at a given frequency from Honolulu received at the San Francisco

site would fade while received quite strongly at another site 14 km distant.† *Watson* [1919] may have had these results in mind when he stated that his waveguide mode theory could explain observed interference effects.

1.1.3 Advent of Medium and Short Wave Communications and the First Direct Proof of the Existence of the Ionosphere

After World War I the attention of engineers and scientists turned from long-wave to medium- and short-wave communications due to the invention of the vacuum tube amplifier, which permitted continuous-wave transmission at higher frequencies than previously possible. Higher frequencies were attractive not only due to their ability to carry more information but also due to the smaller size and increased efficiency of the transmitting antennas. Marconi himself conducted long-distance short-wave experiments that doomed his existing long-wave networks. By 1925 engineers and scientists on both sides of the Atlantic were conducting experiments aimed at demonstrating directly the existence of the ionosphere using medium and short waves. Although many worked on the theory and experiments, the work of E. V. Appleton and his coworkers in England achieved deserved prominence due to his experimental confirmation of the predictions of the magneto-ionic formulation of the refractive index of the ionized layer, the theory which he and others developed in the late 1920's [*Appleton*, 1932]. Among other things, *Appleton* [1927, 1930] identified the D, E, and F layers of the ionosphere (Figure 1.1), the E layer being the Kennelly-Heaviside layer that had been hypothesized in 1902.

1.1.4 The Luxembourg Effect

In 1933, B. D. H. Tellegen discovered that the Radio Luxembourg (1190 m, 252 kHz) program was audible in the background when a radio in Eindhoven, Netherlands, was tuned to the 460 m (652 kHz) station in Beromünster, Switzerland. Somehow the amplitude-modulation of the Luxembourg signal was being transferred to the Beromünster signal. Tellegen ruled out the possibility that the Luxembourg signal was strong enough to create this "cross-modulation" by driving the electronics into the nonlinear range. Noting that "Luxembourg is situated nearly on the line joining Beromünster and Eindhoven," he

---

† Leonard Fuller later received his Ph.D. in Electrical Engineering from Stanford University, writing his dissertation on the Poulsen arc transmitter that had made these observations possible [*Fuller*, 1919].
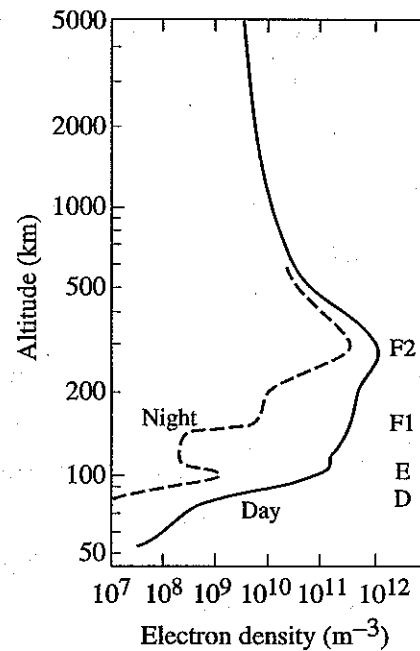
Figure 1.1. Variation of ionospheric electron density with altitude. The ionosphere is divided into layers whose existence was first inferred from radio sounding observations by *Appleton* [1927, 1930]. (After *Davies* [1990, p. 57].)

suggested that the cross-modulation was being caused somewhere between Beromünster and Eindhoven, but gave no mechanism [*Tellegen*, 1933].

The following year, *Bailey and Martyn* [1934] explained this so-called "Luxembourg" effect by showing that a sufficiently strong radio wave could increase the frequency of collisions of ionospheric electrons with neutral molecules, thereby increasing the electron temperature. Any modulation on this "disturbing" or "heating" wave would cause the increased collision frequency, and hence the refractive index of the ionosphere, to vary, thus transferring the modulation to any other wave (the "wanted wave") propagating through the heated region (Figure 1.2). The theory and the extensive research conducted on the "Luxembourg" effect before and after the war were reviewed in a clear manner by *Huxley and Ratcliffe* [1949]. These initial studies of ionospheric modification via the "Luxembourg" effect have evolved into a new field of high frequency (HF) ionospheric modification studies conducted with dedicated experimental heating transmitters [e.g., *Gordon and Carlson*, 1974; *Utlaut*, 1975; *Gurevich*, 1978; *Barr et al.*, 1985; *Wong and Brandt*, 1990; *Barr and Stubbe*, 1993].
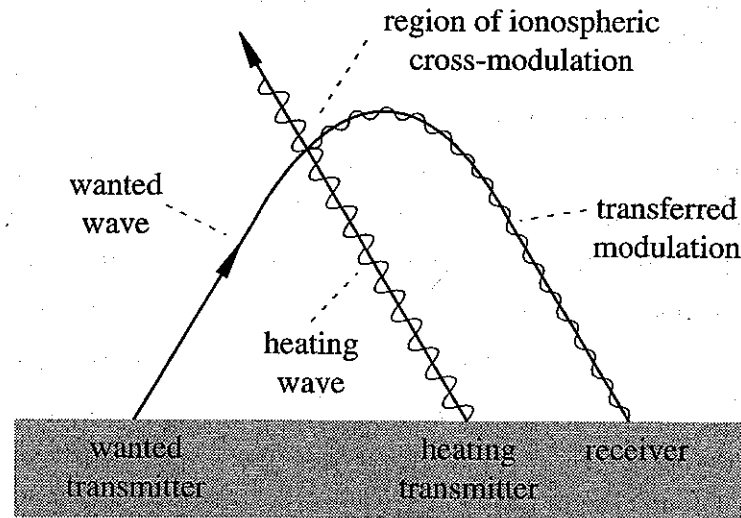
Figure 1.2. Schematic illustration of the Luxembourg effect. Illustration of the nomenclature connected with the Luxembourg effect (after *Ratcliffe and Shaw* [1948] and *Huxley and Ratcliffe* [1949]).

1.2 REMOTE SENSING OF THE LOWER IONOSPHERE USING SUBIONOSPHERIC VLF PROBE WAVES

Since World War II the venerable field of VLF communications has been rejuvenated by the development of accurate frequency standard [*Pierce*, 1957] and navigation [*Swanson*, 1983] networks operating at VLF as well as the construction of new, powerful VLF transmitters for military communications [*Watt*, 1967]. At the same time, accurate theories of propagation in the waveguide formed by the surface of the Earth and the D region (Figure 1.1) have been developed [e.g., *Budden*, 1961, 1962; *Wait*, 1962; *Pappert et al.*, 1967; *Galejs*, 1972a] that treat the waveguide signal as a sum of modes, or solutions of Maxwell's equations that satisfy the boundary conditions at the Earth's surface and the lower ionosphere. Advanced electromagnetic codes based on these theories have been developed that permit quantitative analysis and prediction of subionospheric VLF probe wave propagation in support of the new VLF applications [*Ferguson et al.*, 1989]. Dedicated VLF/LF ionospheric sounders have provided detailed information about the structure of the D region [e.g., *Rasmussen et al.*, 1980; *Kossey et al.*, 1983]. Signals from VLF transmitters propagating in the Earth-ionosphere waveguide also allow continuous remote sensing of the D region, which is sometimes referred to as the "ignorosphere" due to its inaccessibility to long-term observations from aircraft, balloons, and satellites [*Forbes*, 1989]. These signals serve as subionospheric VLF probe waves.

1.2.1 Observations of D Region Ionization Enhancements Using Subionospheric VLF Probe Waves

Many causes of D region ionization enhancements have been identified by observing the phases and amplitudes of subionospheric VLF probe waves, including solar flares [*Bracewell and Straker*, 1949], meteor showers [*Chilton*, 1961], nuclear detonations in the atmosphere [*Zmuda et al.*, 1963], nighttime precipitation at middle latitudes of energetic electrons from the Earth's radiation belts associated with geomagnetic disturbances [*Potemra and Rosenberg*, 1973], energetic ($>$ 300 keV) electron precipitation in the auroral oval [*Kikuchi and Evans*, 1983], and galactic gamma ray bursts [*Fishman and Inan*, 1988], among others. Extensive studies have been made of the perturbation of VLF waveguide signals by bursts of energetic electrons precipitated from the Earth's radiation belts through interactions with the VLF radiation from lightning [e.g., *Helliwell et al.*, 1973; *Lohrey and Kaiser*, 1979; *Inan et al.*, 1988, 1990; *Dowden and Adams*, 1990; *Wolf and Inan*, 1990; *Burgess and Inan*, 1993]. The electron density at D region altitudes is enhanced in a region of $\sim$ 100 km radius [*Inan et al.*, 1990] by the secondary ionization created by these bursts of energetic electrons. The resulting perturbations of subionospheric VLF signals are characterized by a $\sim$ 1-s delay between the occurrence of the causative lightning flash and the onset of the subionospheric VLF signal perturbation. Similar perturbations with observed onsets within 20–100 ms (depending on the time resolution of the recording system) following the occurrence of the causative lightning flash [*Armstrong*, 1983; *Inan et al.*, 1988; *Inan et al.*, 1993] have been attributed to direct heating and ionization of the D region by the powerful ($\sim$ 20 GW) electromagnetic pulse radiated by lightning discharges [*Inan et al.*, 1991; *Rodriguez et al.*, 1992; *Inan and Rodriguez*, 1993; *Taranenko et al.*, 1993a], as well as to downward acceleration of energetic electrons in the radiation belts by the lightning electric field transient [*Inan et al.*, 1988; *Burke*, 1992].

1.2.2 Observations of High Frequency Heating Using Subionospheric VLF Probe Waves

The first successful observations of ionospheric heating made with probe waves with frequencies below 167 kHz involved the experimental high frequency (HF, 3-30 MHz) transmitter in Platteville, Colorado (50 MW effective isotropic radiated power (EIRP)) [*Jones et al.*, 1972]. It was located at the midpoint of a 128-km path from 20 kHz

(WWVL) and 60 kHz (WWVB) transmitters in Fort Collins, Colorado. Transmissions at 5.1 and 7.4 MHz were used to heat the midday D region directly overhead. At the VLF and LF reflection height of ~ 70 km the diameter of the heated region was ~ 25 km. Only the sky wave component of the VLF and LF probe waves was observed. The largest amplitude perturbation observed (on the 60 kHz signal) was 0.53% (0.046 dB); the largest phase perturbation observed (on the 20 kHz signal) was 0.3°.

A more recent experiment conducted by *Barr et al.* [1984, 1985] used subionospheric VLF probe waves to probe D region heating by the 2.759 MHz 200 MW maximum effective radiated power (ERP) steerable heater at Tromsø, Norway. The VLF probe waves were the 12.1 kHz Omega navigation signal from Aldra, Norway [*Swanson*, 1983], and the 16.4 kHz JXN signal from nearby Helgeland. The heated spots were located near the end of < 500 km great circle paths from the transmitters. When the Tromsø beam was focused on the 12.1 kHz path (38° from vertical), the heated region was a 27 by 34 km ellipse at 80 km altitude. The perturbations ranged from ~ 0.05 dB and $\sim -0.3°$ during the day to as much as 6 dB and 50° at night. The latter observation was probably due to interference among the waveguide modes of the 12.1 kHz signal that caused a minimum in the signal amplitude at the receiver at the time of heating. When the Tromsø beam was scanned from 12°N to 56°S of the heater (angle from vertical) during stable sunlit ionospheric conditions, amplitude and phase perturbations on the Aldra and JXN signals went through two to three minima and maxima, with maximum perturbations of ~ 0.05 dB and $\sim 0.5°$. *Dowden et al.* [1991] conducted a similar experiment during nighttime conditions with the 4.040 MHz heater at Tromsø. The analysis considered the variation of the relative phase of the scattered signal with the location of the heated region rather than treating the probe wave as a sum of waveguide modes.

More recently, heating of the D region by the 2.8 MHz High Power Auroral Stimulation (HIPAS) transmitter near Fairbanks, Alaska, has been detected using the 23.4 kHz signal from the NPM transmitter on Oahu received at Fort Yukon, Alaska, as a subionospheric probe wave [*Bell et al.*, 1993]. Changes in the NPM amplitude of –0.2 to +0.4 dB, simultaneous with the HIPAS modulation pattern, were measured using superposed epoch analysis.

1.3 NONLINEAR INTERACTIONS OF VLF TRANSMITTER SIGNALS WITH THE IONOSPHERE

At the time the review paper by *Huxley and Ratcliffe* [1949] was written, no ionospheric heating had been observed to be caused by or detected by any wave of frequency less than 167 kHz. *Ratcliffe and Shaw* [1948] had attempted to detect ionospheric cross-modulation by heating waves at 90.2 kHz (from a 20 kW transmitter) and 68 kHz (from a 80 kW transmitter) on a 767 kHz and a 1050 kHz wanted wave, respectively. Although *Ratcliffe and Shaw* [1948] predicted observable ionospheric cross-modulation by the heating waves, no such effects were observed. They concluded that this was due to the low-frequency signals being reflected or absorbed below the altitude of maximum absorption of the high-frequency signals.

1.3.1 First Theoretical Prediction of VLF Heating

The first theoretical discussion of VLF heating [*Galejs*, 1972b] modeled the nighttime D region as a homogeneous magnetized plasma with a sharp lower boundary at 85 km. Using a theory of electron heating similar to that of *Huxley and Ratcliffe* [1949] and a full solution of Maxwell's equations to calculate the fields in the ionosphere from a 16 kHz transmitter, *Galejs* [1972b] predicted a north-south asymmetry to the heated region over a VLF transmitter, with most of the heating occurring for poleward propagation at angles where the wave's electric field is nearly parallel to the Earth's magnetic field. He predicted temperature increases on the order of 10% for a 1000 kW transmitter and a short term 5% increase in electron density due to the decrease with increasing electron temperature of the rate of dissociative recombination of electrons with NO^+ and O_2^+ (e.g., $NO^+ + e \rightarrow N + O$).

1.3.2 Possible Early Evidence of VLF Heating of the D Region

Several methods of generating ultra-low-frequency (ULF, < 3 Hz) signals have been proposed and implemented [*Fraser-Smith*, 1981]. One such method is the modification of the ionosphere using powerful VLF transmitter signals modulated at rates < 3 Hz. Such ULF waves synchronized with the modulation (0.02 - 0.5 Hz) of a VLF transmitter have been observed and attributed to demodulation of the VLF wave through heating of the lower ionosphere [*Kopytenko et al.*, 1977; *Chmyrev et al.*, 1976] or to the modulation

of energetic electron fluxes precipitated from the Earth's radiation belts [*Chmyrev et al.*, 1976].

In another experiment of the same era, observations were made on the ground 500-4500 km from high- and mid-latitude Soviet VLF transmitters of equal radiated power [*Molchanov et al.*, 1977]. When these transmitters were operated in a 60-s ON/60-s OFF or 120-s ON/120-s OFF format, the amplitude of the signal on a loop antenna perpendicular to the direction of propagation was sometimes observed to increase steadily from the beginning to the end of the 60-s transmission. *Molchanov et al.* [1977] proposed that the observed effect resulted from a change in the D region electron density due to thermal diffusion and a change in the ion chemistry equilibrium. For a discussion of this observation in the context of this dissertation see Chapter 6.

1.3.3 First Observations of VLF Heating Using Subionospheric VLF Probe Waves

A VLF wave-injection experiment intended to precipitate energetic electrons from the inner radiation belt led to the serendipitous first observation of heating by a VLF transmitter using subionospheric VLF probe waves [*Inan*, 1990a]. The NAU transmitter in Aguadilla, Puerto Rico, radiating a total of 100 kW at 28.5 kHz was keyed in a 3-s ON/2-s OFF pattern for two fifteen minute periods nightly during May, June, October, and December 1989. Signals from various VLF transmitters in the U. S. were monitored at Arecibo, Puerto Rico, and at Palmer Station, Antarctica for signatures of precipitation. Superposed-epoch and spectral analyses of the VLF signal amplitudes were performed to look for a signature of ionospheric disturbances with a 5-s periodicity. Such a periodicity was indeed found in a few cases in the amplitude of the 24.0 kHz NAA signal from Cutler, Maine, observed at Palmer Station. However, there was no measurable delay between the NAU keying and the perturbation of the NAA amplitude, the keying (modulation) pattern of the NAU signal being transferred weakly to NAA. No 5-s periodicity was found in any other signal observed at Palmer. *Inan* [1990a] suggested that the effect was the VLF analogue of the ionospheric "cross-modulation" or heating effect discovered years earlier at medium- and higher frequencies [*Huxley and Ratcliffe*, 1949], supporting his hypothesis with an analysis of the change in the D region refractive index, and hence the reflection height of subionospheric VLF probe waves, due to an increased (heated)

electron-neutral collision frequency. (For another review of this discovery see *Robinson* [1990].)

Analysis of the complete data set revealed signatures of heating in 7 of 102 keying episodes during May and June and in 9 of 42 episodes during October and November 1989 [*Inan et al.*, 1992], the criterion being the presence of a spectral peak at 0.2 Hz in the spectrum of the NAA probe wave amplitude (envelope) at least 1 dB greater than any other spectral component above 0.1 Hz. The size of the perturbations ranged from —0.04 to +0.12 dB. (Although phase measurements were made, no clear signatures in the phase of heating were revealed by spectra or superposed-epoch analyses, due perhaps to the phase receiver occasionally losing track of the NAA signal.) Predictions of a model of VLF propagation in the Earth-ionosphere waveguide in the presence of a D region disturbance due to heating [*Poulsen*, 1991] using three model nighttime D regions (characterized by electron density profiles I, II, and III shown in Figure 2.3) were in general agreement with observations.

The fact that the perturbations of subionospheric signals due to heating by the 100 kW NAU transmitter were of the same order as those caused by the HF transmitter in Tromsø operating with an effective radiated power of 200 MW [*Barr et al.*, 1985] raised questions about the relative abilities of existing ground-based VLF and HF heating transmitters to affect the propagation of subionospheric VLF probe waves [*Dowden and Adams*, 1991]. Indeed, *Taranenko et al.* [1992a] showed that, for the power levels involved in the NAU and Tromsø experiments, VLF heating should be at least as effective as HF heating in disturbing a subionospheric VLF wave, owing to the fact that VLF heating is maximized near the D region reflection height of subionospheric VLF waves, thus maximizing the effect of the heater wave on the probe wave. This conclusion was supported by the work of *Barr and Stubbe* [1992], who furthermore determined that the relative heating efficiency of VLF and HF waves depends on geomagnetic latitude, with VLF generally being more efficient than HF below $\sim 80°$ geomagnetic.

1.4 CONTRIBUTIONS

The research that led to this dissertation involved the design and execution of a controlled experiment aimed at determining the extent to which the ionosphere is modified by powerful VLF radio waves and the geophysical circumstances that are most conducive to the occurrence and observation of this phenomenon. The determination of the characteristics and extent of VLF heating is important since (i) there exist a number of continuously operating man-made VLF transmitters around the globe, and since (ii) the controlled modification of a localized region of the ionosphere would allow us to test current quantitative models of VLF heating and propagation in the Earth-ionosphere waveguide

The contributions of this dissertation are presented as follows:

Chapter 3.   The first field experiment targeted to measure ionospheric heating at night by VLF transmitters was carried out in Gander, Newfoundland. Clear evidence for ionospheric heating by NAA was observed during daily breaks in transmission in the course of normal operations. During December 1992 the amplitude or phase of the 21.4 kHz NSS probe wave propagating from Annapolis, Maryland, to Gander was perturbed in 41 of 52 NAA OFF/ON episodes observed at night. The observed amplitude and phase perturbations ranged from –0.11 to +0.84 dB and from 0 to –5.3 degrees, respectively. A review of subionospheric VLF data recorded by the Stanford VLF group since 1986 revealed two serendipitous VLF heater-probe wave configurations: the great circle path of the 23.4 kHz NPM signal from Lualualei, Oahu, to Saskatoon, Saskatchewan, passing near the 24.8 kHz NLK transmitter in Jim Creek, Washington, and the great circle path of the NAA signal from Cutler to Huntsville, Alabama, passing near the NSS transmitter. In 44 NLK OFF/ON episodes monitored between October 29 and November 23, 1987, four perturbations of the NPM-Saskatoon probe wave amplitude were observed, ranging from 0.3 to 1.6 dB (absolute magnitude). In 29 NSS OFF/ON episodes monitored at Huntsville during February 1990, five perturbations of the NAA-Huntsville probe wave amplitude were observed, ranging from +0.2 to +0.5 dB.

Chapter 4.   A three-dimensional model of heating in the weakly-ionized D region plasma above a ground-based VLF transmitter is developed. The model is applied to calculate the increase in electron temperature and collision frequency for several existing VLF transmitters under different D region electron density and collision frequency profiles. Substantial heating of the nighttime D region is found to occur over an area $\sim$ 150 km in radius, with the electron temperature increasing by as much as a factor of 3.

Chapter 5.   The collision frequency changes predicted by the heating model are used in a three-dimensional model of VLF propagation in the Earth-ionosphere waveguide to predict the effect of existing VLF transmitters on subionospheric VLF signals. The results of this modeling are found to be generally consistent with the observations of Chapter 3, lending credence to the hypothesis that these observations are of D region heating by powerful VLF transmitters.

Chapter 6.   The effects of VLF heating on the ion chemistry of the nighttime D region are theoretically modeled, with results indicating that the electron number density may be reduced by as much as 25% at $\sim$ 80 km altitude. Such density depletions should be detectable in a carefully designed VLF heating experiment involving the periodic keying of the heating transmitter.

2

The Nighttime D Region: Structure and Effect on Very-Low-Frequency Radio Waves

The region of the Earth's ionosphere between 50 and 100 km altitude, known as the D region, is so weakly ionized that its maximum ionization content (i.e., the number of free electrons per unit volume) at night is about one part per billion (at 100 km). Nevertheless, radio waves are absorbed substantially as they propagate through the D region due to the high frequency of collisions between electrons and neutrals. At frequencies below 100 kHz reflection effects are also important. In the first section of this chapter, the models of temperature, neutral density, and electron density used in this dissertation are discussed in connection with a brief overview of the physical processes in the D region. Next, a model of radio-wave propagation in a magnetized, weakly ionized plasma is briefly described and applied to a discussion of the electrical properties of the ambient D region. The final section describes a theory of heating of free electrons by radio waves in a weakly ionized plasma. Both models will be used in the heating calculations of Chapter 4.

2.1 STRUCTURE AND COMPOSITION OF THE ATMOSPHERE BELOW 100 KM

2.1.1 The Neutral Atmosphere below 100 km

The neutral atmosphere is commonly divided into regions based on the gradient of the temperature with respect to altitude [*Reid*, 1976]. Next to the Earth's surface lies the troposphere, in which the primary heat source is the surface of the Earth. The temperature decreases with altitude to a minimum at the tropopause ($\sim$ 10 km), then increases through the stratosphere, where the main source of heat is the photodissociation of ozone, to a maximum around 50 km at the stratopause. Above this altitude the temperature decreases through the mesosphere up to the mesopause at $\sim$ 85 km, where the lowest temperatures are found. The coldest spot globally is the summer polar mesopause, where the temperature is $\sim$ 130 K [*von Zahn and Meyer*, 1989]; a temperature as low as 111 K has been measured at 94 km at 68° N [*Philbrick et al.*, 1984]. Above $\sim$ 90 km lies the thermosphere, in which the temperature increases up to a maximum of 500–2000 K depending on time of day and place in the solar cycle [*Ratcliffe*, 1972, p. 6]. The source of heat in the thermosphere is the photodissociation and photoionization of neutrals, including N_2, O_2, and O, by solar extreme ultraviolet radiation and long-wavelength X rays [*Ratcliffe*, 1972, pp. 38–39; *Reid*, 1976]. In Figure 2.1, these atmospheric regions are identified on a plot of a model neutral temperature profile from the U. S. Standard Atmosphere [*National Oceanic and Atmospheric Administration et al.*, 1976].

In terms of the relative proportions of neutral species, the atmosphere can be divided into two regions [*Ratcliffe*, 1972, pp. 3–4]. Below $\sim$ 100 km, the relative proportions of the gases remain constant due to mixing by turbulence; the composition is 78% diatomic nitrogen (N_2) and 21% diatomic oxygen (O_2) by volume (Figure 2.2). Above the "turbopause" at $\sim$ 100 km, where molecular diffusion becomes faster than turbulent diffusion [*Forbes*, 1989], the constituents are individually in an equilibrium determined by the balance between the downward force of gravity and the upward pressure force due to the greater densities below.
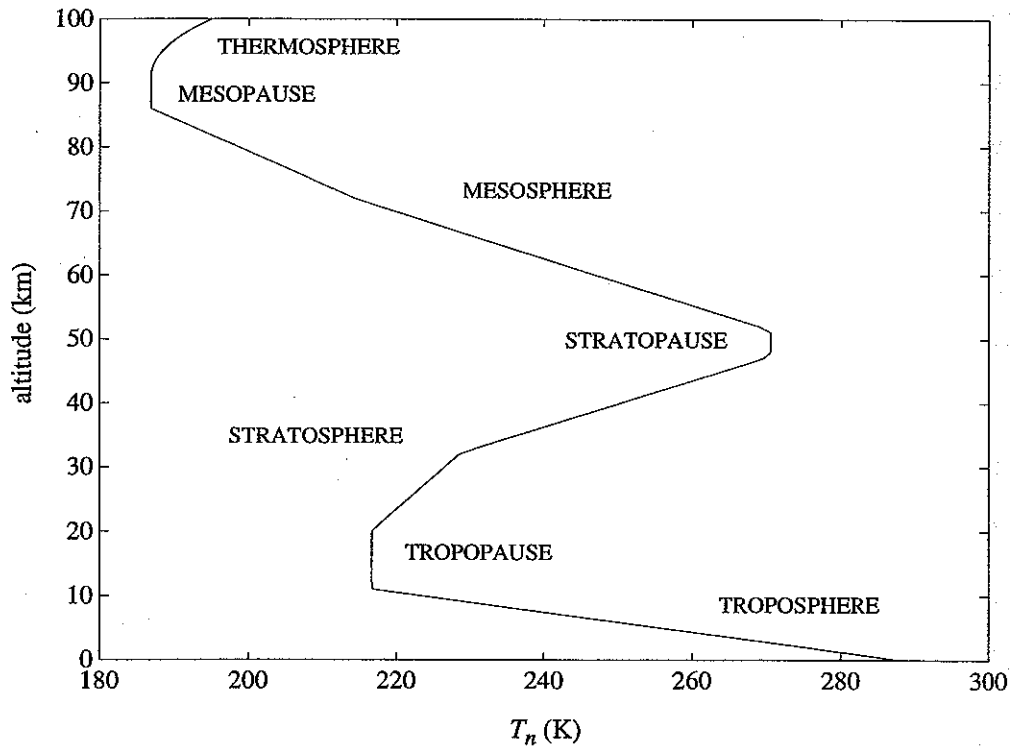
Figure 2.1. **Thermal structure of the atmosphere below 100 km.** The ambient neutral and electron temperature T_n as a function of altitude, from the U. S. Standard Atmosphere [*National Oceanic and Atmospheric Administration et al.*, 1976].

2.1.2   The Ionized Atmosphere below 100 km

The region between the tropopause and the mesopause is sometimes referred to as the "ignorosphere" [*Forbes*, 1989] due to its inaccessibility to long-term observations from aircraft, balloons (in all but the lower stratosphere) and satellites. In general, *in situ* measurements of the "ignorosphere" can only be made with sounding rocket flights, which permit observations of a few minutes' duration of a relatively small region [e.g., *Goldberg*, 1989]. However, remote sensing of the mesosphere is possible at frequencies below ~ 100 kHz since the existence of a small component of ionization in the mesosphere makes this region a good reflector of electromagnetic waves at these frequencies. Such remote sensing can be a powerful diagnostic tool to study the "ignorosphere."

The mesosphere (50–90 km) coincides with the weakly-ionized *D* region, which is generally considered the lowest region of the ionosphere. (There is evidence from pulsed VLF/LF sounding of the ionosphere of a distinct daytime "*C*" layer at 63-69 km altitude
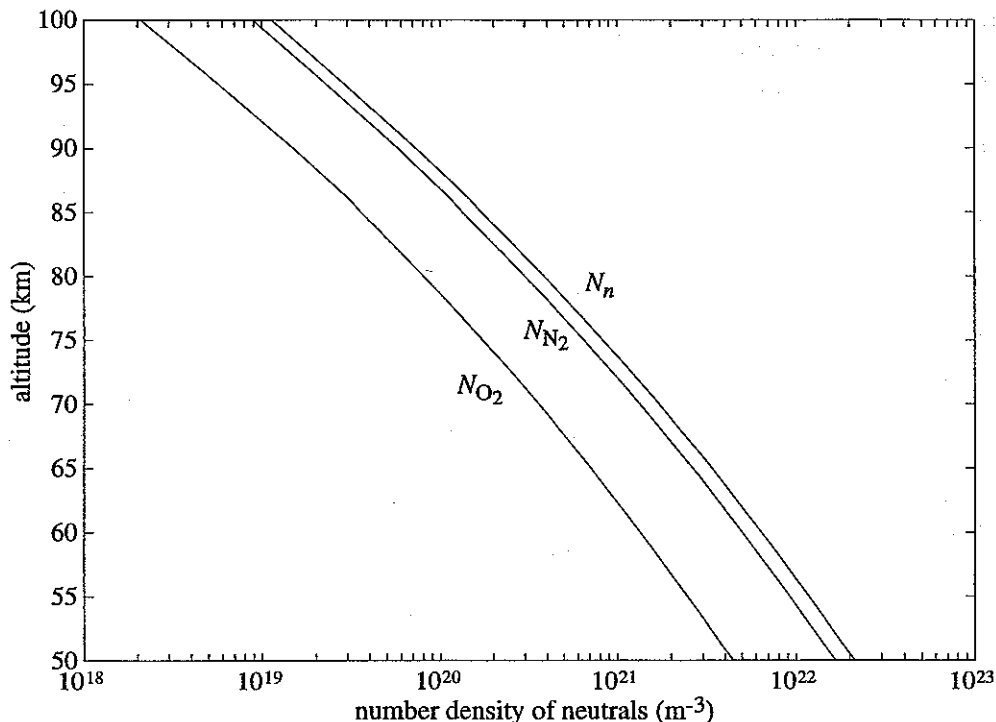
Figure 2.2. Neutral density profiles. Total neutral number density N_n and densities of N_2 and O_2. Profiles below 86 km are from the U. S. Standard Atmosphere [*National Oceanic and Atmospheric Administration et al.*, 1976], and the profiles above 86 km are from the MSIS-86 thermospheric model [*Hedin*, 1987].

[*Rasmussen et al.*, 1980].) The E region lies between 90 and 160 km, with the F region being above 160 km (Figure 1.1). According to one standard definition of the D region, it is "responsible for most of the attenuation of radio waves in the range 1 to 1000 MHz" [*Wave Propagation Standards Committee*, 1977]. This definition, while stating an important effect of the D region on radio propagation, ignores the reflection properties of the D region at lower frequencies that lie at the root of the theory and experimental techniques used in this dissertation. In this work, we are concerned with the region between 50 and 100 km, that is, strictly speaking, the D region and the lower edge of the E region. Henceforth, this region will be referred to simply as the D region. For a lucid discussion of the ionosphere above 100 km see the introductory text by *Ratcliffe* [1972].

The major source of free electrons in the daytime D region is probably the ionization

of nitric oxide (NO) by ultraviolet solar Lyman α radiation (1215.7Å wavelength) [*Reid*, 1976]. The next most important source is the ionization of excited oxygen molecules $O_2(^1\Delta)$ by ultraviolet radiation in the 1027-1118Å range. Solar X rays are important above 90 km. At night, NO^+ is the dominant primary positive ion in the *D* region, with O_2^+ a distant second [*Danilov and Semenov*, 1978]. It is likely that the nighttime midlatitude *D* region is maintained in part by hydrogen Lyman α radiation scattered from the exosphere (the atmosphere above 500-700 km [*Davies*, 1990, p. 57]) and in part by a steady flux of energetic (> 40 keV) electrons precipitated from the Earth's radiation belts [*Potemra and Zmuda*, 1970; *Reid*, 1976; *Goldberg*, 1989]. Galactic cosmic rays (> 10^9 eV protons [*Ratcliffe*, 1972, p. 19]) are the most important source below 50 km during both day and night [*Ratcliffe*, 1972, p. 40].

Model Nighttime D Region Electron Density Profiles

Several techniques have been developed to measure the electron density in the *D* region [*Sechrist*, 1974], including ground-based measurements of the differential phase of two high-frequency signals transmitted from a sounding rocket [*Kane*, 1962], partial reflections of signals from high-frequency radio sounders [*Belrose and Burke*, 1964], and inversion of data on the reflection of subionospheric VLF waves from the *D* region using trial electron density profiles [*Deeks*, 1966*a*]. The VLF technique involves a difficult data interpretation task, yet long-term observations of the phase of subionospheric VLF signals provide perhaps the best indication of the day-to-day variability of the *D* region electron density over long periods. Observations made using all these methods have revealed that the electron number density in both the daytime and the nighttime *D* region is quite variable [*Davies*, 1990, p. 143]. In this dissertation, we represent this variability by using four different model nighttime *D* region electron density profiles, designated 0, I, II, and III (Figure 2.3), that span 2–3 orders of magnitude at any given altitude in the VLF reflection region ($\sim 75 - 90$ km). Profiles 0 and I are based on the commonly used exponential profiles of *Wait and Spies* [1964]

$$N_e = 1.43 \times 10^{13} \; \exp[(\beta - 0.15)h - \beta h'] \quad m^{-3} \tag{2.1}$$

where h is the altitude in km and $\beta = 0.5$ km^{-1} at night [*Wait and Spies*, 1964], corresponding respectively to $h' = 87.0$ km [*Barr and Stubbe*, 1992] and $h' = 85.0$ km [*Inan*, 1990*a*]. Model predictions using (2.1) with $\beta = 0.5$ km^{-1} and 84 km < $h' < 87$ km
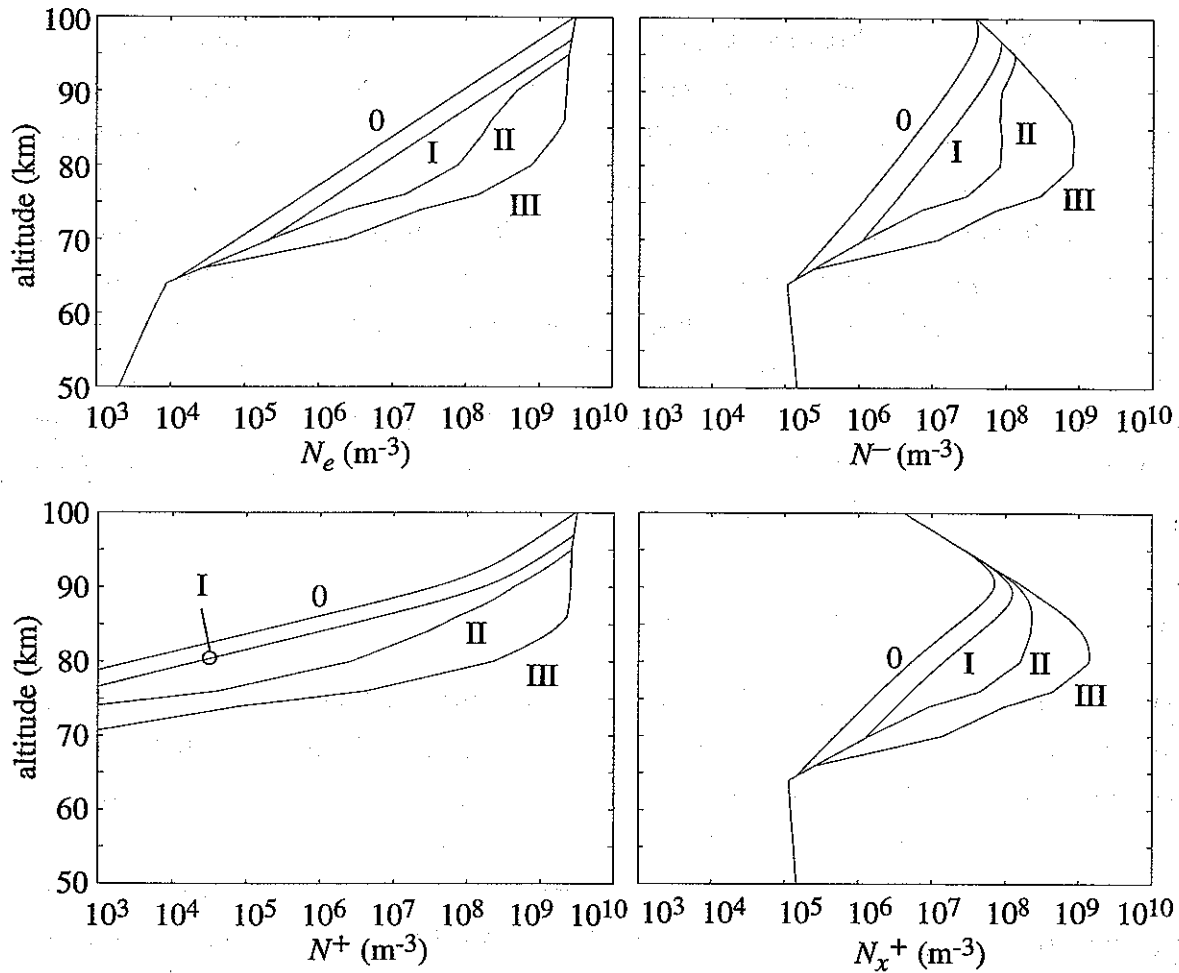
Figure 2.3. Electron and ion density profiles. Electron number density profiles used in this dissertation and ion profiles consistent with these profiles and the *D* region ion chemistry model of Chapter 6.

were shown to be in good agreement with observations of nighttime VLF propagation in the Earth-ionosphere waveguide [*Bickel et al.*, 1970]. Profile II [*Reagan et al.*, 1981] was used in recent studies of the effect of lightning-induced electron precipitation on VLF signals propagating in the Earth-ionosphere waveguide [*Poulsen*, 1991; *Poulsen et al.*, 1990, 1993*a,b*]. Profile III represents densities greater by a factor of 10 than those of profile II between 70 and 90 km. The International Reference Ionosphere [*Rawer et al.*, 1978] is adopted above 100 km, 97 km, 90 km, and 95 km for profiles 0, I, II, and III, respectively. All four profiles have been used in previous studies of VLF heating [*Inan*, 1990*a*; *Barr and Stubbe*, 1992; *Inan et al.*, 1992].

In a later chapter, we use a four-species model [*Glukhov et al.*, 1992] of the nighttime *D* region chemistry to investigate the long-term consequences of heating. This model lumps the ion species into four groups: electrons, number density denoted N_e; primary positive ions (e.g., NO^+ and O_2^+), denoted N^+; negative ions (e.g., O_2^-, CO_3^-, NO_2^-, NO_3^-), denoted N^-; and positive water cluster ions or proton hydrates ($H^+(H_2O)_n$), denoted N_x^+. In the context of this model, the altitude profiles of the three groups of heavy ions can be derived from an assumed electron density profile. The profiles of the heavy ion groups corresponding to the four different electron density profiles assumed here are also shown in Figure 2.3.

D Region Collision Frequency Profiles

The two different electron-neutral collision frequency profiles used in this dissertation are shown in Figure 2.4. The simple exponential profile is an approximation put forth by *Wait and Spies* [1964] to represent experimental profiles obtained from sounding rocket [*Kane*, 1962] and partial reflection data [*Belrose and Burke*, 1964]. It is intended to be used as an "effective" collision frequency (ν_{eff}) in refractive index models that assume a collision frequency independent of electron energy [*Appleton*, 1932; *Ratcliffe*, 1959]. The second profile [*Banks*, 1966], which has a scale height that varies slightly with altitude, is the sum of the average momentum-transfer collision frequencies ν_{av} of electrons in nitrogen and oxygen, weighted according to the proportions of the two molecules below the turbopause (Figure 2.2). The momentum-transfer frequencies (given in Appendix B) were derived from momentum-transfer cross sections measured in the laboratory [*Banks*, 1966] and are commonly used in aeronomic studies [e.g., *Schunk and Nagy*, 1978]. The neutral density and temperature profiles described above are used in their calculation. The theoretical relation between ν_{eff} and ν_{av} is discussed in section 2.2.3.

2.2 REFRACTIVE INDEX OF THE *D* REGION

Theories of radio wave propagation in an ionized gas, or a plasma, make assumptions of varying severity about the composition of the plasma and the motion of the plasma constituents under the influence of externally imposed electric and magnetic fields. One of the goals of such theories is the derivation of a refractive index or, more generally, a permittivity matrix for the plasma. The simplest theory describes the fully-ionized collisionless "cold plasma" in which the electrons and ions are at "zero" temperature.
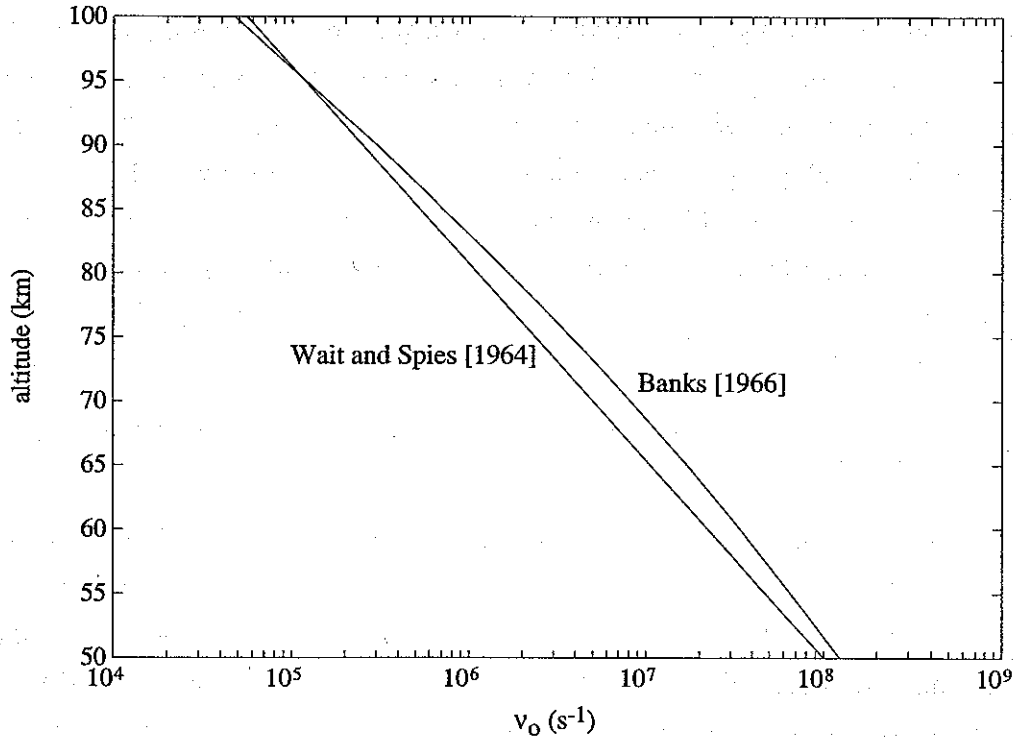
Figure 2.4. Electron-neutral collision frequency profiles.

That is, thermal agitation is neglected, and only the motion of the electrons and ions under the influence of an electromagnetic wave is considered. The cold plasma theory is quite powerful in predicting small-amplitude time-harmonic perturbations in a multicomponent plasma [*Stix*, 1992, p. 2]. In the present work, the D region plasma is modeled as a weakly ionized Lorentzian gas, in which the ions and neutral molecules are immobile and the electrons collide with the immobile particles at a rate that is in general a function of the electron and neutral temperatures [*Chapman and Cowling*, 1970, p. 188]. The theory that describes the propagation of an electromagnetic wave in a Lorentzian gas is known as the "magneto-ionic" theory [*Appleton*, 1932; *Ratcliffe*, 1959]. Mathematically the magneto-ionic theory is almost identical to the cold plasma theory, and the theoretical distinction is subtle. The magneto-ionic theory is useful in the weakly ionized D and E regions of the ionosphere, where the dominant ion species are very heavy (and thus relatively immobile) and most electron collisions are with neutral particles. The derivation of permittivity matrices that include the effect of electron and ion temperatures through

the solution of the Boltzmann equation can be found in plasma wave textbooks such as *Stix* [1992].

The purpose of the treatment here is not to rederive the magneto-ionic theory in detail but merely to present a form of the magneto-ionic theory that is particularly flexible for computation. For a complete treatment, the interested reader is referred to the excellent monograph by *Ratcliffe* [1959] and Chapters 1–5 of *Budden's* [1985] comprehensive treatise.

2.2.1   Refractive Index for Collision Frequency Independent of Electron Energy

The simplest derivation of a refractive index for a radio wave in a magnetized, weakly-ionized plasma involves the solution of the equations of motion for an "average" electron under the influence of an oscillatory electric field (the radio wave) in the presence of a constant magnetic field (the Earth's field), with a frictional force proportional to the velocity and mass of the electron and to the average frequency of collisions that the electron makes with the immobile neutral particles. The two Maxwell's equations that describe the propagation of time-harmonic electromagnetic waves are

$$\nabla \times \mathbf{E} = -i\omega \mathbf{B}$$
$$\nabla \times \mathbf{H} = \mathbf{J} + i\omega \mathbf{D}$$

(2.2)

where $\mathbf{E}$ is the electric field strength, $\mathbf{D}$ is the electric displacement or flux density, $\mathbf{H}$ is the magnetic field strength, $\mathbf{B}$ is the magnetic flux density, and $\mathbf{J}$ is the current density. Propagation in the plasma is treated by separating the right-hand side of the second equation above into the free space displacement current density $i\omega\varepsilon_o\mathbf{E}$ and the current density $\mathbf{J}$ due to the movement of charges under the influence of a time-harmonic electric field.

The linearized Lorentz force equation is

$$i\omega m_e \mathbf{v} = e(\mathbf{E} + \mathbf{v} \times \mathbf{B_o}) - m_e \nu \mathbf{v}$$

(2.3),

where e and m_e are the charge and mass of the electron, $\mathbf{v}$ is the average electron velocity, $\mathbf{B_o}$ is the Earth's magnetic field (the wave $\mathbf{B}$-field is neglected), and ν is the average momentum-transfer collision frequency (see Appendix B). This equation can be

rewritten as $\mathbf{J} = N_e e \mathbf{v} = \bar{\bar{\sigma}} \cdot \mathbf{E}$, where N_e is the number density of electrons and $\bar{\bar{\sigma}}$ is the conductivity matrix:

$$\bar{\bar{\sigma}} = \begin{pmatrix} \sigma_{xx} & \sigma_{xy} & \sigma_{xz} \\ \sigma_{yx} & \sigma_{yy} & \sigma_{yz} \\ \sigma_{zx} & \sigma_{zy} & \sigma_{zz} \end{pmatrix} \qquad (2.4).$$

In a Cartesian coordinate system in which the Earth's magnetic field $\mathbf{B_0}$ is antiparallel to the z-axis, following the convention of *Budden* [1985], the elements of the conductivity matrix are

$$\sigma_{xx} = \sigma_{yy}$$
$$= \frac{\epsilon_0 \omega_{pe}^2 (\nu + i\omega)}{(\nu + i\omega)^2 + \omega_{ce}^2}$$
$$\sigma_{xy} = -\sigma_{yx} \qquad (2.5)$$
$$= \frac{\epsilon_0 \omega_{pe}^2 \omega_{ce}}{(\nu + i\omega)^2 + \omega_{ce}^2}$$
$$\sigma_{zz} = \frac{\epsilon_0 \omega_{pe}^2}{\nu + i\omega}$$
$$\sigma_{xz} = \sigma_{yz} = \sigma_{zx} = \sigma_{zy} = 0$$

where

$$\omega_{pe} = \sqrt{\frac{N_e e^2}{\varepsilon_0 m_e}} \qquad (2.6)$$

is the electron plasma frequency and

$$\omega_{ce} = \frac{|e| B_o}{m_e} \qquad (2.7)$$

is the electron cyclotron frequency.

The second Maxwell equation above can now be rewritten as

$$\nabla \times \mathbf{H} = i\omega\varepsilon_o \left(\bar{\bar{I}} - i\frac{\bar{\bar{\sigma}}}{\omega\varepsilon_o} \right) \mathbf{E} = i\omega\varepsilon_o \bar{\bar{\varepsilon}} \qquad (2.8)$$

where $\bar{\bar{I}}$ is the identity matrix and $\bar{\bar{\varepsilon}}$ is the relative permittivity matrix of the plasma

$$\bar{\bar{\varepsilon}} = \begin{pmatrix} \varepsilon_{xx} & \varepsilon_{xy} & 0 \\ \varepsilon_{yx} & \varepsilon_{yy} & 0 \\ 0 & 0 & \varepsilon_{zz} \end{pmatrix} \qquad (2.9).$$

As described by *Budden* [1985, pp. 50–53] this permittivity matrix can be diagonalized by using a transformation from Cartesian coordinates x, y, z to "principal axes" $(x-iy)/\sqrt{2}$, $(x+iy)/\sqrt{2}$, z, under which

$$\bar{\bar{\varepsilon}} = \begin{pmatrix} \varepsilon_1 & 0 & 0 \\ 0 & \varepsilon_2 & 0 \\ 0 & 0 & \varepsilon_3 \end{pmatrix} \tag{2.10}$$

where

$$\varepsilon_1 = \varepsilon_{xx} - i\varepsilon_{xy}$$
$$\varepsilon_2 = \varepsilon_{xx} + i\varepsilon_{xy} \tag{2.11}$$
$$\varepsilon_3 = \varepsilon_{zz}$$

Conversely, if the transformation is made from "principal axis" coordinates to Cartesian coordinates as above and the coordinate axes are rotated so that the vector $\mathbf{Y} = e\mathbf{B_0}/m_e\omega$ lies in the x-z plane at angle Θ with the z axis, the permittivity matrix is given by [*Budden*, 1985, p. 53]

$$\bar{\bar{\varepsilon}} = \begin{pmatrix} \frac{1}{2}(\varepsilon_1 + \varepsilon_2)\cos^2\Theta + \varepsilon_3\sin^2\Theta & +\frac{i}{2}(\varepsilon_1 - \varepsilon_2)\cos\Theta & \left[\frac{1}{2}(\varepsilon_1 + \varepsilon_2) - \varepsilon_3\right]\sin\Theta\cos\Theta \\ -\frac{i}{2}(\varepsilon_1 - \varepsilon_2)\cos\Theta & \frac{1}{2}(\varepsilon_1 + \varepsilon_2) & -\frac{i}{2}(\varepsilon_1 - \varepsilon_2)\sin\Theta \\ \left[\frac{1}{2}(\varepsilon_1 + \varepsilon_2) - \varepsilon_3\right]\sin\Theta\cos\Theta & +\frac{i}{2}(\varepsilon_1 - \varepsilon_2)\sin\Theta & \frac{1}{2}(\varepsilon_1 + \varepsilon_2)\sin^2\Theta + \varepsilon_3\cos^2\Theta \end{pmatrix} \tag{2.12}$$

The refractive index n of a wave whose wave-normal makes an angle Θ with the vector* $\mathbf{Y}$ is derived by solving Maxwell's equations for a homogeneous plasma so that the relations among the electric field components E_x, E_y, and E_z are consistent with the above permittivity matrix. One common expression in terms of the elements of the diagonalized permittivity matrix of the plasma is [*Budden*, 1985, p. 75; *Stix*, 1992, p. 9]

$$n^2 = \frac{\varepsilon_1\varepsilon_2\sin^2\Theta + \frac{1}{2}\varepsilon_3(\varepsilon_1 + \varepsilon_2)(1 + \cos^2\Theta) + S}{(\varepsilon_1 + \varepsilon_2)\sin^2\Theta + 2\varepsilon_3\cos^2\Theta} \tag{2.13}$$

where

$$S = \pm\left\{\left[\varepsilon_1\varepsilon_2 - \frac{1}{2}(\varepsilon_1 + \varepsilon_2)\varepsilon_3\right]^2\sin^4\Theta + \varepsilon_3^2(\varepsilon_1 - \varepsilon_2)^2\cos^2\Theta\right\}^{\frac{1}{2}} \tag{2.14}$$

---

* The vector $\mathbf{Y}$ is directed opposite to $\mathbf{B_0}$ due to the charge of the electron.

This versatile expression for the refractive index n, valid for any magnetized plasma whose constitutive relations are expressed in terms of the diagonalized permittivity matrix, is used for the heating model computations described in Chapter 4 of this dissertation.

A well-known alternative form of the refractive-index equation for a weakly-ionized Lorentzian gas also based on the magneto-ionic theory but which lends itself to intuitive insight is [*Appleton*, 1932; *Ratcliffe*, 1959]

$$n^2 = 1 - \cfrac{X}{1 - iZ - \cfrac{Y^2 \sin^2 \Theta}{2(1 - X - iZ)} \pm \sqrt{\cfrac{Y^4 \sin^4 \Theta}{4(1 - X - iZ)^2} + Y^2 \cos^2 \Theta}} \qquad (2.15),$$

where

$$\begin{aligned} X &= \frac{\omega_{pe}^2}{\omega^2} \\ Y &= \frac{\omega_{ce}}{\omega} \\ Z &= \frac{\nu_{eff}}{\omega} \end{aligned} \qquad (2.16).$$

It can be shown that this form (2.15) is equivalent to the more general form (2.13) by making the substitutions

$$\begin{aligned} \varepsilon_1 &= 1 - \frac{X}{1 + Y - iZ} \\ \varepsilon_2 &= 1 - \frac{X}{1 - Y - iZ} \\ \varepsilon_3 &= 1 - \frac{X}{1 - iZ} \end{aligned} \qquad (2.17).$$

Certain approximations to Appleton's expression (2.15) treat propagation in directions nearly parallel ("quasi-longitudinal (QL)") or nearly perpendicular ("quasi-transverse (QT)") to the Earth's magnetic field [*Ratcliffe*, 1959, pp. 75–80]. They are derived by simplifying the radical in the denominator of Appleton's formula using the binomial expansion and either of the approximations

$$\begin{matrix} \text{QL}: \\ \text{QT}: \end{matrix} \Bigg\} \quad \frac{Y^2 \sin^4 \Theta}{4 \cos^2 \Theta} \quad \begin{Bmatrix} \ll \\ \gg \end{Bmatrix} \quad |(1 - iZ - X)^2| \qquad (2.18).$$

The approximate formulas are

$$\text{QL}: \quad n^2 = 1 - \frac{X}{1 - iZ \pm Y|\cos\Theta|}$$

$$\text{QT}: \quad n^2 = 1 - \frac{X}{1 - iZ + (1 - iZ - X)\cot^2\Theta} \quad \text{(upper sign)} \qquad (2.19).$$

$$= 1 - \frac{X}{1 - iZ - \frac{Y^2 \sin^2\Theta}{1 - iZ - X}} \quad \text{(lower sign)}$$

The applicability of the QL and QT approximations as well as the refractive index of an isotropic (unmagnetized) plasma

$$n^2 = 1 - \frac{X}{1 - iZ} \qquad (2.20)$$

to the nighttime *D* region at VLF is analyzed in Figure 2.5 by comparing the real (μ) and negative imaginary (χ) parts of the refractive index ($n = \mu - i\chi$) calculated using these approximations and the full refractive index expression (2.13). The calculations are performed for a 24.0 kHz wave in a nighttime *D* region represented by electron density profile I (Figure 2.3) at 59.2° N geomagnetic (dip angle = 73.4°) for $\Theta = 16.6°$ (vertical incidence) and $\Theta = 61.6°$ (propagation toward geomagnetic north at a 45° elevation angle). These parameters are appropriate for the NAA transmitter in Cutler, Maine, the ionospheric heating by which is most extensively studied in this work.

It can be seen that the QL approximation predicts μ rather accurately but χ quite poorly for vertical incidence at this location ($\Theta = 16.6°$). The QT approximation accurately predicts both χ and μ up to ~ 90 km for $\Theta = 61.6°$. However, neither approximation is sufficiently accurate over the entire range of altitudes. Note that for both wave normal angles there is one mode that undergoes maximum absorption (χ) below 90 km, with much more absorption occuring under QT conditions. In both cases, $\mu > 1$ for this mode above 90 km, indicating that it penetrates the *D* region. Except in the case of the QT penetrating mode, departure from the isotropic case is substantial above ~ 65 km altitude in the profiles for χ, to which the absorption rate of the wave is proportional, indicating the beginning of the transition from a collision-dominated refractive index to one where the magnetic field plays a dominant role. Since the QT penetrating mode most closely resembles propagation in an isotropic ionosphere, it is known traditionally as the "ordinary" mode. Consequently, in this dissertation, the terms "ordinary" and
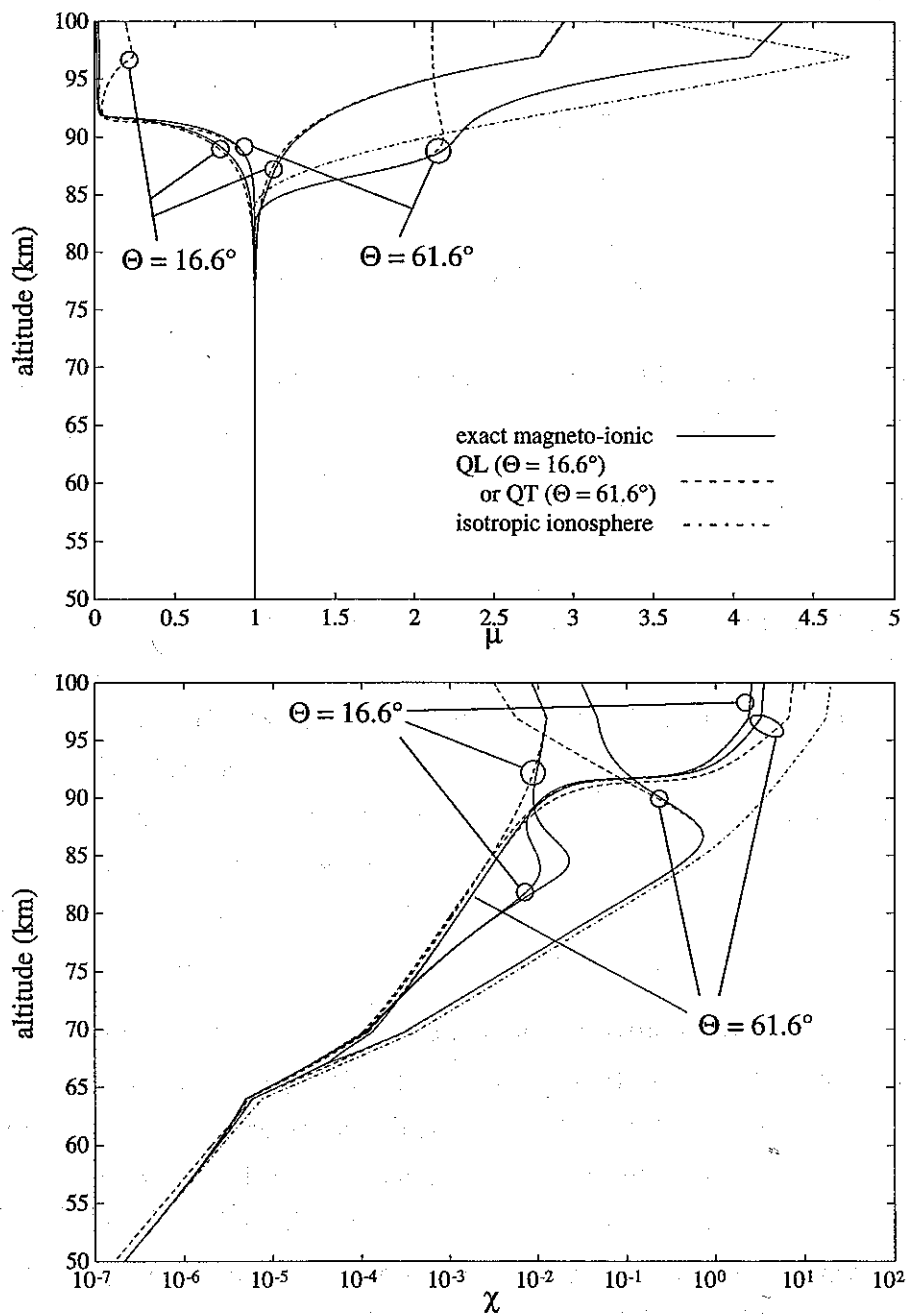
Figure 2.5. Comparison of the isotropic, QL, and QT approximations with the full magneto-ionic expression for the *D* region refractive index. Real (μ) and negative imaginary (χ) parts of the *D* region refractive index at 24.0 kHz, geomagnetic latitude = 59.2° N (dip angle = 73.4°), N_e profile I. Shown for vertical incidence ($\Theta = 16.6°$) are the predictions of the full and QL expressions. Shown for $\Theta = 61.6°$ (propagation toward geomagnetic north at a 45° angle from the ground) are the predictions of the full and QT expressions. Also shown is the result for an isotropic ionosphere (no magnetic field).

"extraordinary" are used to refer to the penetrating and nonpenetrating modes [*Pitteway*, 1965], respectively.

The QL and QT approximations have been used in the past to predict and analyze ionospheric heating [e.g., *Ratcliffe and Shaw*, 1948; *Huxley and Ratcliffe*, 1949] and provide some feel for the properties of the complicated full expression (2.15). However, as demonstrated in Figure 2.5, the full form of the magneto-ionic refractive index formula should be used for sufficient accuracy [*Inan*, 1990*a*].† All refractive indices in this dissertation, apart from some of those in Figure 2.5, are calculated using the full form of the magneto-ionic formula, as given by *Appleton* [1932] or as modified by *Sen and Wyller* [1960] (see below).

2.2.2 Refractive Index for Collision Frequency Proportional to Electron Energy

In the general case where the collision frequency ν is a function of electron energy, the current density **J** in a weakly ionized plasma of electrons and immobile ions must be calculated as

$$\mathbf{J} = e \int \mathbf{v} f(\mathbf{r}, \mathbf{v}, t)\, d^3 \mathbf{v} \tag{2.21}$$

where the distribution function $f(\mathbf{r}, \mathbf{v}, t)$ is a function of the electric field of the electromagnetic wave. This distribution function can be determined by solving the collisional Boltzmann equation [*Gurevich*, 1978]

$$\frac{\partial f}{\partial t} + \mathbf{v} \cdot \nabla_{\mathbf{r}} f + \frac{e}{m}(\mathbf{E} + \mathbf{v} \times \mathbf{B}) \cdot \nabla_{\mathbf{v}} f + S = 0 \tag{2.22}$$

where S an integral describing the effect of collisions on the distribution function. In practice it is necessary to make important assumptions for the solution to be tractable. One such assumption concerns the energy dependence of the electron collision frequency.

In terms of the free path l or cross section q, the collision frequency of an individual electron $\nu(v) = v/l = vNq$, where N is the number density of scatterers, e.g., neutral particles. Thus, for ν independent of v, $l \propto v$ and $q \propto v^{-1}$. A common assumption made in the derivations of electron velocity distribution functions, ionospheric refractive indices, and ionospheric heating is that l and q are constant, hence $\nu(v) \propto v$ [*Bailey and*

---

† In fact, *Budden* [1985, pp. 95–99] recommends that with modern computing resources available the full formula should be used for all computations.

Martyn, 1934; *Druyvesteyn*, 1934; *Huxley and Ratcliffe*, 1949; *Budden*, 1985, pp. 60–61]. Laboratory experiments have shown that $\nu(v) \propto v^2$ in the dominant component of air, N_2, for $5.9 \times 10^4 < v < 5.9 \times 10^5$ m s^{-1}, corresponding to electron energies between 0.01 and 1 eV [*Phelps and Pack*, 1959].‡ *Gurevich* [1978, pp. 62, 67] has shown that in air the relation is more properly $\nu \propto v^{\frac{5}{3}}$. However, more readily usable refractive index formulas have been derived for the case of $\nu(v) \propto v^2$ [*Sen and Wyller*, 1960; *Hara*, 1963; *Budden*, 1965], and it is this theory that is used for the heating calculations in this dissertation.

The excellent tutorial paper by *Budden* [1965] presents the derivation of the refractive index formula for $\nu(v) \propto v^2$ [*Sen and Wyller*, 1960] in the notation of the magneto-ionic theory. The distribution function is assumed to be the sum of the ambient Maxwellian distribution and a small perturbation that represents current flow. All second-order terms (those containing squares and products of the wave electric field and the small perturbation to the distribution function) are dropped, and spatial homogeneity is assumed. Only elastic collisions are considered in the collision integral. The distribution function is assumed to oscillate at the same frequency as the wave. The result of these approximations is a linearized Boltzmann equation, analogous to the Lorentz force equation, which is solved for the distribution function matrix. This matrix in turn is integrated to give the current density **J**, from which the permittivity matrix is derived exactly as outlined above (section 2.2.1). The resulting elements of the diagonalized permittivity tensor are

$$\varepsilon_1 = 1 - X \left\{ (1+Y)w^2 C_{\frac{3}{2}} [(1+Y)w] + i\frac{5}{2} w C_{\frac{5}{2}} [(1+Y)w] \right\}$$

$$\varepsilon_2 = 1 - X \left\{ (1-Y)w^2 C_{\frac{3}{2}} [(1-Y)w] + i\frac{5}{2} w C_{\frac{5}{2}} [(1-Y)w] \right\} \qquad (2.23)$$

$$\varepsilon_3 = 1 - X \left\{ w^2 C_{\frac{3}{2}} [w] + i\frac{5}{2} w C_{\frac{5}{2}} [w] \right\}$$

where ν_m is the collision frequency corresponding to the most probable electron speed ($|v|$) in a Maxwellian distribution [*Sen and Wyller*, 1960], $w = \omega \, \nu_m$, and

$$C_p(x) = \frac{1}{p!} \int_0^\infty \frac{u^p e^{-u}}{u^2 + x^2} \, du \qquad (2.24).$$

In this context $u = m_e v^2 / 2kT_e$ and $\nu(v) = u\nu_m$, where m_e is the electron mass, v

---

‡ The average electron energy at a temperature of 200 K is 0.026 eV for a Maxwellian distribution.

is the electron velocity, k is Boltzmann's constant, and T_e is the electron temperature. Approximate formulas for the integrals $C_{\frac{3}{2}}$ and $C_{\frac{5}{2}}$ have been derived by *Hara* [1963].§

As *Budden* [1985, p. 59] comments, it is preferable from a physical point of view to refer to the average momentum transfer collision frequency $\nu_{av} = \frac{3}{2}\nu_m$ rather than ν_m, but the reader should be aware of the difference since ν_m is used commonly in the literature, including the refractive index formulas rederived by *Budden* [1965]. The average collision frequency ν_{av} is theoretically identical to the collision frequency profile of *Banks* [1966] shown in Figure 2.4 (see also Appendix B).

2.2.3 Relation between the Magneto-Ionic Theories of *Appleton* [1932] and *Sen and Wyller* [1960]

In order to relate ν_m or ν_{av} to the effective collision frequency ν_{eff}, the expressions for the elements of the diagonalized permittivity tensor given by the two theories are set equal, with the result that [*Wait*, 1962, pp. 256–259; *Deeks*, 1966*b*]*

$$\frac{\nu_{eff}}{\nu_m} = \frac{\frac{5}{2}C_{\frac{5}{2}}(w_q)}{\left[\frac{5}{2}C_{\frac{5}{2}}(w_q)\right]^2 + \left[w_q C_{\frac{3}{2}}(w_q)\right]^2} + i\left\{\frac{w_q C_{\frac{3}{2}}(w_q)}{\left[\frac{5}{2}C_{\frac{5}{2}}(w_q)\right]^2 + \left[w_q C_{\frac{3}{2}}(w_q)\right]^2} - w_q\right\} \quad (2.25)$$

where $q = 1$, 2, or 3:

$$w_1 = \frac{\omega + \omega_{ce}}{\nu_m} = (1 + Y)w$$

$$w_2 = \frac{\omega - \omega_{ce}}{\nu_m} = (1 - Y)w \qquad\qquad (2.26).$$

$$w_3 = \frac{\omega}{\nu_m} = w$$

Figure 2.6 shows the real and imaginary parts of ν_{eff}/ν_m as functions of w_q. Theoretically, the conversion between ν_m and ν_{eff} is different for each element of the diagonalized permittivity matrix ε_1, ε_2, and ε_3. Since $w_1 \simeq -w_2 \simeq \omega_{ce}/\nu_m$ at VLF, however, the conversion is the same for matrix elements ε_1 and ε_2. Based on a similar analysis,

---

§ In order to evaluate the expression for ε_2 using *Hara's* [1963] approximations, the argument of $C_{\frac{3}{2}}$ and $C_{\frac{5}{2}}$ must be the absolute value of $(1 - Y)w$, a quantity which is negative at VLF.

* Note that *Wait's* [1962, p. 258] equation (173), which is supposed to give the inverse α_e of the real part of equation (2.25) above, is incorrect. The right-hand side should be inverted. The values of α_e in Table 1 on p. 259 of *Wait* [1962] are correct.

Deeks [1966b] used an approximate conversion in which the imaginary part of ν_{eff}/ν_m was set to zero and the real part was as shown in Figure 2.6 with $w_q = \omega_{ce}/\nu_m$. The simple conversion used by *Budden* [1965] is $\nu_{eff} \simeq \frac{5}{2}\nu_m$ for the case $\nu_m \ll |\omega \pm \omega_{ce}|$, or $\nu_m \ll \omega_{ce}$ at VLF, consistent with Figure 2.6. For the model D region used here, this condition is true above 80 km (see Figure 2.9 below).
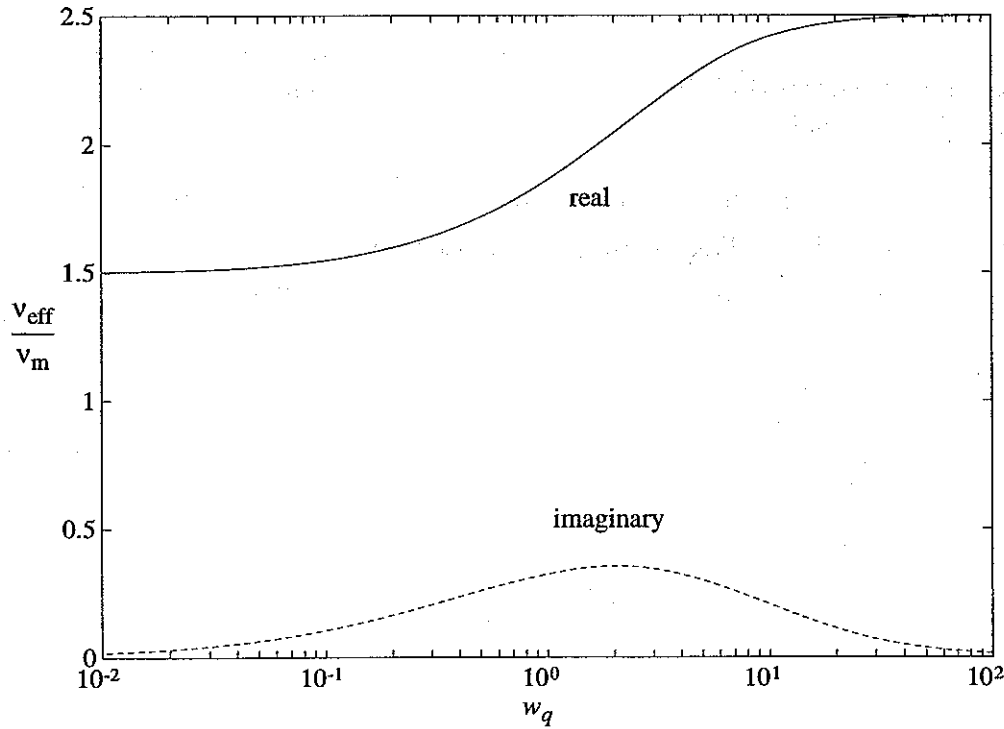
Figure 2.6. Conversion of average to effective collision frequency. Real and imaginary parts of ν_{eff}/ν_m as a function of w_q, where $q = 1$, 2, or 3, and $w_1 = (\omega + \omega_{ce})/\nu_m$, $w_2 = (\omega - \omega_{ce})/\nu_m$, and $w_3 = \omega/\nu_m$.

However, as shown in Figure 2.5, maximum absorption (and therefore heating) occurs over the altitude range 80-90 km when the QT approximation is valid (i.e., when the wave electric field is nearly parallel to the static magnetic field $\mathbf{B_o}$) [*Galejs*, 1972b; *Inan et al.*, 1992]. In this approximation, the ordinary refractive index is similar to the refractive index of an isotropic (unmagnetized) collisional plasma, which in turn is

equal to the square root of the element ε_3 of the diagonalized permittivity matrix. Since we are interested in determining maximum heating, the relation (2.25) between $\nu_{\rm eff}$ and $\nu_{\rm m}$ should properly be evaluated for $q = 3$. For ε_3, $w_q = w_3 = \omega/\nu_{\rm m}$ in Figure 2.6 and the approximation $\nu_{\rm eff} = \frac{3}{2}\nu_{\rm m} = \nu_{\rm av}$ is adequate below 90 km, where $\nu_{\rm m} \simeq \omega$, and strictly true below 80 km, where $\nu_{\rm m} \gg \omega$. In the light of the uncertainties in D region collision frequency and (especially) electron density profiles, the simple conversion $\nu_{\rm eff} = \nu_{\rm av}$ is adopted in this dissertation. This way, consistency is established between the predictions of maximum heating in Chapter 4, which assume $\nu(v) \propto v^2$, and the waveguide propagation calculations in Chapter 5, which assume ν constant with respect to v.

2.2.4 Application of a W.K.B. Propagation Model to the *D* Region at VLF

Although the refractive index of an anisotropic plasma is derived from the permittivity matrix assuming spatial homogeneity, it can be used to describe wave propagation in a medium that varies little in the space of a wavelength. Such solutions for a "slowly-varying" medium, known as "Wentzel-Kramers-Brillouin" or W.K.B. solutions after three scientists who used them in the 1920's to solve quantum mechanics problems, are treated comprehensively by *Budden* [1985].

For the purpose of evaluating the applicability of the W.K.B. approximation to VLF propagation through the D region, the real (μ) and negative imaginary (χ) parts of the refractive index have been calculated using the *Sen and Wyller* [1960] model, assuming $f = 24.0$ kHz, vertical incidence upon the lower edge of the ionosphere, and a dip angle of 73.4° (Figure 2.7). Since the free-space wavelength of a 24.0 kHz signal is 12.5 km, it is clear from Figure 2.7 that the D region may not be "slowly-varying." A quantitative definition of "slowly-varying" for an isotropic ionosphere and for vertical incidence upon an anisotropic ionosphere is that [*Budden*, 1985, pp. 177, 489–490]

$$\frac{1}{k}\left|\frac{1}{n^2}\frac{dn}{dh}\right| = \frac{\lambda_o}{2\pi\left(\mu^2 + \chi^2\right)}\sqrt{\left(\frac{d\mu}{dh}\right)^2 + \left(\frac{d\chi}{dh}\right)^2} \ll 1 \qquad (2.27)$$

where $\lambda_o = 2\pi/k$ is the free-space wavelength, h is the altitude, and $n = \mu - i\chi$ is the refractive index.† This criterion was applied to the refractive index profiles shown in·

---

† *Ratcliffe* [1959, p. 175] shows that this value is in fact four times the amplitude of a wave reflected from a "slowly-varying" medium when the incident wave has unit amplitude.
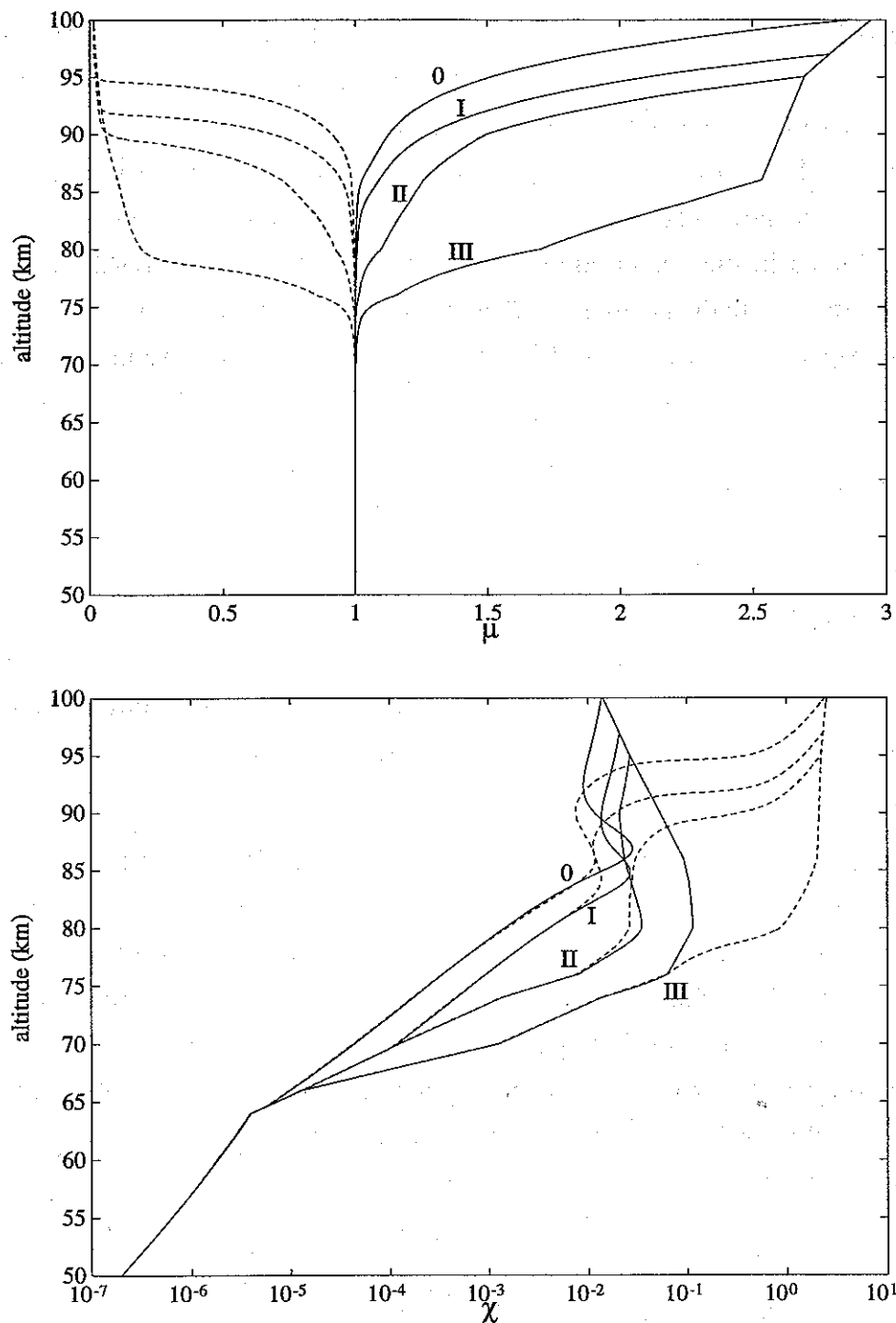
Figure 2.7. Refractive indices as functions of altitude. Real (μ) and negative imaginary (χ) parts of the Sen-Wyller refractive index of the D region for the four electron density profiles in Figure 2.3, assuming vertical incidence, $f = 24.0$ kHz, $\Theta = 16.6°$. Solid lines represent ordinary magneto-ionic component, dashed lines represent extraordinary component.

Figure 2.7 by approximating the derivatives by backward differences, i.e.,

$$\frac{d\mu}{dh}\bigg|_i \approx \frac{\mu_i - \mu_{i-1}}{\Delta h} \tag{2.28}$$

and similarly for $d\chi/dh$. For the results shown in Figure 2.8 we have used $\Delta h = 100$ m. The same criterion was also applied to refractive index profiles (not shown) calculated for the same conditions, except that the wave propagates in the geomagnetic north direction and is incident upon the ionosphere at a 45° angle. The results are shown in Figure 2.8 for the case of ambient electron density profile 0. Listed in Table 2.1 are the maximum values of the W.K.B. criterion (2.27) and the altitudes at which they occur for the ordinary (o) and extraordinary (x) modes.

Table 2.1
Evaluation of the W.K.B. approximation in the *D* region.

N_e Profile	mode	$\gamma = 90°$ $\max(k^{-1}|n^{-2}dn/dz|)$	h (km)	$\gamma = 45°$ $\max(k^{-1}|n^{-2}dn/dz|)$	h (km)
0	o	0.13	96.5	0.35	87.1
	x	87.9	94.6	70.0	94.6
I	o	0.13	93.7	0.32	85.0
	x	42.7	91.8	34.1	91.8
II	o	0.12	91.7	0.32	89.5
	x	17.8	89.5	14.2	89.5
III	o	0.20	76.0	0.54	76.0
	x	3.86	78.8	3.08	78.8

It is clear that the W.K.B. criterion (2.27) is violated in all cases to some degree in the *D* region. Because the non-penetrating or extraordinary mode undergoes total reflection, the criterion for this mode is violated substantially for both $\gamma = 45°$ and $\gamma = 90°$. For the ordinary mode at vertical incidence, the W.K.B. approximation is marginally valid,
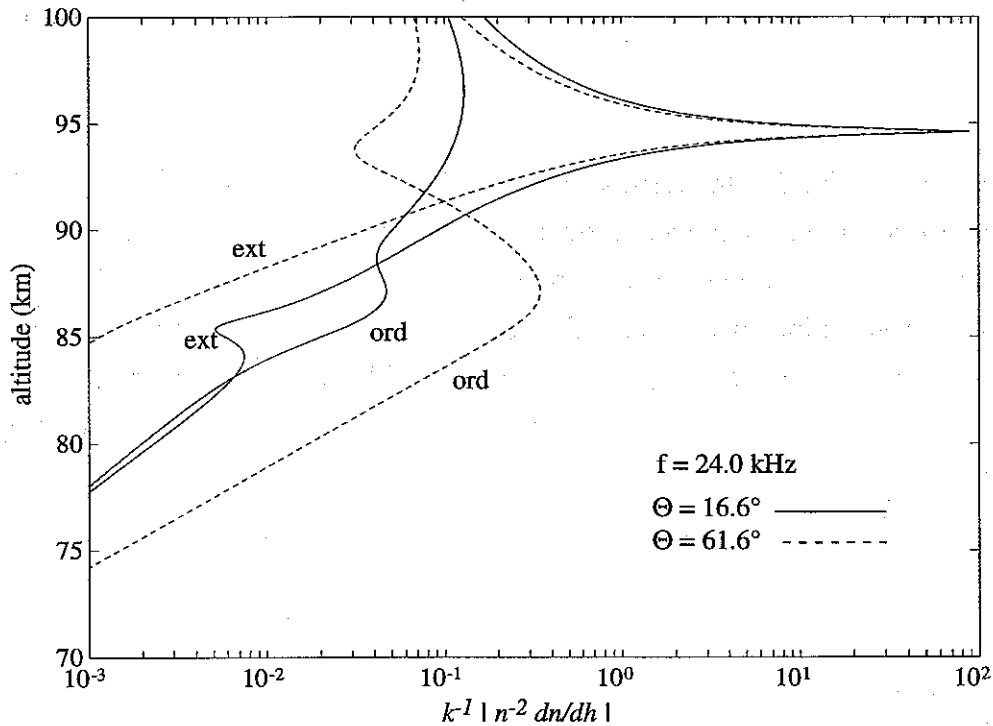
Figure 2.8. Validity of W.K.B. solution as function of altitude. Validity of W.K.B. solution expressed as $k^{-1}|n^{-2}dn/dz|$, plotted as a function of altitude in a D region represented by N_e profile 0, for f = 24.0 kHz. The two cases shown are Θ = 16.6° (vertical incidence, γ = 90°) and Θ = 61.6° (γ = 45° in the geomagnetic north direction).

consistent with a weak partial reflection. At $\gamma = 45°$, the ordinary mode undergoes a substantial partial reflection due in part to the very large χ typical of the ordinary mode under quasi-transverse conditions (Figure 2.5).

It is instructive to compare these results with the predictions of a simpler approximate method for determining the D region reflection height that uses the normalized frequencies of the magneto-ionic theory $X = (\omega_{pe}/\omega)^2$, $Y = \omega_{ce}/\omega$, and $Z = \nu_{\text{eff}}/\omega$. The normalized frequencies are plotted in Figure 2.9 for the four D regions represented by electron density profiles 0, I, II, and III. The D region is characterized by an electron density (X) increasing exponentially with altitude, an electron collision frequency (Z) decreasing exponentially with altitude, and an electron gyrofrequency (Y) essentially constant with altitude (Figure 2.9). According to *Ratcliffe* [1959, pp. 90, 139–140], reflection at VLF in a typical D region occurs both at the altitude where $X \simeq Z$ and at the altitude where
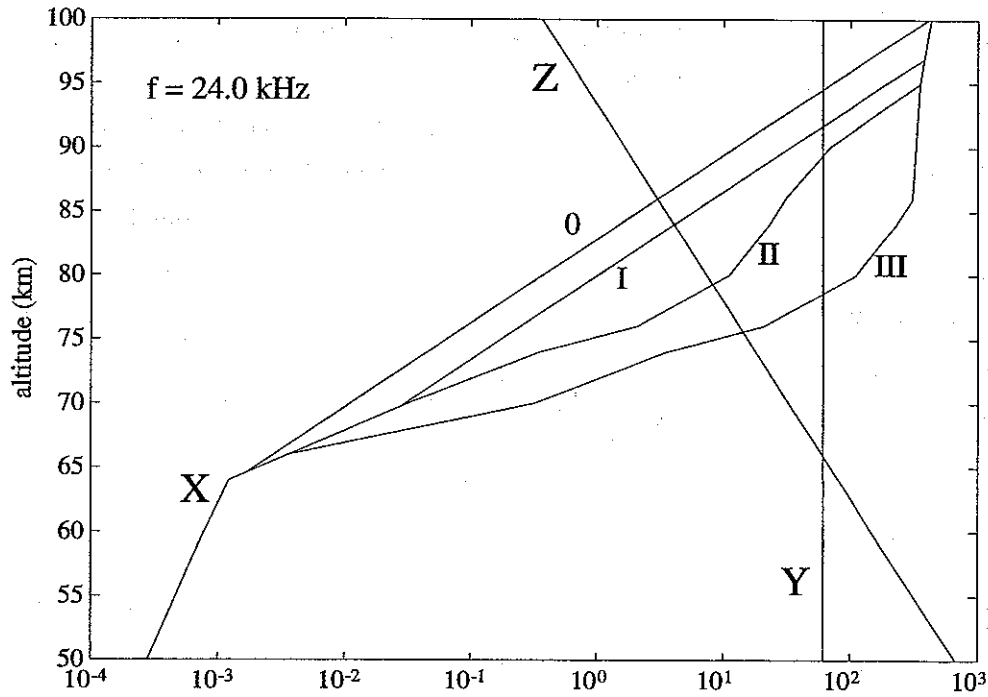
Figure 2.9. Normalized frequencies X, Y, **and** Z. Normalized frequencies $X = (\omega_{pe}/\omega)^2$, $Y = \omega_{ce}/\omega$, and $Z = \nu_{\mathrm{eff}}/\omega$ in the notation of the magneto-ionic theory [*Ratcliffe*, 1959], for the four electron density profiles 0, I, II, and III (Figure 2.3) and the collision frequency profile of *Wait and Spies* [1964] (Figure 2.4). The frequency and geomagnetic latitude are those of the NAA transmitter ($f = 24.0$ kHz, dip angle $= 73.4°$).

$X \simeq Y$ (if $\nu \ll \omega_{ce}$). Comparing Figure 2.9 to Figure 2.7, it can be seen that maximum absorption (χ) for the ordinary wave occurs near where $X \simeq Z$ [*Inan*, 1990a]. By comparing Figure 2.9 to Table 2.1 it can be seen that the altitudes at which the W.K.B. criterion is violated most strongly for each mode suggest reflection near $X \simeq Y$ for the extraordinary mode and in the case of the ordinary mode at vertical incidence, while the ordinary mode at $\gamma = 45°$ undergoes partial reflection near $X \simeq Z$, the region of maximum absorption. The latter is consistent with the similarity of quasi-transverse (QT) propagation in the ordinary mode to propagation in an isotropic (unmagnetized) collisional ionosphere (Figure 2.5). (The differences between the predictions of the magneto-ionic theories of *Appleton* [1932] and *Sen and Wyller* [1960] are not significant in this context.)

For the ordinary wave, with the exception of QL conditions, the reflection height is above the height of maximum absorption, where most of the heating is expected to occur.

For the extraordinary wave, and for the ordinary wave under QL conditions, the height of maximum absorption coincides roughly with the reflection height. Thus, in all cases, the W.K.B. approximation gives the incident wave accurately up to near the altitude of maximum absorption. Reflection may result in standing waves that cause the strength of the total field to oscillate about the value predicted for the incident wave [*Pitteway*, 1965; *Maslin*, 1974, 1975], with corresponding departures from the electron heating predicted using the W.K.B. model. In the region between the altitudes of maximum absorption and reflection where the W.K.B. approximation fails, the ordinary and extraordinary modes do not propagate independently of each other. However such effects should not be significant in the estimates of the heating up to the altitude of maximum absorption.

2.3   RADIO-WAVE HEATING OF A WEAKLY-IONIZED PLASMA

Noting that "the original theory of Bailey and Martyn was developed in terms of ideas more familiar to students of electrical discharges in gases than to students of the ionosphere," *Huxley and Ratcliffe* [1949] presented the theory in terms familiar to the ionospheric scientist and engineer. Although the theory of radiowave heating of plasmas has grown in scope and sophistication since then [e.g., *Gurevich*, 1978], the "elementary" theory of *Huxley and Ratcliffe* [1949] is still of practical interest and serves as a good introduction to the study of nonlinear thermal effects of electromagnetic waves in plasmas.

In the absence of a perturbing wave, the electrons, ions, and neutrals in a partially ionized plasma are in thermal equilibrium at temperature T_n. Under heated conditions, the electron temperature T_e is greater than T_n. As the electrons gain energy from the field in excess of the ambient value, they will on average tend to lose energy in collisions with neutrals and ions. Heuristically, then, the balance between the energy gained by the electron from the electromagnetic wave and the energy lost in collisions with neutrals is given by

$$\frac{dQ}{dt} = -G\nu_{\mathrm{av}}(Q - Q_o) + \frac{U}{N_e} \tag{2.29}$$

where Q is the average electron kinetic energy, Q_o is its ambient equilibrium value, G is the fraction of an electron's energy beyond equilibrium lost in one collision, U is the power dissipated in a unit volume by the wave, N_e is the ambient electron number density, and ν_{av} is the average electron-neutral momentum transfer collision frequency

[*Huxley and Ratcliffe*, 1949]. For a Maxwellian distribution, $Q_o = \frac{3}{2}kT_n$ and $Q = \frac{3}{2}kT_e$. In general, the loss factor G is of order 10^{-3}, mostly due to rotational excitation of N_2 and O_2, with very little contribution from elastic collisions [*Huxley*, 1949, 1959; *Mentzoni*, 1968]. The first analyses of observations of VLF heating [*Inan*, 1990a; *Inan et al.*, 1992] were carried out using a value $G = 1.3 \times 10^{-3}$ derived from laboratory measurements in air assuming a Druyvesteyn distribution of electron velocities [*Huxley and Zaazou*, 1949; *Druyvesteyn*, 1934] and attributed to rotational excitation of N_2 and O_2 [*Huxley*, 1949]. A review of more recent laboratory and ionospheric cross-modulation experiments indicates that a value of $G \simeq 6 \times 10^{-3}$ is more appropriate [*Fejer*, 1970]. Furthermore, the G-factor is in general a function of both T_e and T_n [*Gurevich*, 1978, p. 86].

Based on laboratory observations of electrons in N_2 [*Phelps and Pack*, 1959] the velocity-dependent collision frequency is assumed to be proportional to electron kinetic energy, i.e., $\nu(v) = Cv^2$, where C is some constant. For a Maxwellian distribution [*Maslin*, 1974],

$$\nu_{\mathrm{av}} = C\langle v^2 \rangle = \frac{3CkT_e}{m_e} \tag{2.30}$$

where k is Boltzmann's constant, T_e is the temperature of the electron gas, and m_e is the electron mass. In the rest of this dissertation, it will be assumed based on the discussion in the previous section that $\nu = \nu_{\mathrm{av}} = \nu_{\mathrm{eff}}$. Equation (2.29) can then be rewritten as [*Inan et al.*, 1991]

$$\frac{d\nu}{dt} = -G\nu(\nu - \nu_o) + \frac{2\nu_o U}{3N_e kT_n} \tag{2.31}$$

where ν_o is the ambient collision frequency and T_n is the ambient (unheated) electron and neutral temperature. Then, for a given U, if G is independent of T_e,

$$\Delta\nu(t) = \nu - \nu_o = \left(\frac{\gamma}{2G} - \frac{\nu_o}{2}\right)\left(\frac{1 - e^{-\gamma t}}{1 + \epsilon e^{-\gamma t}}\right) \tag{2.32}$$

where

$$\gamma = \sqrt{\frac{8G\nu_o U}{3kT_n N_e} + G^2\nu_o^2} \tag{2.33}$$

and

$$\epsilon = \frac{1 - \frac{G\nu_o}{\gamma}}{1 + \frac{G\nu_o}{\gamma}} \tag{2.34}.$$

In cases of moderate to strong heating, such as by lightning, $\epsilon \simeq 1$, which is the approximation used by *Inan et al.* [1991]. In the case of relatively weak heating by man-made transmitters, the full expression for ϵ must be used.

Equation (2.29) also may be rewritten as

$$\frac{3}{2}kN_e\frac{dT_e}{dt} = -L + U \quad (\text{J m}^{-3} \text{ s}^{-1}) \tag{2.35}$$

where L is an electron cooling rate given by

$$L = \frac{3}{2}kN_eG\nu(T_e - T_n) \tag{2.36}$$

and G is in general a function of T_e and T_n [*Gurevich*, 1978, p. 86]. For the radio wave power levels considered in this work, the total cooling rate is given by

$$L_{tot}(T_e, T_n) = \sum_{i=1}^{3} \left[L_i(\text{e}, \text{N}_2) + L_i(\text{e}, \text{O}_2) \right] \tag{2.37}$$

where i represents elastic collisions and rotational and vibrational excitation of N_2 and O_2 [*Schunk and Nagy*, 1978; *Rietveld et al.*, 1986; *Barr and Stubbe*, 1992]. These various cooling or loss rates L_i have been determined both empirically and theoretically for Maxwellian distributions and are discussed in Appendix B.

(Expressions for the average momentum-transfer collision frequencies that are consistent with the above cooling rates for elastic collisions [*Banks*, 1966; *Schunk and Nagy*, 1978] are given in Appendix B. According to these expressions, the momentum-transfer collision frequencies for N_2 and O_2 are only approximately proportional to electron temperature.)

3

Remote Sensing of VLF Transmitter Heating Using Subionospheric VLF Probe Waves

As discussed in Chapter 1, the first experimental evidence for heating of the nighttime D region by very-low-frequency (VLF) transmitters [*Inan*, 1990a] was in the form of cross-modulation of the 24.0 kHz NAA waveguide signal, observed at Palmer Station, Antarctica, by the signal radiated by the 28.5 kHz NAU transmitter in Aguadilla, Puerto Rico. Using a model of propagation in the Earth-ionosphere waveguide in the presence of D region disturbances due to VLF heating, it was shown that the observations were consistent with the heating mechanism presented in the last section of Chapter 2 [*Inan et al.*, 1992]. In this chapter, we present three new sets of experimental evidence of cross-modulation between subionospheric VLF signals that is interpreted to be due to VLF heating. These new data sets, involving powerful and continuously operating VLF signal sources, suggest that VLF transmitters may substantially heat the nighttime D region overhead on a regular basis and produce easily detectable changes in other VLF signals propagating in the Earth-ionosphere waveguide.

3.1 DESCRIPTION OF THE EXPERIMENT

In recent years, Stanford University has conducted VLF remote-sensing experiments at multiple sites across the continental United States and Canada [e.g., *Inan et al.*, 1990] and Antarctica [e.g., *Burgess and Inan*, 1993]. These observations rely on narrowband (±150 or ±250 Hz), high-time-resolution (10, 20, or 50 ms) recordings of the amplitudes and phases of VLF transmitter signals ("probe waves") propagating in the Earth-ionosphere

waveguide. The VLF transmitters and one low-frequency (LF, 30-300 kHz) transmitter whose probe waves are analyzed in this dissertation are listed in Table 3.1. The data sets examined consisted of continuous recordings on digital magnetic tape made typically at night for up to 12 hours and summary charts printed daily and archived for quick look purposes.

Table 3.1
VLF and LF transmitter sources of subionospheric probe waves.

Call Letters	Frequency (kHz)	Latitude (N)	Longitude (W)	Site Name
NSS	21.4	38°59'	76°27'	Annapolis, Maryland
NPM	23.4	21°25'	158°09'	Lualualei, Oahu, Hawaii
NAA	24.0	44°39'	67°17'	Cutler, Maine
NLK	24.8	48°12'	121°55'	Jim Creek, Washington
NAU	28.5	18°25'	67°09'	Aguadilla, Puerto Rico
—	48.5	41°30'	97°36'	Silver Creek, Nebraska

The original purpose of these observations was to study the spatial distribution and occurrence characteristics of localized and transient disturbances of the nighttime D region that occur in association with atmospheric lightning discharges [e.g., *Inan et al.*, 1988, 1990]. In 1989, as part of an experiment funded by the Office of Naval Research (ONR), one of the Stanford VLF systems was deployed at Arecibo, Puerto Rico, in order to measure (by means of associated ionospheric disturbances) the precipitation of energetic radiation belt electrons by radio waves injected into the ionosphere [*Imhof et al.*, 1983a, b] using the NAU transmitter in Aguadilla, Puerto Rico, operating at 28.5 kHz and radiating a total power of 100 kW. The first experimental evidence for VLF transmitter heating was discovered in the course of controlled VLF wave-injection experiments with the NAU transmitter designed to induce detectable electron precipitation signatures [*Inan*, 1990a].

This serendipitous discovery led to the suggestion [*Inan*, 1990*b*] of heating experiments with the more powerful (1000 kW) NAA transmitter in Cutler, Maine (Figure 3.1). Such an experiment was organized in 1992, again with ONR support, and constitutes the primary experiment on which this thesis is based. In this experiment, ionospheric heating by the 24.0 kHz NAA transmitter is measured using the 21.4 kHz NSS signal propagating from Annapolis, Maryland, to Gander, Newfoundland (NSS-GA), as the primary probe wave (Figure 3.1).

Although plans to operate NAA in specially designed modulation patterns (in collaboration with and by courtesy of the U. S. Navy) have not yet been realized, cross-modulation of the NSS-GA probe wave amplitude and phase was observed at times when NAA turned OFF in the course of normal operations for durations of < 1 s to several hours (referred to here as OFF/ON episodes). By analogy with the NAU heating results, it was hypothesized that these cross-modulation events were signatures of ionospheric heating by NAA. Similar cross-modulation suggestive of ionospheric heating was found subsequently in single OFF/ON episodes in data (amplitude only) from two other suitable VLF heater-probe wave configurations: the NPM-Saskatoon probe wave detecting heating by NLK (Figure 3.7) and the NAA-Huntsville probe wave detecting heating by NSS (Figure 3.10). In each case, one month of summary plots of narrowband probe wave amplitudes (and phases, in the case of Gander), selected based on data availability, was examined for heater OFF/ON episodes.

3.2 THE NAA TRANSMITTER AS AN IONOSPHERIC HEATER

At Gander, two 1.7 m × 1.7 m vertical loops (made of 11 turns of wire) were erected so that the NAA signal was nulled on antenna A and received nearly at full strength on antenna B. The NLK-GA and NAU-GA data analyzed in this dissertation were received on antenna A whereas the NSS-GA and NAA-GA data were received on antenna B. During December 1992, NAA turned OFF/ON 52 times at night, for 8 of which only amplitude data are available. In 41 of the 52 episodes, the amplitude and/or phase of the NSS-GA probe wave were detectably perturbed. Of the 52 total OFF/ON episodes, 38 occurred during the period 0000-0030 UT. In one well-defined case, shown in the right half of Figure 3.2, the amplitude and phase of NSS-GA are perturbed in response to NAA
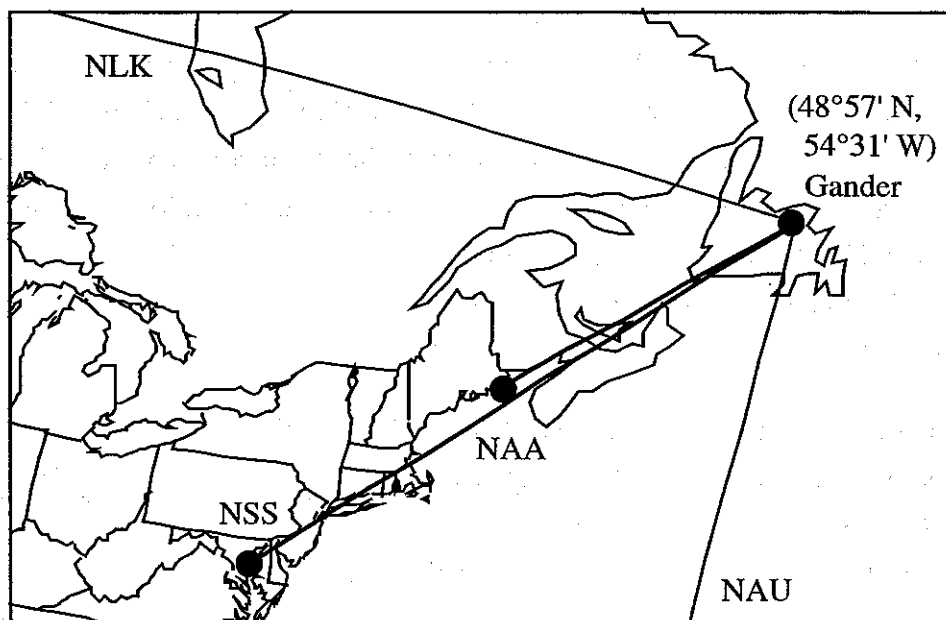
Figure 3.1. Configuration of subionospheric VLF probe wave paths monitored at Gander during December 1992. Map of North America and the Atlantic Ocean showing the great circle paths of subionospheric VLF probe waves observed at Gander, Newfoundland. This observational configuration was targeted to observe heating by the NAA transmitter using the NSS-Gander probe wave, whose 2063-km great circle path passes within 53 km of NAA.

heating by +0.32 dB and −2.7°, respectively.* These perturbations are superposed on slow background variations that, in the case of phase, are largely due to local oscillator drift.

It is important to understand that the signal perturbations shown in Figure 3.2 represent a temporary *cooling* of the D region electrons when the NAA transmitter turns OFF. In the light of the emphasis of this research on ionospheric *heating*, the leading edges of the amplitude and phase perturbations were measured and subsequently inverted before being tabulated. The leading edges were measured because NAA does not always turn back ON immediately to full power (e.g., Figure 3.2, right side). Indeed, in four cases NAA simply turned OFF at 1000 UT for the rest of the night. A scatter plot of the 41 observed pairs of amplitude and phase changes recorded in this manner is shown in Figure 3.3. The amplitude perturbations ranged from −0.11 to +0.84 dB while the phase

---

* It is standard practice to give amplitude changes in dB as $20\log(1 + \Delta A/A_o)$, where A_o is the signal amplitude immediately prior to the disturbance and ΔA is the amplitude change caused by the disturbance.
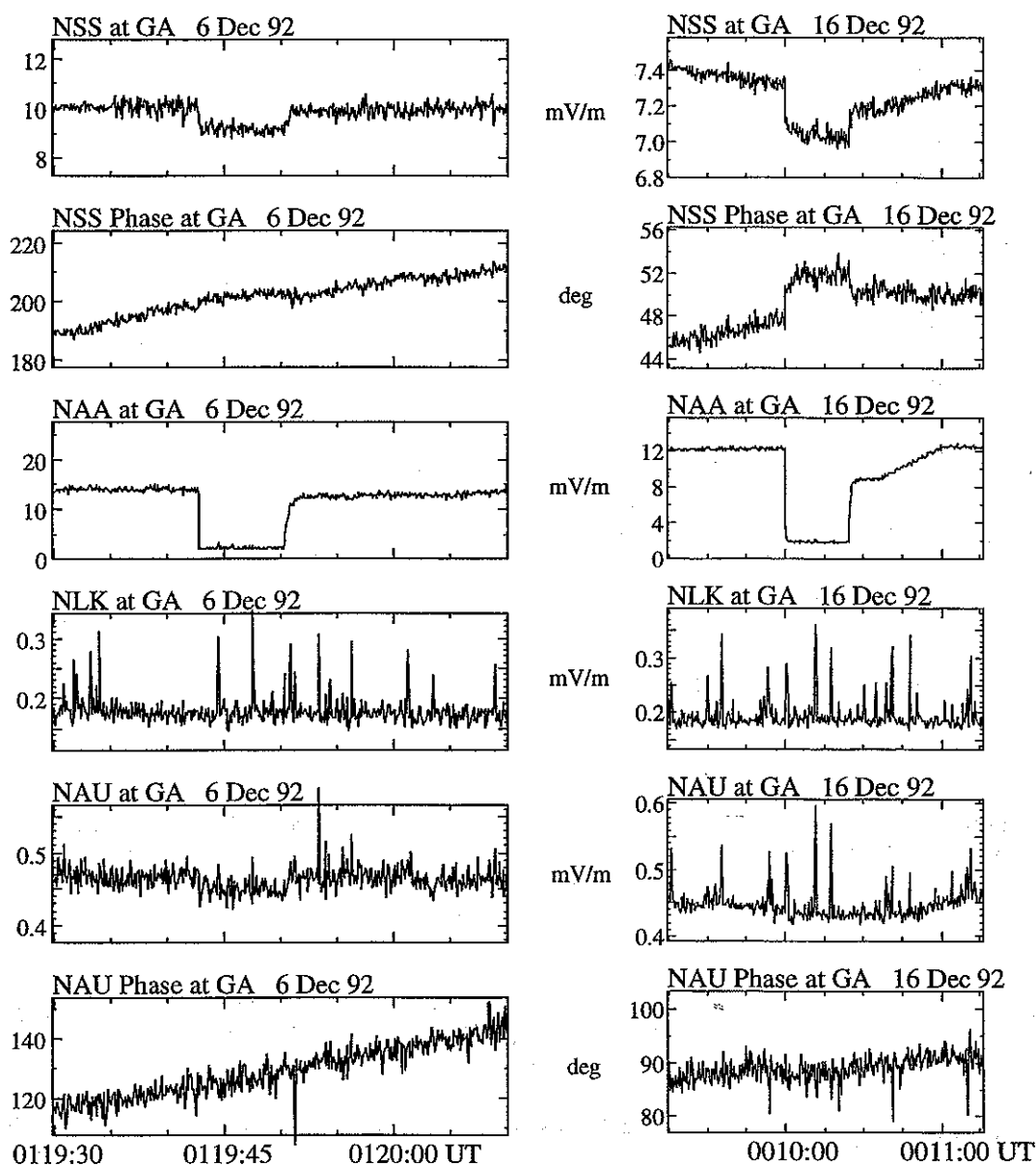
Figure 3.2. Heating by NAA observed at Gander. (LEFT) NAA heating measured with the NSS-GA probe wave amplitude and phase and the NAU-GA amplitude on December 6, 1992. The NAA-GA field strength on antenna A (not shown) is 3.5 mV m^{-1}. NLK-GA amplitude and NAU phase are not affected. (RIGHT) NAA heating measured with the NSS-GA probe wave amplitude and phase on December 16, 1992. NLK-GA amplitude and NAU-GA amplitude and phase are not affected. Note that the horizontal scales of the left and right panels are different. In both cases the linear vertical scale shows electric field in mV m^{-1} or phase in degrees.
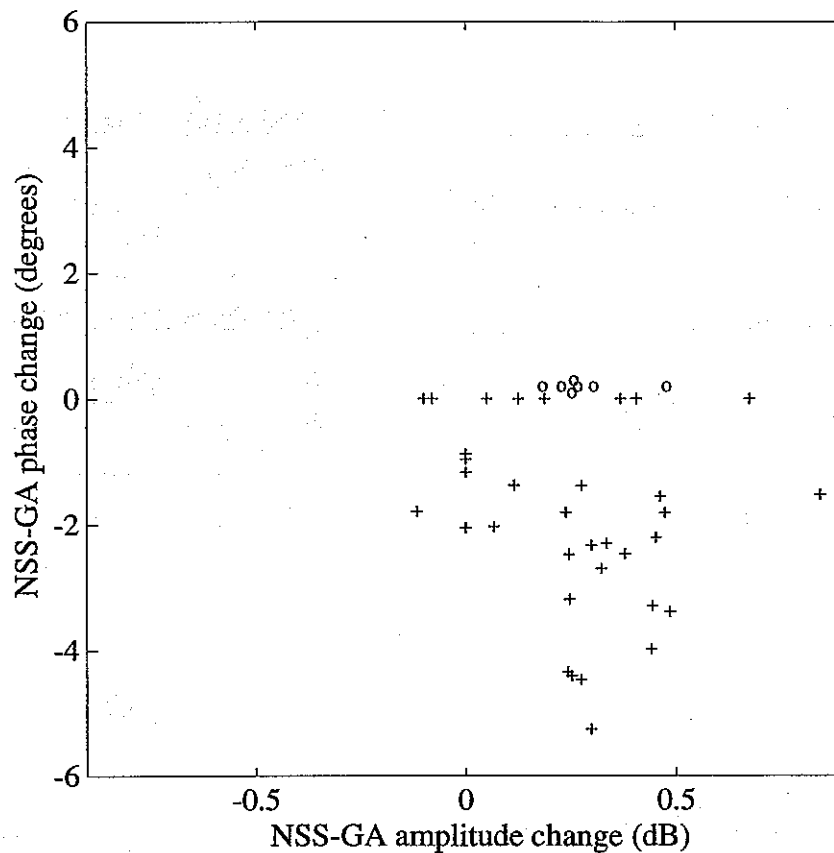
Figure 3.3. Amplitude and phase perturbation pairs observed on the NSS-GA signal during NAA OFF/ON episodes, December 1992. Open circles indicate no phase (ϕ) data available; these points have been plotted slightly off the $\Delta\phi = 0$ axis for clarity.

changes ranged from 0 to −5.3 degrees. The thresholds of detectability of amplitude and phase changes were approximately 0.1 dB and 0.5°, respectively.

In 6 of these 41 episodes, the NAU-GA probe wave amplitude was also perturbed (Table 3.2). In the case shown in the left half of Figure 3.2, the amplitude perturbation on NAU-GA due to NAA heating is +0.29 dB, and the associated amplitude and phase perturbations on NSS-GA are 0.84 dB and −1.5°, respectively. All but one of the six perturbations on NAU-GA were positive, and no phase perturbation was ever observed. In contrast, no detectable associated perturbations were observed on the NLK-GA signal. The observations of perturbations on the NAU-GA signal caused by NAA are surprising in the light of the > 770 km distance between NAA and the NAU-GA great circle path

Table 3.2
NAA heating detected with the NAU-GA probe wave.

Date, 1992	Time (UT)	amplitude (mV m^{-1})	NAU-GA amplitude change (dB)	phase change (°)
06 Dec	01:19	0.46	+0.29	0
06 Dec	04:07	0.68	+0.07	0
07 Dec	09:14	0.50	+0.23	0
07 Dec	10:00	0.57	+0.22	0
17 Dec	00:10	0.56	+0.20	0
28 Dec	00:10	1.00	−0.09	0

(Figure 3.1). A discussion of these anomalous observations based on the theory of VLF propagation in the Earth-ionosphere waveguide is presented in Chapter 5.

3.2.1 Field Strengths of VLF Probe Waves at Gander

The effectiveness of VLF heating, as well as the sensitivity of a subionospheric VLF probe wave to the heating, are likely to depend on the ambient D region conditions, which vary from day to day [*Davies*, 1990, p. 143]. One possible measure of the state of the ambient D region is the absolute amplitude of the transmitter signals at the receiver, since the propagation characteristics of VLF signals depend on the ambient D region electron density and temperature [e.g., *Galejs*, 1972*a*].

A scatter plot of the field strengths of NAA-GA and NSS-GA observed immediately prior to the 52 NAA OFF/ON events during December 1992 shows a tendency for the NSS-GA probe wave to be sensitive to NAA heating when the NAA signal observed at Gander is lower and the NSS signal is higher in strength (Figure 3.4). Comparison of the magnitude of the NSS-GA signal perturbations with the total NAA-GA field strength indicates a possible trend for the absolute magnitudes of the NSS-GA amplitude and phase perturbations to decrease as the NAA-GA field strength increases (Figure 3.5).

The data in Figure 3.4 are presented again in Chapter 5 (Figure 5.4) together with the theoretical NAA and NSS vertical electric field strengths predicted for different ambient
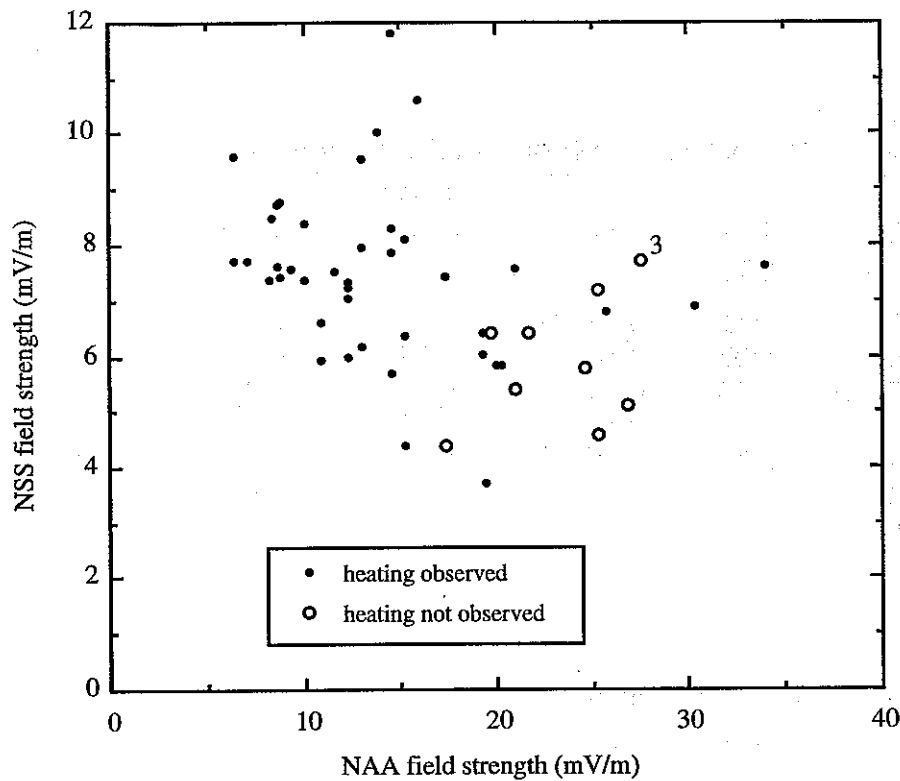
Figure 3.4. Signal strengths of NAA and NSS at Gander. Vertical electric field of NAA-GA and NSS-GA immediately prior to NAA OFF-ON episodes during December 1992. The "3" indicates three OFF/ON events occurring within the same minute on December 22, 1992.

model D region electron density profiles (Figure 2.3). The predicted field strengths are greater for the denser profiles (II and III) than for the more tenuous profiles (0 and I). Although a denser profile might be expected to lead to more attenuation and hence weaker waveguide signals, such is not necessarily the case due to the multiple mode nature of waveguide propagation, which results in pronounced minima and maxima in the field strength at the ground as a function of distance along the propagation path. Furthermore, the waveguide propagation model used to predict the total field strengths of NAA-GA and NSS-GA also predicts that the magnitudes of the NSS-GA phase perturbations tend to increase as the D region becomes more tenuous (Figure 5.3). Thus, the observations both of probe wave perturbations and of total field strength presented in this chapter are consistent with the mode predictions of Chapters 4 and 5 that VLF heating is more effective in a more tenuous ionosphere.
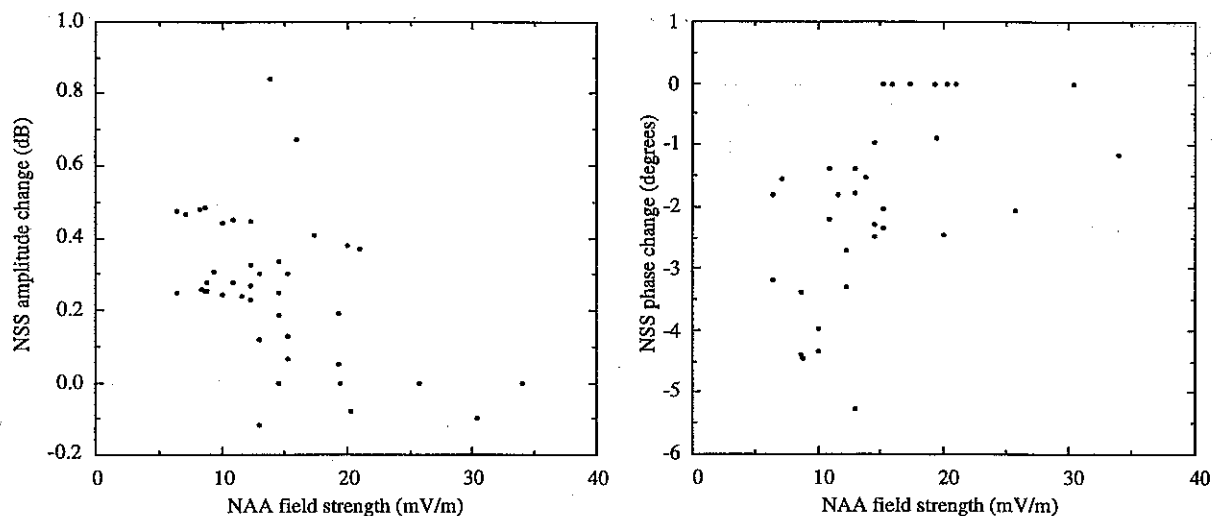
Figure 3.5. NSS-GA amplitude and phase changes due to NAA heating as functions of NAA amplitude received at Gander. Amplitude and phase changes on NSS-GA vs. vertical electric field of NAA-GA measured immediately prior to NAA OFF/ON episodes during December 1992.

A scatter plot of the field strengths of NAA-GA and NAU-GA (Figure 3.6) shows that NAU-GA was generally of average strength at times when it registered NAA heating signatures, while NAA-GA ranged from lowest to highest at these times. (At the time of the clearest signature of NAA heating on NAU-GA (0119 UT, December 6, 1992; Figure 3.2), NAA-GA was 13.8 mV m^{-1} and NAU-GA was 0.48 mV m^{-1}, neither being extreme values.) Despite the limited number of observations, it appears that the occurrence of ionospheric cross-modulation of NAU-GA by NAA depends much more strongly on the ionospheric conditions along the NAU-GA great circle path, which determine the NAU field strength at Gander, than on the conditions along the NAA-GA path.

3.2.2   Evaluation of Receiver Cross-Modulation

Since both the probe and heater wave signals are measured with the same apparatus, it is important to determine whether the observed cross-modulation between the two signals could have occurred within the receiver [*Inan*, 1990a]. The nonlinear cross-modulation response of the receiver at Gander was determined by locally injecting a 3-s ON/2-s OFF 24.0 kHz signal into the terminals of either antenna and performing superposed-epoch analysis of (typically) 60 min of data from VLF transmitter signals received concurrently. With a 24.0 kHz 140 mV m^{-1}-equivalent signal injected into the
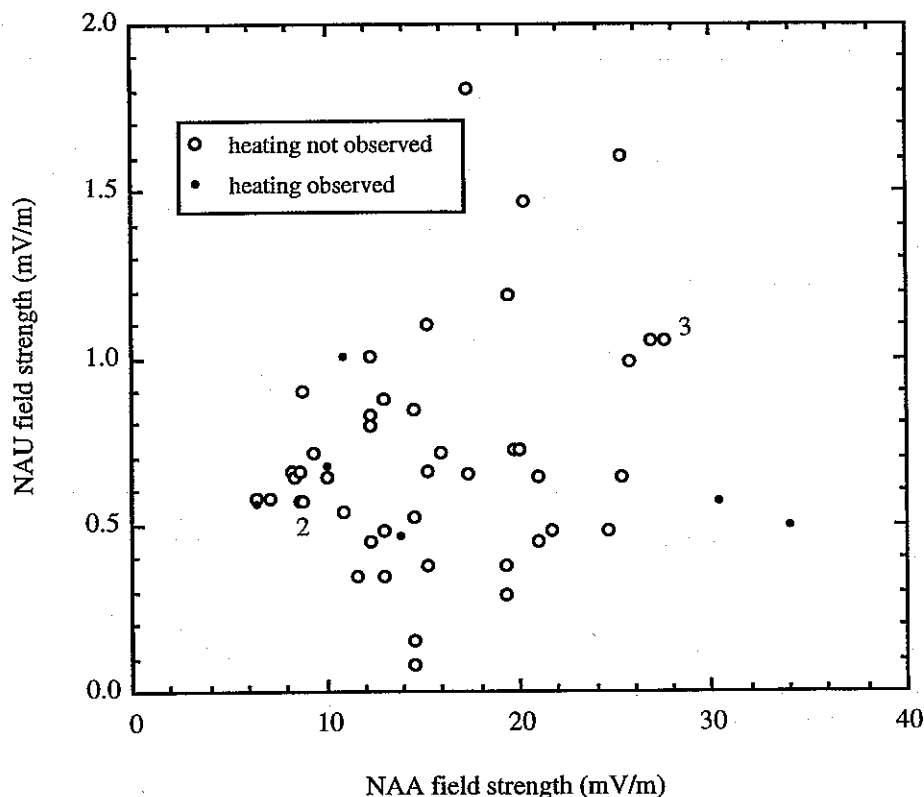
Figure 3.6. Signal strengths of NAA and NAU at Gander. Vertical electric field of NAA-GA and NAU-GA immediately prior to NAA OFF-ON episodes during December 1992. The "2" indicates 2 OFF/ON episodes occurring within 2 s of each other on December 6, 1992. The "3" indicates 3 OFF/ON episodes occurring within the same minute on December 22, 1992.

terminals of antenna B, the cross-modulation on NSS-GA was +0.02 dB and +0.2°, while at 34 mV m^{-1}-equivalent there was no perturbation of NSS phase or amplitude. With a 24.0 kHz 82 mV m^{-1}-equivalent signal injected into the terminals of antenna A, the cross-modulation on NAU-GA was −0.1 dB and −1°; NLK was perturbed +1.6 dB due to its proximity in frequency to NAA. At 31 mV m^{-1}-equivalent there was no perturbation of NAU phase or amplitude. By comparison the field strength of NAA-GA received on antenna B at times of NAA OFF/ON episodes during December 1992 ranged from 6.5 to 34 mV m^{-1}, while on antenna A it was always <8.4 mV m^{-1}. That is, the received NAA-GA field strengths were much less than the injected 24.0 kHz equivalent field strengths required to cause measureable cross-modulation within the receiver. We therefore conclude that the observed cross-modulation between NAA and the NSS-GA and NAU-GA probe waves (Figure 3.2) occurred in the ionosphere, consistent with NAA
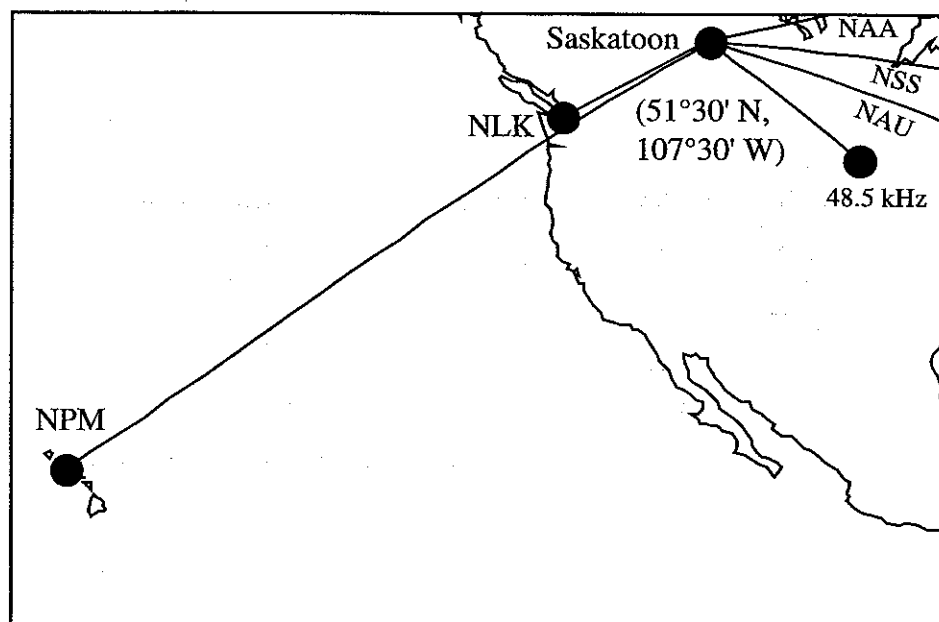
Figure 3.7. Configuration of subionospheric VLF probe wave paths monitored at Saskatoon during October-November 1987. Map of North America and the Pacific Ocean showing the great circle paths of subionospheric VLF probe waves observed at Saskatoon, Saskatchewan. Heating by NLK was discovered serendipitously using this configuration. The only probe wave affected by NLK heating was the NPM-Saskatoon probe wave, whose 5469-km great circle path passed within 79 km of NLK.

heating the D region. (For a detailed description of the instrumental cross-modulation tests see Appendix A.)

3.3 THE NLK TRANSMITTER AS AN IONOSPHERIC HEATER

In the second VLF heater/probe wave configuration considered here (Figure 3.7) the 23.4 kHz NPM signal propagating from Lualualei, Oahu, to Saskatoon, Saskatchewan (NPM-SA), was used to detect ionospheric heating by the NLK transmitter operating at 24.8 kHz with a nominal total radiated power of 850 kW. Between October 29 and November 23, 1987, 18 days of usable VLF probe wave amplitude data were recorded at Saskatoon from a geomagnetic north-south loop antenna, including 44 NLK OFF/ON episodes, in four of which the NPM-SA probe wave was perturbed (Table 3.3).

In the clearest of the four detectable cases, which occurred on October 29, 1987 (Figure 3.8), the response of the NPM-SA amplitude to heating (NLK ON) is -1.0 dB. In all four cases, the other probe waves observed at Saskatoon (Figure 3.7) are not

Table 3.3
NLK heating detected with the NPM-SA probe wave.

Date, 1987	Time (UT)	NPM-SA amplitude	
		% full scale	change (dB)
29 Oct	07:04	18	−1.0
07 Nov	08:56	5	−1.6
07 Nov	12:42	12	+0.6
21 Nov	05:48	22	−0.3

affected. The two observations of heating on November 7 are a subset of 30 OFF/ON episodes that occurred on November 6 and 7. In both cases, NLK had turned OFF/ON less than 10 min earlier, but without an effect on NPM-SA.

We note that intermittent interference at Saskatoon in the 23.40 ± 0.15 kHz band may have impaired our ability to measure NLK heating using the NPM-SA probe wave. One of a series of reports on radio time standards issued by the U. S. Naval Observatory confirms that NPM was off the air October 16 (0001 UT) through October 29 (0400 UT), 1987 [*U. S. Naval Observatory*, 1987]. During this period, the signal measured in the 23.4 ± 0.15 kHz band at Saskatoon was indeed much lower than before or after this period. However, there was a relatively weak intermittent signal in the same band that probably emanated from the 23.4 kHz transmitter in Rhauderfehn, Germany. The Rhauderfehn signal is readily observable in the Canadian Arctic [*Lauber and Bertrand*, 1993].

Shown in the upper half of Figure 3.9 is the amplitude of the signal in the 23.4 ± 0.15 kHz band at Saskatoon during the period 0600-0800 UT on October 28, 1987. There was a component in the signal that turned OFF and ON three times between 0600 and 0710 UT, then turned off for most of the rest of the 0700 hour. Shown in the lower half of Figure 3.9 is the same band during the period 0600-0800 UT on November 14, 1987, when the NPM transmitter was in operation. The amount of apparent noise (i.e., fluctuations in signal amplitude around its mean value) on the NPM signal suddenly decreased at around 0655 UT and remained low until around 0754 UT, when it increased to near its former level. Such step changes in the signal-to-noise ratio were evident on
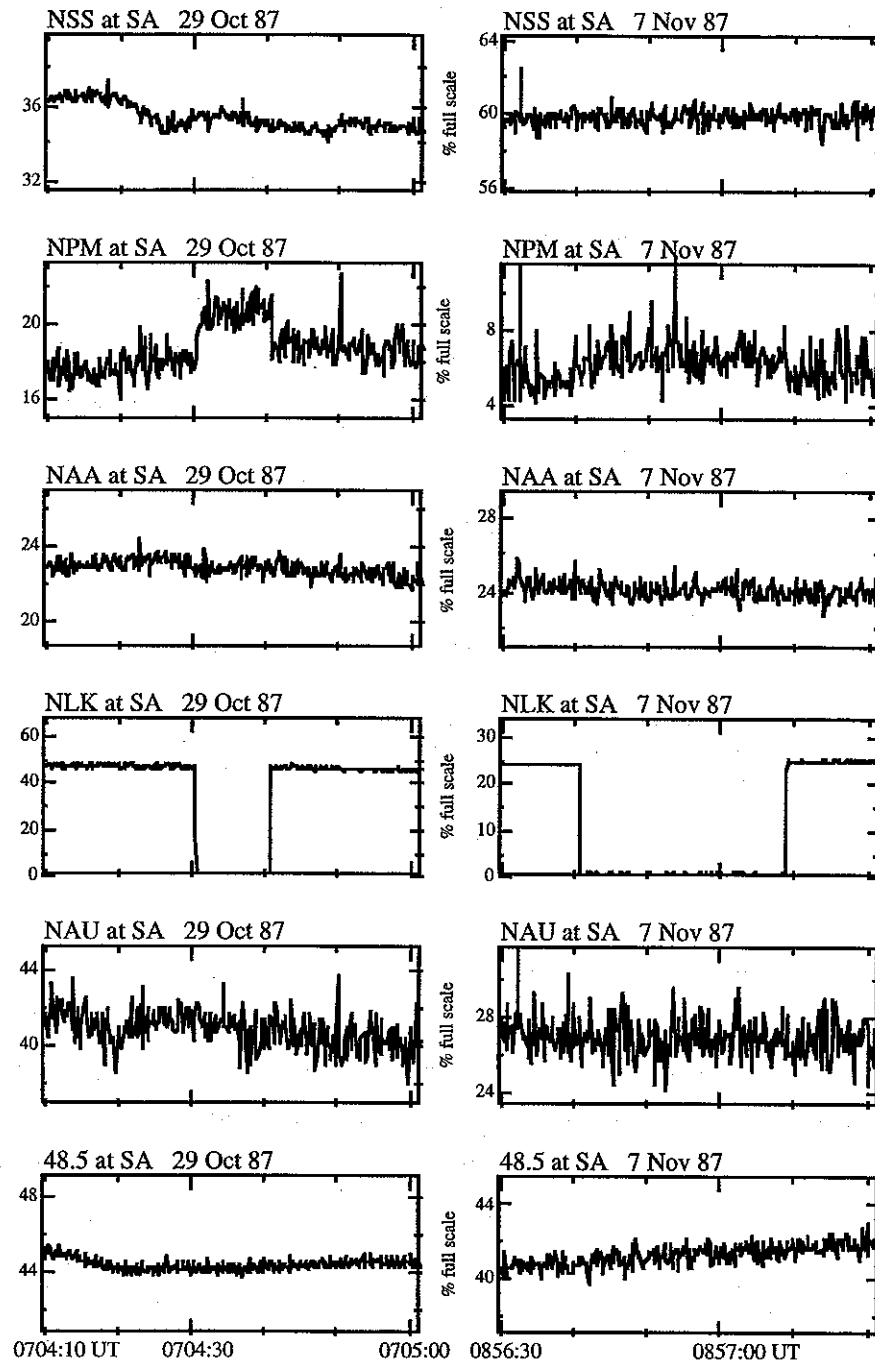
Figure 3.8. Heating by NLK observed at Saskatoon. (LEFT) Fifty seconds of amplitude data showing NLK heating as detected using the NPM-SA probe wave on October 29, 1987. The response to NLK turning ON (heating) at 07:04:40 UT is −1.0 dB. (RIGHT) Fifty seconds of amplitude data showing NLK heating as detected using the NPM-SA probe wave on November 7, 1987. The response to NLK turning ON (heating) at 07:04:40 UT is −1.6 dB. In both cases, the NSS, NAA, NAU, and 48.5 kHz signal amplitudes are not affected by the NLK heating.
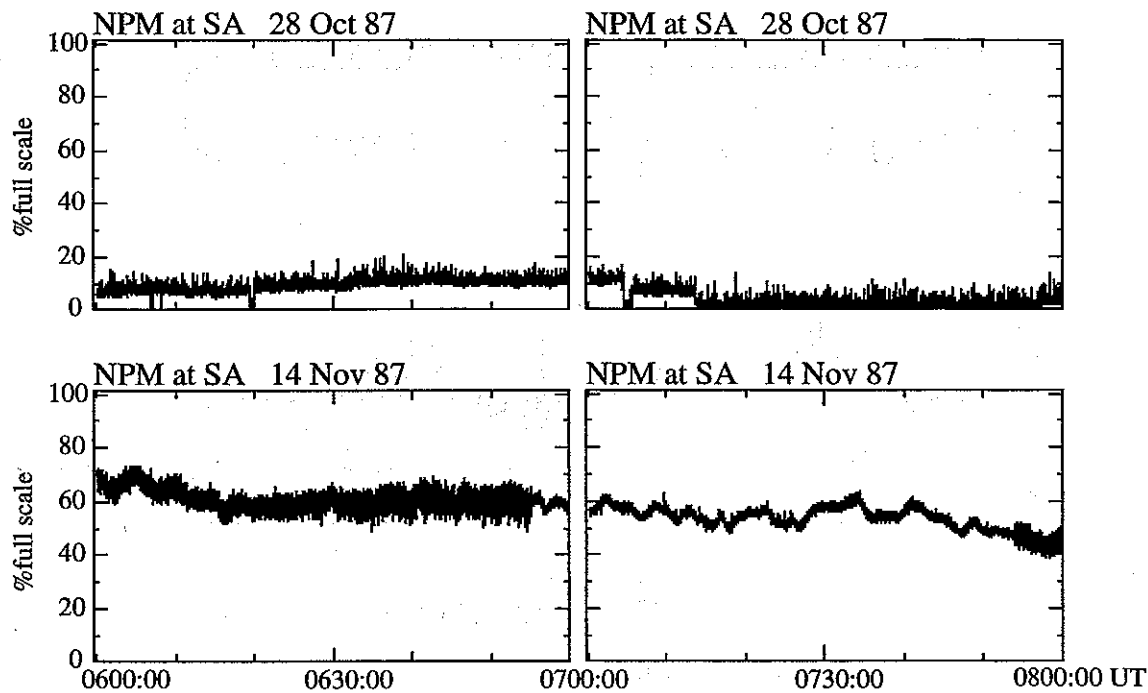
Figure 3.9. Interference at Saskatoon in the 23.4 ± 0.15 **kHz band.** Signal level in
the 23.40 ± 0.15 kHz band measured during 0600-0800 UT at Saskatoon on October 28,
1987, when NPM was not transmitting, and on November 14, 1987, when NPM was
transmitting.

other days when the NPM transmitter was in operation. The similarity of the OFF/ON
pattern of the 23.4 ± 0.15 kHz amplitude in the absence of NPM transmissions on October
28, 1987, to the variation of the signal-to-noise ratio on NPM-SA on November 14, 1987
suggests that they have the same origin. Indeed, *Lauber and Bertrand* [1993] show
data indicating that the Rhauderfehn amplitude alternately increases and decreases by
~ 15 dB approximately every hour. The interference from the Rhauderfehn signal thus
may have affected our ability to detect NLK heating using the NPM-SA probe wave, in
particular on November 6 and 7 when there were 30 NLK OFF/ON episodes but only
two observations of heating affecting the NPM-SA signal.
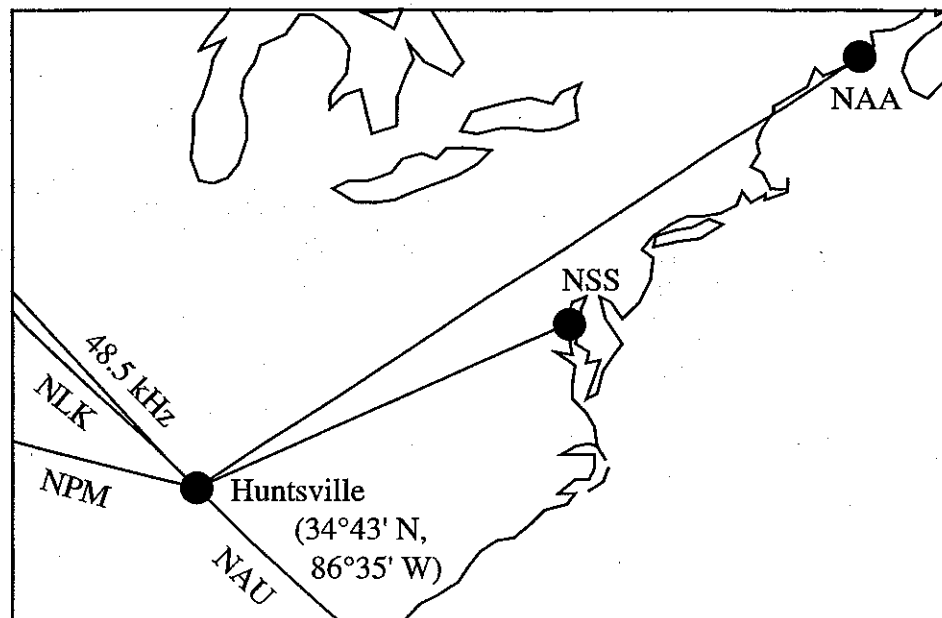
Figure 3.10. Configuration of subionospheric VLF probe wave paths monitored at Huntsville during February 1990. Map of a portion of North America showing the great circle paths of subionospheric VLF probe waves observed at Huntsville, Alabama. Heating by NSS was discovered serendipitously using this configuration. The only probe wave affected by NSS heating was the NAA-Huntsville probe wave, whose 1977-km great circle path passed within 160 km of NSS.

3.4 THE NSS TRANSMITTER AS AN IONOSPHERIC HEATER

In the third VLF heater/probe wave configuration considered here (Figure 3.10) the NAA signal observed at Huntsville, Alabama (NAA-HU), was used to detect ionospheric heating by the NSS transmitter operating at 21.4 kHz with a nominal total radiated power of 265 kW. During February 1990 there were 29 NSS OFF/ON episodes, in five of which the NAA-HU amplitude increased in response to NSS heating (Table 3.4). Four of the five cases occurred within 2 min of 0000 UT, while only eight of the 29 OFF/ON episodes occurred at this time. The other probe waves, received off the single loop antenna at Huntsville (its plane oriented geomagnetic north-south), were not affected in any of the episodes. In the clearest case, which occurred on February 14, 1990 (Figure 3.11), the response of the NAA-HU amplitude to heating (NSS ON) is +0.5 dB. The small decrease in the NAU-HU amplitude occurring 10 s after NSS turned OFF may have been due to a lightning-induced disturbance along the NAU-HU great circle path. The 48.5 kHz OFF/ON episodes occurred at the transmitter. In the case of February 12, 1990, the perturbation is much weaker (Figure 3.11).

Table 3.4
NSS heating detected with the NAA-HU probe wave.

Date, 1990	Time (UT)	NAA-HU amplitude	
		% full scale	change (dB)
12 Feb	23:58	43	+0.2
14 Feb	08:08	22	+0.5
16 Feb	23:58	30	+0.2
26 Feb	23:58	33	+0.3
27 Feb	00:00	33	+0.5

Note that, in principle, the OFF/ON episodes in the 48.5 kHz signal might have allowed the detection of heating by the 48.5 kHz transmitter, especially on the NLK-HU great circle path, which passes near this source. However, cursory examination of data in this and other studies has not revealed evidence of heating by the 48.5 kHz signal, consistent with its relatively low radiated power (60 kW) [*Naval Ocean Systems Center*, 1989].

3.5   DEPENDENCE ON GEOMAGNETIC CONDITIONS

The ability of VLF transmitters to heat the D region (Chapter 4) and the sensitivity of subionospheric VLF probe waves to this heating (Chapter 5) depend on the ambient electron density and temperature of the D region. Geomagnetic activity is one possible cause of night-to-night variability in the D region electron density since it is associated with increased levels of energetic (> 20 keV) electrons precipitated from the Earth's radiation belts into the nighttime D region, resulting in secondary ionization and hence increased electron density, which in turn affects subionospheric VLF propagation [*Potemra and Rosenberg*, 1973; *Voss and Smith*, 1980].

One commonly-used measure of geomagnetic activity is the planetary three-hour Kp index [*Mayaud*, 1980]. This index, which ranges in 28 steps from 0 to 9, is a quasi-logarithmic measure of variations in the magnetic field derived from observations at eleven mid- to sub-auroral latitude observatories ranging in geomagnetic latitude from 44° to 63° [*Mayaud*, 1980, p. 42].
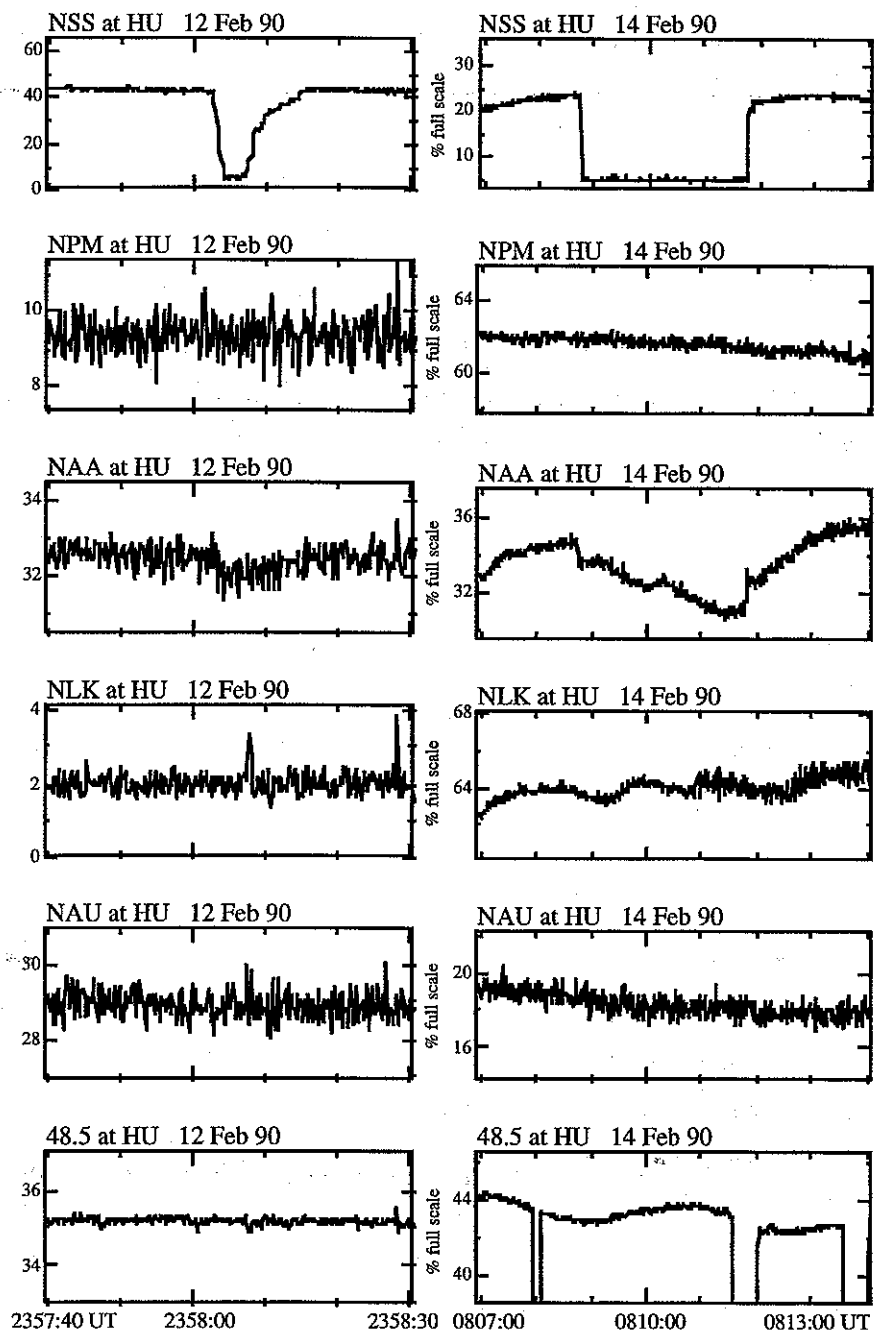
Figure 3.11. Heating by NSS observed at Huntsville. (LEFT) Fifty seconds of amplitude data showing NSS heating as detected by the NAA-HU probe wave on February 12, 1990. The response to NSS turning gradually back ON (heating) is +0.2 dB. (RIGHT) Seven minutes of amplitude data showing NSS heating as detected by the NAA-HU probe wave on February 14, 1990. The response to NSS turning ON (heating) at 08:11:45 UT is +0.5 dB. The slower variations are typical of NAA during this period. In both cases, the NPM, NLK, NAU, and 48.5 kHz amplitudes are not affected by the NSS heating.

In the case of NAA heating measured by the NSS-GA probe wave during December 1992, the global three-hour Kp indices [*Coffey*, 1993] for the periods preceding and concurrent with the 52 NAA OFF/ON episodes ranged from 0 to 6^+, with no apparent relation between size of perturbation and Kp. For the six NAA heating events observed on NAU-GA during December 1992, the preceding and concurrent Kp indices ranged from 0 to 5^-.

Although the number of observations of heating by NLK and NSS are quite limited, it is nevertheless useful to examine in this context the relevant Kp indices. In the case of the four observed NLK heating events observed on NPM-SA during October and November 1987, Kp indices during the preceding and concurrent three-hour period ranged from 1^- to 4 [*Coffey*, 1988a, b]. As regards the five NSS heating events observed on NAA-HU, February 1990 was a fairly disturbed month according to the Kp indices, with even the quietest day (February 12) being "not really quiet" [*Coffey*, 1990]. The Kp indices for the three-hour periods preceding and including the NSS heating event of February 12, 1990, were 0^+; for the other four events, the Kp indices ranged from 4 to 6^+.

In general, therefore, there is no evidence in the data analyzed here that either the VLF heating process itself or its detection by subionospheric VLF probe waves is dependent on geomagnetic activity as measured by the planetary three-hour Kp indices. This finding is consistent with the conclusions of *Inan et al.* [1992] based on an analysis of a different data set.

In this connection it is interesting to consider whether some of the observed perturbations attributed to VLF heating could instead be due to transmitter-induced precipitation of energetic electrons from the Earth's radiation belts, whose population depends on geomagnetic activity. The original purpose of the experiment of *Inan* [1990a] was to detect the effect of such precipitation using subionospheric VLF probe waves. Precipitation was ruled out as a possible cause of the events observed in that experiment because there was no delay between the observed cross-modulation on NAA-Palmer and the ON/OFF pattern of the NAU heating transmitter, an observation strengthened by the presence of immediate, sharp event onsets and cessations.

In the data sets analyzed in this chapter, some of the observed events appear not to have such sharp onsets and cessations due to high levels of atmospheric noise which necessitate substantial averaging of the signal to reveal the perturbation. However, the lack of such sharp signatures does not necessarily allow for precipitation to be a possible

cause. Satellite-based *in situ* observations of energetic electrons precipitated by the keying of NAA and NSS reveal a $\sim 1 - 2$-s delay between transmitter turn-on and the electron precipitation [*Imhof et al.*, 1983a,b], consistent with theoretical expectations [*Inan et al.*, 1985]. No such delay is observed in the events studied here, and none of the observed perturbations lasts beyond the end of the causative heater OFF/ON episode. In fact, some NAA OFF/ON episodes and their associated NSS perturbations last less than 1 s. Even without the evidence of *Imhof et al.* [1983a,b], it would be possible to rule out precipitation by considering the nature of the observations: the signal perturbations considered here are due to the disturbing transmitter turning OFF, then back ON. If precipitation were the cause, the nature of the observations would imply that electrons are continuously precipitated by man-made VLF transmitters, with the radiation belt populations being replenished continuously regardless of the level of geomagnetic activity. The unreasonability of such a circumstance, along with the timing aspects of the present data set and that of *Imhof et al.* [1983a,b] enable us to conclude that there is no evidence of transmitter-induced electron precipitation in the data studied here.

3.6 SUMMARY

The use of subionospheric VLF probe waves to detect VLF heating of the D region is an outgrowth of long-term observations of lower ionospheric disturbances due to lightning-induced electron precipitation from the Earth's radiation belts. Following the serendipitous observation of VLF heating during a VLF transmitter keying experiment designed to induce electron precipitation in a controlled manner [*Inan*, 1990a], the primary heater-probe wave configuration used here (Figure 3.1) was suggested [*Inan*, 1990b; *Inan and Rodriguez*, 1993] as the first experiment targeted to observe VLF transmitter heating repeatedly, using the NAA transmitter as the heater and the NSS-GA signal as the primary probe wave.

Although plans to operate NAA in specially designed modulation patterns (in collaboration with and by courtesy of the U. S. Navy) have not yet been realized, signatures of cross-modulation between the NAA and NSS signals were observed at Gander at times of NAA OFF/ON episodes that took place in the course of normal operations. Based on their similarity to the observations of *Inan* [1990a] and *Inan et al.* [1992], they were identified as likely signatures of heating by NAA. During December 1992, NAA turned OFF/ON 52 times at night, and in 41 of these episodes, the amplitude or phase of the

NSS-GA probe wave was perturbed. Amplitude and phase changes ranged from –0.11 to +0.84 dB and from 0 to –5.3 degrees, respectively. Analysis of total NAA-GA and NSS-GA field strengths indicates that perturbations tended to occur, and were larger in absolute magnitude, when the NAA field strength was lower. As shown in Chapter 5, both a smaller NAA-GA signal and a larger perturbation on NSS-GA are consistent with the existence of a more tenuous D region. The smaller NAA-GA signal is due to the multimode nature of waveguide propagation, while the larger perturbation is due to the fact that more heating occurs for the same wave power in the more tenuous D region models used here.

Heating by VLF transmitters was also observed using two serendipitous VLF heater-probe wave configurations. Heating by the 24.8 kHz NLK transmitter in Washington state was observed at Saskatoon, Saskatchewan, using the subionospheric VLF probe wave from the 23.4 kHz NPM transmitter in Hawaii (Figure 3.7). In the 44 NLK OFF/ON episodes monitored between October 29 and November 23, 1987, four perturbations of the NPM-SA probe wave amplitude were observed, ranging from 0.3 to 1.6 dB (absolute magnitude). Intermittent interference at Saskatoon from the 23.4 kHz transmitter in Rhauderfehn, Germany, may have prevented detection of weaker signatures. In a reversal of the primary experimental configuration of this dissertation, heating by the 21.4 kHz NSS transmitter was observed at Huntsville, Alabama, using the subionospheric VLF probe wave from the 24.0 kHz NAA transmitter in Maine (Figure 3.10). In the 29 NSS OFF/ON episodes monitored at Huntsville during February 1990, five perturbations of the NAA-HU probe wave amplitude were observed, ranging from +0.2 to +0.5 dB (all positive).

Based on experience with an earlier data set [*Inan*, 1990*a*; *Inan et al.*, 1992] the data presented in this chapter strongly indicate ionospheric cross-modulation between the subionospheric VLF "heater" and "probe" waves. Nevertheless a quantitative comparison with the predictions of theoretical models is necessary in order to establish the consistency of these data with the implied process of VLF heating. Calculations of the magnitude and shape of the heated regions over powerful VLF transmitters are presented in Chapter 4. These model disturbances of the electron-neutral collision frequency are used in Chapter 5 to calculate the effect of VLF heating on the amplitude and phase of VLF signals propagating in the Earth-ionosphere waveguide.

4

Heating of the Nighttime D Region by Very-Low-Frequency Transmitters

The nature of the evidence presented in Chapter 3 of cross-modulation between VLF transmitter signals in the Earth-ionosphere waveguide suggests that the cross-modulation is due to heating of the D region over one of the transmitters resulting in a change in the electron collision frequency (and thus the electrical conductivity), which in turn affects the propagation of the other signal [*Inan*, 1990; *Inan et al.*, 1992]. The first step in the interpretation of the data in comparison with the predictions of theoretical models is a quantitative description of the heated region using the model of electron heating described in Chapter 2. A similar model was used by *Inan* [1990] to explain the first observations of VLF heating by treating the case of vertical incidence on the ionosphere. This model was soon modified to account for the self-action of the wave, that is, the change in the attenuation rate due to the increase in collision frequency [*Inan et al.*, 1991; *Taranenko et al.*, 1992a]. The model was extended to three dimensions by *Rodriguez et al.* [1992] and *Inan et al.* [1992]. The dependence of the heating on the electron and neutral temperatures has been treated more realistically in other recent work [*Barr and Stubbe*, 1992]. The simple heating model has also been used to investigate ionospheric heating by the electromagnetic pulses from lightning discharges [*Inan et al.*, 1991; *Rodriguez et al.*, 1992].

The first part of this chapter is a detailed description of the three-dimensional implementation of the W.K.B. propagation model and ionospheric heating model described in Chapter 2. Next, these models are used to calculate the magnitude of the heating and

the three-dimensional shape of the heated regions above six powerful U. S. Navy VLF transmitters. In section 4.3, results are discussed in the light of a theoretical analysis by *Barr and Stubbe* [1992] of the latitudinal dependence of VLF heating.

4.1 THREE-DIMENSIONAL MODEL OF *D* REGION HEATING BY RADIO WAVES FROM A VLF TRANSMITTER

A Cartesian coordinate system is used to represent the space heated by a VLF transmitter, with the x-axis directed toward geomagnetic north, the y-axis directed toward geomagnetic west, and the z-axis directed vertically upward (Figure 4.1). The transmitter antenna lies at the origin of this coordinate system. The Earth's magnetic field $\mathbf{B_0}$ lies entirely in the x-z plane, making an angle I (referred to as the *dip angle*; see equation (4.11) below) with the x-axis. For the wavelengths considered here (10–15 km), the entire D region (taken to start at 50 km altitude) lies in the radiation field of the antenna. Thus, the D region plasma affects only the propagation of the transmitter signal. The propagation effects of the D region considered in this study include the attenuation of the wave, due to the complex refractive index of the plasma, and the self-action of the wave, that is, the effect that the wave has on its own propagation as it heats the medium. Refraction and reflection are neglected, as discussed in Chapter 2. Thus, the Poynting flux and the resulting heating are calculated along straight lines originating at the transmitter. Each direction of propagation is identified by an azimuth angle ϕ directed counterclockwise from geomagnetic north, and an elevation angle γ measured upward from the ground plane.

4.1.1 Radiation Pattern of a VLF Transmitting Antenna

Practical transmitting antennas at VLF are large, complicated, expensive structures consisting of vertical down leads and horizontal "top-loading" wires, which provide capacitance to ground, supported by multiple $\sim$ 200-m towers [*Watt*, 1967]. However, due to the large wavelengths involved (10–15 km), such antennas can be accurately modeled in terms of their ability to radiate as electrically short, vertical monopoles on and perpendicular to a perfectly conducting plane [*Watt*, 1967, p. 15]. Due to reflections of the radiated signal from the conducting plane, a monopole of height $h/2$ radiates the same power into the upper hemisphere as if it were a dipole of height h in free space [*Jordan and*
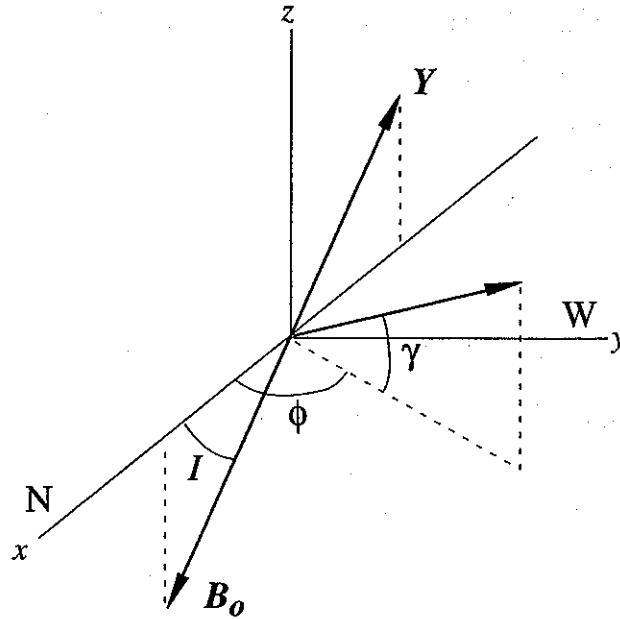
Figure 4.1. Coordinate system and angles used in the heating calculations. The heating transmitter is at the origin of a Cartesian coordinate system with the x- and y-axes pointing in the geomagnetic north and west directions, respectively, and the z-axis pointing toward the ionosphere. I is the dip angle between the Earth's magnetic field $\mathbf{B_0}$ and the geomagnetic north direction, and is defined to be positive in the Northern Hemisphere. $\mathbf{Y}$ is a vector directed opposite to $\mathbf{B_0}$ with a magnitude given by the ratio of the electron gyrofrequency to the wave frequency. The azimuth and elevation angles of a line along which heating is calculated are ϕ and γ, respectively.

Balmain, 1968, p. 327]. This fact and the large top-loading capacitances permit analysis of practical VLF transmitting antennas as the classical short electric dipole [*Kraus*, 1988, p. 200], characterized by a uniform current distribution I_0 along the antenna with equal and opposite charges at the ends maintaining continuity with the current. The time-harmonic total fields radiated by a short dipole in free space are [*Ramo et al.*, 1984, p. 583]

$$E_r = \frac{I_o h}{4\pi} \cos\theta \; e^{-ikr} \left(\frac{2}{i\omega\epsilon_o r^3} + \frac{2\eta_o}{r^2} \right)$$

$$E_\theta = \frac{I_o h}{4\pi} \sin\theta \; e^{-ikr} \left(\frac{1}{i\omega\epsilon_o r^3} + \frac{\eta_o}{r^2} + \frac{i\omega\mu_o}{r} \right) \qquad (4.1)$$

$$H_\phi = \frac{I_o h}{4\pi} \sin\theta \; e^{-ikr} \left(\frac{1}{r^2} + \frac{ik}{r} \right)$$

where h is the length of the dipole ($h \ll \lambda$), θ is the polar angle measured from the dipole axis, $k = \omega/c = 2\pi/\lambda$ is the free space wavenumber, and $\eta_o = (\mu_o/\epsilon_o)^{1/2} = 377 \ \Omega$ is the wave impedance of free space.† These equations can be applied to the case of a top-loaded vertical monopole at a perfectly conducting plane by replacing h with $2h_e$, where h_e is the effective height of the monopole. If the current distribution is not uniform, then h_e is related to the physical height h_p by

$$h_e = \frac{1}{I_o} \int_0^{h_p} I(h)dh \qquad (4.2)$$

where I_o is the full amplitude of the current at the base of the antenna [*Watt*, 1967, p. 16]. (Note that equations (4.1) correspond to the first-order transverse magnetic (TM) solution of Maxwell's equations in spherical coordinates for axial symmetry ($\partial/\partial\phi = 0$) [*Ramo et al.*, 1984, p. 585].)

In this work, the radial Poynting flux S is calculated from the total radiated power P_{tot} and the radiation pattern of the transmitter, assumed to be that of a short dipole. The time-average Poynting flux is

$$S(r,\theta) = \frac{1}{2}\text{Re}\left\{E_\theta H_\phi^*\right\} = \frac{E_\theta^2(r,\theta)}{2\eta_o} = S_o \frac{\sin^2\theta}{r^2} \qquad (4.3)$$

where E_θ is considered to be the radiation component of the electric field and

$$S_o = \frac{\eta_o k^2 I_o h_e^2}{8\pi^2} \qquad (4.4)$$

is the average Poynting flux at $r = 1$ m, $\theta = \pi/2$. The total radiated power is the integral of the Poynting flux over the upper hemisphere,

$$P_{tot} = \int_0^{2\pi} \int_0^{\frac{\pi}{2}} S(r,\theta)r^2 \sin\theta d\theta d\phi = \frac{4}{3}\pi S_o \qquad (4.5)$$

---

† The three summed terms in the expression for E_θ represent the electrostatic (r^{-3}), induction (r^{-2}), and radiation (r^{-1}) components, which are equal in magnitude at $r = \lambda/2\pi$. This distance is considered to be the boundary between the "reactive near-field region" inside and the "far-field region" outside [*Antenna Standards Committee*, 1983].

from which we have

$$S(r, \theta) = \frac{3P_{tot}\sin^2\theta}{4\pi r^2} = \frac{3P_{tot}(x^2 + y^2)}{4\pi(x^2 + y^2 + z^2)^2} \qquad (4.6)$$

where the x-, y-, and z-directions are defined in Figure 4.1.

Radiated Powers of U. S. Navy VLF Transmitters

From (4.3) and (4.6), the electric field perpendicular to a perfectly conducting ground plane at a distance $r = d$ along the ground plane from the antenna is

$$E_v(d) = \left(\frac{3\eta_o P_{tot}}{2\pi}\right)^{\frac{1}{2}} d^{-1} = 13.4 P_{tot}^{\frac{1}{2}} d^{-1} \qquad (4.7).$$

This expression is commonly given in terms of the RMS vertical electric field [*Watt*, 1967, p. 17; *Wait*, 1978]:

$$E_{v,\text{RMS}}(d) = 9.5 P_{tot}^{\frac{1}{2}} d^{-1} \quad (\text{V m}^{-1}; P_{tot} \text{ in W}, d \text{ in m})$$
$$= 300 P_{tot}^{\frac{1}{2}} d^{-1} \quad (\text{mV m}^{-1}; P_{tot} \text{ in kW}, d \text{ in km}) \qquad (4.8).$$

Therefore, P_{tot} can be determined by measuring E_v at points that lie in the radiation zone yet close enough to the transmitter so that there is negligible return from the ionosphere [*Watt*, 1967, pp. 17-18].

As seen in Table 4.1, the radiated powers P_{tot} of individual U. S. Navy VLF transmitters given in the literature vary greatly. Unless otherwise noted, the powers used in this dissertation are those quoted by *Inan et al.* [1984]. The operating frequencies have varied throughout the years; the frequencies listed in Table 4.1 are the operating frequencies at present. Since the publication of *Inan et al.* [1984], only NAA has changed its frequency (from 17.8 kHz to 24.0 kHz), and its power radiating capability at 24.0 kHz is within 1 dB of that at 17.8 kHz [*Watt*, 1967, p. 140]. The numbers attributed in Table 4.1 to *Watt* [1967] were determined for the current operating frequencies from graphs of maximum power radiating capability versus frequency [*Watt*, 1967, pp. 135, 140, 151, 155]. Note that *Willis and Davis* [1976] quote a radiated power of 1.3 MW for NAA at an operating frequency of 14.7 kHz.

Table 4.1
Radiated powers of U. S. Navy VLF transmitters.

Call Letters	Site Name	Frequency (kHz)	P_{tot}, Total Radiated Power (kW)				
			a	b	c	d	e
NSS	Annapolis, Md.	21.4	265	225	85	213	400
NWC	Exmouth, Aus.	22.3	1000	–	1000	1800	1000
NPM	Lualualei, Oahu	23.4	300	230	140	502	630
NAA	Cutler, Me.	24.0	1000	1800	1000	1200	1000
NLK	Jim Creek, Wa.	24.8	850	250	250	245	–
NAU	Aguadilla, P. R.	28.5	–	–	–	100	100

a. *Inan et al.* [1984]
b. *Watt* [1967]
c. *Swanson* [1974]
d. *Naval Ocean Systems Center* [1989]
e. *Barr and Stubbe* [1992]

4.1.2   Model of the Earth's Magnetic Field

For the heating calculations, the Earth's magnetic field $\mathbf{B_0}$ is represented by a centered dipole model. In spherical coordinates, its components are given by

$$B_r = -\frac{2M}{r^3}\sin\lambda$$

$$B_\theta = -\frac{M}{r^3}\cos\lambda \qquad\qquad (4.9)$$

$$B_\phi = 0$$

where M is the dipole moment of the Earth and λ is the geomagnetic latitude [*Roederer*, 1970, p. 52]. Setting $r = R_\oplus + h$ where $R_\oplus = 6371.2$ km is the Earth's radius and h is the altitude, the magnitude of the field is

$$B_o = B_{eq}\left(\frac{R_\oplus}{R_\oplus + h}\right)^3 \left(1 + 3\sin^2\lambda\right)^{\frac{1}{2}} \qquad\qquad (4.10)$$

where $B_{eq} = M/R_\oplus^3 = 30854$ nT is the magnitude of $\mathbf{B_0}$ at the geomagnetic equator at

the Earth's surface [*Davies*, 1990, p. 42]. At any point on the surface of the Earth, the geomagnetic north-south meridional plane is defined by $\mathbf{B_0}$ and the vertical direction.

The dip angle is the angle that $\mathbf{B_0}$ makes with the horizontal:

$$I = \tan^{-1}\left(\frac{B_r}{B_\theta}\right) = \tan^{-1}(2 \tan \lambda) \tag{4.11}$$

It is defined to be positive if $\mathbf{B_0}$ points below the horizontal, so that $I > 0$ represents the northern hemisphere. In this dissertation, I is calculated using the 1985 International Geomagnetic Reference Field [*Langel*, 1992]. The geomagnetic latitude is therefore calculated using the centered dipole model:

$$\lambda = \tan^{-1}\left(\frac{1}{2} \tan I\right) \tag{4.12}$$

The dip angle and geomagnetic latitude of several VLF transmitters calculated using (4.11) and (4.12) are given in Table 4.2. Unless otherwise noted, these numbers are used in the heating calculations.

Table 4.2
Geomagnetic characteristics of VLF transmitters.

Call Letters	Site Name	IGRF 1985 (PRESEG) Dip Angle	Latitude
NSS	Annapolis, Md.	70.6°	54.8°
NWC	Exmouth, Aus.	−55.7°	−36.2°
NPM	Lualualei, Oahu	39.2°	22.2°
NAA	Cutler, Me.	73.4°	59.2°
NLK	Jim Creek, Wa.	71.0°	55.4°
NAU	Aguadilla, P. R.	50.9°	31.6°

Angle Between the Earth's Magnetic Field and the Wave Normal

As stated in Chapter 2, the refractive index of a radio wave in the D region depends on the angle that the wave normal vector makes with the Earth's magnetic field. If ϕ_1 and γ_1 are the azimuth (from geomagnetic north) and elevation angles of the ray, respectively, the direction cosines (l_1, m_1, n_1) of the ray are

$$
\begin{aligned}
l_1 &= \cos\phi_1 \cos\gamma_1 \\
m_1 &= \sin\phi_1 \cos\gamma_1 \\
n_1 &= \sin\gamma_1
\end{aligned}
$$
(4.13).

The direction cosines (l_2, m_2, n_2) of $\mathbf{Y} = e\mathbf{B_0}/m_e\omega$ are

$$
\begin{aligned}
l_2 &= -\cos I \\
m_2 &= 0 \\
n_2 &= \sin I
\end{aligned}
$$

where $I > 0$ in the northern hemisphere. The angle Θ between the direction of propagation and $\mathbf{Y}$ is then given by

$$
\begin{aligned}
\cos\Theta &= l_1 l_2 + m_1 m_2 + n_1 n_2 \\
&= -\cos\phi_1 \cos\gamma_1 \cos I + \sin\gamma_1 \sin I
\end{aligned}
$$
(4.14).

4.1.3   Calculation of D Region Heating over a VLF Transmitter

In a slowly-varying lossy medium for which the W.K.B. approximation holds (Chapter 2), the Poynting flux for each magneto-ionic component, ordinary (o) or extraordinary (x), is

$$
S_{o,x}(r,\theta) = \frac{3P_{tot}\sin^2\theta}{8\pi r^2} \exp\left(-\frac{2\omega\chi_{o,x}r}{c}\right)
$$
(4.15)

where r is the straight-line distance from the transmitter, ω is the angular wave frequency, c is the speed of light in vacuum, and $-\chi_{o,x}$ is the imaginary part of the refractive index of the D region plasma. Following *Maslin* [1974], the power $U_{o,x}$ dissipated in a unit

volume by one magneto-ionic component of the electromagnetic wave is determined from the derivative of the Poynting flux with respect to r:

$$\frac{dS_{o,x}}{dr}(r, \theta) = -\frac{2}{r}S_{o,x}(r, \theta) - U_{o,x}(r, \theta),$$
(4.16)

where

$$U_{o,x}(r, \theta) = \frac{2\omega\chi_{o,x}S_{o,x}(r, \theta)}{c}.$$
(4.17)

The initial value of $S_{o,x}$ in a given direction (ϕ, θ) for each magneto-ionic component is determined by evaluating (4.15) at a low altitude (e.g., 50 km) where $\chi \simeq 0$. The Poynting flux is evaluated at 0.1 km steps in altitude along straight lines originating at the transmitter and distributed regularly in azimuth (ϕ) and elevation $(\gamma = \pi/2 - \theta)$ angles (Figure 4.2). As discussed in Chapter 2, the W.K.B. nature of the propagation up to the altitudes of maximum absorption and reflection permits us to neglect refraction and reflection effects as well as the coupling between the ordinary and extraordinary components.

Following *Barr and Stubbe* [1992], the refractive indices are determined assuming a momentum-transfer collision frequency proportional to electron kinetic energy and a Maxwellian electron distribution [*Sen and Wyller*, 1960; *Hara*, 1963; *Budden*, 1965]. At each altitude $U = 2\omega\chi S/c$ is calculated for each magneto-ionic component. To account for self-absorption, the value of ν used to calculate $\chi_{o,x}$ (and hence $U_{o,x}$ and $\Delta\nu$) at a given altitude is taken to be the sum of ν_o at that altitude and $\Delta\nu$ due to heating at the previous altitude. The proper altitude step size is determined empirically by reducing it until the calculated temperature no longer changes. The step size appropriate for the scale heights of the electron density profiles used here (Figure 2.3) was found to be 0.1 km.

The amount of heating by the VLF wave is determined from the steady-state balance between the rate of energy gained by the electrons from the wave and lost to N_2 and O_2 through elastic collisions and inelastic collisions involving rotational and vibrational excitation of the neutral molecules. The energy-balance equation

$$U_o + U_x = L_{tot}(T_e, T_n) = \sum_{i=1}^{3} \left[L_i(e, N_2) + L_i(e, O_2)\right]$$
(4.18)

is solved iteratively at each altitude for the electron temperature T_e to within an accuracy of ± 0.1 K using the method of false positions [*Press et al.*, 1988, pp. 263–266]. Then, if
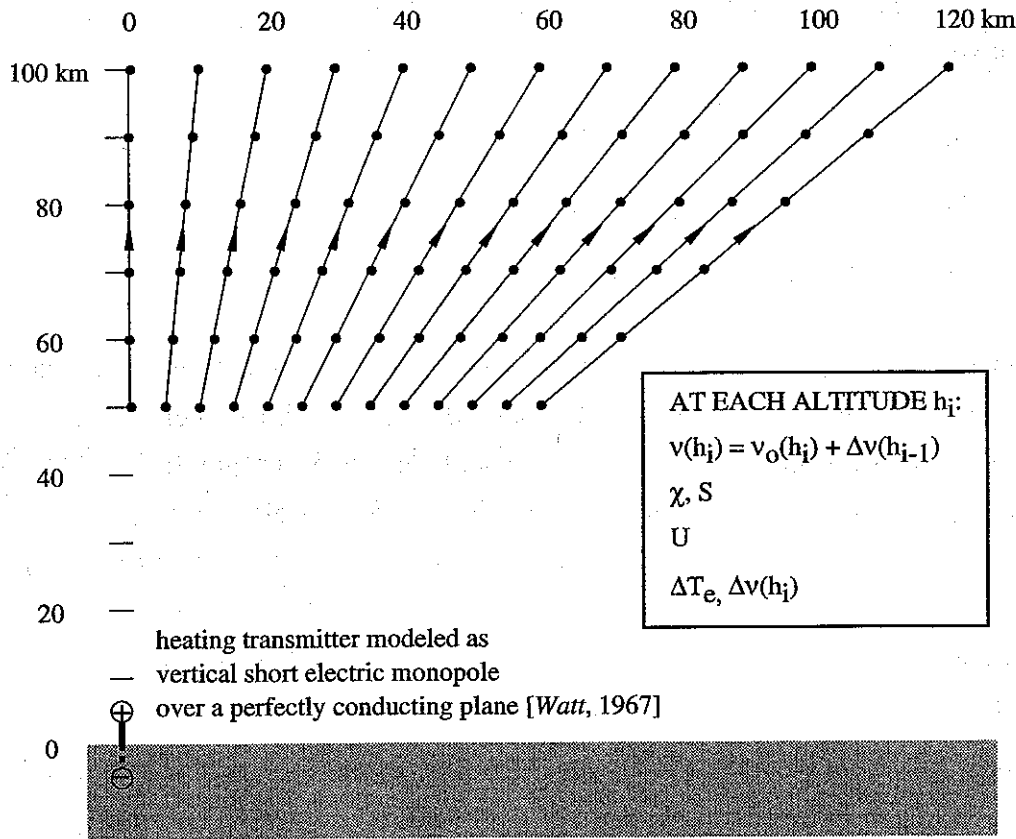
Figure 4.2. Schematic description of the three-dimensional heating calculation. Section of the space heated by a VLF transmitter demonstrating the configuration of the straight lines along which the heating is calculated.

the effective collision frequency profile of *Wait and Spies* [1964] is used (Figure 2.4), the heated collision frequency is calculated as $\nu = (T_e/T_n)\nu_o$, where ν_o and ν are the ambient and heated electron-neutral collision frequencies. If instead the average momentum transfer collision frequency profiles of *Banks* [1966] are used (Figure 2.4), their particular dependence on temperature is utilized (Appendix B).

Alternatively, if a constant collisional loss factor G is used, (2.32) is evaluated for each magneto-ionic component instead of (4.18), and the results are added to obtain a total $\Delta\nu$ [*Inan*, 1990; *Inan et al.*, 1991; *Taranenko et al.*, 1992a; *Rodriguez et al.*, 1992; *Inan et al.*, 1992]. The heated electron temperature is then given by $T_e = (\nu/\nu_o)T_n$.

4.2 HEATING OF THE NIGHTTIME *D* REGION BY THE NAA, NSS, AND NLK TRANSMITTERS

The heated region is represented here as the altitude (h) variation in electron collision frequency through the point of maximum heating (x_m, y_m, h_m), scaled by the transverse structure at the altitude of maximum heating h_m [*Inan et al.*, 1992]:

$$\Delta\nu(x, y, h) = \Delta\nu(x_m, y_m, h)\frac{\Delta\nu(x, y, h_m)}{\Delta\nu(x_m, y_m, h_m)} \qquad (4.19).$$

"Maximum heating" is defined in this dissertation as the maximum relative change in collision frequency $\Delta\nu/\nu_o$ due to heating by a VLF transmitter. This does not in general correspond to the maximum change in electron temperature T_e, although the magnitudes and locations of the maximum $\Delta\nu/\nu_o$ and $\Delta T_e/T_n$ are always quite close.

The changes in electron temperature and collision frequency due to heating by NSS, NLK, and NAA in the nighttime D regions represented by ambient electron density profiles 0 (most tenuous), I, II, and III (most dense) (Figure 2.3) are shown in Figure 4.3. On the left half of the figure are the ambient and heated electron temperature profiles, and on the right half are the corresponding $\Delta\nu(x_m, y_m, h)/\nu_o(h)$ profiles. The heating is more pronounced and has its maximum at a higher altitude for the more tenuous D regions. In the case of the most tenuous ambient D region (profile 0), the electron temperature above NAA increases by as much as a factor of 3. In each case, there is a secondary peak in the heating where the extraordinary component is maximally (and almost completely) absorbed.

The transverse structure of the heated region over NAA at the altitude of maximum heating, given by $\Delta\nu(x, y, h_m)/\Delta\nu(x_m, y_m, h_m)$, is shown in Figure 4.4 over a 700 by 700 km area for each of the ambient density profiles 0, I, II, and III. The heated regions all show a geomagnetic north-south asymmetry, with maximum heating to the north of the transmitter at a $\sim$ 45° elevation angle, due to the ordinary component being maximally absorbed for wave electric fields parallel to the Earth's magnetic field [*Galejs*, 1972*b*; *Inan et al.*, 1992]. The heating is minimum (ideally zero) directly above the transmitter. At h_m = 87.1 km over NAA (profile 0) the radius at the outer half-maximum of $\Delta\nu(x, y, h_m)/\Delta\nu(x_m, y_m, h_m)$ is about 160 km. Although the skirts of the heated region are broader for a denser D region, the radius at the outer half-maximum changes relatively little from profile to profile.
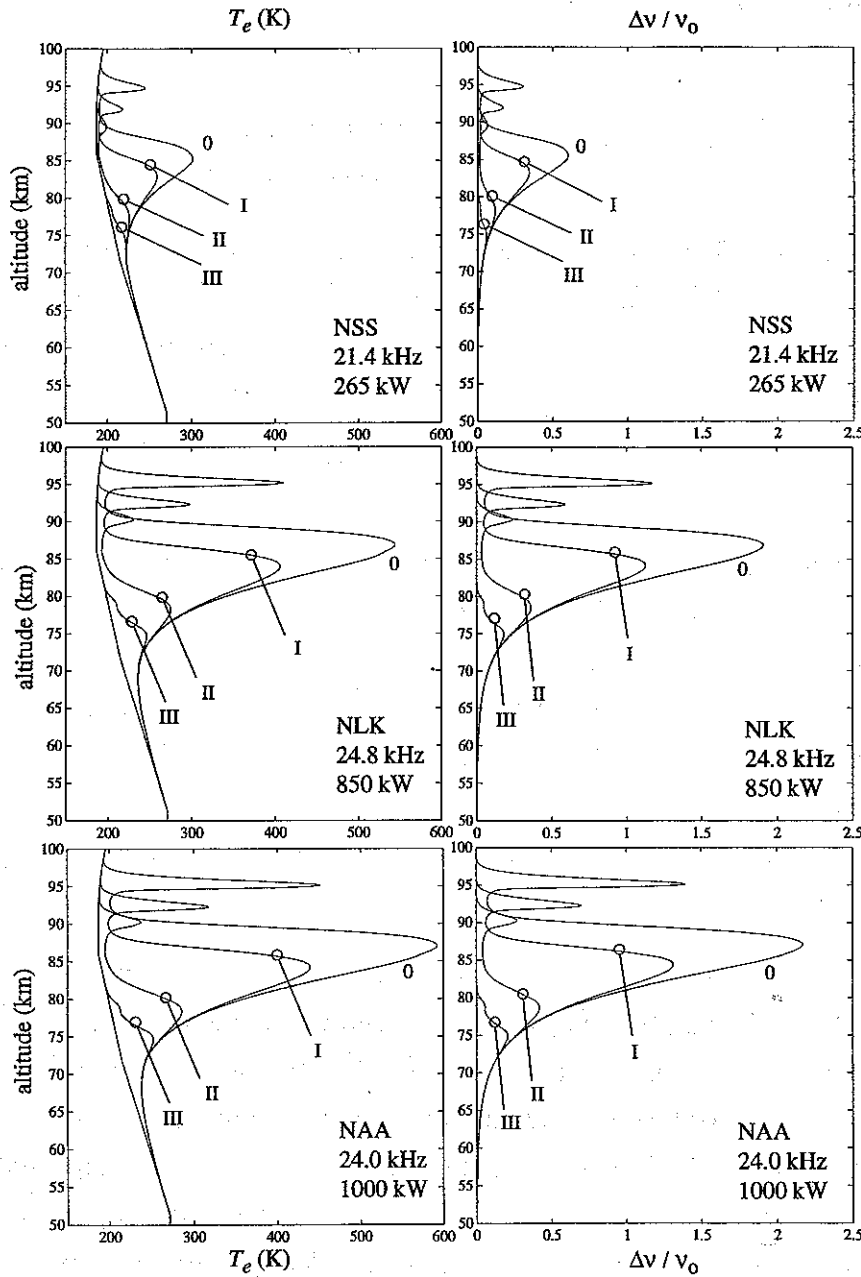
Figure 4.3. Variation with altitude of D **region heating by NSS, NLK and NAA.**
Altitude profiles of electron temperature T_e (LEFT) and the relative change in electron
collision frequency $\Delta\nu/\nu_o$ (RIGHT) through the point of maximum heating (x_m, y_m, h_m).
In general, this point is about as far north (geomagnetic) of the transmitter as it is above
the surface of the Earth.
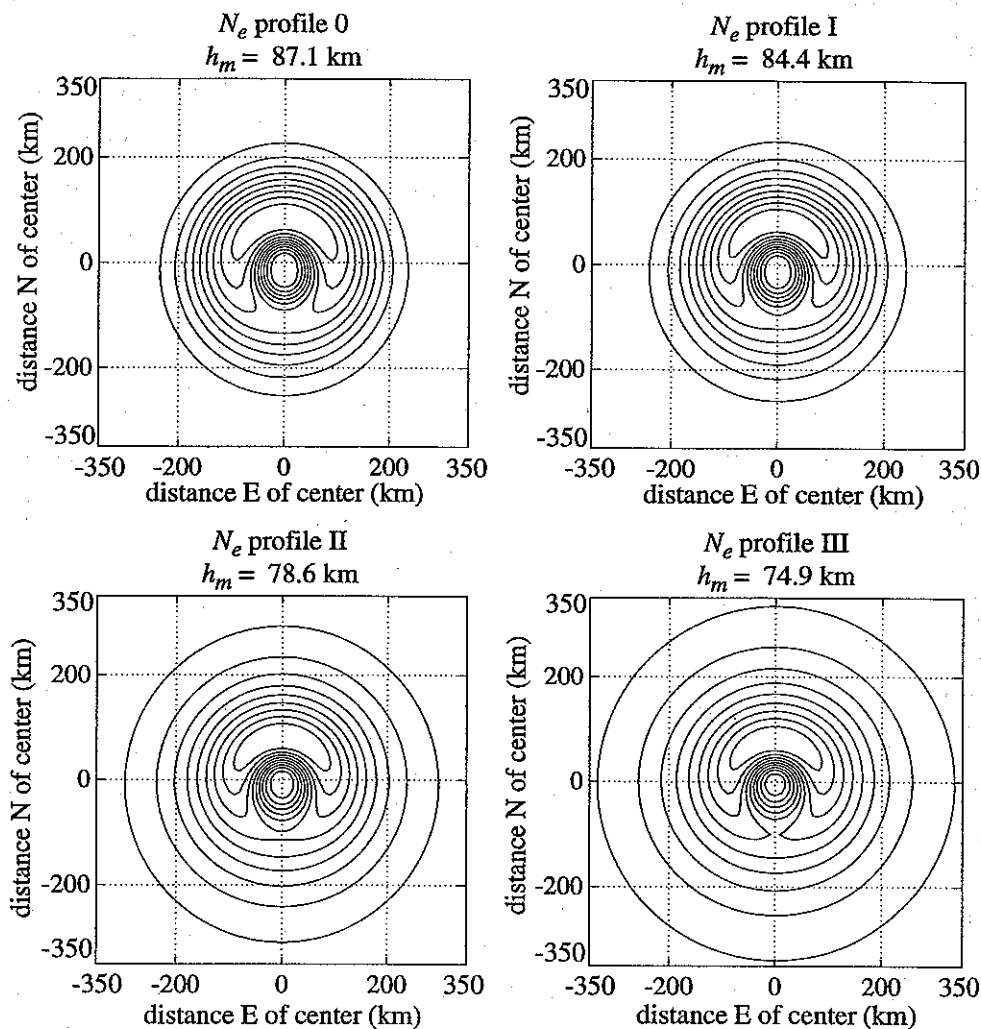
Figure 4.4. Contour plots of heating over NAA. The heated patch of *D* region iono-sphere over NAA is represented here as a contour plot of the normalized collision frequency $\Delta\nu(x, y, h_m)/\Delta\nu(x_m, y_m, h_m)$ over a 700 by 700 km area at the altitude of maximum heating h_m, with each contour representing a 10% interval. The transmitter is directly under the origin. A plot is shown for each of the electron density profiles 0, I, II, and III. Geomagnetic north is toward the top of the page. Heating is maximum to the north of the transmitter and minimum (exactly zero in this model) in the center of the patch directly above the transmitter.

The transverse structure of the heated region does vary with altitude. For the case of NAA heating a D region represented by the electron density profile 0, the transverse extent of the disturbance at the altitude of maximum heating $h_m = 87.1$ km is somewhat narrower than at lower altitudes (Figure 4.5). This may seem contrary to the expectation that the heater wave heats a larger region as it spreads out with altitude. However, as the elevation angle decreases the wave must travel further to reach the same altitude and therefore suffers more attenuation along its path. Note that the extraordinary component is maximally absorbed at 95.1 km, and that in between the altitudes of maximum absorption for the two components, for example at 90 km, the heated region is relatively narrow.

The asymmetry of the heated region is due to the anisotropy of the refractive index of the weakly-ionized magnetized plasma that constitutes the D region. Consider as an example the refractive index $n = \mu - i\chi$ of the 24.0 kHz NAA signal at the altitude of maximum heating for profile 0 ($h_m = 87.1$ km). Figure 4.6 shows μ and χ as a function of the wave normal angle Θ at this altitude for both the ambient collision frequency and the maximum collision frequency due to heating at this altitude. Note that χ is much larger for the ordinary mode near $\Theta = 90°$ than at $\Theta = 0$ or $180°$, while μ varies little between these extremes. The attenuation rate represented by χ does decrease in this case for the ordinary mode at the altitude of maximum heating when the plasma is heated by a factor of 3. However, at the same time, a few kilometers above this point the attenuation rate is larger than the ambient value, corresponding to a raising of the reflection height to an altitude where X is approximately equal to the heated value of Z (Chapter 2).

Such an asymmetry was predicted by *Ratcliffe and Shaw* [1948] for low-frequency (LF) transmitters by considering the quasi-longitudinal and quasi-transverse approximations to the magneto-ionic refractive index formula [*Ratcliffe*, 1959, pp. 75–80]. They predicted maximum absorption of the ordinary component of LF heating waves at 68 and 90.2 kHz for quasi-transverse propagation. However, no heating effect due to these transmitters was observed on the 1050 kHz wanted wave (see Figure 1.2). In explaining this failure, *Ratcliffe and Shaw* [1948] argued that the LF signals were probably reflected below the altitude of maximum absorption of the wanted wave. In retrospect a more important factor was probably the fact that the radiated powers of these LF transmitters were relatively low (20 and 80 kW).
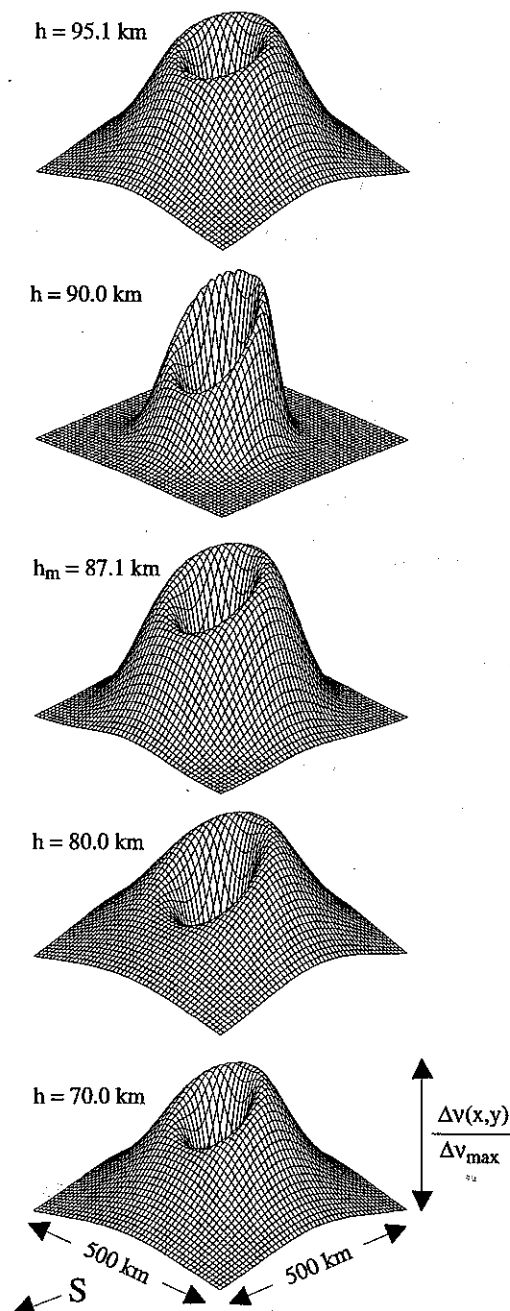
Figure 4.5. Transverse structure of the heated region at different altitudes. Mesh plots of the normalized collision frequency change $\Delta\nu(x, y, h)/\Delta\nu(x_m, y_m, h)$ due to heating by NAA at five altitudes h in the nighttime D region represented by electron density profile 0. The meshes cover a 500 by 500 km area. Maximum heating occurs at $h_m = 87.1$ km, and the maximum heating due to absorption of the extraordinary wave occurs at $h = 95.1$ km.
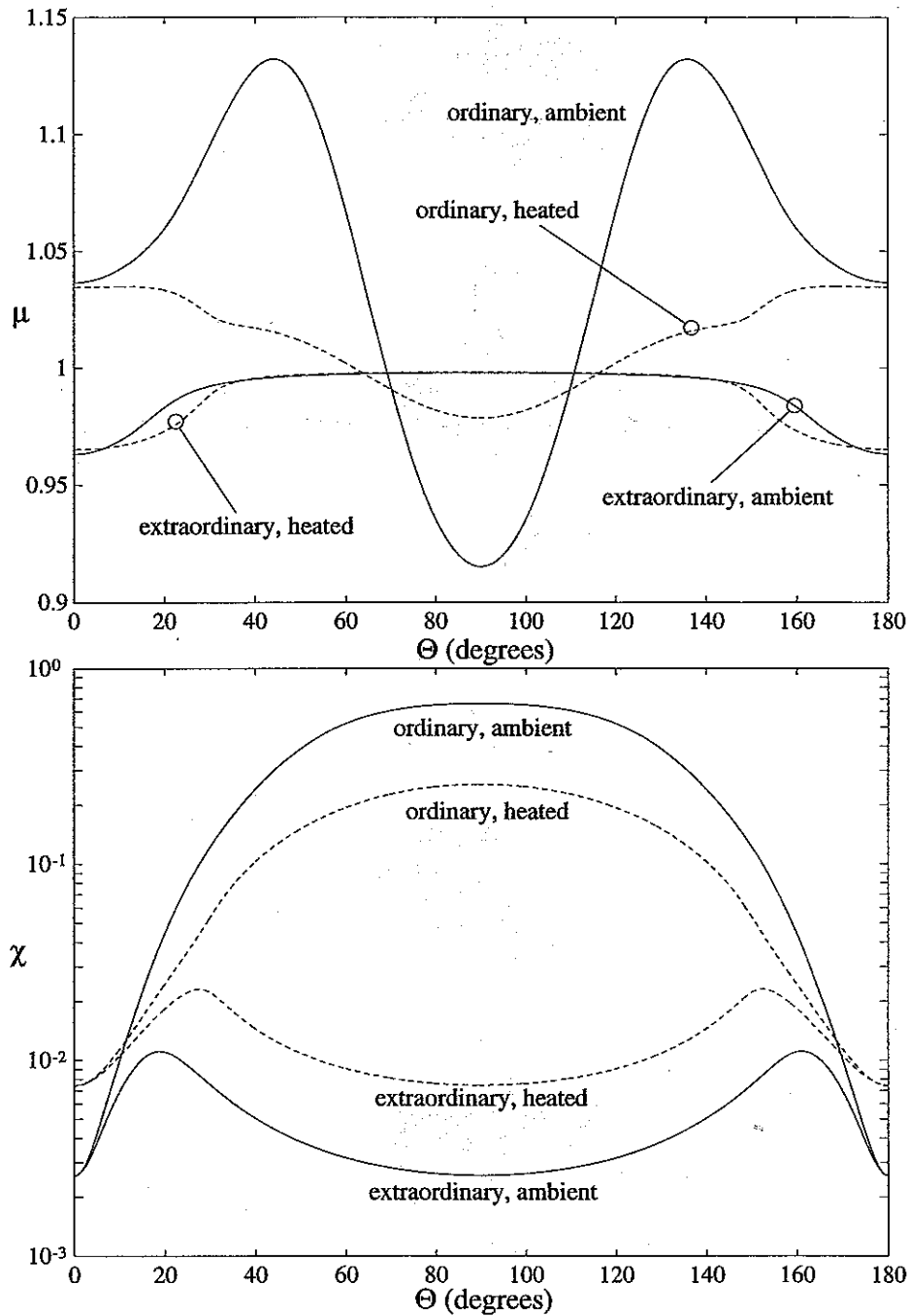
Figure 4.6. Anisotropy of the *D* region refractive index at 24 kHz. Real and negative imaginary parts of Sen-Wyller refractive index $n = \mu - i\chi$ as a function of wave normal angle Θ at altitude of maximum heating (87.1 km) in *D* region characterized by electron density profile 0. Parameters of the medium are $N_e = 3.18 \times 10^7 \text{m}^{-3}$, $B_o = 5.18 \times 10^{-5}$ T, $\nu_o = 3.85 \times 10^5 \text{s}^{-1}$, heated $\nu = 1.22 \times 10^6 \text{s}^{-1}$. Note that this heated collision frequency is predicted only for the signal from NAA propagating toward geomagnetic north at $\Theta = 61.6°$.

4.2.1 Cooling Rates and Collisional Losses

The steady-state energy balance equation (4.18) is solved using the expressions for the cooling rates given in Appendix B (B.7–B.12). The total electron cooling rates L_{tot} used to calculate heating by NAA are shown on the left side of Figure 4.7. To calculate equivalent G factors from these cooling rates, (2.36) is rewritten as

$$G = \frac{2L}{3kN_e\nu(T_e - T_n)} \tag{4.20}$$

where the collision frequency ν is proportional to the increased electron temperature T_e. These equivalent G factors are plotted on the right side of Figure 4.7. Because rotational excitation of N_2 and O_2 is the dominant electron cooling mechanism, a simple expression for the ambient collisional loss factor G_o can be derived by rewriting the above equation using the rotational cooling rates L_{rot} given in Appendix B. Namely,

$$G_o \simeq G_{\mathrm{rot}} = \frac{2.25 \times 10^{-16} N_{N_2} + 5.37 \times 10^{-16} N_{O_2}}{\nu_o T_n^{\frac{1}{2}}} \tag{4.21}$$

The ambient quantity G_{rot} is also plotted on the right-hand side of Figure 4.7.

Although our estimation of the transmitter-induced heating is basically a steady-state calculation, the heating time constant can be approximated by $(G\nu)^{-1}$, based on the time-dependent solution (2.32) for the collision frequency change $\Delta\nu$ derived assuming a constant loss factor G. For the case of heating by NAA under electron density profile 0, $(G\nu)^{-1}$ ranges from 3×10^{-5} s^{-1} at 70 km to 4×10^{-3} s^{-1} at 100 km. The values for ambient (unheated) conditions are similar. Thus, the time scale over which D region electrons heat up and cool down in response to a heater turning ON and OFF is on the order of a millisecond or less [*Tomko*, 1981].

To compare our results with those of earlier heating models, we consider the case of NAA heating for a D region represented by the ambient electon density profile II (Figure 2.3) and a collision frequency profile used by *Wait and Spies* [1964] (Figure 2.4). With the present heating model, the maximum heating is $\Delta\nu/\nu_o = 0.42$ at $h = 78.6$ km (Figure 4.3). If we now assume that $G = 1.3 \times 10^{-3}$ rather than as shown in Figure 4.7, the maximum heating is $\Delta\nu/\nu_o = 1.0$ at $h = 79.2$ km. Using the model of *Inan et al.* [1992] ($G = 1.3 \times 10^{-3}$, $T_n = 300$ K at all altitudes, ν independent of electron energy), maximum heating occurs at $h = 78.8$ km with $\Delta\nu/\nu_o = 0.76$ [*Inan and Rodriguez*, 1993].
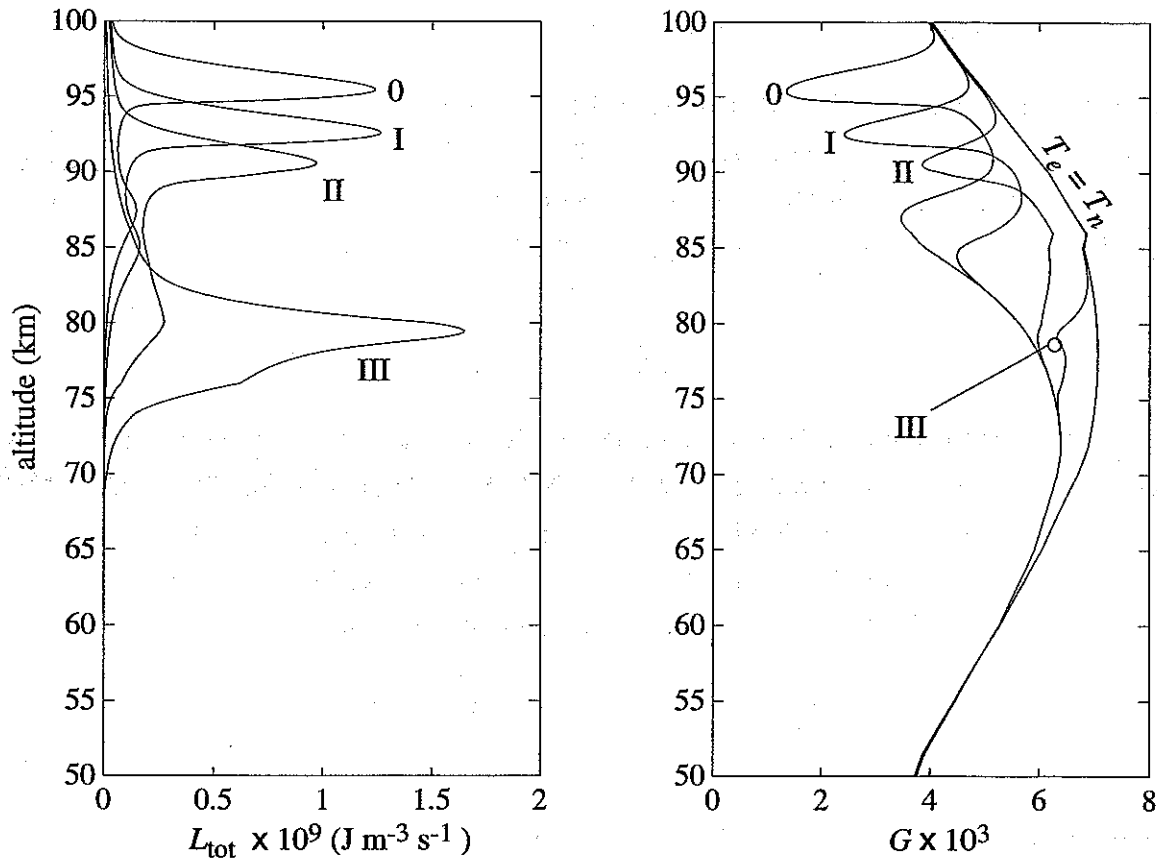
Figure 4.7. Cooling rates L_{tot} and collisional loss factor G as functions of altitude.
Total cooling rates L_{tot} (left) and equivalent G-factors (right) for NAA heating, profile
0, I, II, and III. Shown also is an ambient ($T_e = T_n$) G-factor that accounts only for
rotational excitation of N_2 and O_2.

It is thus clear then that a lower G-factor results in more heating, while the assumption
that $T_n = 300$ K at all altitudes leads to underestimation of the heating since the predicted
collision frequency change is smaller for a larger ambient temperature [*Inan et al.*, 1992].

4.3 LATITUDINAL DEPENDENCE OF HEATING BY VLF TRANSMITTERS

The asymmetry of the transverse structure of the heated region suggests that the magnitude
of maximum heating may depend on the geomagnetic latitude of the VLF transmitter.
One of the conclusions reached by *Barr and Stubbe* [1992] was that VLF heating of the
nighttime D region is strongly enhanced as the geomagnetic latitude of the transmitter
is decreased. Therefore, the lowest-latitude transmitters, such as NPM in Oahu and

NWC in northwestern Australia, might be expected to produce the greatest effects. In reaching this conclusion, *Barr and Stubbe* [1992] treated only vertical incidence of the VLF transmitter signal on the *D* region. Using the three-dimensional heating model developed in this dissertation, we show in this section that the actual dependence on geomagnetic latitude may be much less pronounced than predicted by *Barr and Stubbe* [1992]. To facilitate direct comparison, we use an average momentum transfer collision frequency profile (ν_{av}) (Figure 2.4) and an ambient nighttime electron density profile (Figure 2.3, profile 0) similar to those used by *Barr and Stubbe* [1992].‡ In the light of the discrepancies among reported VLF transmitter radiated powers (Table 4.1), the power levels used in these calculations are chosen as follows. For consistency with the rest of this dissertation the radiated powers for NSS, NLK, and NAA are taken to be 265 kW, 85 kW, and 1000 kW, respectively [*Inan et al.*, 1984], whereas those of NAU, NPM and NWC are assumed to be 100 kW, 630 kW, and 1000 kW, respectively [*Barr and Stubbe*, 1992; *Inan et al.*, 1992]. The latitudes and dip angles of the transmitters referred to are listed in Table 4.2.

The increased electron temperature T_e and the relative change in collision frequency $\Delta\nu/\nu_o$ due to heating by these six transmitters are shown in Figure 4.8. Listed in Table 4.3 is the maximum heating $\Delta\nu/\nu_o$ for each transmitter and the ratio of this value to that for NWC, as well as the corresponding altitude h_m. Also listed is x_B, the horizontal distance from the transmitter at which the ray parallel to $\mathbf{B_0}$ reaches the altitude of maximum heating h_m. (This distance lies along the north-south geomagnetic meridian, with north being positive.) Note that, with the same radiated power, NWC heats 8% more than NAA. Thus, there seems to be a small increase in heating with decreasing geomagnetic latitude. However, the relative amounts of maximum heating are closely in proportion to the total radiated powers of the transmitters, with latitudinal effects being minor.

These findings are not consistent with the predictions by *Barr and Stubbe* [1992] that the maximum $\Delta\nu/\nu_o$ for NAA would be much less than that for NWC (0.72 vs. 2.60), and that NPM would produce slightly more heating than NAA (2.65 vs. 2.60). The likely explanation for this discrepancy in the relative amounts of heating is that *Barr and Stubbe* [1992] considered vertical incidence on the lower ionosphere, as did *Inan* [1990]

---

‡ The *Wait and Spies* [1964] ν_{eff} profile is used throughout the rest of this dissertation. See Chapter 2 for a discussion of the theoretical differences between ν_{eff} and ν_{av}.
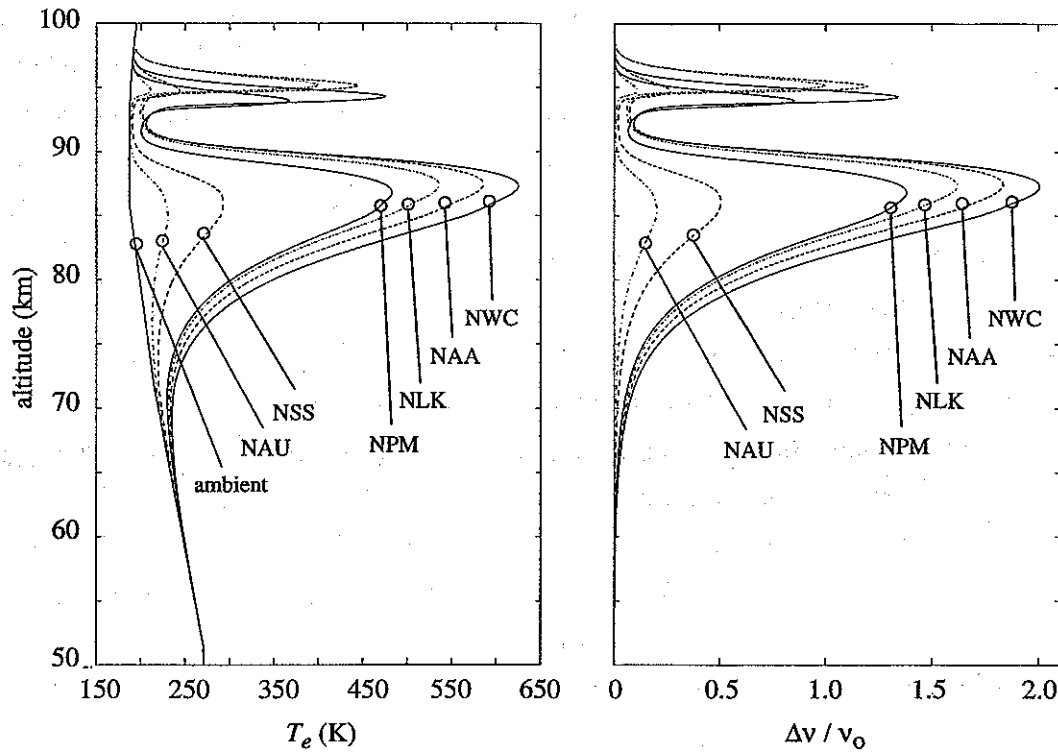
Figure 4.8. Variation with altitude of D region heating by six different VLF transmitters. Altitude profiles of electron temperature T_e (left) and the change in electron collision frequency $\Delta\nu/\nu_o$ (right) through the point of maximum heating (x_m, y_m, h_m), for the VLF transmitters NAU, NSS, NPM, NLK, NAA, and NWC, assuming electron density profile 0 (Figure 2.3) and the collision frequency profile of *Barr and Stubbe* [1992] (Figure 2.4).

and *Taranenko et al.* [1992a]. At vertical incidence, the wave normal angle Θ is larger at low geomagnetic latitudes than at higher latitudes, which would lead to substantially greater heating at low latitudes. In contrast, when the actual three-dimensional geometry of the upward propagation of the wave energy is considered [*Ratcliffe and Shaw*, 1948; *Galejs*, 1972b; *Inan et al.*, 1992] it appears that VLF transmitters at mid- and low latitudes are all capable of heating maximally at wave normal angles nearly transverse to the Earth's magnetic field, with the maximum heating exhibiting only a mild dependence on the geomagnetic latitude of the transmitter.

In contrast to the magnitude of maximum heating, the transverse shape of the heated region is a strong function of geomagnetic latitude, as shown in Figure 4.9. If the transmitters were isotropic radiators, heating would be minimum along an equatorward direction at an elevation angle γ equal to the dip angle. At mid-latitudes, this direction

Table 4.3
Maximum heating by six U. S. Navy VLF transmitters.

Call Letters	Radiated Power (kW)	Maximum Heating		h_m (km)	x_B (km)
		$\Delta\nu/\nu_o$	Relative to NWC		
NWC	1000	2.01	1.00	87.3	+59.6
NAA	1000	1.84	0.92	87.5	−26.1
NLK	850	1.62	0.81	87.4	−30.1
NPM	630	1.38	0.69	86.8	−106.4
NSS	265	0.51	0.25	86.2	−30.4
NAU	100	0.20	0.10	85.4	−69.4

falls within the null of the assumed $\cos\gamma$ radiation pattern of the VLF transmitters, resulting in a slight equatorward extension of the central minimum of the heated region (NAA, NLK, NSS). At sufficiently low latitudes (NWC, NAU, NPM), however, a relative minimum is indeed seen in the heating approximately where $x = x_B$ (Table 4.3), corresponding to an elevation angle equal to the dip angle.
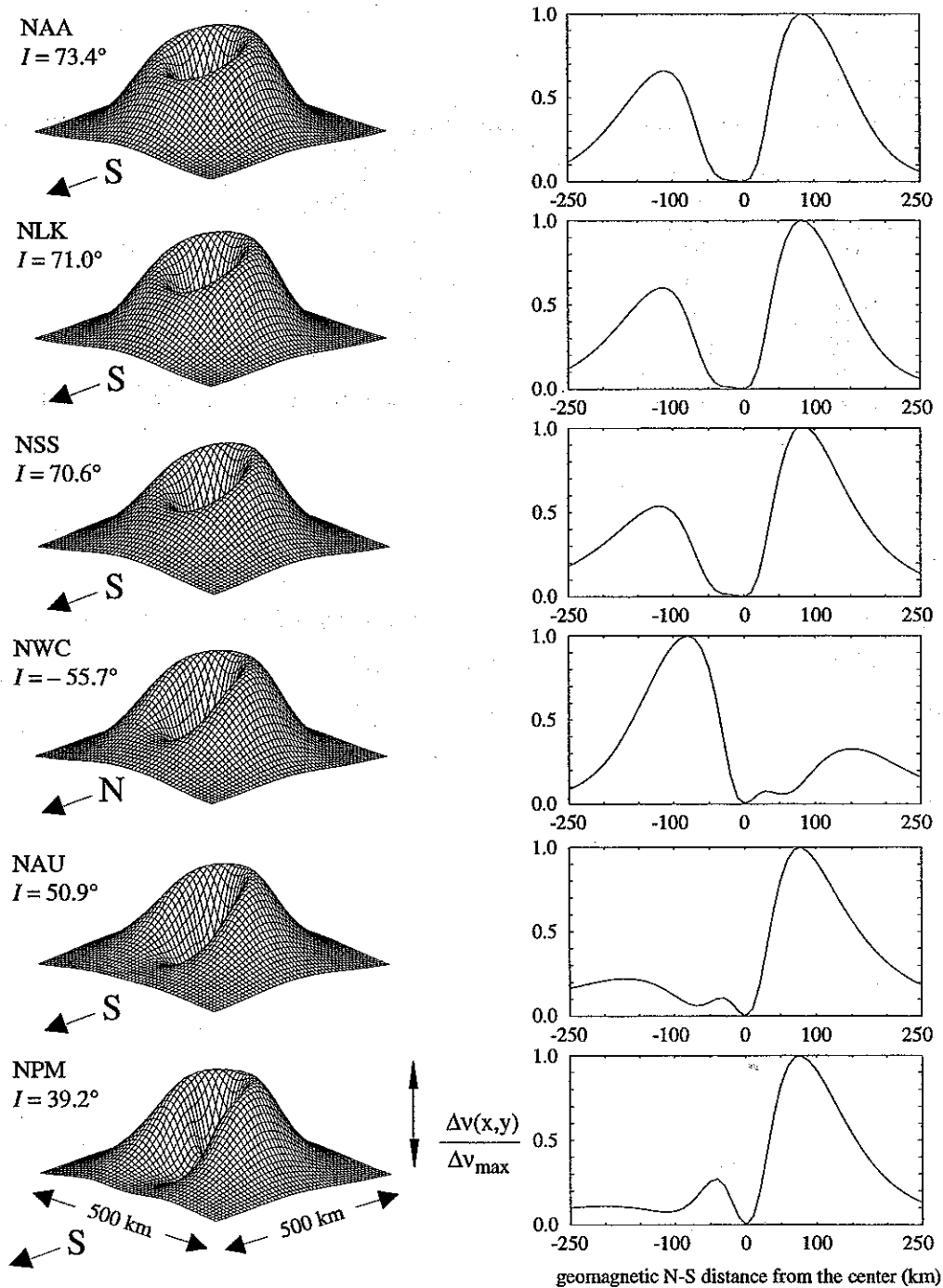
Figure 4.9. Transverse variation of heated region over six different VLF transmitters. Mesh plots and geomagnetic north-south sections of the normalized collision frequency change $\Delta\nu(x, y, h_m)/\Delta\nu(x_m, y_m, h_m)$ due to heating by NAA at the altitudes of maximum heating h_m for the VLF transmitters NAU, NSS, NPM, NLK, NAA, and NWC, assuming electron density profile 0 (Figure 2.3) and the collision frequency profile of *Barr and Stubbe* [1992] (Figure 2.4). The meshes cover a 500 by 500 km area.

4.4 SUMMARY OF HEATING MODEL RESULTS

Models of radio wave propagation and heating in a magnetized and weakly ionized plasma (Chapter 2) were used in this chapter to investigate the hypothesis of Chapter 3 that the observed cross-modulation of subionospheric VLF radio waves was due to heating of the *D* region by powerful VLF transmitter signals. The extent and magnitude of the *D* region electron temperature enhancements caused by the three U. S. Navy transmitters NAA, NSS, and NLK were calculated assuming four different model nighttime *D* region electron density profiles. The heated patches were predicted to be roughly annular with a radius of $\sim$150 km at the half-maximum of the increase in electron-neutral collision frequency. In each case the heating maximum was predicted to be poleward of the heating transmitter, corresponding to absorption of the ordinary (penetrating) component of the wave propagating nearly perpendicular to the Earth's magnetic field. The largest temperature increase (a factor of 3) was predicted for the most powerful transmitter considered here (NAA, 1000 kW radiated power) in the most tenuous *D* region. The corresponding increases in the electron collision frequency are used in the next chapter to represent ionospheric disturbances in a model of VLF propagation in the Earth-ionosphere waveguide. In the final section of this chapter it was shown that the heated region becomes more asymmetric as geomagnetic latitude decreases, although the magnitude of the maximum heating is nearly independent of latitude.

5

Three-Dimensional Modeling of Propagation in the Earth-Ionosphere Waveguide in the Presence of D Region Heating over Very-Low-Frequency Transmitters

The transverse structures of D region electron temperature enhancements over powerful VLF transmitters were determined in Chapter 4 to be roughly annular, about 150 km in radius (at the outer half maximum), and asymmetric in the geomagnetic north-south direction, with maximum heating poleward of the transmitter at $\sim 75 - 87$ km altitude. The resulting changes in the D region collision frequency constitute disturbances in the upper boundary of the Earth-ionosphere waveguide from which signals propagating in the waveguide can scatter. In this chapter, we show that the perturbations of VLF probe waves observed during OFF/ON episodes of powerful VLF transmitters located near subionospheric VLF propagation paths (Chapter 3) are consistent with scattering from such disturbances.

The effect of VLF heating of the D region on subionospheric VLF probe waves is determined quantitatively using a waveguide propagation model that treats the waveguide signal as a sum of modes, that is, a series of solutions to Maxwell's equations that satisfy the boundary conditions at the Earth's surface and the lower edge of the D region. The first section gives a brief overview of the model, which was developed by *Poulsen* [1991] and *Poulsen et al.* [1990, 1993a,b] based on the Long Wave Propagation Capability (LWPC) code of the Naval Ocean Systems Center [*Ferguson et al.*, 1989].

Predictions of amplitude and phase changes for the three experimental VLF heater-probe wave configurations discussed in Chapter 3 are presented in detail in the second section, followed by a discussion of the predicted mode structure of the probe waves. Next is an evaluation of the validity of several important assumptions. The last section of analysis considers the anomalous detection of NAA heating by the NAU-Gander probe wave that was discussed in Chapter 3.

5.1 OVERVIEW OF THE THREE-DIMENSIONAL MODEL OF VLF PROPAGATION IN THE EARTH-IONOSPHERE WAVEGUIDE

The theory underlying the Long Wave Propagation Capability (LWPC) model was developed in the 1960's and 1970's by R. A. Pappert and his colleagues at the Naval Ocean Systems Center [e.g., *Pappert et al.*, 1967], based on the waveguide mode formulation of *Budden* [1962], which accounts for the curvature of the Earth, the D region electron density profile, and the Earth's magnetic field. The LWPC model is two-dimensional in that it treats the Earth as an infinitely long cylinder whose axis of symmetry is perpendicular to the direction of propagation. This model accounts for variation of the waveguide in the vertical direction and along the direction of propagation of the VLF probe wave. Inhomogeneities in the ionospheric and ground conductivities along the direction of propagation are represented as slabs of infinite transverse dimension, and mode coupling is calculated at the interfaces between slabs [e.g., *Pappert and Ferguson*, 1986].

The two-dimensional LWPC model was extended by *Poulsen* [1991] and *Poulsen et al.* [1990, 1993a,b] to three dimensions by treating variations in the ionosphere transverse to the direction of propagation as scatterers, and by linearly superposing the results of three two-dimensional calculations: the signal that propagates directly from the transmitter to the receiver (leg 0), the signal from the transmitter that is incident on the scatterer (leg 1), and the signal scattered by the heated region toward the receiver (leg 2) (Figure 5.1). The theory used to calculate the amplitude and phase of the scattered signal assumes that the transverse extent of the heated region is much larger than the wavelength of the probe wave and that it represents a relatively small change in the conductivity of the D region [*Wait*, 1964a,b,c].

The following is a brief overview of the three-dimensional waveguide propagation model. For a complete description the reader is referred to *Poulsen's* [1991] dissertation.
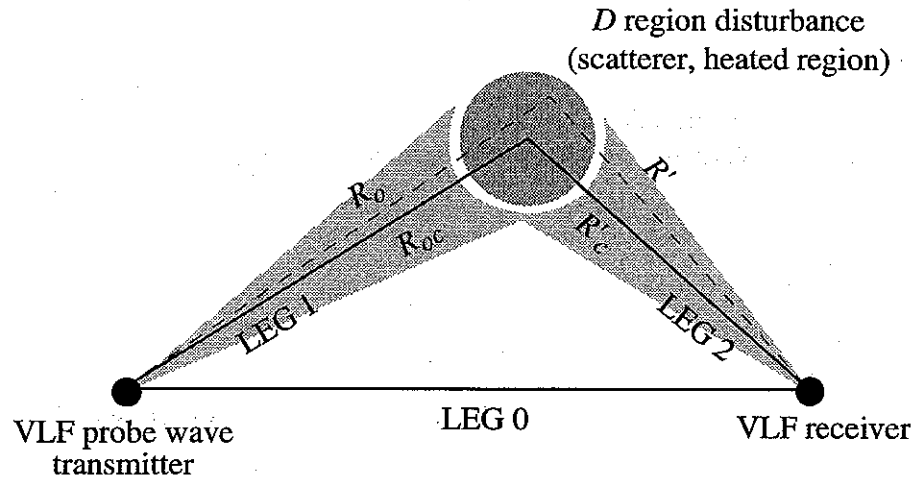
Figure 5.1. Map showing the configuration of the three two-dimensional LWPC runs (legs 0, 1, and 2) that comprise the three-dimensional waveguide model of *Poulsen et al.* **[1993a,b].** The total field at the receiver is the superposition of the direct (leg 0) field and the field scattered toward the receiver by the ionospheric disturbance. The shaded region on the left indicates the angular distribution of paths incident on the heated region that are scattered toward the receiver. The shaded region on the right represents the locus of the paths of these scattered signals.

5.1.1 Model of the Waveguide Boundaries

The Earth-ionosphere waveguide is modeled as a series of segments (minimum length 5 km) in each of which the ground and the ionospheric refractive indices are held constant. Since we do not in general know the ambient D region electron density (N_e) and collision frequency (ν) profiles, the model profiles are typically assumed not to vary along the great circle path of the probe wave, although such an assumption is not a constraint of the model. In all calculations reported in this chapter we have used the ambient collision frequency profile of *Wait and Spies* [1964] (Figure 2.4) and four different model electron density profiles (Figure 2.3) that represent the variability of the ambient nighttime D region electron density near the reflection height of subionospheric VLF probe waves. The International Reference Ionosphere [*Rawer et al.*, 1978] is adopted in the lower E region above 100 km, 97 km, 90 km, and 95 km for electron density profiles 0, I, II, and III, respectively. For the magnetic dip angles I considered in this work ($30° < I < 80°$) new waveguide slabs are created when the angle between the great circle path and the magnetic field changes by $20°$ ($I > 70°$) or $15°$ ($I < 70°$). The electrical properties of the ground at VLF are derived from a data base that divides the Earth's surface into regions

Table 5.1
Ground conductivity and permittivity

Code	Type	σ (S m^{-1})	ε_r
1	ice cap	1.0×10^{-5}	5
2		3.0×10^{-5}	5
3	ice shelf	1.0×10^{-4}	10
4		3.0×10^{-4}	10
5	soil	1.0×10^{-3}	15
6		3.0×10^{-3}	15
7		1.0×10^{-2}	15
8		3.0×10^{-2}	15
9		1.0×10^{-1}	80
10	sea water	4.0	81

of different conductivity (σ) and relative permittivity (ε_r), as listed in Table 5.1 [*Hauser et al.*, 1969].

5.1.2   Waveguide Modes

In *Budden's* [1962] waveguide mode formulation, the curvature of the earth is incorporated in an ingenious manner that permits the problem to be solved in Cartesian coordinates. A ray propagating along a straight line from the ground to the ionosphere in a cylindrical geometry is equivalent under a conformal transformation [*Richter*, 1966] to a ray curving upward in a Cartesian geometry. This curvature can be thought of as being due to an equivalent "free space" refractive index n that increases slightly with altitude. If the expression for the "free space" n^2 due to the transformation is expanded in a series and only the first two terms retained, then $n = \sqrt{1 + (2/R_\oplus)(h - h')}$, where h is the altitude and h' is some reference altitude chosen to be near the bottom of the ionosphere [*Budden*, 1962; *Pappert et al.*, 1967; *Pappert*, 1968]. With this refractive index, the second-order differential equations (derived from Maxwell's equations) that describe the spatial variation of the wave fields in the waveguide have analytical solutions that are the weighted sums of special functions known as "modified Hankel functions." These

functions have the attractive property of being single-valued and have been tabulated for easy use in computations [*Staff of the Computation Laboratory*, 1945]. The weights or coefficients of the special functions are determined from the boundary conditions at the surface of the Earth and the D region. The solutions are known as the height-gain functions or eigenfunctions (G_n). This conformal transformation also permits the use of standard numerical ("full wave") methods for solving Maxwell's equations in Cartesian coordinates for the wave fields inside the D region [*Budden*, 1962]. In this calculation the three elements ε_1, ε_2, and ε_3 of the diagonalized permittivity matrix are given by equations (2.17), which assume that the collision frequency is independent of electron energy, plus a small correction to account for curvature [*Pappert*, 1968].

A waveguide mode can be thought of as the superposition of two plane waves reflected repeatedly off the upper and lower boundaries of the waveguide at an angle θ with respect to the vertical such that the waves interfere constructively along the axis of propagation of the waveguide. The "eigenangle" θ_n unique to each mode is a function of the waveguide boundary conditions and is in general complex. More formally, for a waveguide slab specified by the ground conductivity and an ionospheric conductivity profile, the waveguide modes correspond to solutions of the determinant

$$|\mathbf{R}_h^i(\theta_n^h)\mathbf{R}_h^g(\theta_n^h) - \mathbf{I}| \tag{5.1}$$

where $\mathbf{R}_h^i$ is the complex reflection coefficient matrix looking up towards the ionosphere from a height h, $\mathbf{R}_h^g$ is the complex reflection coefficient matrix looking down at the ground from height h, and θ_n^h is the eigenangle referred to height h [*Budden*, 1961, 1962]. The reflection coefficients are derived by determining the components of the electric and magnetic fields of the wave in the waveguide, as described above. When the reflection coefficient matrices are known, excitation factors Λ_n that give the amplitudes and phases of the n modes excited by the transmitting antenna (e.g., Figure 5.6) can be determined [e.g., *Pappert and Ferguson*, 1986].

In cylindrically symmetric waveguides with perfectly conducting walls, which are well approximated by man-made metallic waveguides, modes are categorized as transverse magnetic (TM) or transverse electric (TE), in reference to the field vector that is entirely transverse (perpendicular) to the direction of propagation down the waveguide [*Ramo et al.*, 1984, p. 395]. Analogous to this terminology, modes in the Earth-ionosphere wave-guide can be classified as quasi-transverse magnetic (QTM) or quasi-transverse electric

(QTE), based on the magnitude of the ratio of the horizontal magnetic field (multiplied by $\eta_o = 377 \; \Omega$, the wave impedance of free space) to the horizontal electric field of the mode [*Pappert*, 1968]. If the magnitude of this "polarization mixing ratio" $|\rho|$ is greater than 1, the mode is QTM; otherwise, if $|\rho| < 1$, the mode is QTE. The QTE and QTM modes are separately numbered according to the number of half-period variations of the mode field in the vertical direction in the Earth-ionosphere waveguide [*Poulsen et al.*, 1993a]. Note that an electrically short antenna perpendicular to a perfectly conducting surface is not efficient in exciting TE modes in a parallel-plate waveguide since the electric field parallel to the surface is zero.* In the Earth-ionosphere waveguide, VLF transmitting antennas can excite QTE modes due to the finite conductivity of the Earth, but generally at weaker levels compared to the QTM modes (see Figure 5.6 below) [*Pappert*, 1968; *Galejs*, 1972a, b]. However, QTE modes are excited during propagation by mode coupling at abrupt decreases in the ground conductivity, as typically is the case at coastlines [e.g., *Inan et al.*, 1992].

5.1.3 Summation of Modes

In a waveguide consisting of a single slab, or in the first slab of a segmented waveguide as described above, the vertical electric field at the ground is

$$E_v = \frac{Q}{\sqrt{|\sin(d/R_\oplus)|}} \sum_n \Lambda_n G_n^T G_n^R \exp\left[-ikS_n d\right] \tag{5.2}$$

where Q is a function of transmitter frequency and power, $k = \omega/c$, d is the distance along the surface of the Earth from the transmitter to the receiver, Λ_n is the excitation factor of the vertical electric field by a vertical electric dipole, G_n^T and G_n^R are the values of the height-gain functions evaluated at the location of the transmitter and the receiver, respectively, and the sine of the eigenangle S_n is the refractive index of mode n. The factor

$$\frac{1}{\sqrt{|\sin(d/R_\oplus)|}} \tag{5.3}$$

---

* A wire extending well into a man-made metallic waveguide of rectangular cross-section can excite a TE$_{10}$ mode, in which the electric field does not vary in the direction of the axis of the antenna and has a half-cycle cosine variation in the direction perpendicular to both the antenna axis and the axis of the waveguide [*Ramo et al.*, 1984]. This method of excitation is roughly equivalent to using a horizontal dipole antenna at $40 - 45$ km altitude in the Earth-ionosphere waveguide to excite a QTE mode.

describes the spreading of a wave over a sphere of radius $R_\oplus$ at a distance d that is not near the transmitter or in the antipodes of the transmitter (i.e., $d/R_\oplus \neq 0$ or π) [*Watson*, 1918, 1919; *Wait*, 1962, p. 161].

With an amplitude factor $Q = 682\sqrt{f}$, where f is the transmitter frequency in kHz, (5.2) gives the electric field in μV m^{-1} from a 1 kW transmitter. This form of Q is consistent with similar numerical forms given by *Pappert and Snyder* [1972] and *Pappert and Morfitt* [1975] and with an analytic form given by *Pappert and Bickel* [1970]:

$$Q = \frac{\eta_o k^{\frac{3}{2}} I_{\text{RMS}} h_e}{\sqrt{8\pi R_\oplus}} \qquad (5.4),$$

where η_o is the impedance of free space, and $I_{\text{RMS}} h_e$ is the root-mean-squared current moment of a VLF transmitting monopole. The numerical forms can be derived by combining equations (4.4) and (4.5) to derive the following expression

$$I_o h_e = \frac{1}{k} \sqrt{\frac{6\pi P_{tot}}{2\eta_o}} \qquad (5.5),$$

where $I_o = \sqrt{2} I_{\text{RMS}}$, and substituting this expression in equation (5.4).

5.1.4 Coupling of Modes at Slab Boundaries

As discussed above, waveguide inhomogeneities along the direction of propagation are represented by dividing the great circle path into slabs in which the ground and ionospheric refractive indices differ from those of previous and succeeding slabs. In general, the amplitude and phase of each waveguide mode is different on either side of a slab interface due to the different waveguide boundary conditions. Consequently, coupling among the various modes occurs at slab interfaces. In effect, each mode is a weighted sum of all the modes on the other side of the interface; the coefficients of the terms in this sum are elements of a complex $n \times m$ matrix, where n and m are the number of significant modes on either side of the slab interface [*Poulsen*, 1991]. The mode coupling is determined using the LWPC program "FASTMC" [*Ferguson and Snyder*, 1980] or "fast mode coupling," which calculates the elements of the matrix using analytical approximations to the modal eigenfunctions inside the waveguide between the Earth's surface and the height at which $\omega_{pe}^2/\nu = 2.5 \times 10^5$ s^{-1}. In an isotropic ionosphere this is the height

below which most of the energy contained in waveguide modes is reflected [*Wait and Walters*, 1963; *Wait and Spies*, 1964]. In the "FASTMC" method, mode coupling above this approximate reflection height is neglected. *Pappert and Ferguson* [1986] have shown that this approximate solution is similar in accuracy to a more computationally intense "full wave" solution that solves Maxwell's equations to determine the eigenfunctions numerically for each mode on either side of the interface and hence the mode coupling coefficients.

5.1.5   Scattering Integral

The configuration of the three two-dimensional runs combined to predict the effect of VLF transmitter heating on a subionospheric VLF probe wave is shown in Figure 5.1. The line labeled R_{oc} is the great circle path from the probe wave transmitter to the center of the heated region (leg 1). The line labeled R_c' is the great circle path from the center of the heated region to the receiver (leg 2). The direct path from NSS to Gander is referred to as "leg 0." The shaded region on the left indicates the angular distribution of paths incident on the heated region that are scattered toward the receiver. The shaded region on the right represents the locus of the paths of these scattered signals.

The guided nature of the waves permits a two-dimensional formulation of the scattering problem which treats the horizontal variation of the waveguide mode refractive indices $S_n(x', y')$ [*Wait*, 1964a,b,c], where x' and y' are horizontal Cartesian coordinates measured from the transmitter location. The third (vertical) dimension is implicit in the refractive indices or eigenangles $\theta_n(x', y') = \sin^{-1}\left[S_n(x', y')\right]$ which represent an integrated measure of the vertical variation of the waveguide mode fields. Assuming that the horizontal extent of the D region disturbance is much larger than a wavelength so that there is no mode coupling (W.K.B. approximation), the expression for the scattered vertical electric field of a single mode observed at the receiver location (x, y) is [*Wait*, 1964a,b,c; *Poulsen et al.*, 1990]

$$E_n^s(x, y) = -\frac{ik^2}{4}\left(\frac{2i}{\pi k S_n^o}\right)^{\frac{1}{2}} \iint \left[S_n^2(x', y') - \left(S_n^o\right)^2\right] E_n(x', y')\frac{\exp(-ikS_n^o R')}{(R')^{\frac{1}{2}}}dx'\,dy'$$

(5.6)

where $E_n(x', y')$ is the VLF probe wave electric field from the transmitter in the waveguide under the disturbance, R' is the distance between the infinitesimal scatterer at

(x', y') and the receiver (Figure 5.1), and

$$\left(\frac{2i}{\pi k S_n^o R'}\right)^{\frac{1}{2}} \exp(-ik S_n^o R') \tag{5.7}$$

is the asymptotic expression for the spreading of the scattered wave over a cylindrical surface at a distance R' greater than one wavelength from the transmitter. Equation (5.7) can be corrected slightly by replacing the factor $1/\sqrt{R'}$ by the factor (5.3) that describes the spreading of a wave over a spherical surface.

An important step at this point is the replacement of $E_n(x', y')$ with $E_n^o(x', y')$, the VLF probe wave field that would be observed at (x', y') in the absence of heating. This constitutes the Born approximation, which is justified if the change in the modal refractive indices S_n is small, i.e., $|S_n^2(x', y') - (S_n^o)^2| \ll 1$ [*Poulsen et al.*, 1990]. By further assuming that the ground conductivity map is the same between the transmitter and each point in the heated region, and that the ground conductivity pattern is the same from each of these points to the receiver, it can be shown [*Poulsen*, 1991; *Poulsen et al.*, 1990, 1993a,b] that the above expression for E_n^s is equivalent to

$$E_n^s = c_n\, E_n^{LWPC}(R_{oc})\, \frac{E_n^{LWPC}(R_c')}{\Lambda_n G_n^T G_n^R \left(R_\oplus\right)^{\frac{1}{2}}} \iint \left[S_n^2(x', y') - \left(S_n^o\right)^2\right] F_n(x', y') dx'\, dy' \tag{5.8}$$

where

$$c_n = \frac{-ik^2}{4} \left(\frac{2i}{\pi k S_n^o}\right)^{\frac{1}{2}} \tag{5.9}$$

$$F_n(x', y') = \left(\left|\frac{\sin(R_{oc}/R_\oplus)\sin(R_c'/R_\oplus)}{\sin(R_o/R_\oplus)\sin(R'/R_\oplus)}\right|\right)^{\frac{1}{2}} \exp\left\{-ik S_n^o[(R_o - R_{oc}) + (R' - R_c')]\right\} \tag{5.10}$$

and $E_n^{LWPC}(R_{oc})$ and $E_n^{LWPC}(R_c')$ are the vertical electric fields calculated at the ends of leg 1 and leg 2, respectively, using the two-dimensional LWPC model. R_o is the distance from the transmitter to the infinitesimal scatterer at (x', y').

Although the complex refractive index S_n of mode n in general depends nonlinearly on the collision frequency ν, even an order of magnitude increase in the collision frequency due to heating may have a relatively small effect on the refractive index of waveguide signals since $\nu \ll \omega_{ce}$ above 75 km in the midlatitude nighttime ionospheres considered

here [*Barr et al.*, 1985]. Indeed, numerical analysis shows that for the cases considered here ΔS_n is approximately proportional to $\Delta \nu$ for all but the highest order modes, which contribute insignificantly to the received signals. (One example of such an analysis is given in section 5.4.6.). Therefore, the refractive index for each mode is calculated at each point in the Earth-ionosphere waveguide under the heated region as

$$S_n(x',y') = S_n^o + \left[S_n(x'_m, y'_m) - S_n^o \right] \frac{\Delta\nu(x',y',h_m)}{\Delta\nu(x'_m, y'_m, h_m)} \qquad (5.11),$$

where S_n^o and $S_n(x'_m, y'_m)$ are the refractive indices of mode n for the ambient and heated ν profiles, respectively.

The normalized collision frequency change at the altitude of maximum heating, given by $\Delta\nu(x',y',h_m)/\Delta\nu(x'_m, y'_m, h_m)$, is calculated using the heating model of Chapter 4 in the form of a two-dimensional table of values specified on a 10-km grid on which bilinear interpolation [*Press et al.*, 1988, p. 105] is performed when the scattering integral is evaluated numerically.

5.2   COMPARISON OF OBSERVED AND PREDICTED VLF PROBE WAVE PERTURBATIONS DUE TO VLF HEATING

In this section we present the amplitude and phase changes predicted for the three experimental heater-probe wave configurations discussed in Chapter 3. The altitude profiles of increased collision frequency due to VLF heating that are used to determine $S_n(x',y')$ were calculated in Chapter 4. On the left half of Figure 5.2 are the $\Delta\nu(x'_m, y'_m, h)/\nu_o(h)$ profiles due to heating by NSS, NLK, and NAA, assuming four electron density profiles (Figure 2.3). On the right half are contour plots of $\Delta\nu(x',y',h_m)/\nu_o(h_m)$ over a 500 km by 500 km area for the case of electron density profile 0 (Figure 2.3). The contour plots are normalized to the maximum relative heating, $\Delta\nu(x',y',h_m)/\nu_o(h_m)$, predicted for NAA. Heating is zero at the center of the regions and maximum directly north of center. The contour lines are shown at increments of 10% of the maximum relative heating $\Delta\nu(x'_m, y'_m, h_m)/\nu_o(h_m)$ due to NAA. Superposed on the contour plots is the great circle path of the subionospheric VLF probe wave that most closely approaches the heater in question.

The NSS-GA signal perturbations due to NAA heating predicted for electron density
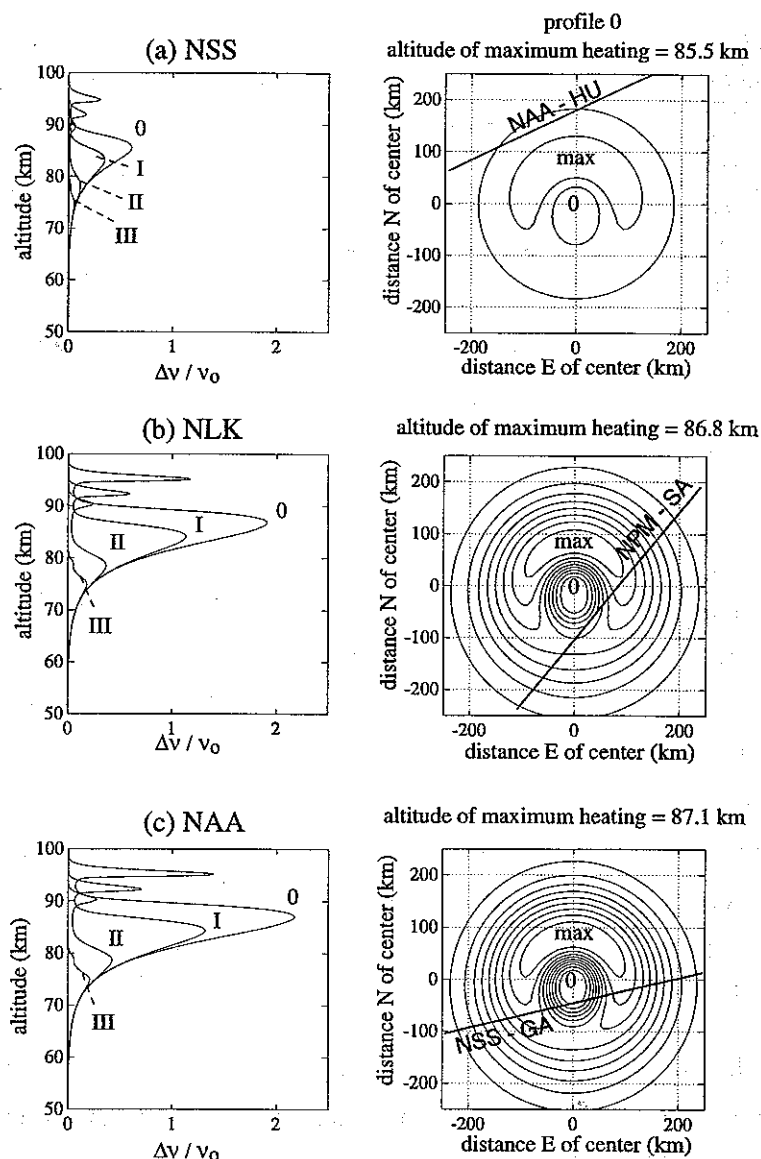
Figure 5.2. Vertical and transverse variation of the increase in D region electron collision frequency over NSS, NLK, and NAA. Calculated $\Delta\nu(x'_m, y'_m, h)/\nu_o(h)$ profiles (left) and contour plots of $\Delta\nu(x', y', h_m)/\nu_o(h_m)$ (right) over (a) NSS, (b) NLK, and (c) NAA. The profiles are shown for electron density profiles 0 (most tenuous), I, II, and III (most dense), and the transverse variations are shown for profile 0. In each case the great circle path of the probe wave that is closest to the heating transmitter is superposed on the contour plot. Geomagnetic north is toward the top of the page.

Table 5.2
Calculated NSS-GA perturbations due to NAA heating

N_e profile	ΔA (dB), $\Delta\phi$ (°)	max$|\Delta A|$ (dB)	max$|\Delta\phi|$ (°)
0	+0.01, −3.29	0.51	3.29
I	+0.02, −1.34	0.21	1.35
II	−0.05, −0.77	0.13	0.83
III	−0.06, −0.21	0.07	0.45

profiles 0, I, II, and III (Figure 2.3) are listed in Table 5.2 and are plotted in Figure 5.3 along with the observed amplitude and phase perturbations (Chapter 3). The predictions for profiles I and III are each consistent with a few of the observed perturbations. However, the model fails to predict amplitude and phase changes consistent with the largest observed signal perturbations ($>$ 0.25 dB and $<$ $-2.0°$). If we assume the predicted magnitudes of the scattered fields to be correct to within a factor of 2, then the difference between the phases of the direct and scattered fields is the likely source of the error (see below). From this point of view, the range of predicted scattered field amplitudes is consistent with the observations, with the largest scattered fields being predicted for NAA heating the most tenuous D region (profile 0).

To better view the comparison of data with predictions, consider the loci in Figure 5.3 of all possible phase and amplitude perturbation pairs for the calculated magnitudes of the scattered fields (E_s). The loci are generated by varying the phase ϕ_r of the predicted scattered electric field phasors relative to the unperturbed (E_o) phasors, i.e., $\Delta E = 1 + |E_s/E_o| \exp(i\phi_r)$ where $0 \leq \phi_r < 2\pi$. The maximum possible amplitude and phase changes calculated in this manner for a given scattered field amplitude are also listed in Table 5.2. The locus for the scattered field E_s predicted for profile 0 passes through a group of several observed amplitude and phase perturbation pairs, including the December 16, 1992, event shown in Figure 3.2. It can be seen from Figure 5.3, for example, that if the difference between the phases were $\sim 45°$ smaller for profile 0, then the prediction would be in very good agreement with the observations. A 45° phase
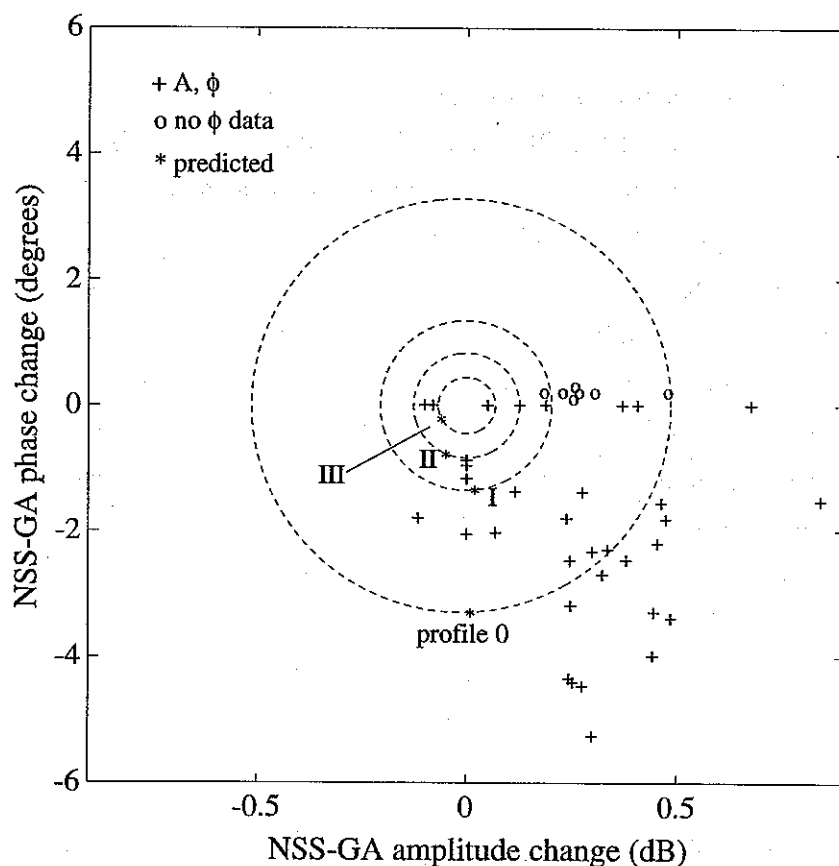
Figure 5.3. NSS amplitude and phase perturbations observed at Gander during NAA OFF/ON episodes in December 1992, and predicted using the heating and waveguide propagation models. Open circles indicate no phase (ϕ) data available; these points have been plotted slightly off the $\Delta\phi = 0$ axis for clarity. The thresholds of detectability were approximately ± 0.1 dB and $\pm 0.5°$. Asterisks labelled 0, I, II, and III indicate the predictions for the corresponding electron density profiles. Loci (dashed lines) are generated by varying the relative phase of the unperturbed and scattered signals from 0 to 2π.

error corresponds to one eighth of a wavelength, which at 21.4 kHz is 1.7 km, or less than 0.1% of the great circle path length between NSS and Gander. In general, given the great uncertainties involved in modeling the D region at all points between NSS and Gander (a distance of 2063 km) with a single electron density profile, an error of such a magnitude ($\sim$ 2 km) in the optical path length for any of the three legs (0, 1, or 2) is not unexpected.

As discussed in Chapter 3, a comparison of the observations of NSS and NAA field strengths immediately prior to NAA OFF/ON episodes during December 1992 with the corresponding predictions of the waveguide model provides an additional measure of the consistency of the observations and predictions. As shown in Figure 5.4, heating was less likely to be detected when the amplitude of NAA-GA was relatively high, and the predicted vertical electric field is somewhat smaller for the more tenuous profiles 0 and I than for the more dense profiles II and III. Both of these facts are consistent with the results of the heating and waveguide propagation models, which indicate that more heating occurs in a more tenuous D region for the same heater power (Chapter 4), resulting in a larger perturbation of the VLF probe wave. However, the vertical electric field predictions do not match the large range of observed NAA and NSS field strengths. The fact that somewhat larger NAA field strengths are predicted for the denser profiles II and III is a result of the multi-mode nature of waveguide propagation and is contrary to the simplistic expectation that a denser D region would result in more attenuation and hence lower field strengths.

In the case of NSS heating detected with the NAA-HU probe wave, the calculated amplitude changes (Table 5.4) are consistent in magnitude for electron density profiles 0 and I, but opposite in polarity to the observed values (Table 3.4). The lack of phase data from Huntsville preclude a comparison with the phase predictions. Note that for profiles 0, I, and II the predicted amplitude changes are essentially the same as the maximum changes possible for the calculated scattered electric field amplitudes.

In the case of NLK heating detected with the NPM-SA probe wave the calculated amplitude changes (Table 5.3) are much smaller, than though mostly of the same polarity as, the observed values (Table 3.3). Even the maximum possible amplitude changes possible for the calculated scattered electric field amplitudes are smaller than the observed amplitude change magnitudes. The lack of phase data from Saskatoon preclude a comparison with the phase predictions.
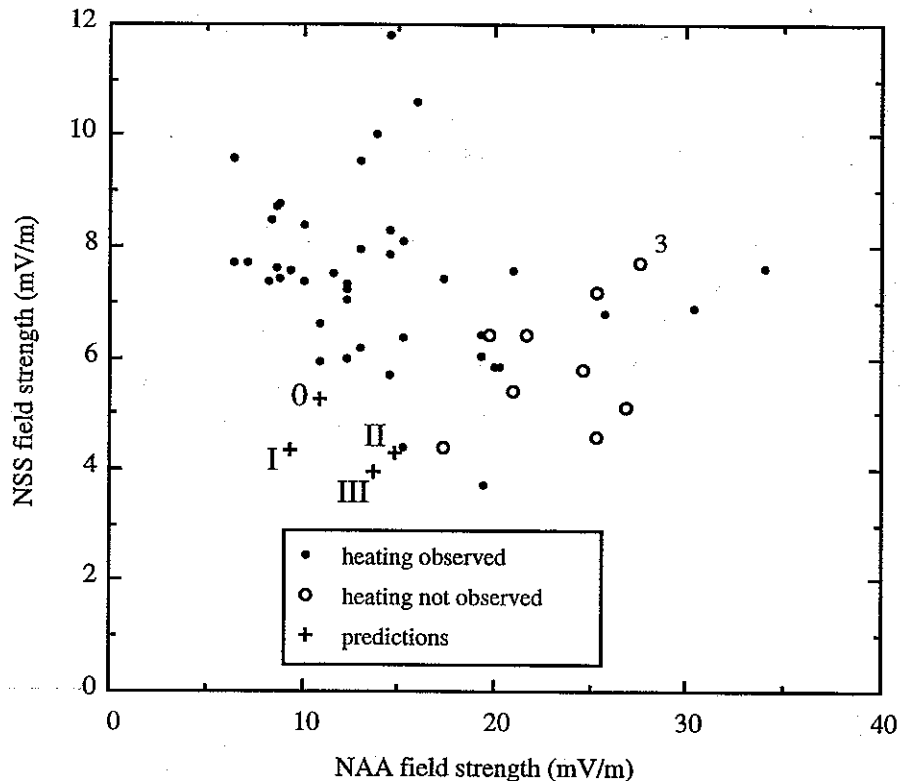
Figure 5.4. Observed and predicted signal strengths of NAA and NSS at Gander.
Equivalent vertical electric field of NAA-GA and NSS-GA immediately prior to NAA
OFF/ON episodes during December 1992. Numerals (e.g., 2, 3) indicate a multiplicity
of observed field strength pairs. Crosses labelled 0, I, II, and III indicate the predictions
for the corresponding electron density profiles.

The fact that, in general, larger perturbations are observed on all the probe waves
considered here than can be predicted with the chosen ionospheric and heating models
may be due in part to the fact that we neglect reflection effects in the heating model.
Galejs [1972b] showed that 20-25% larger vertical electric fields at $h = 85$ km are
predicted when reflection is included. In the case of NLK heating the larger discrepancies
may also stem from the assumption of a single ambient D region electron density profile
along the 5469-km NPM-SA probe wave great circle path. This long path covers a
greater range of geomagnetic latitudes than the other two paths, being oriented nearly
north-south geomagnetic; therefore, it may be more sensitive to latitudinal variations in
electron density profile than the NAA-HU or NSS-GA paths.

Table 5.4
Calculated NAA-HU perturbations due to NSS heating

N_e profile	ΔA (dB), $\Delta \phi$ (°)	max$|\Delta A|$ (dB)	max$|\Delta \phi|$ (°)
0	−0.24, −0.68	0.26	1.71
I	−0.24, −0.19	0.24	1.55
II	−0.11, −0.20	0.11	0.72
III	−0.01, −0.11	0.02	0.12

Table 5.3
Calculated NPM-SA perturbations due to NLK heating

N_e profile	ΔA (dB), $\Delta \phi$ (°)	max$|\Delta A|$ (dB)	max$|\Delta \phi|$ (°)
0	−0.08, −0.58	0.12	0.78
I	−0.07, −1.27	0.21	1.34
II	−0.01, −0.28	0.04	0.29
III	−0.01, −0.26	0.04	0.27

5.3 PREDICTIONS OF THE MODE STRUCTURE OF SUBIONOSPHERIC VLF PROBE WAVES

The mode structures of subionospheric VLF signals are illustrated in this section using polar plots of the vertical electric field phasors for the significant modes at the beginnings and ends of all three legs. The fields are shown in units of μV m^{-1} normalized to the output of a transmitter with a total radiated power of 1 kW. To be converted to the expected field values they must be multiplied by the square root of the actual transmitter radiated power in kW. Only "significant" modes, that is, modes whose electric field is at least one-tenth the magnitude of the strongest mode, are plotted. Also plotted are the

unperturbed probe wave amplitude and phase along the great circle path between the transmitter and receiver (leg 0). On these plots the amplitude is shown in dB relative to $1\ \mu\text{V m}^{-1}$ from a 1 kW transmitter, while the phase delay relative to the transmitter is shown in degrees. For plotting purposes a phase delay $\phi_o = kd$ equivalent to that which would be accumulated in free-space propagation is subtracted from the phase as given in equation (5.2). Thus, only the additional phase variation due to the presence of the waveguide boundaries is calculated. For example, for a wave frequency $f = 24.0$ kHz and a distance $d = 2000$ km, the "free-space" phase delay ϕ_o is approximately 10^3 radians or 5.8×10^4 degrees. By comparison, the phase delay due to the effect of the waveguide boundaries for the paths considered here is $\sim 100 - 1000°$ (Figures 5.7, 5.10, and 5.13).
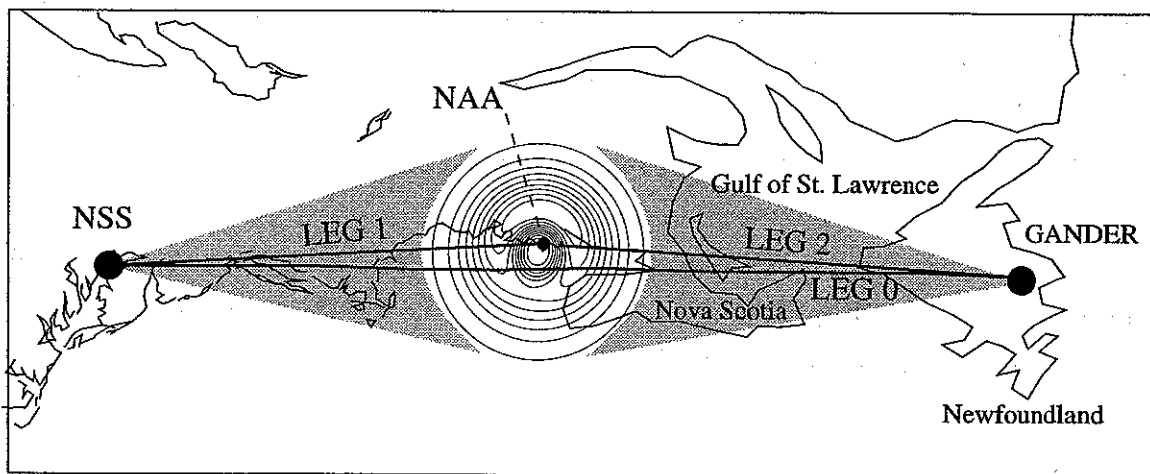
Figure 5.5. Transverse variation of heated region over NAA with respect to the geography of northeastern North America. Contour plot of the normalized transverse variation of collision frequency $\Delta\nu(x', y', h_m)/\Delta\nu(x'_m, y'_m, h_m)$ at the altitude of maximum heating by NAA for profile I, superimposed on a map of the section of the NSS-Gander great circle path near the NAA transmitter. The shaded region on the left indicates the angular distribution of paths from the NSS transmitter incident on the heated region over NAA that are scattered toward the receiver at Gander. The shaded region on the right represents the locus of the paths of these scattered signals.

5.3.1 Mode Structure of the NSS-Gander Probe Wave

The transverse extent of the heated region or scatterer over NAA is indicated in Figure 5.5 by a contour plot of the quantity $\Delta\nu(x', y', h_m)/\Delta\nu(x'_m, y'_m, h_m)$, which is the change in collision frequency at the altitude of maximum heating h_m normalized by the maximum change at this altitude (Chapter 4). The contour plot shown here is that predicted for electron density profile I (Figure 2.3). The outermost contour represents $\Delta\nu(x', y', h_m)/\Delta\nu(x'_m, y'_m, h_m) = 0.1$, with each subsequent contour representing an increment of the same size. The change in collision frequency is minimum (ideally zero) directly above NAA at the center of the heated region. Note that the maximum heating directly to the geomagnetic north of NAA occurs over land. Although most of the heated region is over land, a significant portion lies over water.

The mode structure of the NSS-GA probe wave is described in greater detail here than that of the NPM-SA or NAA-HU probe waves since it is the experiment of primary interest in this dissertation. The wave at the NSS transmitter consists of many significant modes, both QTE and QTM, whose amplitudes are proportional to the antenna excitation factor Λ_n. Shown in Figure 5.6 are the mode structures of the signal excited by the NSS transmitter at the beginning of the NSS-GA great circle path (leg 0) for electron density profiles 0, I, II, and III. The modes excited in the direction of the path to the scatterer (leg 1) differ little in this case from those shown in Figure 5.6 due to the small azimuthal angle between legs 0 and 1. Note that in general QTM modes are more strongly excited than QTE modes. The phase relationship among the modes is more sensitively dependent on the D region electron density profile than the relative mode amplitudes.

In fact, the wave amplitude differs little among the four profiles out to a distance of $\sim$ 100 km. Shown in Figure 5.7 are the amplitude and phase of the NSS-GA probe wave between the NSS transmitter and the receiver at Gander calculated for all four electron density profiles. Beyond 100 km the modes begin to interfere constructively and destructively, with two prominent nulls (15–20 dB) occuring for all four electron density profiles. The distance of these nulls from the transmitter increases as the D region becomes more tenuous. (In the case of profile 0 these nulls are at $\sim$ 600 and $\sim$ 1550 km.) Due to the multiple mode nature of the probe wave the field strength of NSS at Gander predicted for profile 0 is not in general greater than that predicted for the other profiles, despite the lower attenuation rates under a tenuous D region.

The mode structure of the signal at some distance from the transmitter is affected by
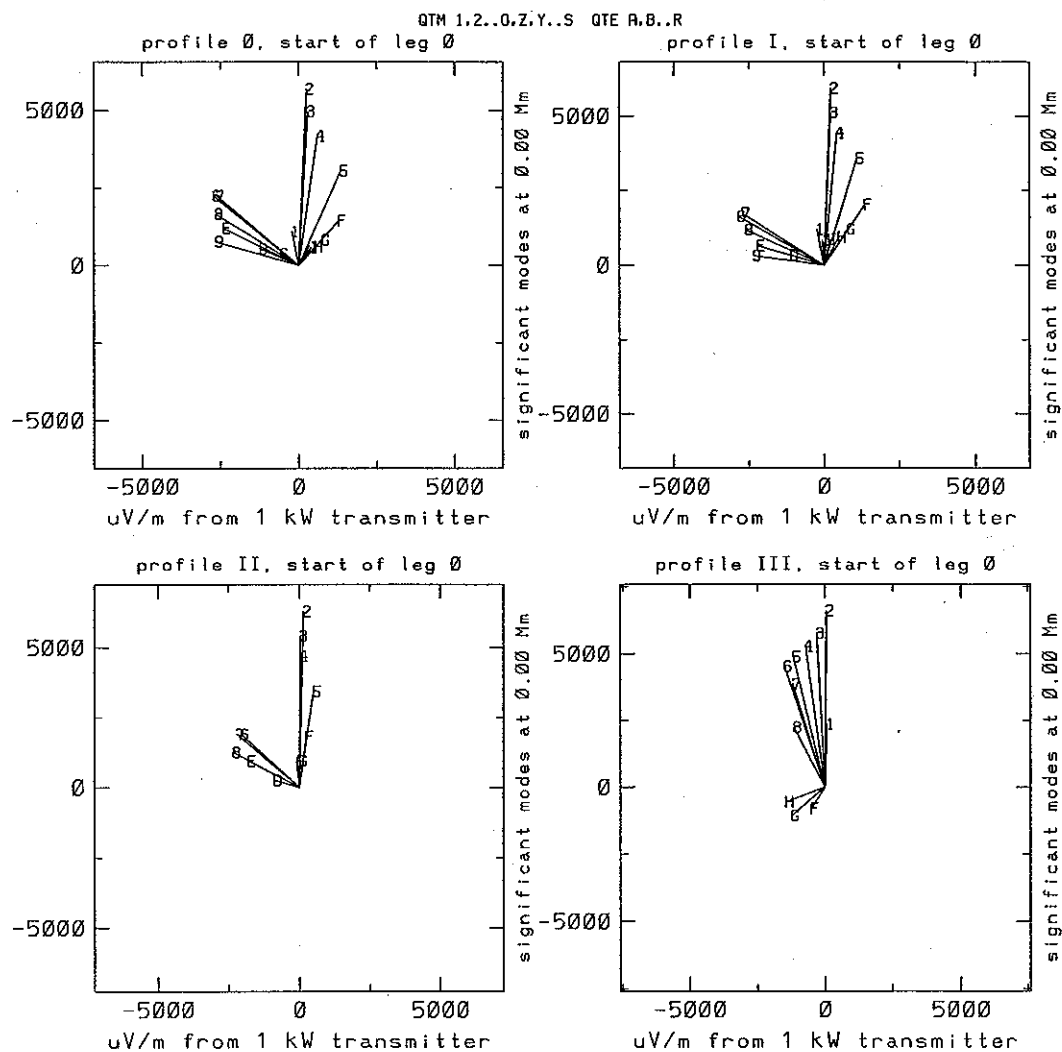
Figure 5.6. Mode structure of the signal excited by the NSS transmitter. Polar plots of the significant modes at the NSS transmitter, for electron density profiles 0, I, II, and III. Significant modes are those at least one-tenth the magnitude of the strongest mode. Mode phasor amplitudes are in units of $\mu V\ m^{-1}$ from a 1 kW transmitter.
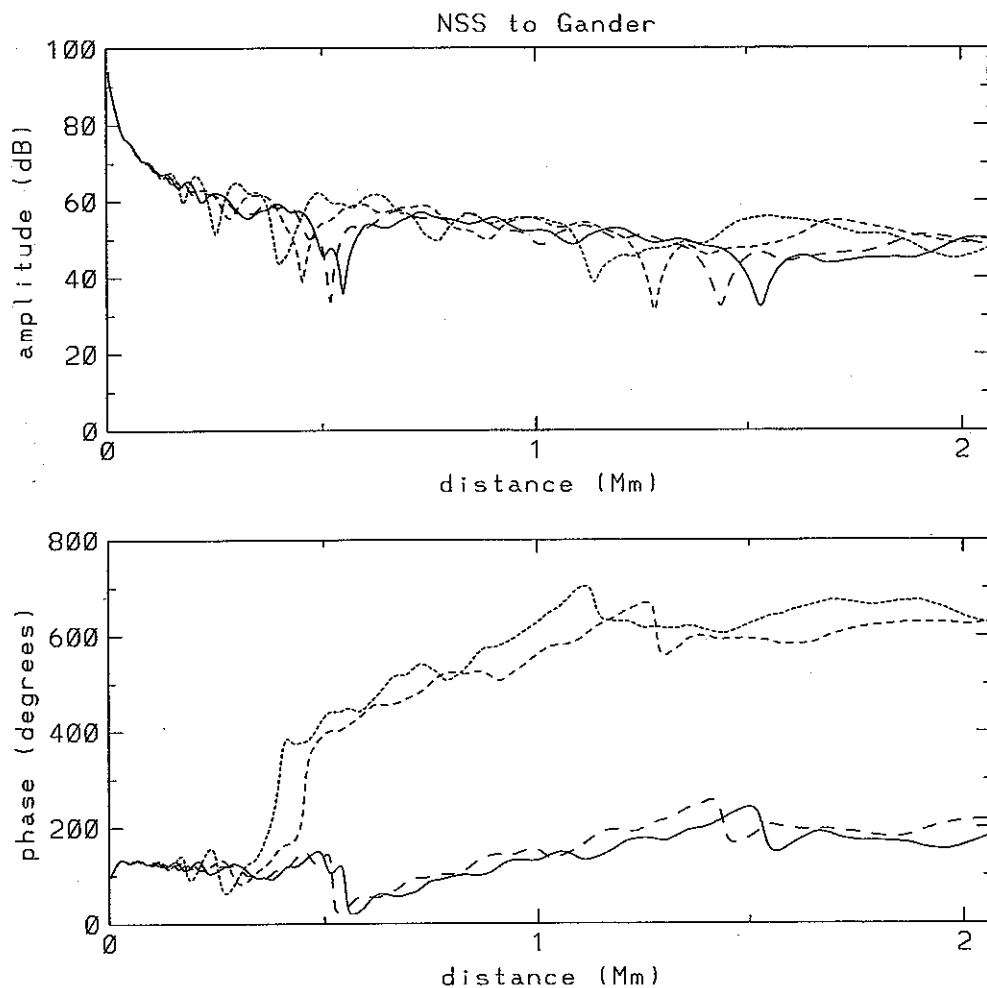
Figure 5.7. Amplitude and phase of the NSS-GA probe wave as a function of distance between the transmitter and receiver for electron density profiles 0, I, II, and III. The solid line is the prediction for profile 0, the coarsely dashed line for profile I, the medium dashed line for profile II, and the finely dashed line for profile III. Amplitude is in dB relative to 1 μV m^{-1} from a 1 kW transmitter. The phase shown is relative to the "free space" phase delay $\omega d/c$, where d is the distance along the surface of the Earth from the transmitter.

the attenuation rates of the different modes as well as mode coupling at discontinuities in the ground or ionospheric conductivities. The attenuation rates $\alpha_n = -8686k\mathrm{Im}\{\sin\theta_n\}$ are listed in Table 5.5 in units of dB Mm^{-1} for the case of the NSS-GA probe wave propagating over sea water, in this case the portion of the Gulf of St. Lawrence between Nova Scotia and Newfoundland (Figure 5.5), and under a D region represented by profile 0. In addition, the mode eigenangles θ_n (referred to the ground), the ratio of the phase velocity to the speed of light $v_\phi/c = 1/\mathrm{Re}\{\sin\theta_n\}$, and the magnitude of the polarization mixing ratio ρ are listed. The modes are designated QTE or QTM depending on the magnitude of ρ, as discussed above. Note that although the QTM_1 mode is weakly excited by the NSS transmitter antenna compared to many other modes (Figure 5.6), it has one of the lowest attenuation rates. Only the QTE_1 and QTE_2 modes have lower attenuation rates, and they are much more weakly excited. The highest order modes listed here have such high attenuation rates that they are negligible at the receiver.

To illustrate the effect of the different modal attenuation rates on the evolution of the probe wave mode structure, the mode phasors at the ends of leg 0 and leg 1 are plotted in the left half of Figure 5.8. By comparing the mode structure impinging on the scatterer at the end of leg 1 ($\sim$ 1000 km from NSS) with the mode structure at the beginning of leg 0 (Figure 5.6, upper left corner) it can be seen that most of the modes are attenuated substantially over the 1000-km-long path. At Gander (2063 km from NSS), at the end of leg 0, the signal consists basically of the QTM_1, QTM_2, and QTM_3 modes. The simplicity of the mode structure at the ends of legs 0 and 1 contrasts with the complicated nature of the modes scattered by the heated region and the mode structure of the scattered field observed at the receiver (Gander), both plotted in the right half of Figure 5.8.

A note of caution must be made about the mode amplitudes at the beginning of leg 2 plotted in the upper right corner of Figure 5.8. Note that some of the scattered phasors are larger than the corresponding input phasors at the end of leg 1 (upper left corner of Figure 5.8). At first glance, such a circumstance is physically impossible since no mode coupling is assumed to occur within the disturbance. In actuality, this particular sum of mode vectors would *not* be observed at the beginning of leg 2. Instead, they represent a backwards extrapolation to the center of the heated region of the field scattered by the *entire* heated region of $\sim$ 150 km radius. Since the complex phase includes the attenuation rates, this backward extrapolation results in a substantial increase of the calculated modal field strengths.

Table 5.5
NSS-GA modes over the Gulf of St. Lawrence for N_e profile 0

Mode Number	θ_n (°) Re	Im	α(dB / Mm)	v_ϕ/c	Mode $|\rho|$	Designation
1	89.953	-5.776	0.325	0.99485	0.41589	QTE_1
2	89.748	-5.224	1.567	0.99578	2.27917	QTM_1
3	86.148	-0.468	2.136	1.00214	3.63410	QTM_2
4	84.295	-0.176	1.188	1.00488	0.29443	QTE_2
5	79.912	-0.465	5.534	1.01558	2.85427	QTM_3
6	78.547	-0.182	2.451	1.02022	0.37461	QTE_3
7	74.512	-0.518	9.399	1.03754	1.92619	QTM_4
8	73.468	-0.268	5.177	1.04301	0.57298	QTE_4
9	69.321	-0.517	12.405	1.06872	1.23037	QTM_5
10	68.452	-0.449	11.211	1.07501	0.91909	QTE_5
11	64.234	-0.462	13.659	1.11026	0.79837	QTE_6
12	63.245	-0.722	22.092	1.11971	1.38903	QTM_6
13	59.126	-0.461	16.069	1.16495	0.61291	QTE_7
14	57.748	-0.994	36.069	1.18216	1.76559	QTM_7
15	53.840	-0.519	20.829	1.23841	0.54430	QTE_8
16	51.902	-1.293	54.242	1.27027	1.95118	QTM_8
17	48.259	-0.629	28.460	1.33998	0.53486	QTE_9
18	45.542	-1.703	81.123	1.40029	1.90619	QTM_9
19	42.251	-0.782	39.379	1.48697	0.58269	QTE_{10}

The scattering efficiency for each mode can be appraised by comparing the mode structure in the upper right-hand corner of Figure 5.8 to the structure of the modes impinging on the disturbance at the end of leg 1, shown in the upper left-hand corner. For example, although QTE_6 ("F" in Figure 5.8) is negligible at the end of leg 1, it is the fourth strongest mode at the beginning of leg 2. Since mode coupling during the scattering process is neglected, the large amplitude of this mode is due to the fact that it is scattered very efficiently by the heated region. Note also the relative amplitudes of the QTM_2, QTM_4, and QTM_5 modes ("2", "4", and "5," respectively, in Figure 5.8) before and after the scattering process. While QTM_2 is the mode with the largest amplitude at the end of leg 1, it is scattered much less efficiently than the higher order modes QTM_4 and QTM_5. Noting that the eigenangles are the angles of the mode wave normals from
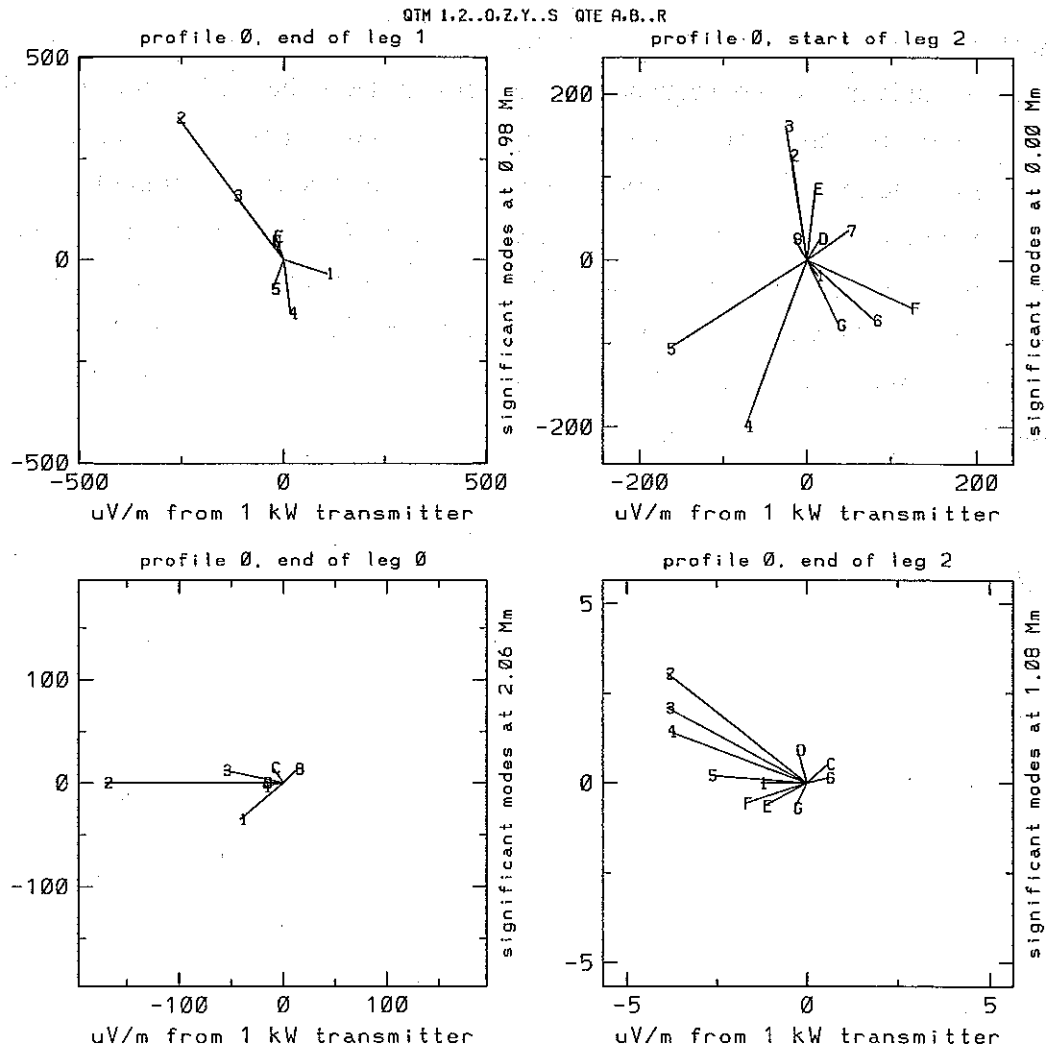
Figure 5.8. Mode structure of the NSS-GA probe wave, for electron density profile 0. Polar plots of the significant NSS modes at the ends of legs 0, 1, and 2, and the NSS modes scattered from the region heated by NAA at the start of leg 2. Significant modes are those at least one-tenth the magnitude of the strongest mode. Mode phasor amplitudes are in units of μV m^{-1} from a 1 kW transmitter.

the vertical direction, the relative scattering efficiencies of the different modes can be understood qualitatively as a consequence of the fact that the higher-order modes consist of a superposition of plane waves that propagate at angles nearer to the vertical and hence undergo more reflections from the disturbed (heated) upper waveguide boundary per unit distance along the waveguide. Despite the relatively large attenuation rates of these higher-order modes, their greater scattering efficiencies result in a rich combination of significant modes in the scattered field at the receiver (Figure 5.8, lower right plot). (For a detailed description of the NSS modes at the scatterer under ambient and heated conditions see Tables 5.8 and 5.9 in the next section.)
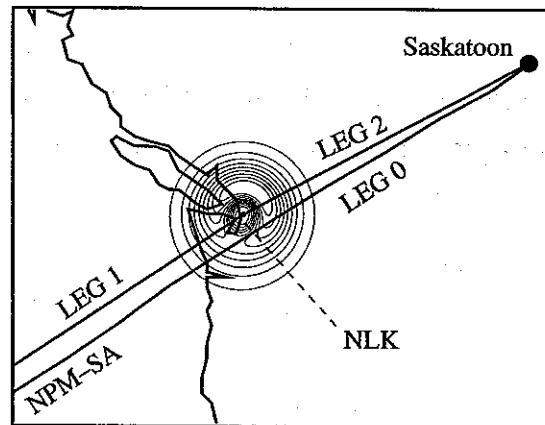
Figure 5.9. Transverse variation of heated region over NLK with respect to the geography of western North America. Contour plot of the normalized transverse variation of collision frequency $\Delta\nu(x', y', h_m)/\Delta\nu(x'_m, y'_m, h_m)$ at the altitude of maximum heating by NLK for electron density profile I, superimposed on a map of the section of the NPM-Saskatoon great circle path near the NLK transmitter.

5.3.2 Mode Structure of the NPM-Saskatoon Probe Wave

The transverse extent of the heated region or scatterer over NLK is indicated in Figure 5.9 by a contour plot of the quantity $\Delta\nu(x', y', h_m)/\Delta\nu(x'_m, y'_m, h_m)$, which is the change in collision frequency at the altitude of maximum heating h_m normalized by the maximum change at this altitude (Chapter 4). The contour plot shown here is that predicted for electron density profile I (Figure 2.3). The outermost contour represents $\Delta\nu(x', y', h_m)/\Delta\nu(x'_m, y'_m, h_m) = 0.1$, with each subsequent contour representing an increment of the same size. The change in collision frequency is minimum (ideally zero) directly above NLK at the center of the heated region. Note that the maximum heating directly to the geomagnetic north of NLK occurs over land. Although most of the heated region is over land, a significant portion lies over water, including a portion in which the heating is > 90% of the maximum predicted.

The calculated amplitude and phase of the NPM-SA probe wave along the direct great circle path from NPM to Saskatoon (leg 0) are shown in Figure 5.10 for all four electron density profiles. The variations shown in Figure 5.10 are generally consistent with predictions by *Bickel et al.* [1970] for an almost identical path (Hawaii-Seattle) using a W.K.B. version of the LWPC model (with no mode coupling), which in turn are consistent with field measurements from an airplane flying along the great circle path

[*Bickel et al.*, 1970]. Although the series of deep nulls in the first 2 Mm of the path over the Pacific Ocean indicate several significant modes, by the time the signal reaches the coast of Washington state the QTM_2 mode is dominant, with the next largest modes (QTM_1 and QTM_3) being only 17% of its size.

To illustrate the mode structure of the NPM-SA probe wave predicted for electron density profile I, the mode phasors at the end of the direct path (leg 0), impinging on the heated region over NLK at the end of leg 1, scattered by the heated region at the beginning of leg 2, and the scattered modes at the receiver (Saskatoon) at the end of leg 2 are plotted in Figure 5.11 in a fashion analogous to that of Figure 5.8. Note that despite the fact that in general higher order modes are scattered more efficiently, QTM_2 is the dominant NPM mode scattered by the heated region over NLK (Figure 5.9).
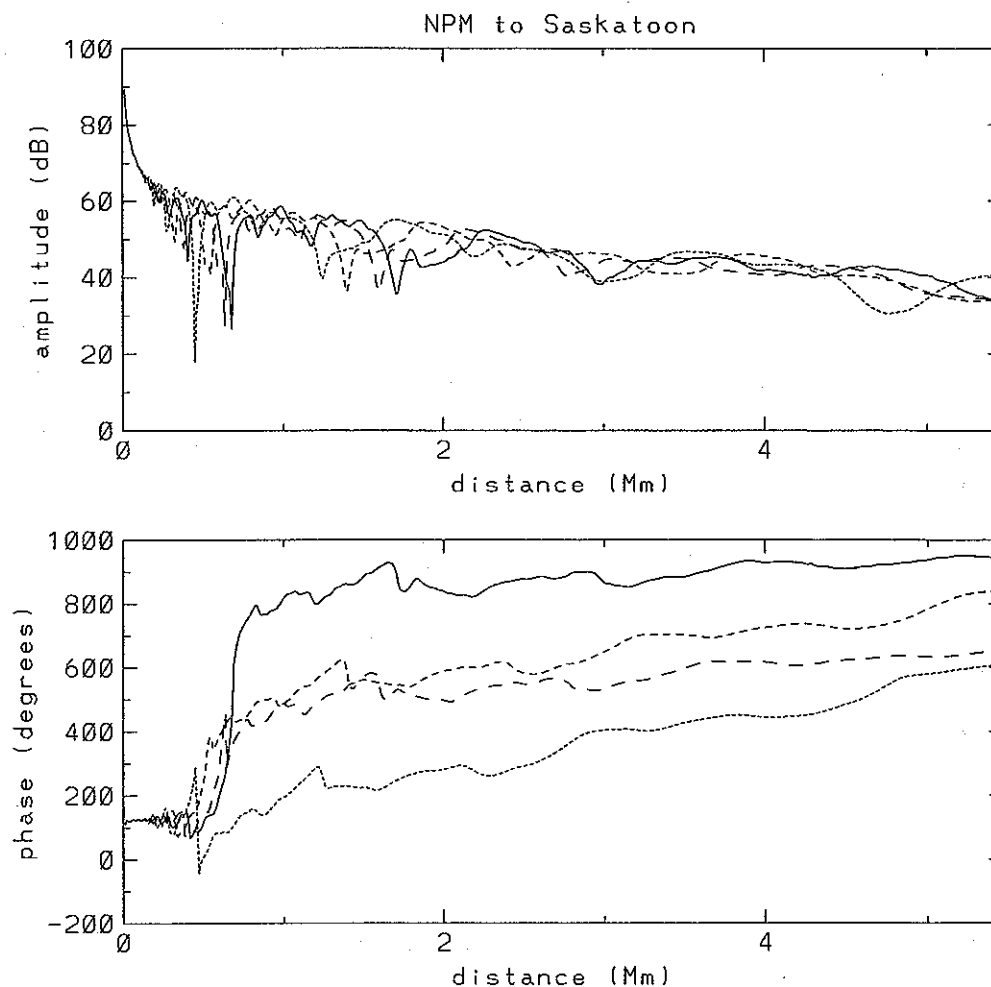
Figure 5.10. Amplitude and phase of the NPM-SA probe wave as a function of distance between the transmitter and receiver for electron density profiles 0, I, II, and III. The solid line is the prediction for profile 0, the coarsely dashed line for profile I, the medium dashed line for profile II, and the finely dashed line for profile III. Amplitude is in dB relative to 1 μV m^{-1} from a 1 kW transmitter. The phase shown is relative to the "free space" phase delay $\omega d/c$, where d is the distance along the surface of the Earth from the transmitter.
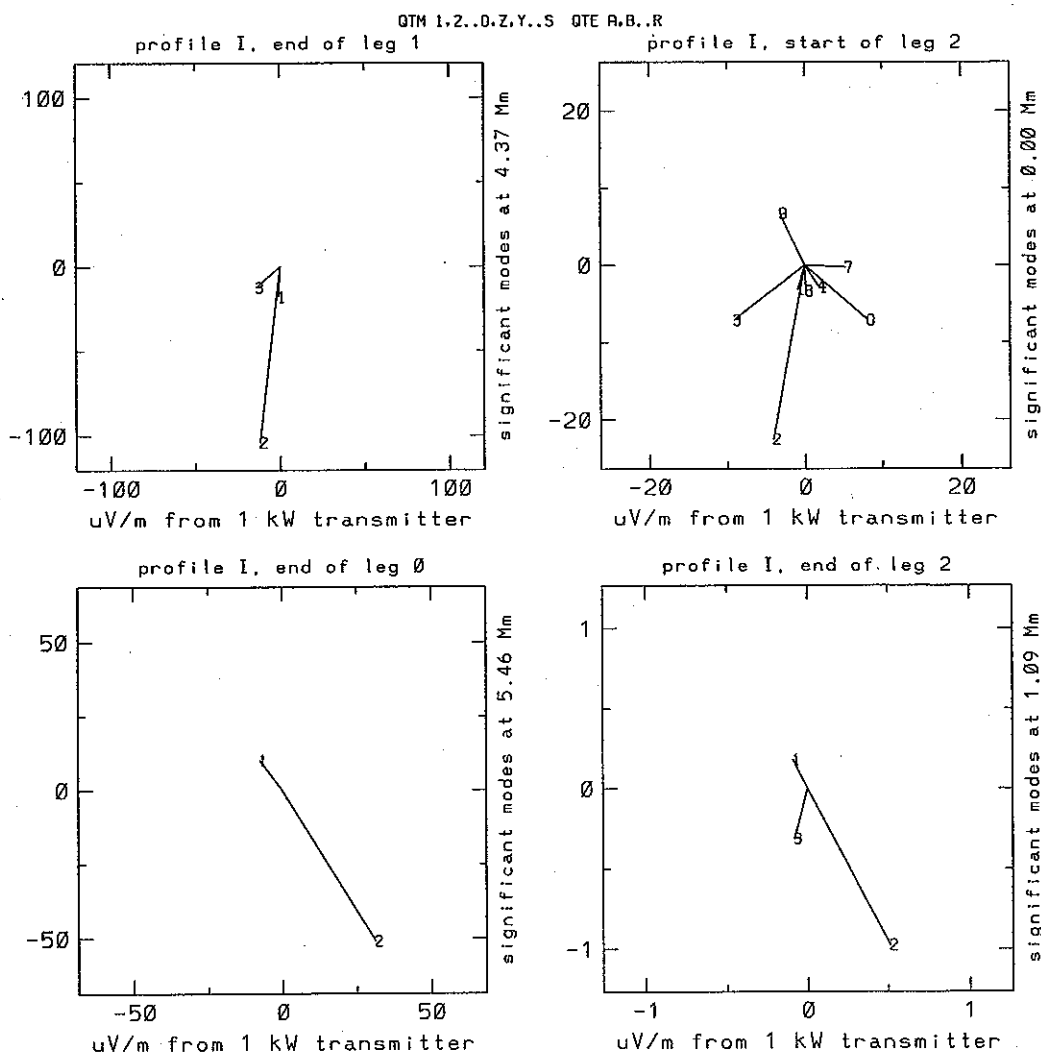
Figure 5.11. Mode structure of the NPM-SA probe wave, for electron density profile I. Polar plots of the significant NPM modes at the ends of legs 0, 1, and 2, and the NPM modes scattered from the region heated by NLK at the start of leg 2. Significant modes are those at least one-tenth the magnitude of the strongest mode. Mode phasor amplitudes are in units of $\mu V \ m^{-1}$ from a 1 kW transmitter.
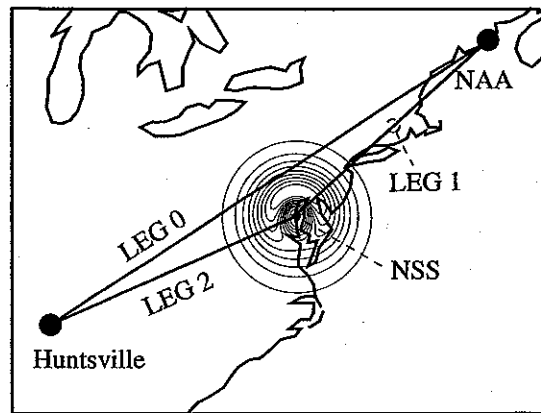
Figure 5.12. Transverse variation of the heated region over NSS with respect to the geography of the eastern United States. Contour plot of the normalized transverse variation of collision frequency $\Delta\nu(x', y', h_m)/\Delta\nu(x'_m, y'_m, h_m)$ at the altitude of maximum heating by NSS for electron density profile 0, superimposed on a map of the NAA-Huntsville great circle path.

5.3.3 Mode Structure of the NAA-Huntsville Probe Wave

The transverse extent of the heated region or scatterer over NSS is indicated in Figure 5.12 by a contour plot of the quantity $\Delta\nu(x', y', h_m)/\Delta\nu(x'_m, y'_m, h_m)$, which is the change in collision frequency at the altitude of maximum heating h_m normalized by the maximum change at this altitude (Chapter 4). The contour plot shown here is that predicted for electron density profile 0 (Figure 2.3). The outermost contour represents $\Delta\nu(x', y', h_m)/\Delta\nu(x'_m, y'_m, h_m) = 0.1$, with each subsequent contour representing an increment of the same size. The change in collision frequency is minimum (ideally zero) directly above NSS at the center of the heated region. Note that the maximum heating directly geomagnetic north of NSS occurs over land. Although most of the heated region is over land, a significant portion lies over water.

The calculated amplitude and phase of the NAA-HU probe wave along the direct great circle path from NAA to Huntsville (leg 0) are shown in Figure 5.13 for all four electron density profiles. Note that there are more nulls in the vertical electric field toward the end of the NAA-HU great circle path than predicted for NSS-GA or NPM-SA, indicating a larger number of significant modes near the end of the path.

To illustrate the mode structure of the NAA-HU probe wave predicted for electron density profile 0, the modes at the end of the direct path (leg 0), the modes impinging on the heated region over NAA at the end of leg 1, the modes scattered by the heated region

at the beginning of leg 2, and the scattered modes at the receiver (Huntsville) at the end of leg 2 are plotted in Figure 5.14 in a fashion analogous to that of Figures 5.8 and 5.11. The large number of significant modes is due in part to the tenuous D region electron density profile used; the predictions for the denser profiles I, II, and III show fewer significant modes. Another reason is the presence of slabs of high soil conductivity (Table 5.1, code 8: $\sigma = 3.0 \times 10^{-2}$ S m^{-1}) along legs 0 and 2 that are associated with a significant amount of mode conversion into higher order modes.
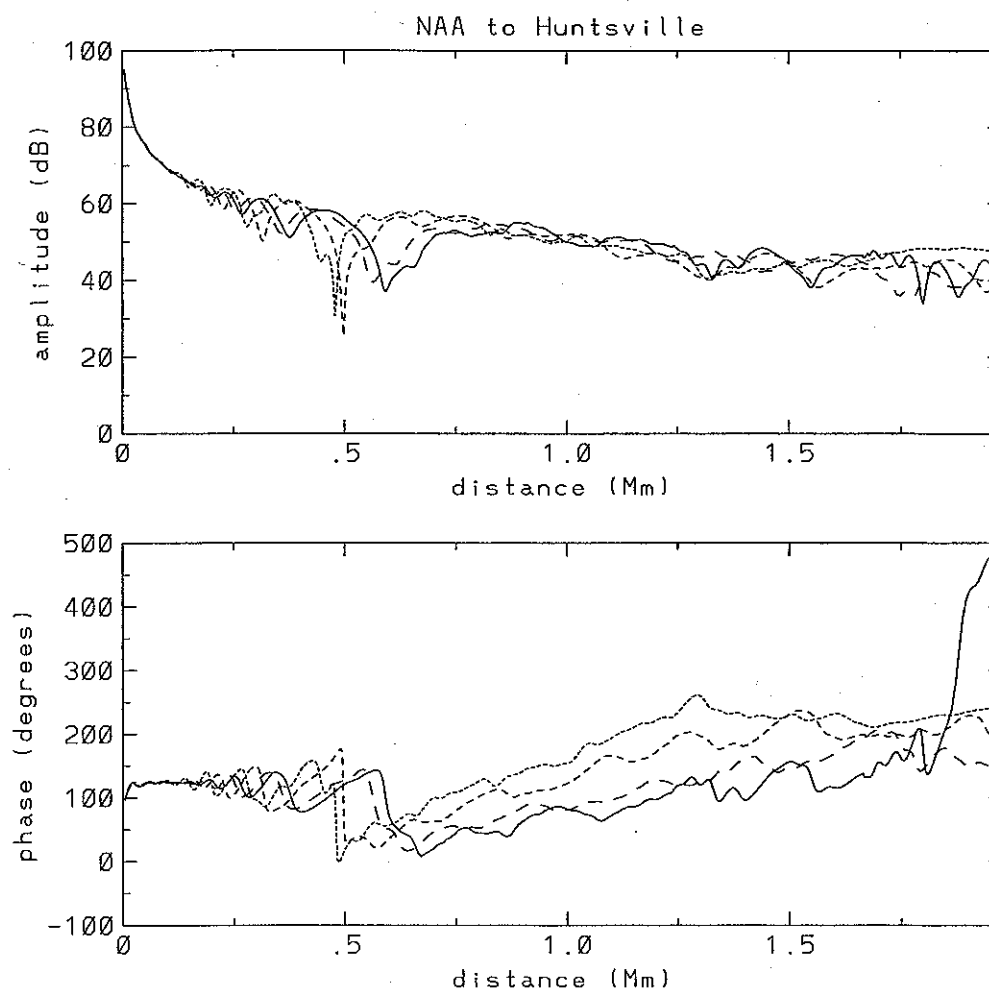
Figure 5.13. Amplitude and phase of the NAA-HU probe wave as a function of distance between the transmitter and receiver for electron density profiles 0, I, II, and III. The solid line is the prediction for profile 0, the coarsely dashed line for profile I, the medium dashed line for profile II, and the finely dashed line for profile III. Amplitude is in dB relative to 1 μV m^{-1} from a 1 kW transmitter. The phase shown is relative to the "free space" phase delay $\omega d/c$, where d is the distance along the surface of the Earth from the transmitter.
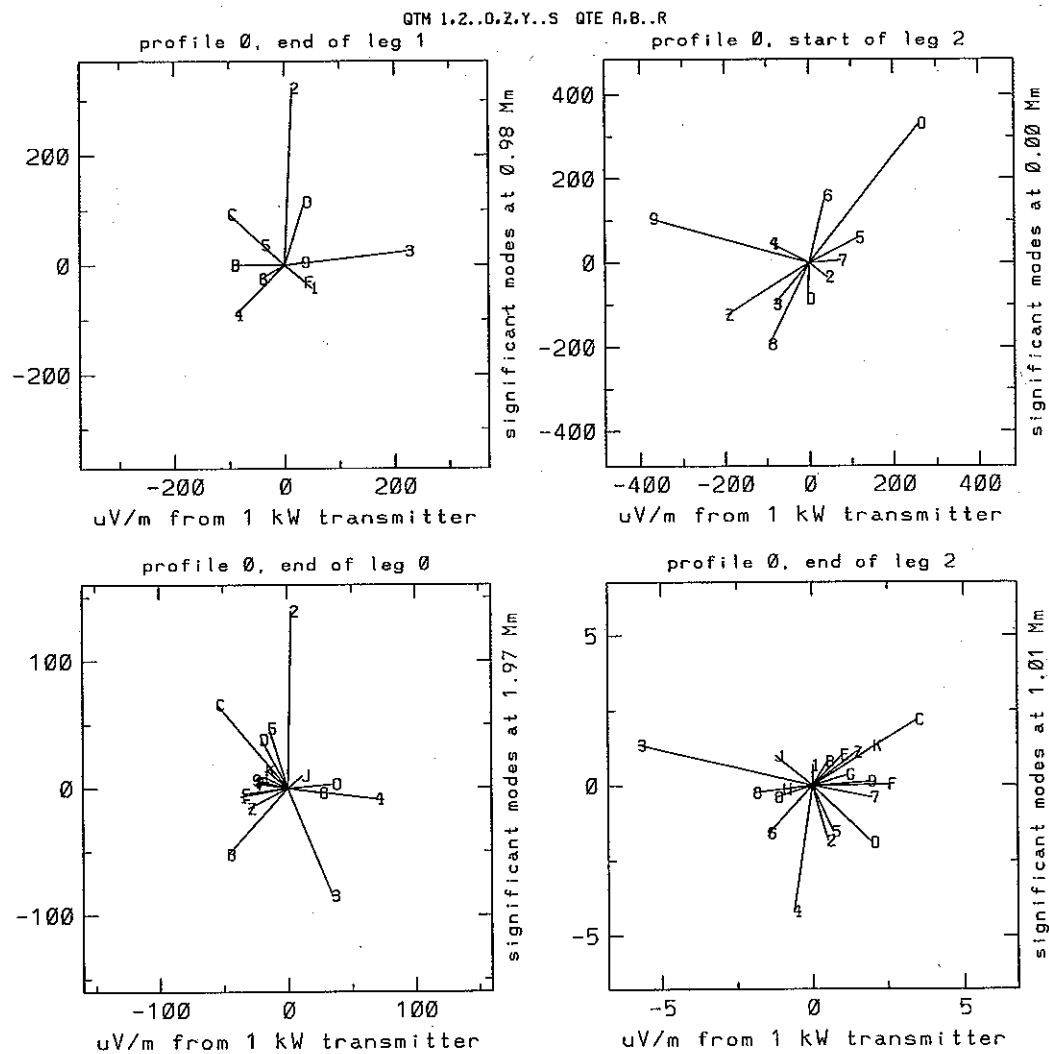
Figure 5.14. Mode structure of the NAA-HU probe wave predicted for electron density profile 0. Polar plots of the significant NAA modes at the ends of legs 0, 1, and 2, and the NAA modes scattered from the region heated by NSS at the start of leg 2. Significant modes are those at least one-tenth the magnitude of the strongest mode. Mode phasor amplitudes are in units of $\mu V\ m^{-1}$ from a 1 kW transmitter.

5.4   EVALUATION OF THE VALIDITY OF MODEL ASSUMPTIONS

This section consists of an analysis of several important assumptions used in the calculations of the previous section.

5.4.1   Equivalence of Predicted Wave Vertical Electric Fields and Observed Horizontal Magnetic Fields

The transmitting and receiving antennas are assumed to be vertical electric monopoles at the surface of the Earth; consequently, the field component of interest is the vertical electric field. The vertical electric field of the probe wave at the receiver is calculated for propagation in the absence and in the presence of an ionospheric disturbance due to VLF heating. The difference between these two calculations gives the amplitude and phase changes due to VLF heating. In contrast, the vertical loop antennas used with the Stanford narrowband VLF receivers (Chapter 3) respond to the horizontal magnetic field of the probe wave. The conversion assumed in the calibration of the Gander data is that the ratio of the vertical electric field strength and the horizontal magnetic field flux density is the speed of light in free space c, which holds for a plane wave in free space. The only guided wave for which this is strictly true is the transverse electromagnetic (TEM) mode (eigenangle = 90°) between two infinitely conducting parallel plates, for which there is only a vertical electric field and a horizontal magnetic field perpendicular to the direction of propagation along the axis of the waveguide. In general, both electric and magnetic horizontal field components exist in this direction in the Earth-ionosphere waveguide, where all eigenangles are less than 90° and the ground has a finite conductivity. However, these components are negligible for low-order modes [*Poulsen*, 1991], which usually constitute the significant modes at ~ 1000 km or greater from a transmitter or scatterer. Furthermore, the vertical plane of the loop antenna that was used to receive the NSS-GA probe wave data studied here was aligned nearly along the probe wave great circle path, thus nearly nulling any horizontal magnetic field in the direction of propagation.

5.4.2 Ground Conductivity Variations Transverse to the LWPC Great Circle Paths

In the cases of NAA-HU and especially NSS-GA, the great circle paths sometimes skirt coastlines. This is a violation of our assumption in the context of the two-dimensional LWPC model that there are no significant transverse variations in the conductivity of the waveguide boundaries. Although the three-dimensional model of *Poulsen* [1991] treats transverse ionospheric inhomogeneities, transverse variations in the ground conductivity may cause slight deviations in the direction of propagation that the current model cannot predict. In order to evaluate the sensitivity of the waveguide propagation model to the ground conductivity, calculations are performed for NSS-GA assuming alternately all sea and all land paths, all other parameters being held the same.

Table 5.6
Effect of ground conductivity on NSS-GA perturbations

N_e profile	NSS-GA amplitude and phase change (dB, °) realistic	all sea $(10)^a$	all land $(5)^a$
0	+0.01, −3.29	−0.15, −4.98	+0.03, −3.31
I	+0.02, −1.34	+0.01, −2.77	+0.01, −2.48
II	−0.05, −0.77	−0.05, −1.01	−0.01, −0.93
III	−0.06, −0.21	−0.06, 0.00	−0.04, −0.09

a. Conductivity codes from Table 5.1.

The results for all sea and all land paths are listed in the second and third columns of Table 5.6, with the conductivity indicated by the code from Table 5.1. The model results from Table 5.2 for the realistic ground conductivity map of *Hauser et al.* [1969] are repeated in the first column of Table 5.6. The perturbations predicted for an all sea path under profiles 0, I, and II are somewhat larger than those for the realistic or all land paths. For profiles 0 and II the predictions for all land and the realistic ground conductivity map are consistent, but a substantially larger perturbation is predicted under

profile I for all land than for the realistic conductivity map. In the light of the detection thresholds of $\sim \pm 0.1$ dB and $\sim \pm 0.5°$ (Chapter 3), the results predicted for profile III are not significantly different. Although this calculation is not a direct test of the importance of diffraction effects due to transverse inhomogeneities in the ground conductivity, it provides some insight into the effect of the ground conductivity on the calculations in the context of the observations.

We note here for future reference that pack ice gathers along the coast of Canada during the winter and spring months, resulting in a change in the ground conductivity. While northern Baffin Bay (near Thule, Greenland) is covered by ice all year, pack ice appears off the northern Newfoundland coast in mid-January, extending southward until it reaches 47–48°N at the end of March [*Smith et al.*, 1994]. After this, the ice retreats northward.† Although *Smith et al.* [1994] only discuss the sea ice on the eastern and northern coasts of Newfoundland, other maps show winter sea ice in the Gulf of St. Lawrence to the west and southwest of Newfoundland [*National Geographic Society*, 1994]. The maximum extent of winter sea ice forms a line from the southwestern tip of Newfoundland southwest around Cape Breton Island to Nova Scotia. The last sea portion of the NSS-GA path passes over this region of winter sea ice. The ice pack consists of floes 10–30 m in diameter and 0.3–1.0 m thick [*Smith et al.*, 1994]. Such a surface could perhaps be represented by a conductivity $\sigma = 10^{-4}$ S m^{-1} and relative permittivity $\varepsilon_r = 10$, appropriate for ice shelves and shallow ice-covered ground [*Poulsen et al.*, 1993b]. Analysis of Gander data from the winter and spring months should take this seasonal variability into account.

5.4.3   Effect of Heating by the Probe Wave Transmitter on Mode Excitation

Our results in Chapter 3 demonstrate that the ionosphere above VLF transmitters is regularly heated. However, in our modeling so far of the propagation and mode structure of the VLF probe waves we have neglected the effect of D region heating by the probe wave transmitters on the amplitude and phase of the waveguide modes they themselves excite. In order to evaluate the significance of this "self-action" effect of the probe wave, we consider the case of the NAA transmitter signal observed at Huntsville as the probe

---

† In early May 1993 the author saw ice floes in the harbor of Twillingate, Newfoundland, and what may have been pack ice at the horizon looking north from North Twillingate Island, 80 km northwest of Gander.

wave for an ambient ionosphere given by electron density profile 0 (Figure 2.3). This case includes the maximum heating expected over a probe wave transmitter (Figure 5.2) and the greatest number of significant modes (Figure 5.14) considered in this dissertation. In modeling the effect of the heating on the signal propagating on legs 0 and 1 (Figure 5.1) we treat the heated region over NAA as a series of nine two-dimensional slabs between 0 and 230 km horizontal distance from the probe wave transmitter. Each of these slabs represents an increase in the collision frequency equal to an integral multiple of 20% of the maximally heated collision frequency profile over NAA. When the effect of NAA heating is included in this manner the predicted NAA-HU amplitude and phase changes due to NSS heating are −0.25 dB and −0.57° for electron density profile 0, not too different from the −0.24 dB and −0.68° predicted originally without accounting for the disturbance over the probe wave transmitter (Table 5.4). Using the same method, the predicted amplitude and phase changes for electron density profile I are −0.18 dB and +0.17°, compared with the original predictions of -0.24 dB and −0.19°. In this case, although the amplitudes are consistent, the polarity of the phase has switched. Without phase data from Huntsville, however, it is not possible to determine whether the two-dimensional treatment considered here in fact results in a more accurate prediction. We expect that in the other two cases (NSS-GA and NPM-SA), which involve weaker probe wave transmitters and fewer significant modes, the difference between the original predictions and modified predictions accounting for the heated region over the probe wave would be even smaller.

5.4.4 Outer Radius of Integration of the Scattering Integral

In all the calculations presented so far, the outer radius of integration of the scattering integral (5.8) has been set to 350 km, based on the following considerations. As shown in Chapter 4 the heated region at the altitude of maximum heating is narrower for a more tenuous D region electron density profile. Therefore, heated regions calculated assuming profiles 0 and III are chosen to assess the appropriateness of this assumption. Predictions of heating by NAA are used since this is the transmitter of greatest interest in this work. Shown in the lower left half of Figure 5.15 is the absolute value of the scattered field E_s in dB (relative to 1 μV m^{-1} from a 1 kW transmitter) as a function of the outer radial limit of integration. Shown in the lower right half is the phase of E_s (the phase of E_s for profile III is in fact opposite in polarity from that plotted). Shown also in Figure 5.15 (top panel) are the cross-sections of $\Delta\nu(x', y', h_m)/\Delta\nu(x'_m, y'_m, h_m)$ for profiles 0 and III

in the geomagnetic east-west direction. Analysis indicates that, for both disturbances, the result of the numerical integration stabilizes for outer limits of 300-450 km, although, as expected, the wider disturbance predicted for profile III requires a larger radius of integration. An outer integration limit that is too small (e.g., 100 km) omits most of the scatterer, while one that is too large (e.g., 500 km) is not suitable because the step size of the Gaussian quadrature method used to integrate the scattering integral (5.8) is too large to accurately sample the oscillatory integrand. Based on this analysis, an outer radius of 350 km has been chosen for evaluating (5.8).

5.4.5 Ground Conductivity Variations under the Heated Region

Since the heated regions have radii of order 350 km they are likely to lie over regions of different ground conductivity. However, our model assumes that the conductivity of the ground under the heated region is uniform and has the value of the conductivity directly beneath the center of the heated region. This assumption neglects the possible effects of different ground conductivities on the infinitesimal scatterers within the heated region as well as the possibility that mode-coupling may occur at ground-sea boundaries under the scatterer [*Poulsen et al.*, 1993a]. The effect of this assumption is evaluated for the NSS-GA probe wave since the heated region over NAA lies over more ocean than in the case of the heaters NSS or NLK. Note however that due to the asymmetry of the heated regions, the maximum heating occurs over land in all three cases (NAA, NLK, and NSS) (Figures 5.5, 5.9, and 5.12). Scattering is calculated here assuming sea water ($\sigma = 4.0$ S m^{-1}, $\varepsilon_r = 81$) under the heated region for comparison with the results already presented in Table 5.2 that assumed land under NAA ($\sigma = 10^{-3}$ S m^{-1}, $\varepsilon_r = 15$), all else being equal.

Changing the conductivity under the scatterer has the largest effect on the predictions for profile 0, with the scattered field and resulting amplitude and phase perturbations increasing substantially when the conductivity is increased. The effect in this case is not too different from the corresponding case in Table 5.6 for an all-sea path. The increase in the phase in these two calculations indicates that for profile 0 the scattered field calculated for the case of all ground beneath the heated region (Table 5.4) may be an underestimate. When evaluated in comparison with the results of section 5.2, the results shown in Tables 5.6 and 5.7 indicate that the effect of the ground conductivity is relatively small compared to the differences between the data and the theoretical predictions.
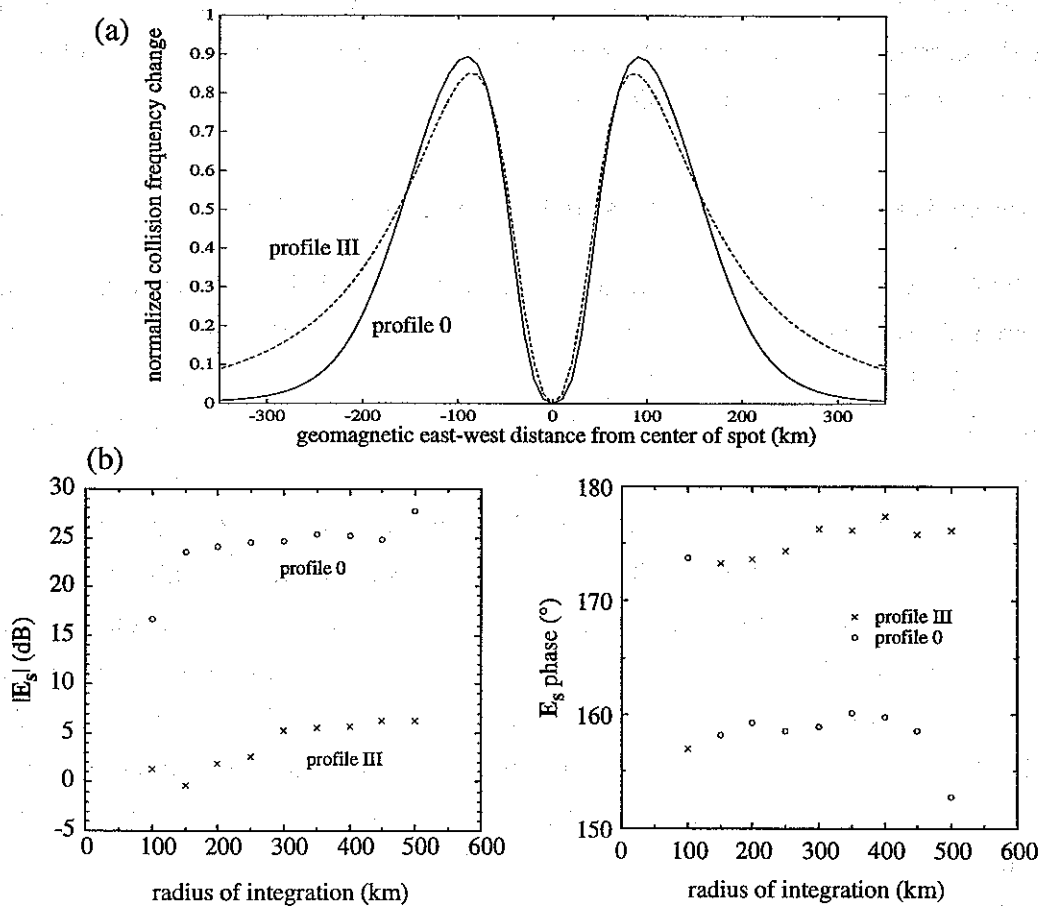
Figure 5.15. Variation of scattered field amplitude and phase with outer radius of integration. (*a*) East-west sections of the collision frequency change due to NAA heating predicted for electron density profiles 0 and III. The sections are taken through the center of the heated region. (*b*) Magnitude and phase of the NSS vertical electric field scattered from heated region over NAA toward Gander, for outer radii of integration between 100 and 500 km. The sign of the phase of E_s predicted for profile III has been changed before being plotted.

Table 5.7
Effect of ground conductivity under NAA on NSS-GA perturbations

N_e profile	NSS-GA amplitude and phase change (dB, °)	
	all earth (5)	all sea (10)
0	+0.01, −3.29	−0.08, −4.44
I	+0.02, −1.34	0.00, −1.86
II	−0.05, −0.77	−0.05, −0.82
III	−0.06, −0.21	−0.06, −0.13

5.4.6 Dependence of Modal Refractive Index Changes (ΔS_n) on Collision Frequency Changes ($\Delta \nu$)

We analyze here the assumption that that the change in the mode refractive index is proportional to the change in the collision frequency in the heated region over a VLF transmitter (i.e., $\Delta S_n \propto \Delta \nu$). We consider specifically the case of the NSS-GA probe wave scattering off the region heated by NAA, with the ambient electron density given by profile II (Figure 2.3) and for the collision frequency profile of *Wait and Spies* [1964] (Figure 2.4). The incremental change in S_n in the heated region is determined by calculating the eigenangles for eleven collision frequency profiles given by $\nu_o(h) + 0.1 m \Delta \nu_{max}(h)$, where $\nu_o(h)$ is the ambient collision frequency profile, $\Delta \nu_{max}$ is the change in the profile corresponding to maximum heating, and m is some integer such that $0 \leq m \leq 10$. The particular probe wave and ambient density profile considered here were chosen from among the different cases because the relation between ΔS_n and $\Delta \nu$ exhibits typical regularity for most of the 18 modes while exhibiting striking departure from the assumption for a few higher order modes (Figures 5.16 and 5.17). For each mode, the real and imaginary parts of ΔS_n are normalized to the largest absolute value of either and plotted as a function $\Delta \nu / \Delta \nu_{max}$ in the heated region in question. In this case, modes 15 (QTE$_8$), 16 (QTM$_8$), and 17 (QTE$_9$) contribute very little to the total scattered field, so the failure of the assumption of $\Delta S_n \propto \Delta \nu$ in these three cases has negligible impact on the accuracy of the calculation. In general this proportionality holds equally well for all of the

collision frequency changes used in this dissertation to model the effect of VLF heating on subionospheric VLF probe waves.

5.4.7 Born and W.K.B. Approximations in the Scattering Integral

In this section we evaluate the applicability of the Born and W.K.B. approximations used in the scattering model described in section 5.1.5. The example used here is the factor of 3 change in collision frequency due to NAA heating of the tenuous D region represented by profile 0, i.e., the largest change considered in this chapter. Listed in Table 5.8 for the unheated ionosphere over NAA and in Table 5.9 for the maximum heating by NAA predicted for profile 0 are the eigenangles θ_n (referred to the ground) of the NSS-GA modes, the attenuation rates $\alpha_n = -8686k\text{Im}\{\sin\theta_n\}$ in units of dB Mm^{-1}, the ratio of the phase velocity to the speed of light $v_\phi/c = 1/\text{Re}\{\sin\theta_n\}$, and the magnitude of the polarization mixing ratio ρ. The modes are designated QTE or QTM depending on the magnitude of ρ. Shown in the top half of Figure 5.18 are the eigenangles in the complex θ_n plane for the NSS-GA probe wave modes under the region heated by NAA (profile 0) for $\Delta\nu = 0$ and for $\Delta\nu = \Delta\nu_{\text{max}}$. It is clear that the eigenangles θ_n of the modes, and therefore the refractive indices $S_n = \sin\theta_n$, change little, even for this relatively large collision frequency change [*Barr et al.*, 1985], confirming the applicability of the Born approximation to these calculations.

The small shaded portion of the complex θ_n plane is shown on an expanded scale in the bottom half of Figure 5.18 in order to demonstrate how the QTE_6 and QTM_6 modes approach each other very closely and even exchange designations. The eigenangles are shown for $\Delta\nu$ ranging in eleven steps from 0 to $\Delta\nu_{\text{max}}$. The close approach of the QTE_6 and QTM_6 modes may indicate that although the transverse dimensions of the heated region are much larger than the wavelength of the VLF probe waves used here, the QTE_6 and QTM_6 modes may couple, thus violating the W.K.B. approximation. However, although these modes are not insignificant components of the scattered field at the receiver (6 and F, respectively, in Figure 5.8), the QTM modes 2, 3, and 4 are larger.

The modes that switch designation (QTE or QTM) as the ionosphere changes from ambient to maximally heated, e.g., modes 11 and 12, display a continuous change in $|\rho|$, consistent with the gradual change in eigenangle. That is, for a given mode, the relative strengths of the electric and magnetic field components and their spatial variations (i.e. the mode eigenfunctions) are uniquely associated with an eigenangle. The QTE or QTM
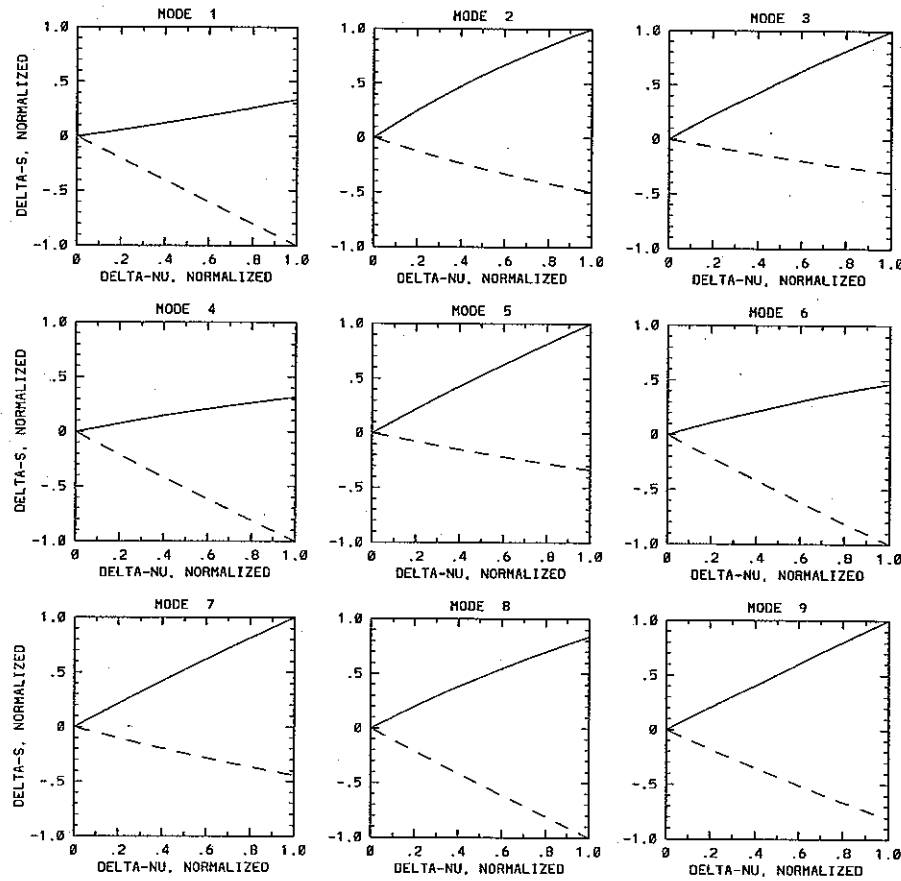
Figure 5.16. The change in the refractive indices (ΔS_n) of NSS-GA modes 1–9 as a function of the change in collision frequency $\Delta\nu$ due to heating by NAA, for electron density profile II. The collision frequency changes are normalized to the maximum collision frequency change $\Delta\nu_{max}$ due to NAA heating predicted for profile II. For each mode, the real and imaginary parts of ΔS_n are normalized to the largest absolute value of either part; $\mathrm{Re}\{\Delta S_n\}$ is represented by the solid line, $\mathrm{Im}\{\Delta S_n\}$ by the dashed line. Results are shown for modes 1 through 9 (modes are numbered in order of increasing phase velocity).
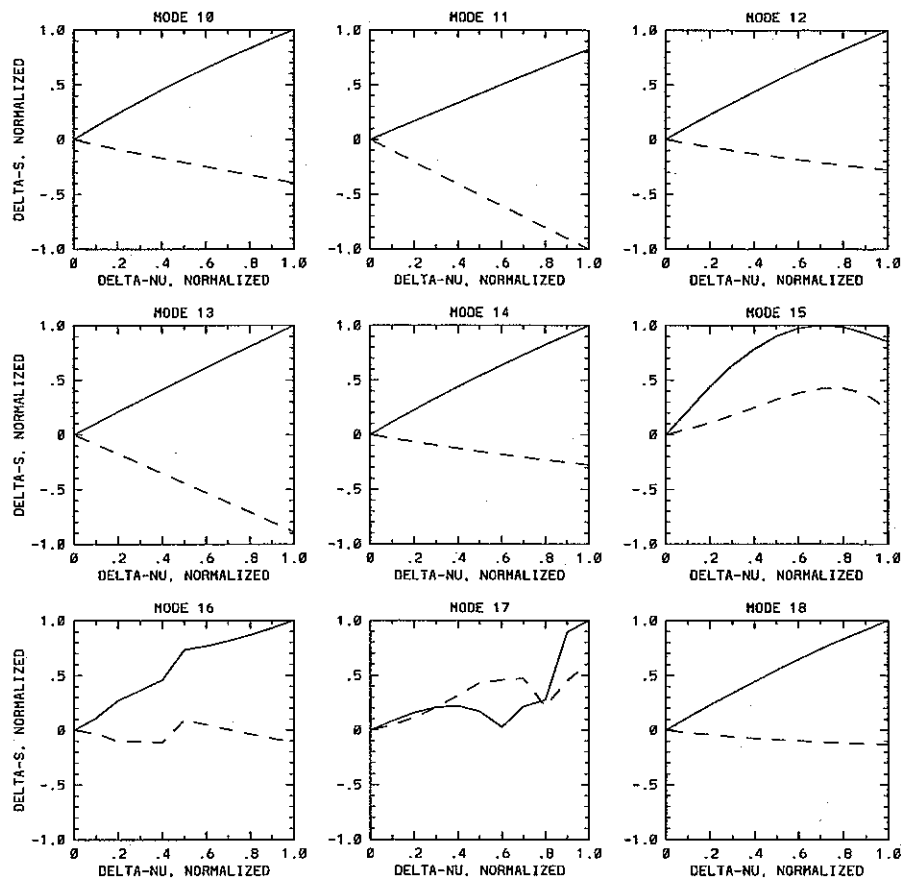
Figure 5.17. The change in the refractive indices (ΔS_n) of NSS-GA modes 10–18 as a function of the change in collision frequency $\Delta \nu$ due to heating by NAA, for electron density profile II. The collision frequency changes are normalized to the maximum collision frequency change $\Delta \nu_{max}$ due to NAA heating predicted for profile II. For each mode, the real and imaginary parts of ΔS_n are normalized to the largest absolute value of either part; $\text{Re}\{\Delta S_n\}$ is represented by a solid line, $\text{Im}\{\Delta S_n\}$ by a dashed line. Results are shown for modes 10 through 18 (modes are numbered in order of increasing phase velocity).

designation is physically less important, particularly when the polarization mixing is so significant (Tables 5.8 and 5.9).

5.5 DETECTION OF NAA HEATING USING THE NAU-GANDER PROBE WAVE

During December 1992 the NAU-GA probe wave amplitude was perturbed in 6 of the 41 NAA OFF/ON episodes in which cross-modulation was observed on the NSS-GA signal (Table 3.2, Figure 3.2). This was surprising in the light of the > 770 km distance between NAA and the NAU-GA great circle path (Figure 3.1). Due to this great distance, scattering from the center of the heated region (Figure 5.2) should be negligible since the heated region satisfies the W.K.B. and Born approximations [*Poulsen et al.*, 1993*b*]. In order to model the effect of NAA on NAU-GA, therefore, we estimate heating by the direct (half-hop) rays from NAA impinging on the ionosphere directly above the point on the NAU-GA great circle path closest to NAA (770 km in the direction 124° E of N geomagnetic from NAA) using spherical geometry. A two-dimensional waveguide calculation is then performed in which the heated region is modeled as a 100-km-long slab centered at this point. The calculated changes in electron temperature and collision frequency for the four model electron density profiles are shown in Figure 5.19. Note that the calculated increases at a distance of 770 km from the heating transmitter are very small compared to the maximum changes in temperature and collision frequency predicted to occur near the transmitter (Figure 5.2).

Predictions of the perturbation on the NAU-GA probe wave due to the collision frequency changes shown in Figure 5.19 are listed in Table 5.10. Except for the result predicted for profile I, they are all more than one order of magnitude too small to match the observations (Table 3.2). The smallest perturbation observed (0.07 dB) is still a factor of 2.4 larger than the 0.029 dB perturbation predicted for profile I. This relatively large perturbation on the NAU-GA probe wave is predicted to occur because Gander is in a ~ 10 dB null in the spatial pattern of the NAU-GA vertical electric field that makes it more sensitive to the heating by NAA. The NAU field strengths from Gander at the times of heating signatures are relatively low (Figure 3.6) but do not strongly indicate the presence of a 10 dB null. Nevertheless, in the absence of knowledge of the actual state of the nighttime D region, the presence of a deep null in the NAU probe wave
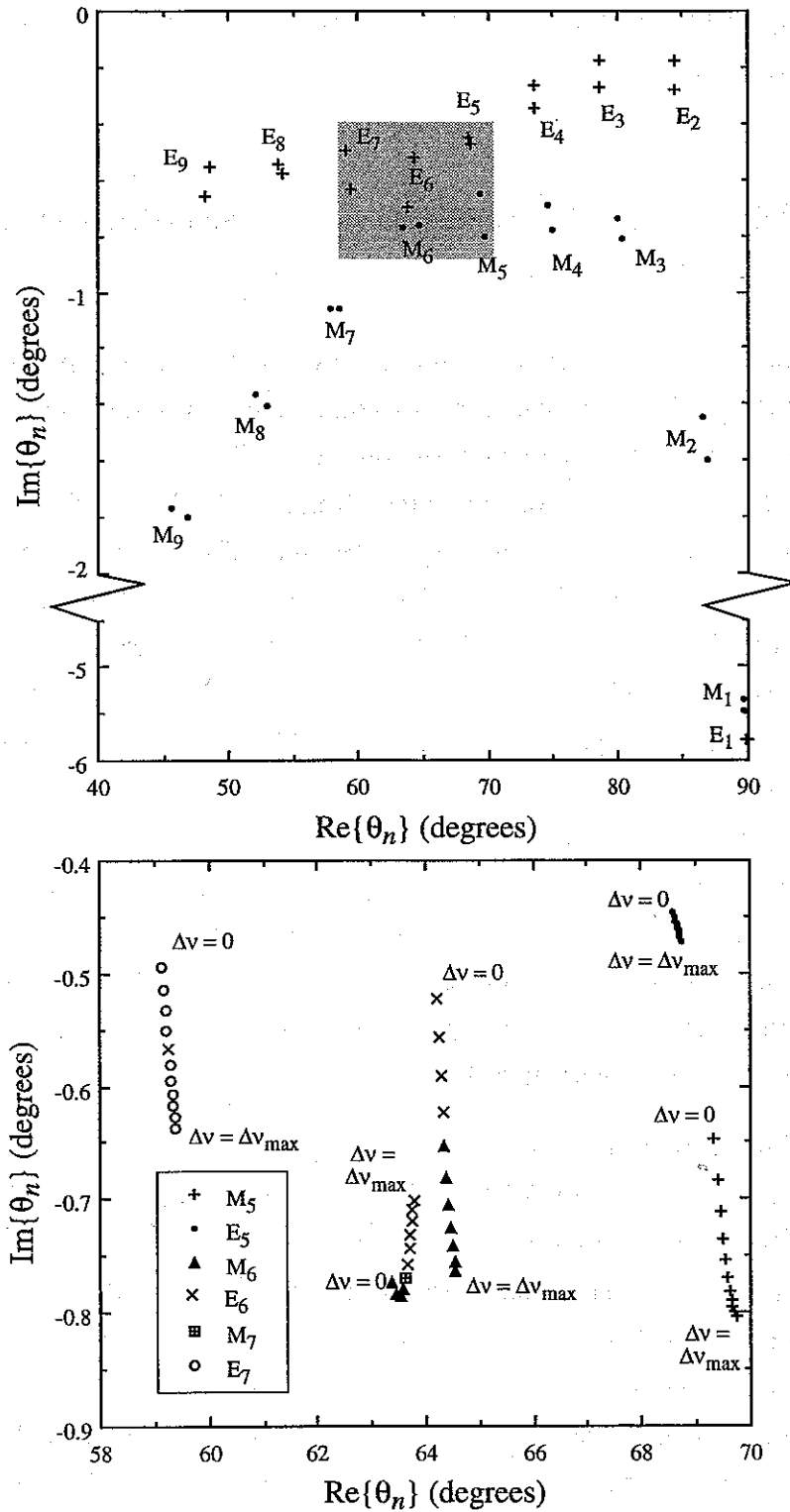
Figure 5.18. Eigenangles of the NSS-GA modes under the region heated by NAA, for electron density profile 0. The portion of the complex θ_n plane shaded in the upper figure is shown in detail in the lower figure.

Table 5.8

NSS modes at the NAA transmitter, ambient conditions $(N_e$ profile 0)

(Calculated for propagation in the direction of Gander.)

Mode Number	θ_n (°) Re	Im	α(dB / Mm)	v_ϕ/c	Mode $|\rho|$	Designation
1	89.938	-5.787	0.425	0.99483	0.38712	QTE_1
2	89.637	-5.345	2.309	0.99559	2.07611	QTM_1
3	86.561	-1.448	5.904	1.00139	3.78596	QTM_2
4	84.358	-0.174	1.161	1.00477	0.18920	QTE_2
5	80.109	-0.738	8.618	1.01491	3.03508	QTM_3
6	78.604	-0.181	2.426	1.02001	0.29096	QTE_3
7	74.610	-0.689	12.435	1.03702	2.10696	QTM_4
8	73.544	-0.262	5.055	1.04260	0.47346	QTE_4
9	69.347	-0.648	15.540	1.06851	1.34806	QTM_5
10	68.570	-0.447	11.093	1.07414	0.80698	QTE_5
11	64.230	-0.522	15.446	1.11029	0.81525	QTE_6
12	63.382	-0.773	23.540	1.11835	1.37353	QTM_6
13	59.143	-0.495	17.257	1.16475	0.61780	QTE_7
14	57.863	-1.063	38.445	1.18063	1.84049	QTM_7
15	53.871	-0.549	22.024	1.23792	0.55371	QTE_8
16	52.009	-1.362	57.027	1.26838	2.08068	QTM_8
17	48.304	-0.661	29.900	1.33905	0.54960	QTE_9
18	45.651	-1.770	84.151	1.39763	2.05342	QTM_9
19	42.310	-0.821	41.289	1.48528	0.60213	QTE_{10}

vertical electric field at Gander appears to be a reasonable qualitative explanation for the observations of ionospheric cross-modulation between NAA-GA and NAU-GA during December 1992.

5.6 SUMMARY AND CONCLUSIONS

Calculations of scattering of VLF signals in the Earth-ionosphere waveguide by patches of increased D region collision frequency are in general consistent with the observed cross-modulation between subionospheric VLF waves being due to heating of the nighttime D region by VLF transmitters. The predicted magnitudes of the NSS signal scattered

Table 5.9

NSS modes at the NAA transmitter, heated conditions (N_e profile 0)

(Calculated for propagation in the direction of Gander.)

Mode Number	θ_n (°) Re	Im	α(dB / Mm)	v_ϕ/c	Mode $|\rho|$	Designation
1	89.902	-5.788	0.671	0.99483	0.42862	QTE_1
2	89.603	-5.461	2.579	0.99541	1.88127	QTM_1
3	86.782	-1.599	6.106	1.00110	4.37587	QTM_2
4	84.390	-0.278	1.849	1.00471	0.15909	QTE_2
5	80.382	-0.815	9.258	1.01406	3.69785	QTM_3
6	78.651	-0.275	3.677	1.01984	0.23373	QTE_3
7	74.948	-0.781	13.797	1.03534	2.77692	QTM_4
8	73.629	-0.347	6.647	1.04214	0.35116	QTE_4
9	69.749	-0.803	18.896	1.06568	2.00006	QTM_5
10	68.728	-0.472	11.644	1.07298	0.52400	QTE_5
11	64.566	-0.764	22.321	1.10712	1.36673	QTM_6
12	63.773	-0.701	21.079	1.11458	0.78014	QTE_6
13	59.404	-0.637	22.036	1.16156	0.96954	QTE_7
14	58.529	-1.059	37.582	1.17216	1.11222	QTM_7
15	54.146	-0.574	22.880	1.23362	0.84163	QTE_8
16	52.904	-1.404	57.593	1.25322	1.30634	QTM_8
17	48.587	-0.556	25.003	1.33322	0.80356	QTE_9
18	46.848	-1.797	83.589	1.36993	1.37545	QTM_9
19	42.549	-0.551	27.626	1.47861	0.81233	QTE_{10}

from the region heated by NAA, calculated for four nighttime D-region electron density profiles varying over two orders of magnitude, are consistent with the amplitude and phase changes observed repeatedly on NSS-GA during December 1992. The discrepancy between the observed and predicted relative phases of the direct and scattered NSS signals at Gander may be attributable in part to the particular models of the nighttime D region used in these calculations. The anomalous detection of NAA heating by the NAU-GA probe wave, whose great circle path is 770 km from NAA at its closest approach, can be explained qualitatively by a null in the probe wave spatial pattern near Gander that makes the probe wave amplitude unusually sensitive to weak heating by NAA along the NAU-GA great circle path under relatively tenuous nighttime D region conditions.
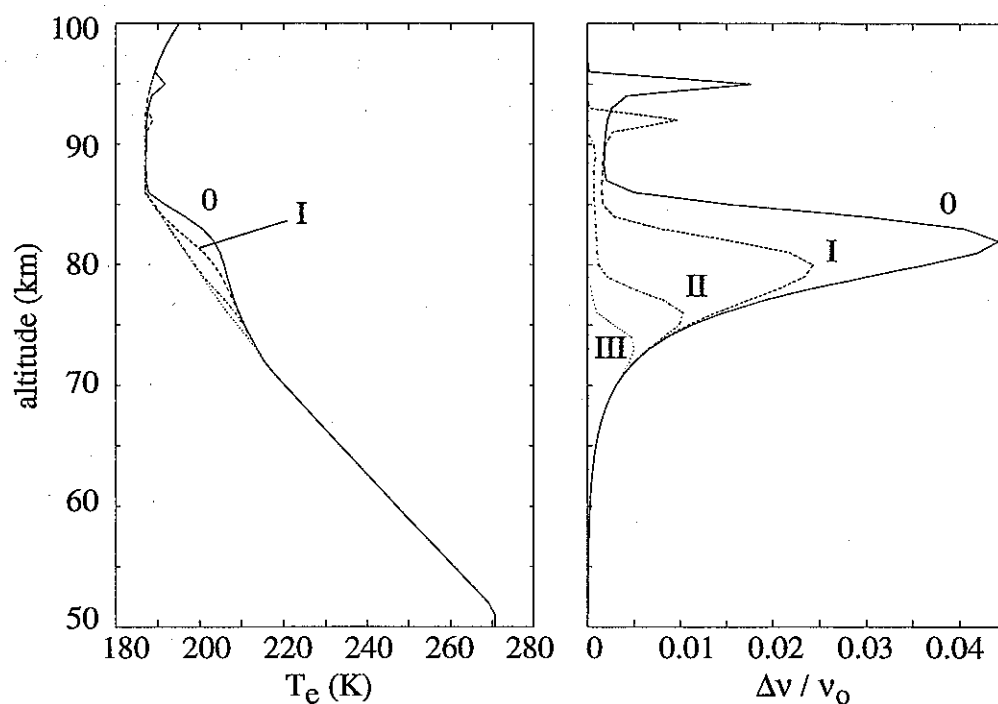
Figure 5.19. Heating by NAA at 770 km from NAA on the NAU-GA great circle path.

Table 5.10
Calculated signatures of NAA heating on NAU-GA

N_e profile	NAU-GA amplitude change (dB)	phase change (°)
0	0.000	−0.093
I	0.029	−0.015
II	0.009	−0.004
III	0.000	−0.004

Heating by NSS and NPM has also been observed, using the NAA-HU and NPM-SA probe waves, respectively. Predictions for NAA-HU are in general agreement with the

limited number of observations, while the predictions for NPM-SA are smaller than the few observed perturbations. Results indicate that powerful VLF transmitters, typically operating continuously, regularly heat the nighttime D region overhead. The effect of this continuous heating on the ion chemistry of the D region is investigated theoretically in the next chapter.

6

Electron Density Changes in the Nighttime D Region Due to Heating by Very-Low-Frequency Transmitters

Heating of the ionosphere by man-made transmitters [*Jones,* 1990] and by lightning [*Inan et al.*, 1991] is believed to result in the modification of the electron number density (N_e). For example, suppression of a solar-flare-induced sudden phase anomaly observed on a 60-kHz signal passing over the high-frequency Platteville heater [*Utlaut*, 1975] has been ascribed by *Tomko et al.* [1980] to an increase in electron attachment in the heated daytime D region. In the case of heating by powerful ($\sim$ 20 GW radiated power) electromagnetic pulses ($\sim$ 100 μs duration) from lightning discharges, the dominant processes affecting the D region electron density are two-body attachment to O_2 and collisional ionization by electrons in the tail of the velocity distribution [*Taranenko et al.*, 1993a]. In contrast, heating by continuously-operating man-made transmitters ($\sim$ 1 MW radiated power) may alter the steady-state ion chemistry that determines the density of electrons and ions. In this chapter we investigate theoretically the modification of electron density in the lower ionosphere due to heating of the nighttime D region by very-low-frequency (VLF) transmitters [*Inan*, 1990a; *Inan et al.*, 1992].*

6.1 MODEL OF NIGHTTIME D REGION CHEMISTRY

Under steady-state conditions, the chemical processes in Figure 6.1a can be represented by a set of linearly-dependent equations [*Glukhov et al.*, 1992] relating the number densities N_e, N^+, N^-, and N_x^+, respectively, of electrons, primary positive ions (NO^+ and O_2^+), negative ions (e.g., O_2^-, CO_3^-, NO_2^-, NO_3^-), and positive water cluster ions or proton hydrates ($H^+(H_2O)_n$):

$$\frac{dN_e}{dt} = 0 = I_o + \gamma N^- - \beta N_e - \alpha_d N_e N^+ - \alpha_d^c N_e N_x^+ \tag{6.1}$$

$$\frac{dN^-}{dt} = 0 = \beta N_e - \gamma N^- - \alpha_i N^-(N^+ + N_x^+) \tag{6.2}$$

$$\frac{dN^+}{dt} = 0 = I_o - BN^+ - \alpha_d N_e N^+ - \alpha_i N^- N^+ \tag{6.3}$$

$$\frac{dN_x^+}{dt} = 0 = -\alpha_d^c N_e N_x^+ + BN^+ - \alpha_i N^- N_x^+ \tag{6.4}$$

where I_o is a steady, external ionization source; α_d [*Tomko et al.*, 1980] and α_d^c [*Reid*, 1977; *Huang et al.*, 1978] are the effective coefficients of electron recombination with primary positive ions and water cluster ions, respectively; α_i is the effective mutual neutralization coefficient for all types of positive ions with negative ions [*Rowe et al.*, 1974]; β is the effective three-body electron attachment rate [*Rowe et al.*, 1974; *Tomko*, 1981, p. 163]; B is the effective rate of conversion of primary positive ions (especially NO^+) into water cluster ions [*Rowe et al.*, 1974]; and γ is the effective collisional electron detachment rate [*Bailey*, 1959]. Reaction rates, coefficients, and their known dependences on the electron and neutral temperatures T_e and T_n are listed in Table 6.1. This four-species model is appropriate since we are interested primarily in the response of electron density (N_e) to heating.

Below 80 km, the most rapid processes under this model are electron attachment

$$e + O_2 + M \rightarrow O_2^- + M \quad (M \text{ is } O_2 \text{ or } N_2)$$
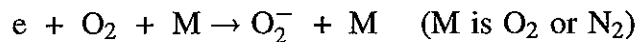
and detachment due to collisions between negative ions and neutrals, e.g.,

$$O_2^- + O \rightarrow O_3 + e \quad .$$
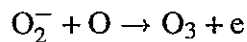
Table 6.1
D region reaction coefficients and rates.

Coefficients ($m^3\ s^{-1}$)

$$\alpha_d = \left(\alpha_{NO^+} N_{NO^+} + \alpha_{O_2^+} N_{O_2^+}\right)/N^+$$

$$\alpha_{NO^+} = 4.1 \times 10^{-13} \left(300\ T_n^{-0.5}\ T_e^{-0.5}\right)$$

$$\alpha_{O_2^+} = 2.1 \times 10^{-13} \left(300^{0.7}\ T_n^{-0.1}\ T_e^{-0.6}\right)$$

$$\alpha_d^c = 3 \times 10^{-12}(T_n/T_e)^b,\ 0 \le b \le 0.08$$

$$\alpha_i = 10^{-13}$$

Rates (s^{-1})

$$\beta = 10^{-43} N_{N_2} N_{O_2} + k_{O_2} N_{O_2}^2$$

$$k_{O_2} = K T_e^{-0.65} \exp\left[-\frac{a_1}{T_e} - \left(\frac{a_2}{T_e}\right)^2 - \left(\frac{a_3}{T_e}\right)^3\right]$$

$$K = 1.1617 \times 10^{-39} - 3.4665 \times 10^{-42} T_n$$
$$+3.2825 \times 10^{-45} T_n^2$$

$$a_1 = 7.8193 \times 10^2 - 3.2964 T_n$$

$$a_2 = -1.9159 \times 10^2 + 3.7646 T_n$$
$$-4.5446 \times 10^{-3} T_n^2$$

$$a_3 = -7.6834 \times 10^1 + 1.2277 \times 10^{-2} T_n$$
$$-7.6427 \times 10^{-3} T_n^2 + 1.7856 \times 10^{-5} T_n^{-3}$$

$$B = 10^{-43} N_n^2,\quad N_n \equiv \text{total neutral number density}$$

$$\gamma = 3 \times 10^{-23} N_n$$

Following *Glukhov et al.* [1992], we adopt a detachment rate γ [*Bailey*, 1959] that effectively represents the entire system of reactions involving collisional electron detachment [*Ivanov-Kholodnyi and Nikol'skii*, 1972, p. 205]. The dependence on γ of changes in electron density due to VLF heating is discussed in a later section. The rates β and γ are shown in Figure 6.1b as functions of altitude.

At night, the positive ion population in the D-region is comprised almost entirely of positive water cluster ions $H^+(H_2O)_n$ below 80 km and NO^+ and O_2^+ above 85 km [*Danilov and Semenov*, 1978]. Therefore, the loss of electrons through dissociative recombination with both primary positive ions (e.g., $NO^+ + e \rightarrow N + O$) and cluster

ions ($H^+(H_2O)_n$ + e $\rightarrow$ neutrals) must be considered. The coefficient of dissociative recombination with cluster ions (α_d^c) is a function of T_n and the relative abundances of the different cluster ion species; however, for simplicity, we adopt a single ambient value of $\alpha_d^c = 3 \times 10^{-12}$ m^3 s^{-1} [*Reid*, 1977], with $\alpha_d^c \sim (T_n/T_e)^b$, where $0 \leq b \leq 0.08$ [*Huang et al.*, 1978; *Tomko*, 1981]. The coefficients of dissociative recombination of electrons with NO$^+$ (α_{NO^+}) and O$_2^+$ ($\alpha_{O_2^+}$) depend more strongly on T_e than α_d^c yet are significant at night only above 85 km. The coefficients $\alpha_d = (\alpha_{NO^+}N_{NO^+} + \alpha_{O_2^+}N_{O_2^+})/N^+$ and α_d^c (heated value only) are shown in Figure 6.1c as functions of altitude.
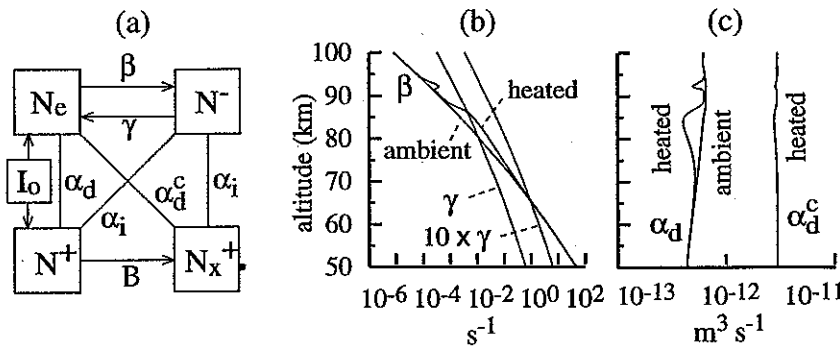
Figure 6.1. Model of the D **region chemistry.** (*a*) Four-component D region ion chemistry model. (*b*) Electron attachment and detachment rates β and γ, and $10 \times \gamma$. Also shown is β in the case of heating by NAA in a D region represented by electron density profile I (Figure 2.3). (*c*) Electron recombination coefficients α_d and α_d^c in the case of heating by NAA, assuming $\alpha_d^c \propto T_e^{-0.08}$ and profile I (Figure 2.3). Also shown is the ambient value of α_d.

6.2 METHOD OF CALCULATION

The first step in the solution of (6.1)–(6.4) is the adoption of an electron density profile. The four ambient electron density profiles used here (Figure 2.3) range from a tenuous (0) to a dense (III) nighttime D region, with the electron density varying over two orders of magnitude in the VLF reflection region. The ambient temperature (T_n) profile is from the U. S. Standard Atmosphere (Figure 2.1) [*National Oceanic and Atmospheric Administration et al.*, 1976], as are the neutral density profiles below 86 km (Figure 2.2).
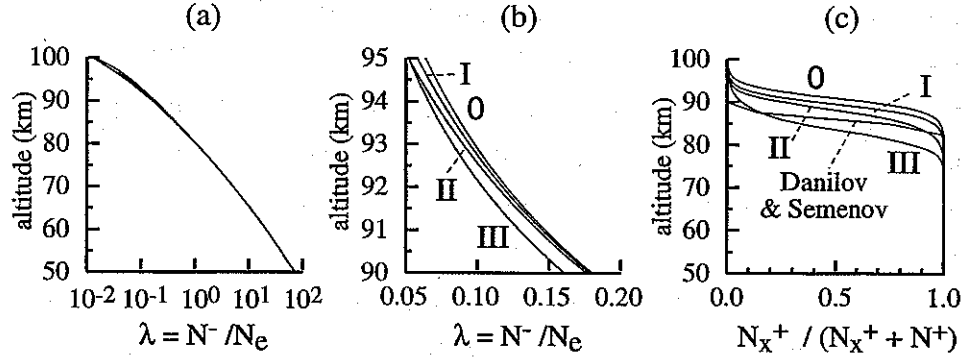
Figure 6.2. Ratios of D region ion populations. (a) Ratio of negative ions to electrons, λ, for the four electron density profiles in Figure 2.3 (logarithmic abscissa). (b) λ between 90 and 95 km (linear abscissa). (c) Relative positive ion composition in the nighttime D region calculated for the four electron density profiles (Figure 2.3), and measured by *Danilov and Semenov* [1978].

The neutral density profiles above 86 km are from the MSIS-86 thermospheric model [*Hedin*, 1987]. The ambient effective electron-neutral collision frequency (ν_{eff}) profile (Figure 2.4) has been used in past VLF propagation studies [*Wait and Spies*, 1964; *Poulsen et al.*, 1993a,b].

Eliminating N^+ and N_x^+ from (6.2) by assuming charge neutrality ($N_e + N^- = N^+ + N_x^+$), we solve for the ratio λ of N^- to N_e:

$$\lambda \equiv \frac{N^-}{N_e} = \frac{\frac{2\beta}{\alpha_i N_e}}{1 + \frac{\gamma}{\alpha_i N_e} + \sqrt{\left(1 + \frac{\gamma}{\alpha_i N_e}\right)^2 + \frac{4\beta}{\alpha_i N_e}}} \tag{6.5}.$$

Below 80 km, λ is independent of the electron density profile (Figure 6.2a) since $\lambda \to \beta/\gamma$ as $N_e \to 0$ [*Glukhov et al.*, 1992]. Above 80 km the λ profiles differ by no more than 13% (Figure 6.2b).

Equation (6.5) is used to solve (6.4) for the ratio of primary positive ions to water cluster ions as a function of electron density:

$$\frac{N^+}{N_x^+} = \frac{\alpha_d^c + \lambda \alpha_i}{B} N_e \tag{6.6}.$$

The relative composition of positive cluster ions $N_x^+/(N^+ + N_x^+) = 1/(1 + N^+/N_x^+)$ is shown in Figure 6.2c for the four electron density profiles along with results from a nighttime rocket mass spectrometer measurement [*Danilov and Semenov*, 1978].

Using the adopted electron density profile and the assumption of charge neutrality, (6.5) and (6.6) are solved for the negative ion (N^-), primary positive ion (N^+), and positive cluster ion (N_x^+) profiles (Figure 2.3). In turn, these profiles are used to determine profiles of the ion-pair production rate I_o from (6.1) that are consistent with each electron density profile (Figure 6.3). This steady, external ionization source is assumed to represent the ambient in the calculation of electron density under heated conditions. It is interesting to note that the production rate profiles corresponding to electron density profiles II and III are fairly consistent in the 70-90 km altitude range with several published profiles of ion-pair production rates in the nighttime D region due to scattered hydrogen Lyman α [*Potemra and Zmuda*, 1970; *Goldberg*, 1989] or electrons precipitated from the Earth's radiation belts at mid-latitudes [*Potemra and Zmuda*, 1970]. Below 70 km there is a discrepancy between the profiles calculated here and the ion-pair production rates expected due to galactic cosmic rays, which should increase from $\sim 10^4$ ion pairs m^{-3} s^{-1} at 70 km to $\sim 10^6$ ion pairs m^{-3} s^{-1} at 50 km [*Potemra and Zmuda*, 1970; *Goldberg*, 1989].

The heated electron temperature profiles are calculated using the VLF heating and propagation model described in Chapters 2 and 4. These profiles are used to calculate new values of α_d, α_d^c, and β. Equations (6.1), (6.3), and (6.5) and the charge-neutrality condition then are combined to obtain an implicit function f of electron density N_e:

$$f = 0 = I_o[B + (\alpha_d^c + \lambda\alpha_i)N_e] + N_e\{(\gamma\lambda - \beta)B + N_e[-\alpha_d^c B(1 + \lambda) \\ + (\gamma\lambda - \beta)(\alpha_d + \lambda\alpha_i) - N_e\alpha_d^c(\alpha_d + \lambda\alpha_i)(1 + \lambda)]\}$$

(6.7)

where λ is a function of electron density and the chemical rates and coefficients, as given by (6.5). Equation (6.7) is solved for N_e iteratively at each altitude using the method of false positions [*Press et al.*,1988, pp. 263–266]. The behavior of this equation around the solution (where $f = 0$) is demonstrated in Figure 6.4 for the case of maximum electron density depletion by NAA in the D region represented by profile I.
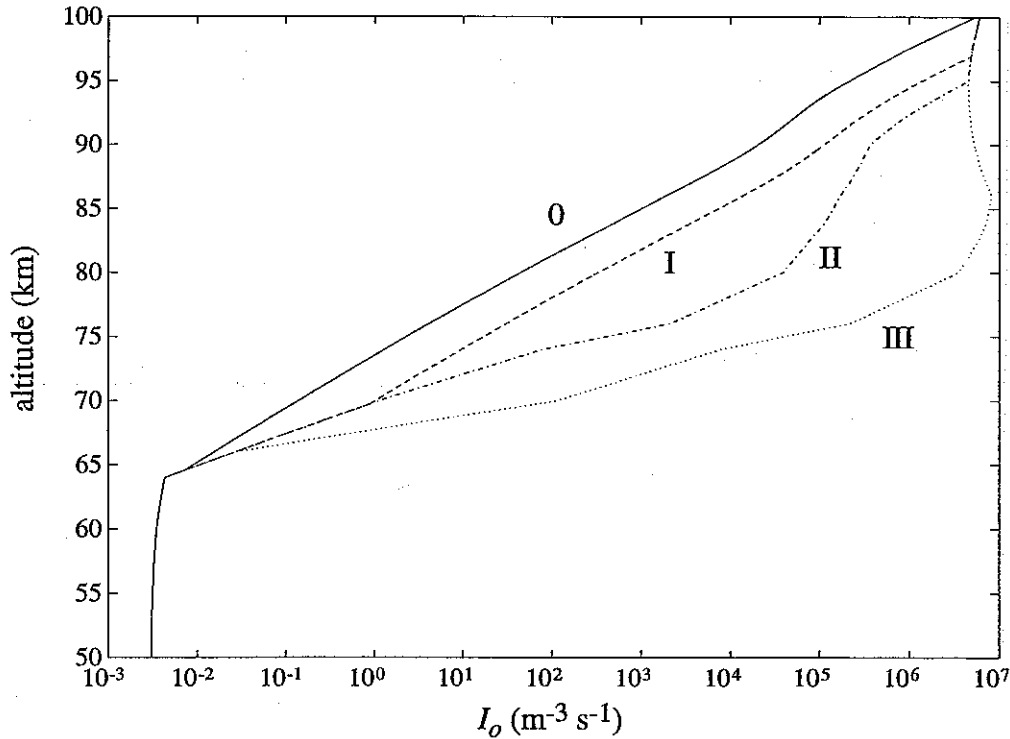
Figure 6.3. External ionization source. Profiles of the hypothetical ion-pair production rates I_o calculated self-consistently from the four assumed electron density profiles and the ion chemistry model.

6.3 RESULTS OF THE CALCULATIONS

We examine the effect of the VLF transmitters NAU (Aguadilla, P.R.; 100 kW; 28.5 kHz; dip angle $I = 49.0°$), NSS (Annapolis, Md.; 265 kW; 21.4 kHz; $I = 70.6°$), and NAA (Cutler, Me.; 1000 kW; 24.0 kHz; $I = 73.4°$) on the nighttime D regions represented by electron density profiles 0, I, II, and III (Figure 2.3). The dip angle for NAU is that used by *Inan et al.* [1992]; the others are from Table 4.2.

First, we assume that α_d^c does not vary with electron temperature ($b = 0$) and that γ is as listed in Table 6.1. The panels on the left side of Figure 6.5 show the ambient and heated T_e profiles through the point of maximum heating ($\Delta\nu/\nu_o$). Assuming a toroidal radiation pattern, the transmitter-induced electron temperature enhancement is minimum directly above the transmitter and maximum due geomagnetic north of the transmitter [*Galejs*, 1972*b*; *Inan et al.*, 1992]. For example, in the tenuous nighttime D region represented by profile I, the point of maximum heating over NAA is at 84.4 km altitude, 84.4 km
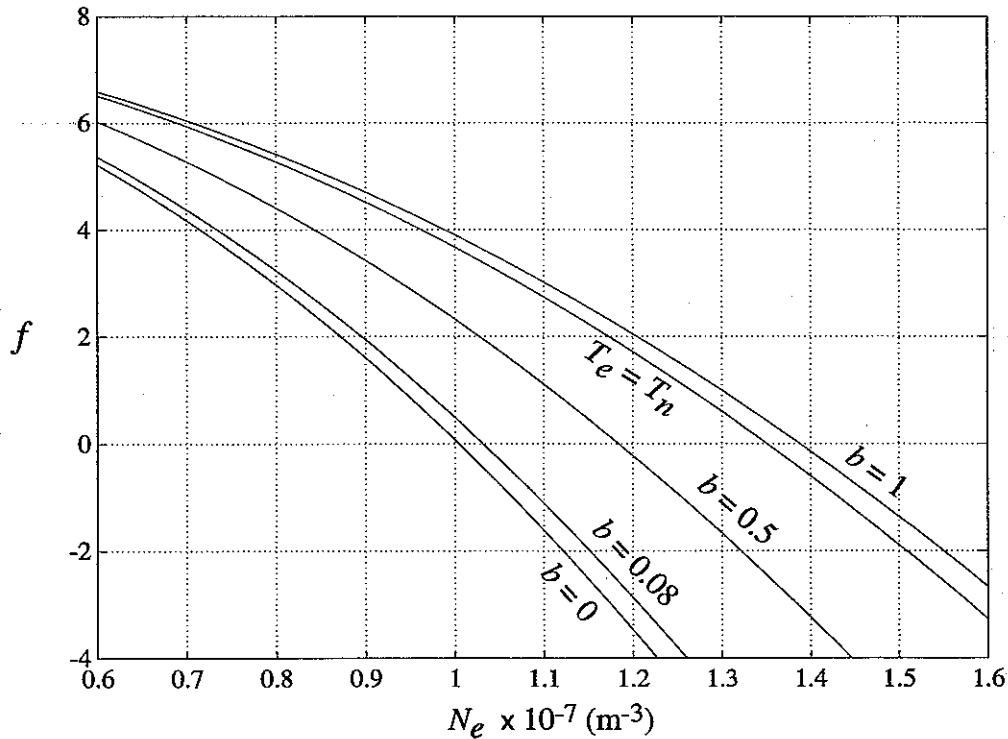
Figure 6.4. Implicit solution of equation (6.7). Equation (6.7) as a function of electron density N_e at $h = 81.8$ km, the altitude of maximum density depletion (26%) by NAA under profile I. The ambient case ($T_e = T_n = 195.09$K) is shown, as is the heated case ($T_e = 398.17$K) for four different assumed temperature dependences for α_d^c ($b = 0$, 0.08, 0.5, and 1.0).

due geomagnetic north of NAA. At this altitude, the radius at the outer half-maximum of the electron temperature enhancement is about 150 km. The shape and extent of the density depletion should be similar.

The panels on the right side of Figure 6.5 show the corresponding ratios of heated to ambient electron density N_e. In all cases, the dominant effect is depletion of electron density due to the increase of β with T_e (Figure 6.1b). In a tenuous D region (I) over NAA, the electron density is reduced by a maximum of 26% at an altitude of 81.8 km (Figure 6.5c). The increase in electron density above 90 km, where NO^+ dominates, is due to the decrease in α_d with increasing T_e (Figure 6.1c). Despite the larger maximum in electron temperature under profile 0, the maximum density depletion is almost the same (27% at 82.2 km), due to the exponentially decreasing effectiveness of three-body
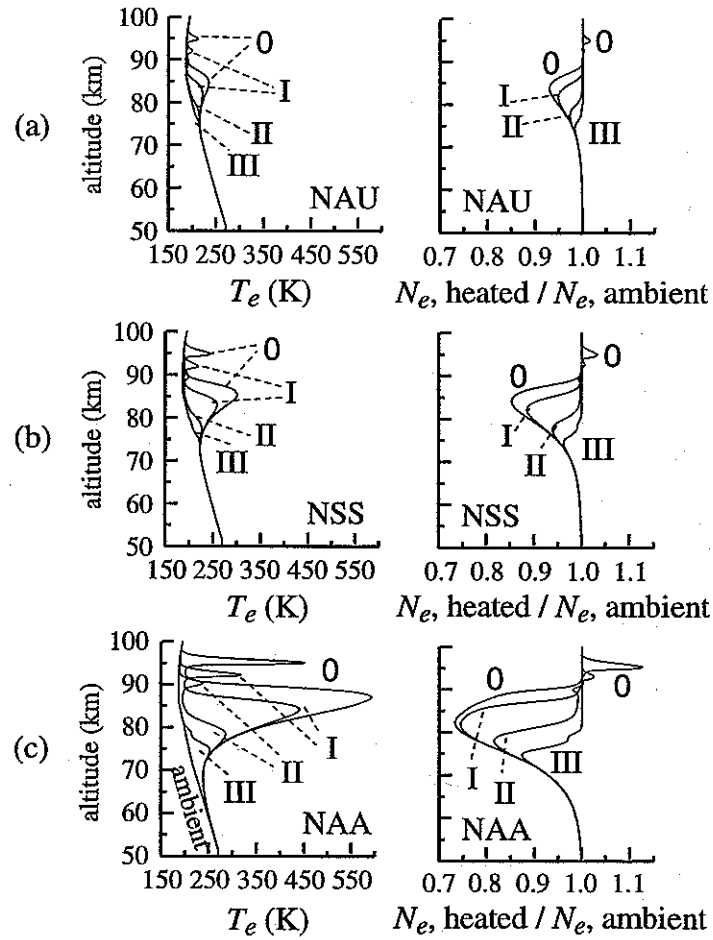
Figure 6.5. Predicted electron density changes. Ambient and heated electron temperatures (T_e), left, and ratio of heated to ambient electron density N_e, right, in the case of heating by (a) NAU, (b) NSS, and (c) NAA, for three N_e profiles (Figure 2.3).

electron attachment (β) and the increasing effectiveness of dissociative recombination (α_d) with altitude.

Next, we perform a similar calculation for each transmitter under the tenuous D region represented by profile I, adopting γ from Table 6.1 and $\alpha_d^c \sim T_e^{-0.08}$. The results differ little from the case of no electron temperature dependence for α_d^c (Figure 6.6a). Finally, in the case where γ is ten times higher (Figure 6.6b), the electron density decreases much less below 90 km (about 6% for NAA and profile I, $b = 0$), and the magnitude of the decrease is much more sensitive to the temperature dependence of α_d^c.

Prior theoretical work on the chemistry of a heated D region differs from the present
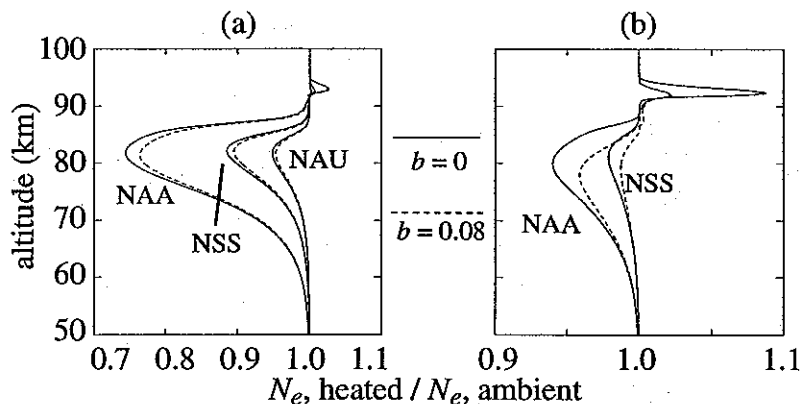
Figure 6.6. Effect of different reaction rates on electron density changes. Ratios of heated to ambient electron density (profile I, Figure 6.2a) for $b = 0$ and 0.08, where $\alpha_d^c \sim T_e^{-b}$. (a) $\gamma = 3 \times 10^{-23} N_n$ (Table 6.1). (b) $\gamma = 3 \times 10^{-22} N_n$. In this case, the density depletion over NAU (not shown) is $< 1\%$.

work in important ways. *Galejs* [1972*b*] predicted an increase in electron density due to VLF heating, just as our results show between 90 and 95 km for a tenuous D region (0 and I). However, he took into account only the decrease in α_d and assumed a sharp lower D region boundary at 85 km, so could not have predicted the density decrease below 90 km due to increased β. The theoretical results of *Tomko et al.* [1980] showing density depletion due to HF heating of the lower D region were for daytime conditions, and therefore are not applicable to the nighttime conditions under which VLF heating has been observed [*Inan*, 1990*a*; *Inan et al.*, 1992].
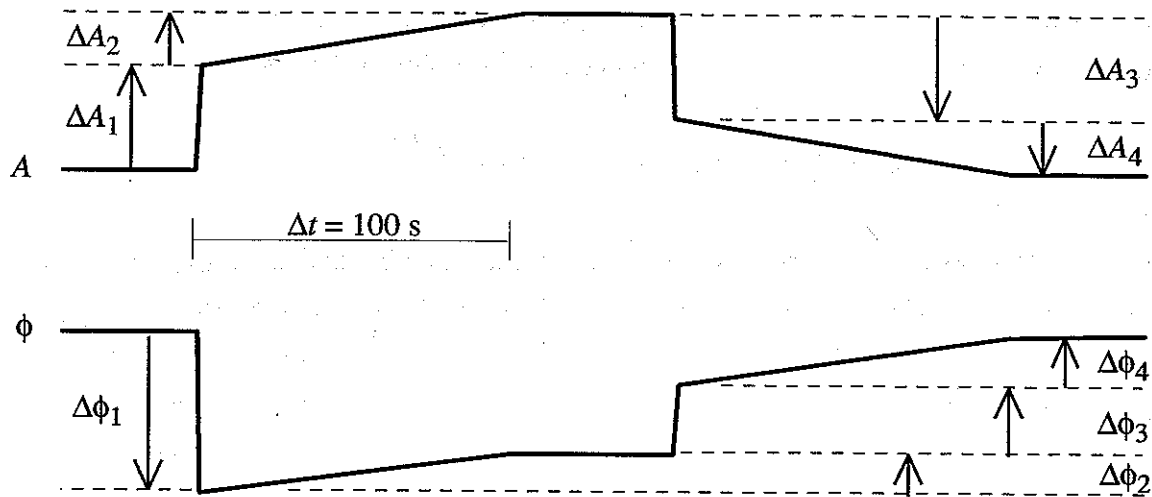
Figure 6.7. Schematic amplitude and phase perturbations on a subionospheric VLF signal due to heating by a VLF transmitter and resultant electron density depletion.

6.4 EFFECT OF ELECTRON DENSITY DEPLETIONS ON VLF WAVES PROPAGATING IN THE EARTH-IONOSPHERE WAVEGUIDE

Remote sensing with subionospheric VLF probe waves, as used to detect lightning-induced ionization enhancements [e.g., *Wolf and Inan*, 1990], may be used to verify experimentally the predicted electron density changes. A schematic representation of the amplitude and phase perturbations that might be observed due to transmitter-induced heating and a resulting electron density depletion is shown in Figure 6.7. Initially the ionosphere is assumed to be in its ambient state with electron density changes due to any previous heating assumed to have disappeared. When the heating transmitter turns ON there is a perturbation $(\Delta A_1, \Delta\phi_1)$ on the probe wave within a few milliseconds, with ΔA_1 and $\Delta\phi_1$ taken to be positive and negative, respectively, as was usually the case with the perturbations due to NAA heating observed at Gander during December 1992 on the NSS probe wave. After a much longer time (10-100 s) a density depletion evolves resulting in an additional perturbation $(\Delta A_2, \Delta\phi_2)$, in which case ΔA_2 and $\Delta\phi_2$ are both taken to be positive. The perturbations $(\Delta A_3, \Delta\phi_3)$ and $(\Delta A_4, \Delta\phi_4)$ are associated with the heater turning OFF and the subsequent disappearance of the density depletion.

The magnitudes of such signal perturbations are calculated using the method of Chapter 5 for the cases of heating by NAA, NSS, and NLK under electron density profiles 0 and I. Whether the ionospheric disturbance consists of $\Delta\nu$ only, $\Delta\nu$ and ΔN_e, or ΔN_e, the refractive index for each mode is calculated at each point in the disturbed region as

$$S_n(x,y) = S_n^o + [S_n(x_m, y_m) - S_n^o] \frac{\Delta\nu_{\text{eff}}(x, y, h_m)}{\Delta\nu_{\text{eff}}(x_m, y_m, h_m)}$$

where S_n^o is the refractive index of mode n for the ambient and $S_n(x_m, y_m)$ is the refractive index of mode n for the disturbed ionosphere represented by the heated collision frequency profile calculated in Chapter 4, or the depleted density profile calculated as in the previous section (assuming $\gamma = 3 \times 10^{-23} N_n$ and no temperature dependence for α_d^c), or both. Heating by the 850 kW NLK transmitter, not considered in section 6.3, results in a maximum depletion of 24% at $h = 82.0$ km under profile I, and a maximum depletion of 26% at $h = 82.5$ km under profile 0.

Table 6.2
Calculated probe wave perturbations due to electron density depletion.

N_e profile	$\Delta A_1, \Delta\phi_1$ (dB, °)	$\Delta A_2, \Delta\phi_2$ (dB, °)	$\Delta A_3, \Delta\phi_3$ (dB, °)	$\Delta A_4, \Delta\phi_4$ (dB, °)
probe wave = NSS-GA, heater = NAA				
0	+0.02, −3.28	+0.10, −0.84	−0.04, +2.85	−0.07, +1.27
I	+0.02, −1.34	+0.07, −0.73	−0.05, +1.33	−0.04, +0.75
probe wave = NAA-HU, heater = NSS				
0	−0.24, −0.68	+0.02, −0.13	+0.22, +0.50	0.00, +0.31
I	−0.24, −0.19	+0.07, −0.68	+0.15, +0.37	+0.02, +0.50
probe wave = NPM-SA, heater = NLK				
0	−0.08, −0.58	−0.02, −0.53	+0.09, +0.78	+0.01, +0.33
I	−0.07, −1.27	+0.04, −0.98	+0.03, +1.43	0.00, +0.83

The results of the waveguide calculations are given in Table 6.2. In general the amplitude changes predicted due to electron density changes are small, but the magnitudes of the associated phase perturbations are substantial, generally between 0.5 and 1.0°, with one phase perturbation as large as 1.27°. The incorporation of electron density depletion in the waveguide calculations does not affect the overall level of agreement of the predictions of Chapters 4 and 5 with the observations of Chapter 3, however. Phase and amplitude perturbations of absolute magnitude $\geq 0.5°$ and ≥ 0.1 dB, respectively, due to lightning-induced electron precipitation are generally observable without superposed epoch analysis [e.g., *Wolf and Inan*, 1990]. Detectability would be improved if the heater were to be keyed so as to allow sufficient ON-time for the density depletion to develop and sufficient OFF-time for it to decay. Note, however, that in contrast to the idealized conditions assumed here, the actual observations of heating presented in Chapter 3 represent the response of a probe wave to a heater turning OFF following hours of transmission, during which transport mechanisms such as ionospheric winds and diffusion may have affected the magnitude and shape of the depleted region.

The time constants of the formation and decay of transmitter-induced density depletions can be estimated by separately considering each term on the right side of (6.1) and plotting the inverse of the associated rate as a function of altitude (Figure 6.8). In fact, for relatively short time scales the time constant below ~ 80 km is $(\beta + \gamma)^{-1}$ [*Glukhov et al.*, 1992], and it is this value that is plotted in Figure 6.8. Based on the fastest reaction time constant at the altitude of maximum electron density depletion (~ 80 km), which is $(\beta + \gamma)^{-1} \simeq 100$ s, the density depletions predicted here should evolve and disappear over tens of seconds following heater ON and OFF, respectively.

Since the D region exhibits natural variations with time constants similar to those predicted here for the transmitter-induced density depletions, it may be difficult to recognize the signatures of these depletions in subionospheric VLF data. It is interesting to note in this connection the observations reported by *Molchanov et al.* [1977] of the self-action of 15 kHz signals propagating in the Earth-ionosphere waveguide. Observations were made on the ground at distances of 500-4500 km from a high- and a mid-latitude Soviet VLF transmitter of equal radiated power. When these transmitters operated in a 60-s ON 60-s OFF or 120-s ON 120-s OFF format, the amplitude observed on a vertical loop antenna perpendicular to the direction of propagation was sometimes observed to increase steadily from the beginning to the end of the 60-s transmission. In other cases this signal showed more irregular variations. No variations were observed on the signals received

on a vertical loop parallel to the direction of propagation. *Molchanov et al.* [1977] proposed that the observed effect resulted from a change in D region electron density due to thermal diffusion and a change in the ion chemistry equilibrium. Unfortunately, the theoretical details of this explanation were not provided, and experimental details such as the radiated power of the Soviet transmitters or control data in the form of the sky wave variations during longer-duration transmissions before and after the experiment were omitted. It is possible, however, that the observed effect was due to the development of density depletions above the transmitter resulting from D region heating, as described in this chapter, rather than thermal diffusion.
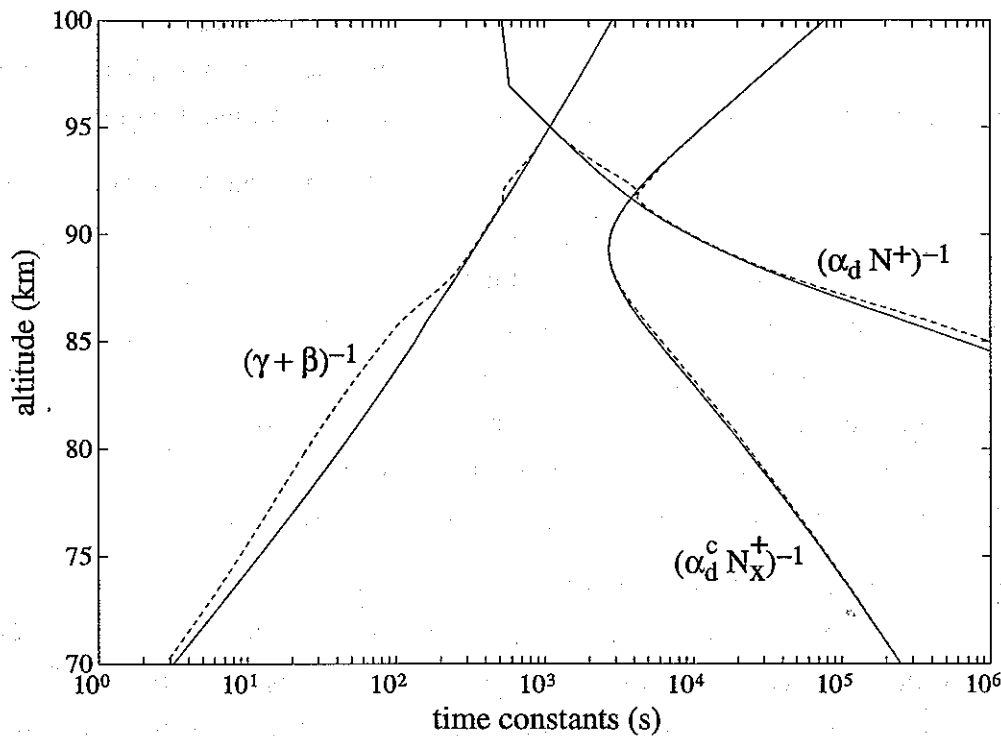
Figure 6.8. Electron density time constants. Time constants from equation (6.1) describing the development of electron density depletions due to heating: $(\beta + \gamma)^{-1}$, $(\alpha_d N^+)^{-1}$, and $(\alpha_d^c N_x^+)^{-1}$. The N^+ and N_x^+ profiles used here are ambient values corresponding to N_e profile I. Heated values (dashed lines) correspond to heating by NAA; $\alpha_d^c \propto T_e^{-0.08}$.

Finally, in the context of the time evolution of the density depletion, it is important to

point out that a decrease in electron density in turn affects the heating, an aspect of the problem that is neglected in the above calculations. Consider the steady-state equation

$$\nu(t) = \frac{\nu_o}{2} + \sqrt{\frac{\nu_o^2}{4} + \frac{2\nu_o U}{3kT_n N_e G}}$$ (6.8),

where ν_o is the ambient collision frequency, U is the power dissipated by the wave in unit volume, k is Boltzmann's constant, and $G \sim 10^{-3}$ is the fraction of an electron's energy beyond equilibrium lost in a collision. It can be seen from (6.8) that the electron temperature, which is proportional to ν, varies roughly as $N_e^{-0.5}$ [*Inan et al.*, 1992]. That is, there is a positive feedback process whereby an increase in electron temperature results in a depletion of electron density, which in turn leads to more heating by the radio wave, and so on. However, the tendency for a runaway decrease in electron density would be inhibited ultimately by a maximum in β around $T_e = 700$ K (Figure B.2). Nevertheless, the magnitude of the density depletions resulting from VLF transmitter-induced heating may in actuality be larger than predicted here.

6.5 SUMMARY

In order to investigate the effect of electron heating by existing ground-based VLF communications transmitters on the electron number density in the nighttime D region, a four-species model of the nighttime D region ion chemistry [*Glukhov et al.*, 1992] has been modified to include the effect of an electron temperature (T_e) different from the neutral temperature (T_n). Of the chemical processes whose rates depend on T_e when $T_e \neq T_n$, electron attachment of electrons to O_2 is dominant below 90 km while dissociative recombination of electrons with NO^+ determines the effect of electron temperature on electron density above 90 km. Electron attachment increases with T_e up to 700 K while dissociative recombination decreases with increasing T_e. Heating by the 1000 kW NAA transmitter in a tenuous nighttime D region results in a 26–27% depletion of electron density between 70 and 90 km altitude due to the dominance of electron attachment, with some density enhancement above 90 km due to dissociative recombination. The effect of the density changes on subionospheric VLF probe waves should be detectable if a controlled VLF heating experiment is designed to separate background ionospheric density variations from the effect of VLF heating.

7

Summary and Suggestions for Future Research

7.1 SUMMARY OF CONTRIBUTIONS

A remote sensing investigation of the nighttime D region has been conducted using very-low-frequency signals from man-made transmitters to disturb as well as to probe the partially-ionized plasma. In past experiments, powerful VLF transmitters have been keyed (modulated) in specially designed patterns to stimulate energetic electron precipitation from the Earth's radiation belts [*Imhof et al.*, 1983a, b] or to heat thermal electrons in the D region [*Inan*, 1990a, b; *Inan et al.*, 1992]. Modulation of ionospheric currents by a modulated VLF heating wave has been suggested as a method to generate extremely-low-frequency (ELF) waves [*Taranenko et al.*, 1992a; *Inan and Rodriguez*, 1993]. Such experiments permit superposed epoch analysis of radio wave data to bring out weak signatures of the physical process being studied. It has been demonstrated experimentally in the present work that ionospheric cross-modulation between two VLF signals also can be observed in real time when the presumed "heater" transmitter turns OFF and ON in the course of its normal operations. That is, with the proper heater-probe wave configuration, ionospheric heating can be monitored essentially every night within the scope of routine subionospheric VLF probe wave observations, resulting in a valuable data set that complements the results of specially scheduled VLF keying experiments. In the light of the continuous operation of the powerful VLF transmitters, with only occasional interruptions, it appears that the ionosphere is normally heated over such transmitters and that the perturbations observed using the OFF/ON episode method represent a temporary cooling of the ionosphere to thermal equilibrium between electrons and neutrals.

Using this method of observation of heater OFF/ON episodes, signatures of VLF cross-modulation were observed in three separate VLF heater-probe wave configurations (Chapter 3). Due to their similarity to the heating observations of *Inan* [1990a] and *Inan et al.* [1992] such events were identified as signatures of ionospheric cross-modulation due to heating by one of the VLF transmitters. One of the experimental configurations was designed to observe ionospheric heating by the 24.0 kHz NAA transmitter in Cutler, Maine, which radiates 1 MW total power, using a VLF receiver in Gander, Newfoundland. In this configuration the primary probe wave was the 21.4 kHz signal from NSS in Annapolis, Maryland, whose great circle path to Gander passed within 53 km of the NAA transmitter. During December 1992 NAA was observed to perturb the amplitude or phase of the NSS-GA probe wave in 41 of 52 OFF/ON episodes at night. The observed amplitude and phase perturbations ranged from −0.11 to +0.84 dB and from 0 to −5.3 degrees, respectively.

Ionospheric heating at VLF was observed similarly using two serendipitous VLF heater-probe wave configurations (Chapter 3). Heating by the 24.8 kHz NLK transmitter in Washington state was observed at Saskatoon, Saskatchewan, using the subionospheric VLF probe wave from the 23.4 kHz NPM transmitter in Hawaii, whose great circle path to Saskatoon passed within 79 km of NLK (Figure 3.7). In the 44 NLK OFF/ON episodes monitored between October 29 and November 23, 1987, four perturbations of the NPM-SA probe wave amplitude were observed, ranging from 0.3 to 1.6 dB (absolute magnitude). Intermittent interference at Saskatoon from the 23.4 kHz transmitter in Rhauderfehn, Germany, may have prevented detection of weaker signatures. In a reversal of the primary experimental configuration of this dissertation, heating by the 21.4 kHz NSS transmitter was observed at Huntsville, Alabama, using the subionospheric VLF probe wave from the 24.0 kHz NAA transmitter in Maine, whose great circle path to Huntsville passes within 160 km of NSS (Figure 3.10). In the 29 NSS OFF/ON episodes monitored at Huntsville during February 1990, five perturbations of the NAA-HU probe wave amplitude were observed, ranging from +0.2 to +0.5 dB (all positive in response to heating).

The consistency of these data with the hypothesized process of VLF heating was determined through a comparison of the data with predictions of quantitative theoretical models of VLF heating and propagation in the Earth-ionosphere waveguide. The first step in this process was the prediction of the extent and magnitude of the regions of increased electron temperature in the D region over the heater transmitters (Chapter 4).

The heated regions were calculated for the three U. S. Navy transmitters NAA, NSS, and NLK assuming four different model nighttime D region electron density profiles that represent over two orders of magnitude variation in the electron density. They were predicted to be roughly annular with a radius of $\sim$ 150 km at the half-maximum of the increase in electron-neutral collision frequency. In each case, the heating maximum was predicted to be poleward of the heating transmitter, corresponding to absorption of the ordinary (penetrating) component of the wave propagating nearly perpendicular to the Earth's magnetic field. The largest temperature increase (a factor of 3) was predicted for the most powerful transmitter considered here (NAA) in the most tenuous D region. It was also shown that the geomagnetic north-south asymmetry of the heated region is accentuated as geomagnetic latitude decreases, though the magnitude of the maximum heating varies little from mid- to low latitudes for the same transmitter radiated power.

The second step in the interpretation of the data was to model VLF propagation in the Earth-ionosphere waveguide in the presence of heating-induced disturbances of the D region electron-neutral collision frequency (Chapter 5). Waveguide propagation was modeled for the three heater-probe wave configurations studied in this dissertation assuming the same four model nighttime D region electron density profiles used to calculate the heated regions in Chapter 4. Results indicated that the amplitude of the NSS signal scattered by the heated region over NAA toward Gander increased with the magnitude of the heating. The range of predicted scattered field amplitudes was in general consistent with the observed perturbations of NSS-Gander during December 1992, as was the range and polarity of the predicted phase perturbations. However, the predicted relative phases of the unperturbed and scattered waves, and hence the magnitude of the amplitude changes, did not match the observations well. One possible reason for the discrepancy is a $\sim$ 2-km error in the optical path length of the scattered signal. In the light of the uncertainty involved in modeling the D region at all points between NSS and Gander (a distance of 2063 km) with a single electron density profile, a $\sim$ 2-km error in the optical path length is not unexpected. In the case of the heating by NLK the predicted scattered NPM signals were about one order of magnitude lower than expected based on the observed perturbations. There was better agreement between the predictions and the data in the case of the NAA signal scattered by the heated region over NSS. However, the limited number of observations in these two cases, including the lack of phase data, preclude a more conclusive comparison.

During December 1992, the amplitude of the NAU signal received at Gander was

perturbed in 6 of the 41 OFF/ON episodes in which ionospheric cross-modulation by NAA was observed on the NSS-GA probe wave (Chapter 3). These observations were surprising in the light of the fact that the NAU-Gander probe wave great circle path is 770 km from NAA at its closest approach. The simultaneity of the OFF/ON episodes and the NAU-Gander perturbations ruled out plasma transport effects as a possible cause of the perturbations. They could be explained qualitatively by a null in the probe wave spatial pattern near Gander making the probe wave amplitude highly sensitive to weak heating by the NAA signal at the upper waveguide boundary over the NAU-Gander path under relatively tenuous nighttime D region conditions.

The possibility that VLF transmitters can alter the number density of electrons in the D region through electron heating was investigated theoretically in Chapter 6 using a four-species model of the nighttime D region ion chemistry, with the general prediction of an electron density depletion below 90 km and an increase above 90 km. For example, heating by the 1 MW NAA transmitter in the most tenuous model nighttime D region was predicted to cause a 26–27% depletion of electron density between 70 and 90 km altitude due to the dominance of electron attachment, whose effectiveness increases with electron temperature up to 700 K. In general some density enhancement was predicted above 90 km due to the suppression of dissociative recombination by increased electron temperature. These electron density changes should develop over time scales (~ 100 s) similar to those of background variations in the amplitude of subionospheric VLF signals normally observed at night. This similarity indicates that the effect of the density changes on subionospheric VLF probe waves may be detectable only through a VLF heating experiment in which the heater is keyed at a very slow rate, e.g., 100-s ON/150-s OFF. Such a rate would allow the electron density changes enough time to develop and disappear, and the repetition would permit superposed epoch analysis to remove the random background variations.

7.2   SUGGESTIONS FOR FUTURE RESEARCH

7.2.1   Improvements to the Heating and Propagation Models

The increasing speed and decreasing cost of computers have made it feasible to solve the equations of physics—such as Maxwell's and Boltzmann's equations—self-consistently at a basic level in the time domain, e.g., with a finite-difference time-domain solution [*Taranenko et al.*, 1993a, b]. This computational method, although significantly more computationally intensive than the models used in this dissertation to predict heating by VLF transmitters, would provide a firmer theoretical basis for interpretation of observations of VLF heating.

Model of Propagation of the Heater Wave Through the D Region

A full-wave model of the propagation of VLF waves through the D region is the next step in determining the vertical and transverse structure of the heated region. It is possible that the VLF standing wave pattern in the Earth-ionosphere waveguide [*Pitteway*, 1965] would result in a oscillatory variation in the heating with altitude that would affect the scattering of incident VLF waves.

Heating Model

The electron distribution in a weakly-ionized collisional plasma under the influence of an electromagnetic wave whose frequency is less than the electron collision frequency has a tail that falls off more rapidly than a Maxwellian distribution [*Gurevich*, 1978]. Average quantities (e.g., T_e) calculated using a Maxwellian may not be significantly different from those predicted for the actual distribution [e.g., *Huxley and Zaazou*, 1949]. However, quantities such as the intensity of optical emissions (airglow) are sensitive to the shape of the distribution function [*Taranenko et al.* 1992b, 1993b]. Solving the collisional Boltzmann equation [*Taranenko et al.*, 1993a,b] for the electron distribution function, and hence a more accurate set of D region constitutive relations [*Budden*, 1965] and electron cooling rates, would permit a self-consistent heating calculation.

7.2.2   Self-Consistent Solution of the Density Depletion

As mentioned in Chapter 6 the increase in heating with decreasing electron density (6.8), combined with the increase in electron attachment (β) with increasing temperature (up to 700 K), leads to a positive feedback process that may result in a larger density depletion than predicted in Chapter 6. An iterative solution at all altitudes would permit a self-consistent solution to this feedback problem as well as the inclusion of the effects of ionospheric winds [*Glukhov et al.*, 1992] on the shape and magnitude of the density depletion. The importance in this problem of physical phenomena with widely different time scales may preclude a reasonable time-domain numerical solution.

7.2.3   Inclusion of Mode Coupling in the Scattering Model

The D region disturbances due to VLF transmitter heating modeled in this dissertation nominally satisfy both the Born approximation, that the change in the refractive index is small, and the W.K.B. approximation, that the disturbances varies slowly with respect to a wavelength. Thus the magnitudes of the scattered fields are expected to be accurate, and this is confirmed by the general agreement of the predictions with the data. However, the sensitivity of the phase calculations to the ionospheric and ground conductivity models indicates that a scattering model should be developed that accounts for mode coupling within the heated ionosphere and at interfaces between different ground conductivities under the heated region.

7.2.4   Future Experiments

Multiple-Point Remote-Sensing Measurements of VLF Heating

Making measurements of the scattered probe wave at points far off the probe wave great circle path that passes under the heated region over a VLF transmitter would permit an evaluation of the scattering pattern of the heated patch. In contrast, making measurements at very closely spaced points, preferably where the scattered signal is expected to be strong, would permit interferometry. The larger effective antenna aperture would permit finer scale "imaging" of the heated region, and cross-correlations of the amplitude and phase at these sites [*Harwood*, 1954] could reveal background drifting ionospheric irregularities that affect the magnitude and shape of the heated region.

Remote-Sensing Measurements of Electron Density Changes due to VLF Heating

Near-vertical incidence reception of the signal from NAA following an OFF/ON episode using antennas parallel and perpendicular to the direction of propagation [e.g., *Bracewell et al.*, 1951; *Kossey et al.*, 1983] can be used to test predictions of electron density depletion by observing the change in ionospheric reflection and conversion coefficients with time. Deductions of the density change from such measurements could be compared with attempts to observe such a depletion using a different (probe) wave such as NSS at distant points in the Earth-ionosphere waveguide. The comparison would in effect be between the effect on a singly (or doubly) reflected ray and the effect on ~ 20 waveguide modes. The use of antennas parallel and perpendicular to the direction of propagation of a probe wave such as NSS would also be useful for distant observations of both heating and electron density changes since the perpendicular antenna favors quasi-transverse electric (QTE) and higher order quasi-transverse magnetic (QTM) modes. All techniques described here would benefit from the increased signal-to-noise ratio that can be achieved by repeated periodic keying of the heating transmitter and subsequent superposed epoch analysis of the radio wave data.

A

Analysis of Instrumental Cross-Modulation in a Very-Low-Frequency Radio Receiver

Cross-modulation in an electronic circuit occurs when, with two signals of different frequencies present, the amplitude of the output of one signal is a function of the amplitude of the other [*Terman*, 1943, p. 466]. When the modulation of one radio wave is observed to be transferred to another, receiver cross-modulation must be ruled out as a cause of such coupling before mechanisms such as ionospheric heating can be considered as a cause. In his report of the first observation of the "Luxembourg" effect, or ionospheric cross-modulation, *Tellegen* [1933] was careful to point out that cross-modulation in the radio receiver he used had been ruled out as the source of the observed effect. Following the first observation of ionospheric heating at VLF [*Inan*, 1990a], in which heating by the 100 kW 28.5 kHz NAU transmitter was detected using the 24.0 kHz NAA subionospheric probe wave received at Palmer Station, Antarctica, a copy of the Palmer VLF receiver was tested at Stanford. No evidence was found for a spurious response at 24.0 kHz due to a locally injected 28.5 kHz signal at expected levels [*Inan*, 1990a].

In late October 1992 a similar VLF receiver was installed in Gander, Newfoundland, in order to measure heating by the 1 MW 24.0 kHz NAA transmitter (Figure 3.1). During preparations at Stanford for this installation it was realized that the cross-modulation of the receiver would have to be reevaluated since the new configuration would involve a more powerful "heater" as well as a shorter distance from the "heater" to the receiver. (NAA is 1080 km from Gander while NAU is 9250 km from Palmer.) The first goal of the tests at Stanford was to determine the amount of cross-modulation in the VLF

receiver in the presence of a 24 kHz signal equivalent to the expected strength of NAA at Gander. Results of these tests were used to reduce the level of receiver cross-modulation. The effectiveness of these preparations was confirmed by tests performed during the installation. The cross-modulation response of the receiver to 24 kHz signal strengths much higher than ever observed from NAA at Gander was determined during a return visit to Gander in May 1993.

Salient results of these tests already were quoted in Chapter 3. This appendix provides a more detailed description of the tests and results. First, hypothetical sources of receiver cross-modulation are discussed briefly with reference to a block diagram of the receiver. Next, the technique used to test for receiver cross-modulation is described. A summary follows of the tests performed at Stanford and at Gander.

A.1 HYPOTHETICAL SOURCES OF RECEIVER CROSS-MODULATION

A device whose output includes the third power of the input signal is a source of cross-modulation [*Terman*, 1943, p. 646]. Given two signals $A_1(t)\cos\omega_1 t$ and $A_2(t)\cos\omega_2 t$ present at the same time in a circuit, the cube of the sum of these signals includes terms at $3\omega_1$, $3\omega_2$, $2\omega_1 \pm \omega_2$, and $2\omega_2 \pm \omega_1$ as well as terms proportional to

$$\left[\frac{1}{2}A_1^2(t) + A_2^2(t)\right] A_1(t)\cos\omega_1 t + \left[\frac{1}{2}A_2^2(t) + A_1^2(t)\right] A_2(t)\cos\omega_2 t \qquad \text{(A.1)}.$$

These terms constitute distortion at the original frequencies, including cross-modulation (e.g., $A_1^2(t)A_2(t)\cos\omega_2 t$).

The linearity of analogue electronic devices is due to their operation in a "small-signal" regime. However, devices such as silicon junction diodes and bipolar junction transistors have a fundamentally exponential current-voltage characteristic. For example, the transistor base-to-emitter current I_{BE} and voltage V_{BE} are related by the expression

$$I_{BE} = I_{OE}\left[\exp\left(\frac{|e|V_{BE}}{kT}\right) - 1\right] \qquad \text{(A.2)}$$

where I_{OE} is the saturation current under reverse bias ($V_{BE} < 0$, $|V_{BE}| \gg kT/|e|$), e is the electronic charge, k is Boltzmann's constant, and T is the temperature of the transistor [*Muller and Kamins*, 1986, p. 293]. In general, such a current-voltage characteristic
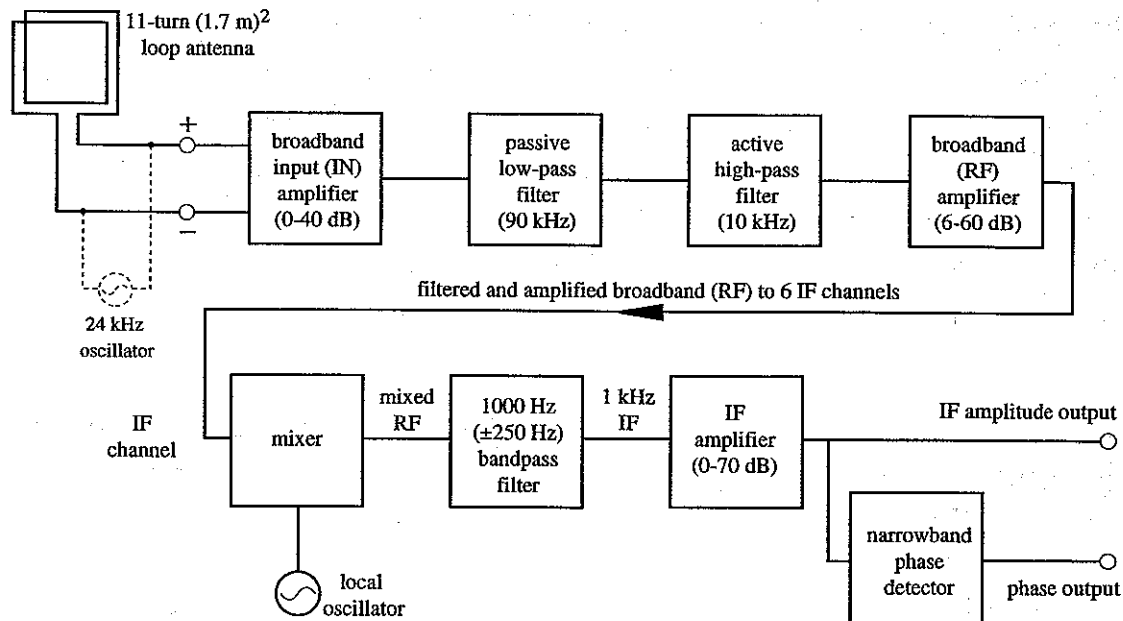
Figure A.1. Block diagram representing one RF and one IF channel in the Stanford tuneable VLF receiver. After *Wolf* [1990, p. 72]. The dashed portion represents the external balanced local oscillator applied to the antenna terminals to test the receiver for cross-modulation at 24 kHz, the frequency of the 1 MW NAA transmitter in Cutler, Maine.

generates all powers of a signal, as would be expected from a Taylor series expansion of the current-voltage characteristic, namely $e^x - 1 = x + \frac{x^2}{2!} + \frac{x^3}{3!} + \ldots$. Third harmonics are also created by magnetic cores used in inductors and transformers [*Terman*, 1943, p. 94]. Because typical radio receivers used in VLF research make extensive use of silicon and magnetic core devices, they cannot be free of cross-modulation entirely.

The Stanford VLF amplitude and phase receivers used at Gander are based on a design by T. G. Wolf; for a detailed description of their operation see his Ph.D. dissertation [*Wolf*, 1990]. The amplitude receiver consists of two radio-frequency (RF) channels feeding six tuneable intermediate-frequency (IF) channels. The 1 kHz IF outputs of these channels are peak-detected to determine the amplitudes of the VLF signals. In addition, the 1 kHz IF outputs are fed to the phase receiver in order that the phase of the signals may be tracked. The phase detector first doubles the frequency of the IF signal and then utilizes a phase locked loop to track one of the resulting sidebands of the modulated signal [*Wolf*, 1990]. A block diagram showing one RF channel and one IF channel is shown in Figure A.1.

In the Stanford tuneable VLF receiver, the amplifiers, active filters, and mixers contain silicon devices composed of transistors, while the passive low-pass filters utilize three ferrite core inductors. Thus, cross-modulation could in theory occur almost anywhere in the VLF receiver where there are two signals of different frequency present. By the same token, cross-modulation is less likely to occur in the amplifier in each IF channel since the 1 kHz bandpass IF filter should effectively remove all but the desired signal. The same argument can be extended to the phase detector.

A.2   EXPERIMENTAL TECHNIQUE TO EVALUATE RECEIVER CROSS-MODULATION

Instead of evaluating the individual nonlinear behavior of each of the receiver components the overall receiver cross-modulation was investigated by injecting a balanced locally-generated 24 kHz signal into the antenna terminals, as shown in Figure A.1. A tuneable, variable-gain calibration module designed and built by W. J. Trabucco and S. C. Reising was used as the source of the local 24 kHz signal. A circuit designed and built by the author was used to "key" the locally-generated 24.0 kHz signal in a 3-s ON/2-s OFF pattern similar to that used in previous transmitter keying experiments [e.g., *Imhof et al.*, 1983*a, b*; *Inan*, 1990*a*]. "Keying" the local signal enabled superposed epoch analysis of the VLF signals being received concurrently in order to bring out weak signatures of instrumental cross-modulation. Phase stability of the "keying" pattern with respect to the data acquisition system was ensured by synchronizing the ON/OFF pattern with the frequency standard used to generate triggers for the analog-to-digital converter as well as to down-convert the broadband to the 1 kHz IF signals [D. C. Shafer, private communication, 1992]. The 24 kHz signal was injected for a duration of at least one half hour for each tested combination of input signal strength and receiver gain levels in order to allow enough repetition of the ON/OFF cycle for superposed epoch analysis. Both RF channels were tested in the same fashion.

A.3 PRE-DEPLOYMENT TESTS: REDUCTION OF RECEIVER CROSS-MODULATION

The receivers were tested at Stanford before deployment by injecting a 24 kHz local oscillator signal equivalent in strength to the NAA field strength expected at Gander. For simplicity the expected field strength (E_w) of NAA at Gander was taken to be 18 mV m^{-1}, approximately the value calculated by *Inan et al.* [1992] at 1000 km along the NAA-to-Palmer Station great circle path, on the assumption that the NAA field strength at Gander (also $\sim$ 1000 km from NAA) would not be significantly different despite the different path azimuth. As shown in Chapter 3 (Figure 3.4) this value is about average for the observed field strengths at the time of OFF/ON events during December 1992.

A series of tests of the RF-A channel on October 10, 1992, was used to investigate the effect of lowering the field strength while keeping the receiver gain constant. An hour of data was superposed in each case. The total gain in the RF-A channel was 80.5 dB, consisting of 26.5 dB in the input (IN) amplifier and 54 dB in the RF amplifier. When a 24 kHz signal equivalent to E_w = 18 mV m^{-1} was injected into the terminals of antenna A, there was measureable cross-modulation in all channels (Figure A.2). When the 24 kHz signal was lowered by 5 dB the cross-modulation was substantially reduced. After the 24 kHz signal was lowered another 5 dB to E_w = 5.6 mV m^{-1} the cross-modulation was essentially eliminated in all but the NLK channel (Figure A.3).

Part of the NLK amplitude and phase traces shown in Figure A.2 have been enlarged in Figure A.4 to demonstrate the special nature of the cross-modulation in the NLK channel. In addition to an average level shift caused probably by the same nonlinearity that caused the cross-modulation in the other channels, there is a 50 Hz oscillatory component that is introduced into the amplitude and the phase as the keyed injected signal turns ON. In order to ascertain the source of this component the following facts must be considered. All the energy transmitted in the VLF transmitter signals considered here is contained in sidebands at ±50 Hz from the nominal center frequency, therefore the local oscillator signal that is mixed with the RF signal to create the 1 kHz NLK IF signal is tuned to a frequency 1000 ± 50 Hz away from 24.8 kHz. Thus, a strong 24.0 kHz signal injected into the receiver results in a spectral island at 1750 or 1850 Hz when the local oscillator is set to 1000 ± 50 Hz ABOVE the NLK signal. This signal is strong enough not to be removed entirely from the IF signal by the 1000 ± 250 Hz IF filter. The subsequent nonlinear full-wave rectification and detection of the IF signal creates spectral islands in
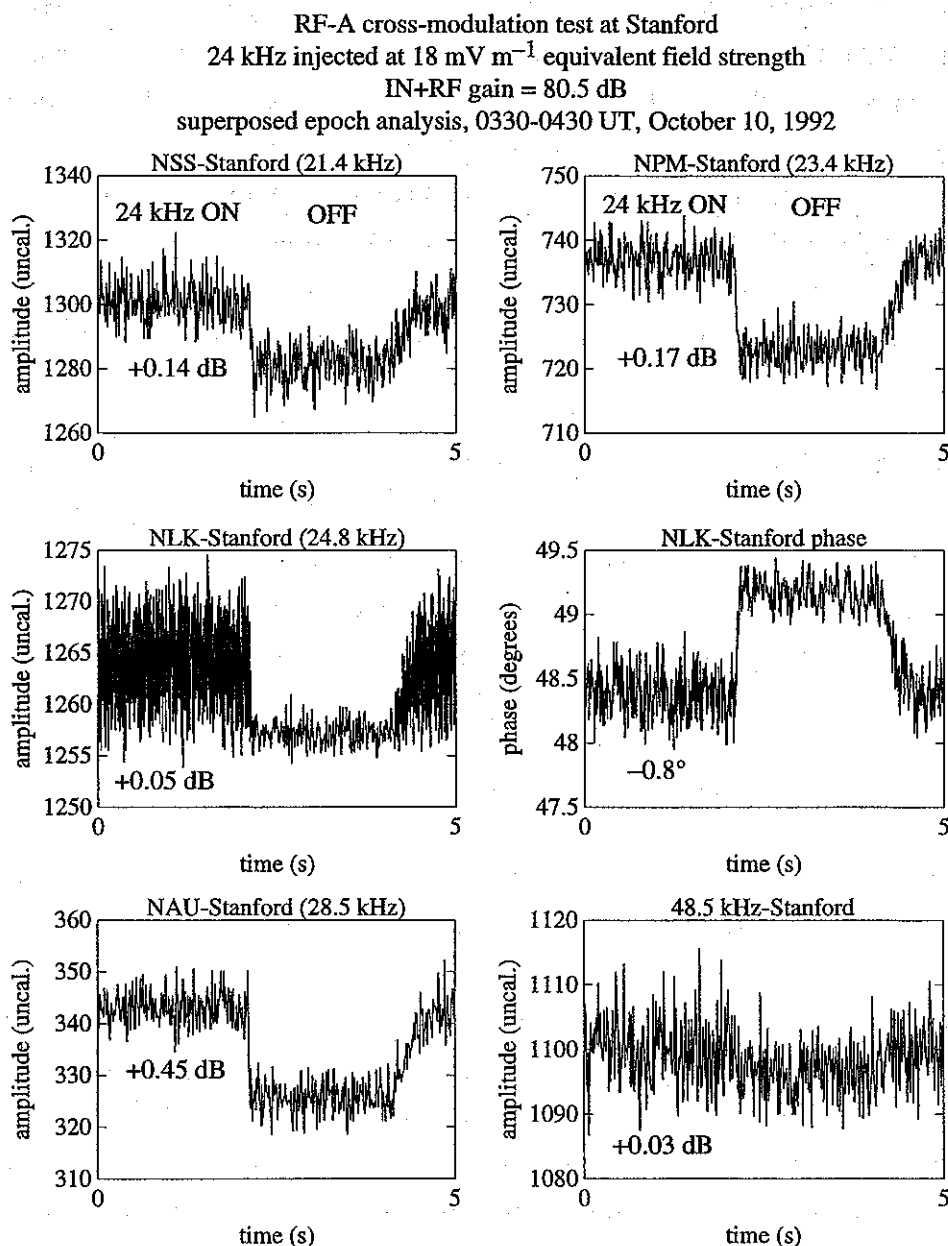
Figure A.2. Cross-modulation test of RF-A channel in VLF receiver, Stanford, October 10, 1992, 0330–0430 UT. Amplitudes of the NSS, NPM, NLK, NAU, and 48.5 kHz signals observed at Stanford, and the phase of NLK. Amplitudes are shown in uncalibrated linear units from 0 to 4095, with 0 representing absence of signal. The injected 24 kHz signal was keyed in a 3-s ON/2-s OFF pattern, with a relatively gradual ramp at key ON. Amplitude and phase changes due to cross-modulation in the receiver are noted on the relevant graphs.

RF-A cross-modulation test at Stanford
24 kHz injected at 5.6 mV m^{-1} equivalent field strength
IN+RF gain = 80.5 dB
superposed epoch analysis, 0730-0830 UT, October 10, 1992
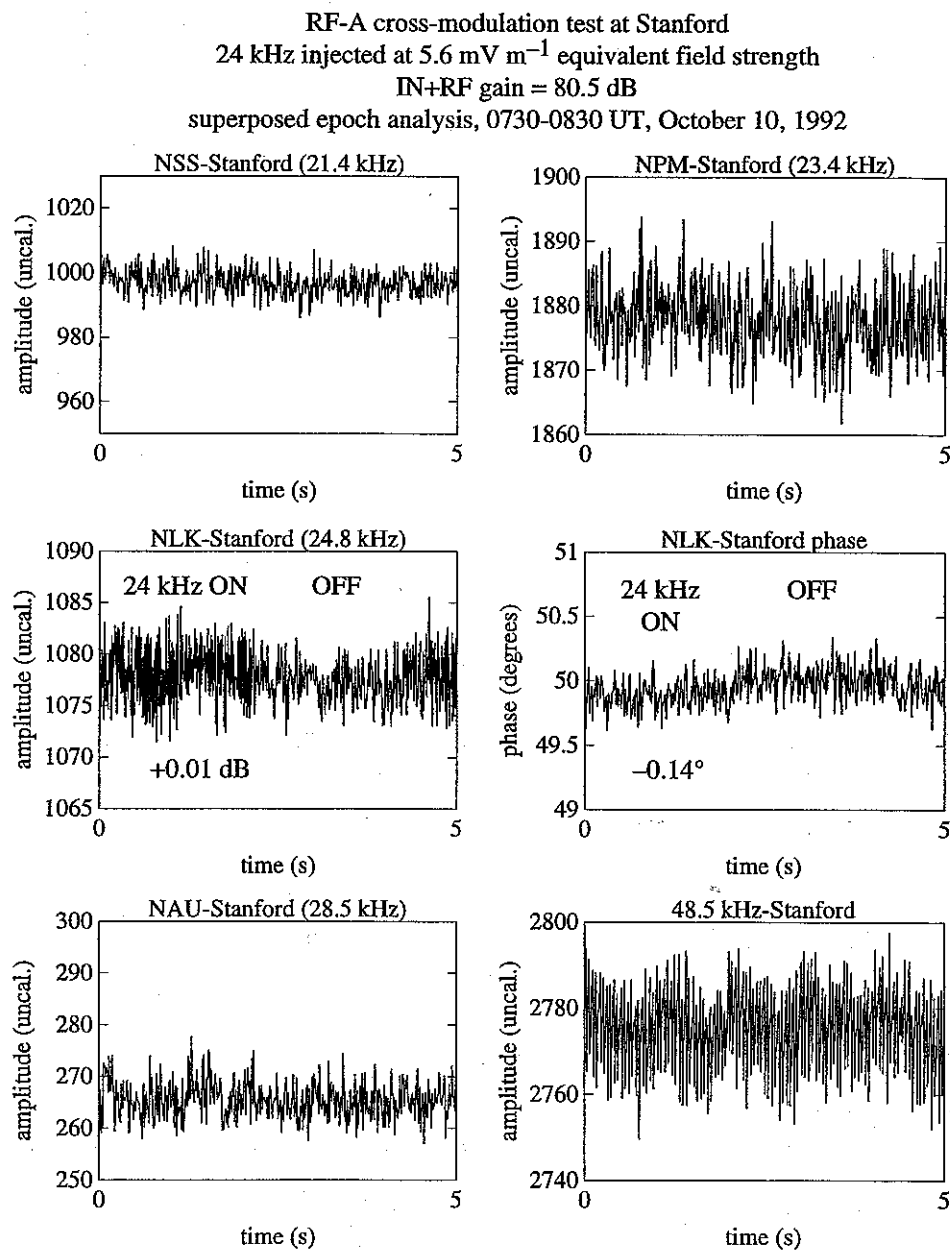
Figure A.3. Cross-modulation test of RF-A channel in VLF receiver, Stanford, October 10, 1992, 0730–0830 UT. Format same as in Figure A.2.
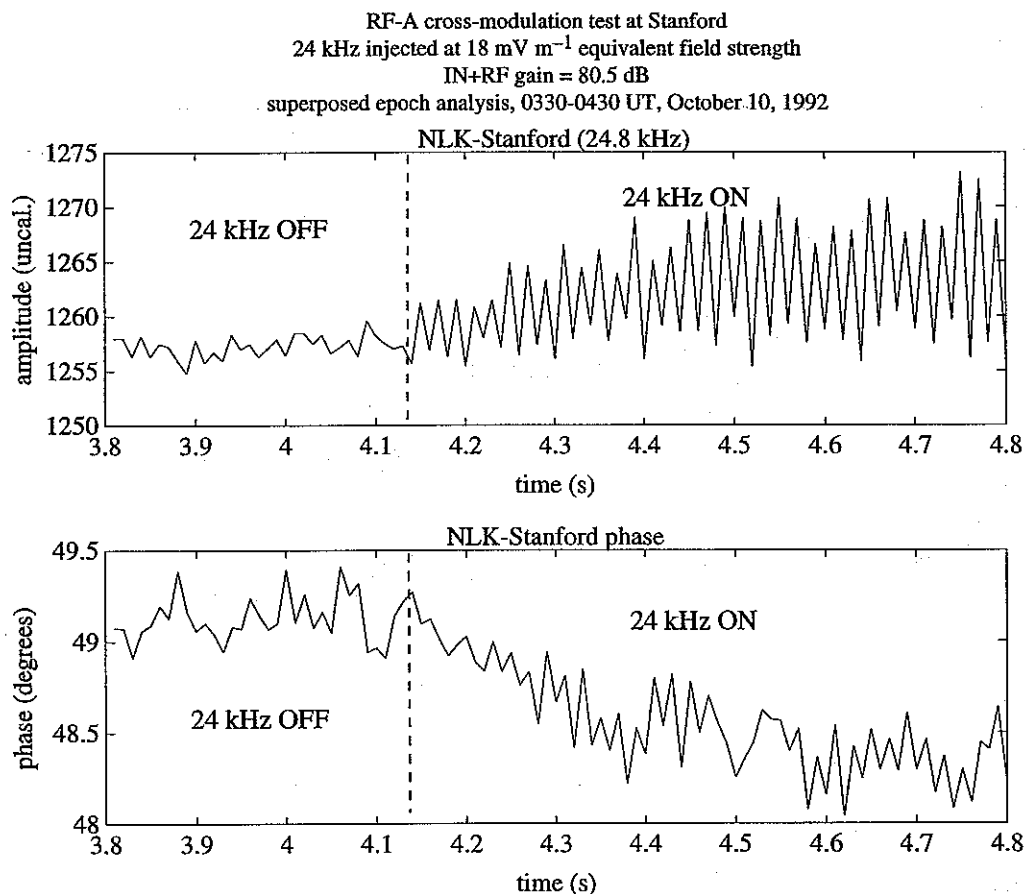
Figure A.4. Detail of Figure A.2 showing nature of cross-modulation in NLK channel, October 10, 1992, 0330–0430 UT. Amplitude (above) and phase (below) of NLK-Stanford during 1 s of superposed data. Amplitude is shown in linear uncalibrated units from 0 to 4095, with 0 representing absence of signal. The locally injected 24 kHz signal turns gradually ON during this second.

the detected amplitude at 50 Hz or at multiples thereof, the latter of which are aliased by the 100 Hz sampling process into a strong 50 Hz component.

We note here that the 50 Hz oscillation due to the aliasing may not be observable if the local frequency standard, from which the IF and the sampling triggers are derived, does not agree precisely with the frequency standards driving the transmitter signals. However, there may still be a level shift or DC bias due to aliasing of a strong interfering signal at close spectral proximity to the desired signal. As it turned out, cross-modulation on NLK due to the injected 24 kHz signal was significantly reduced at Gander by changing the local oscillator from 1 kHz ABOVE to 1 kHz BELOW 24.8 kHz (Table A.7). This

supports our conclusion that much of the cross-modulation in the NLK channel due to the injected 24 kHz signal occurs in the IF mixer rather than in the RF amplifier.

On October 11, 1992, the effect of reducing the RF-A gain while keeping the 24 kHz signal strength constant was investigated. The effect of changing either the IN or the RF gain was investigated by keeping one constant while the other was lowered. In all cases the RF gain was $\leq$ 72.5 dB, and cross-modulation occurred only in the NLK channel.

The RF-B channel was evaluated in a similar fashion on October 12, 1992. The input (IN) amplifier gain was kept constant at 26.5 dB, and the RF amplifier gain was set to 54, 46, and 40 dB. Fifty minutes of data were superposed in each case. Results of the test are shown in Figure A.5 for 54 dB and in Figure A.6 for 46 dB. While there is substantial cross-modulation in all channels at 54 dB the only channel affected at 46 dB is NLK. The nature of the cross-modulation in the NLK amplitude on October 12 is similar to that observed on October 10 (Figures A.2 and A.3) and on October 11 (not shown).*

During the cross-modulation tests, care was taken that no saturation of the man-made VLF signals occurred in the RF or IF stages. The nonlinear behavior of the receiver may be different from the behavior demonstrated in this appendix if and when saturation of a continuous signal occurs. We note also that clipping circuits in the input stage with a turn-on time of < 1 μs prevent the saturation of the receiver by powerful electromagnetic impulses from lightning discharges [Wolf, 1990, p. 69].

---

* During this time the only signal whose phase could be tracked was NLK, and that only on the RF-A channel due to the approximately north-south orientation of antenna A.

RF-B cross-modulation test at Stanford
24 kHz injected at 18 mV m^{-1} equivalent field strength
IN+RF gain = 80.5 dB
superposed epoch analysis, 0300-0350 UT, October 12, 1992
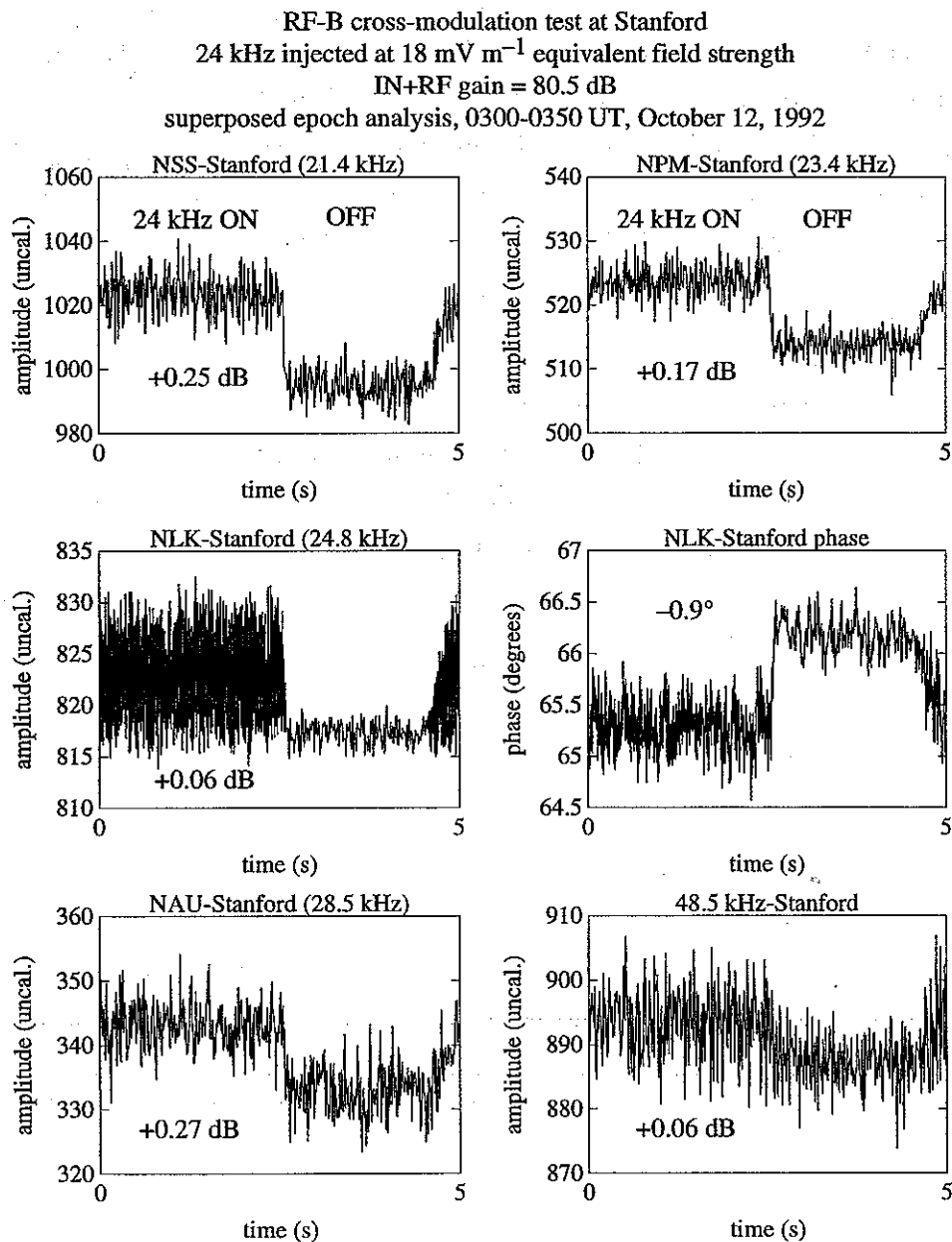
Figure A.5. Cross-modulation test of RF-B channel in VLF receiver, Stanford, October 12, 1992, 0300–0350 UT. Format same as in Figure A.2.

RF-B cross-modulation test at Stanford
24 kHz injected at 18 mV m^{-1} equivalent field strength
IN+RF gain = 72.5 dB
superposed epoch analysis, 0430-0520 UT, October 12, 1992
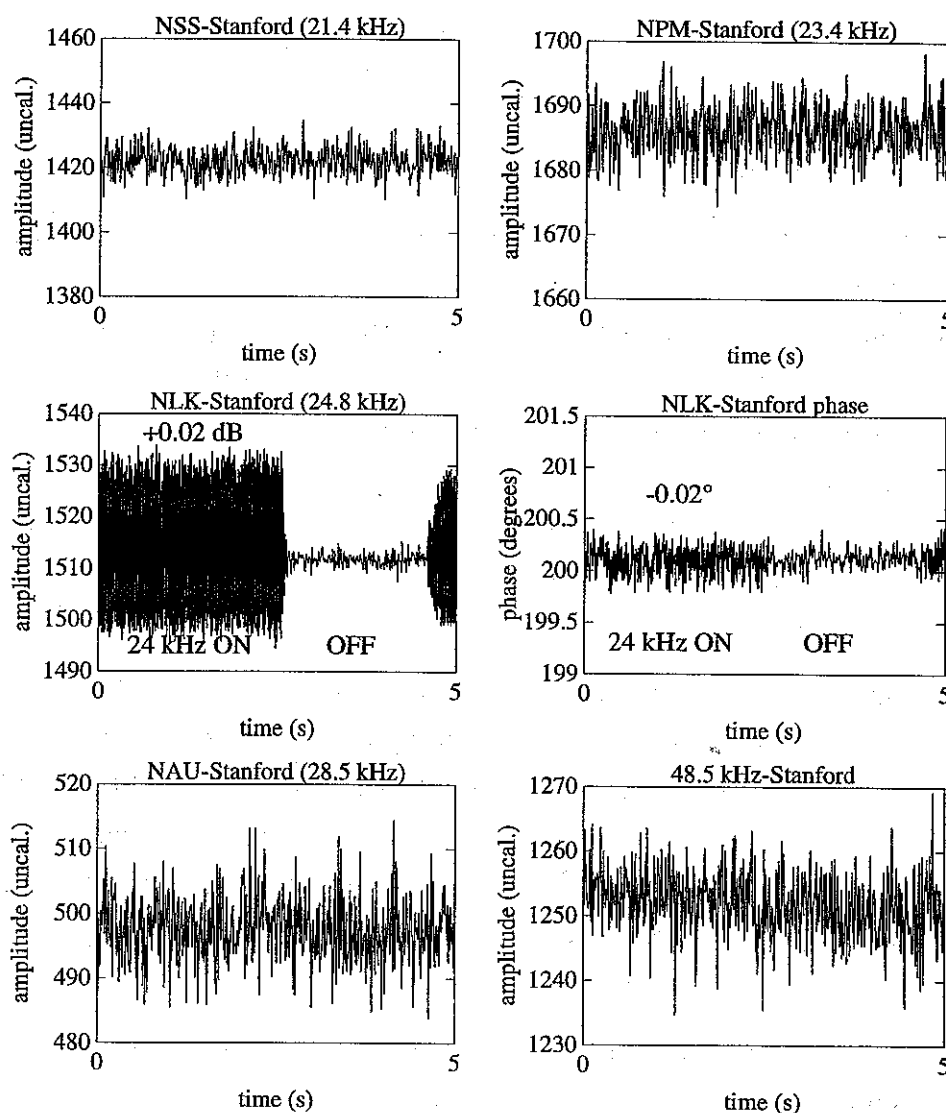
Figure A.6. Cross-modulation test of RF-B channel in VLF receiver, Stanford, October 12, 1992, 0430–0520 UT. Format same as in Figure A.2.

A.4 TESTS AT GANDER: CHARACTERIZATION OF RECEIVER CROSS-MODULATION

Both RF channels were used at Gander. Two vertical 1.7 m × 1.7 m loop antennas (made of 11 turns of wire) were erected at Gander during system installation in October-November 1992, one connected to the input terminals of RF channel A (RF-A), the other connected to channel B (RF-B). Antenna A was oriented with its plane in a southeast-northwest direction so that the nighttime strength of the NAA signal was minimized. Antenna B was erected so that it and antenna A formed an "L" (not quite perpendicular due to site constraints). Thus, NSS and NAA were received on antenna B at nearly full-strength. In May 1993 the loops were crossed in an "×"-shape to reduce the mutual inductance [R. A. Helliwell, personal communication, 1993]. At this time antenna B was constrained to be perpendicular to antenna A, whose orientation was readjusted to maintain its nighttime null of NAA.

Based on the results obtained during pre-deployment tests at Stanford, it was decided that the RF amplifier gain at 24 kHz in the RF-B channel should be set to less than 54 dB at Gander. This was accomplished in part by installing a notch filter designed and built by W. J. Trabucco that reduced the gain at 24.0 kHz by 20 dB. This permitted the RF amplifier gain in the RF-B channel to be set to 60 dB, which improved the NSS signal-to-noise ratio and the quality of the NSS phase measurements. In the light of the spectral proximity of the strong NAA signal to the NLK signal it was also decided that observations of NLK would be made using antenna A. The RF amplifier gain in the RF-A channel was set to 46 dB at Gander.

The tests at Gander were performed at two separate times. At the time of installation in October-November 1992 the purpose of the tests was to determine the amount of cross-modulation at injected 24 kHz signal levels not much larger than the observed NAA-Gander signal levels. The tests performed during a second trip in May were intended to determine cross-modulation levels at very large NAA signal levels that were unlikely to occur, in order to provide a more complete understanding of the receiver's cross-modulation behavior at the chosen RF gains.†

The results of the cross-modulation tests performed on RF-B at the final input and RF amplifier gain settings are summarized in Table A.1. Besides NAA only the NSS probe

---

† The phase drift present in some of the Gander data from December 1992 (Chapter 3) was not present during the tests in October–November 1992 and May 1993.

Table A.1
Cross-modulation tests of RF channel B
(24 kHz injected into RF-B, down-converted in IF channel 4)

| Gain [dB] | | | 24 kHz | NSS (IF2) | | | Analysis | |
IN	RF[a]	IF4	$\left[\frac{mV}{m}\right]$	$\left[\frac{mV}{m}\right]$	ΔA (dB)	$\Delta\phi$ (°)	Date	UT
26	60	15	140	3.3	+0.02	+0.2	6-7.V.93	23:00-03:00
26	60	15	140	6.2	+0.02	+0.2	7.V.93	06:30-07:00
26	60	20	80	6.8	+0.01	+0.06[b]	9.V.93	01:00-02:00
26	60	25	34	7.7	0	0	2.XI.92	00:30-01:30

a. A notch filter reduces the gain at 24 kHz by 20 dB.
b. This extremely small change represents the resolution limit
   of the 12-bit recording system for 245° full scale.

wave was recorded using antenna B at Gander. Note that in the two tests at injected 24 kHz levels of $E_w = 140$ mV m^{-1} the observed perturbations due to cross-modulation in the receiver were the same although the NSS field strength differed by a factor of ~ 2. Results of the superposed epoch analysis of data from the second test (May 7, 1993, 0600-0700 UT) are plotted in Figure A.7. A 140 mV m^{-1}-equivalent 24.0 kHz signal injected into the RF-B channel caused cross-modulation of the NSS signal amplitude and phase of +0.02 dB and +0.2°.

The results of the cross-modulation tests performed on the RF-A channel at the final input and RF amplifier gain settings are summarized in Table A.2. The NSS, NLK, and NAU probe waves as well as the NAA heater wave were recorded from antenna A at Gander. Results of the superposed epoch analysis of data from the test on May 10, 1993, 0100-0115 UT are plotted in Figure A.8. An 82 mV m^{-1}-equivalent 24.0 kHz signal injected into the RF-A channel perturbed the NSS amplitude and phase by −0.1 dB and −0.5°, the NLK amplitude by +1.6 dB, and the NAU amplitude and phase by −0.1 dB and −1°.

RF-B cross-modulation test
140 mV/m-equivalent 24 kHz signal injected
superposed epoch analysis, 0600–0700 UT
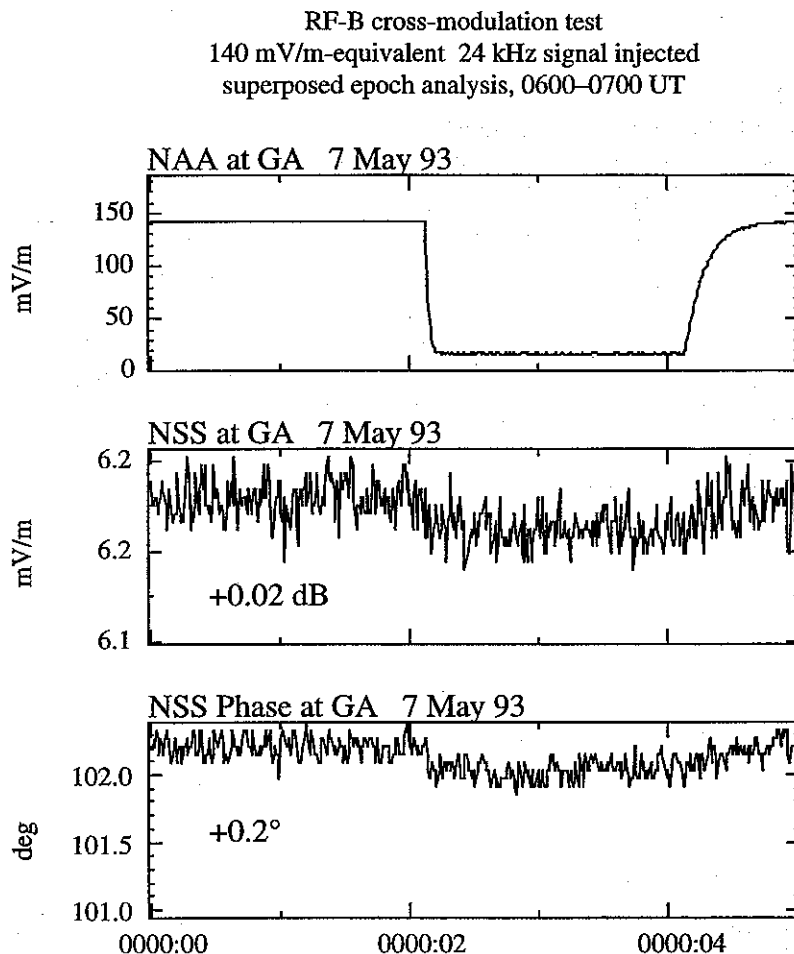
Figure A.7. Cross-modulation test of RF-B channel in VLF receiver, Gander, May 7, 1993, 0600–0700 UT. Each panel represents one hour of data superposed in 5-s segments. The top panel shows the level of the injected local 24 kHz signal. The lower two panels shown the amplitude and phase of the NSS signal received on antenna B during the test.

A.5   SUMMARY AND CONCLUSIONS

The NAA field strengths observed at Gander during December 1992 were much less than the injected 24.0 kHz equivalent field strengths required to cause measureable cross-modulation within the receiver. The field strength of NAA-GA received on antenna B at times of NAA OFF/ON episodes during December 1992 ranged from 6.5 to 34 mV m^{-1}, while on antenna A it was always <8.4 mV m^{-1}. By comparison, the cross-modulation on NSS-GA (IF2) caused by a 24.0 kHz 140 mV m^{-1}-equivalent signal injected into RF-B was +0.02 dB and +0.2°, while at 34 mV m^{-1}-equivalent there was no detectable

Table A.2
Cross-modulation tests of RF channel A
(24 kHz injected into RF-A, down-converted in IF channel 3)

Gain [dB] IN	RF	IF3	24 kHz $[\frac{mV}{m}]$	NSS (IF1) ΔA (dB),	$\Delta\phi$ (°)	NLK (IF5) ΔA (dB),	$\Delta\phi$ (°)	NAU (IF6) ΔA (dB),	$\Delta\phi$ (°)	Analysis Date	UT
26	46	10	82	−0.1	−0.5	+1.6	[a]	−0.1	−1	10.V.93	01:00–:15
26	46	15	56	0	+0.2 [b]	+12.4 [c]	[a]	−0.015[d]	0	31.X.92	23:17–:47
26	46	20	31	0	0[e]	+8.2 [c]	[a]	0	0	1.XI.92	03–05:00
26	46	25	18	0	[a]	[f]	[f]	0	0	27.X.92	01:10–:40

a. Phase did not track.
b. There is also a −1° phase spike at the time the injected 24 kHz signal turns ON.
c. This result is larger than the corresponding effect at 82 mV/m because it was acquired before the NLK local oscillator was set to BELOW at ∼ 1900 UT on November 1, thus reducing cross-modulation of NLK by NAA.
d. This extremely small change represents the resolution limit of the 12-bit recording system at 14.2% of full-scale field strength.
e. There is also a −1° phase spike at the time the injected 24 kHz signal turns ON. The phase of NSS from antenna B (IF2) shows a −0.2° phase spike at the time the injected 24 kHz signal turns ON followed by a 0.06° decrease in the phase of NSS (IF2).
f. 48.5 kHz recorded from RF-B instead of NLK; no cross-modulation observed

perturbation of NSS phase or amplitude. With a 24.0 kHz 82 mV m^{-1}-equivalent signal injected into RF-A, the cross-modulation on NAU-GA was −0.1 dB and −1°, while at 31 mV m^{-1}-equivalent there was no detectable perturbation of NAU phase or amplitude.

We therefore conclude that the tests described in this appendix were necessary and successful in eliminating receiver cross-modulation as a possible cause of the observed coupling between the NAA heater wave and the NSS and NAU probe waves. (No cross-modulation on NLK was observed.) The tests performed at Stanford pinpointed the RF amplifier as the likely cause of receiver cross-modulation. At an equivalent 24 kHz electric field of 18 mV m^{-1} cross-modulation was eliminated in all channels but NLK when the total gain in the RF section at 24 kHz (IN+RF) was reduced to ≤ 72.5 dB. Tests at Gander were used to confirm this result and to evaluate the receiver cross-modulation at much higher 24 kHz signal levels than ever observed. Even at these high input levels, the instrumental cross-modulation levels were substantially lower than most of the signal

RF-A cross-modulation test
82 mV/m-equivalent 24 kHz signal injected
superposed epoch analysis, 0100–0145 UT

NSS at GA   10 May 93   (IF1)

NSS Phase at GA   10 May 93

NAA at GA   10 May 93   (IF3)

NLK at GA   10 May 93   (IF5)

NAU at GA   10 May 93   (IF6)

NAU Phase at GA   10 May 93
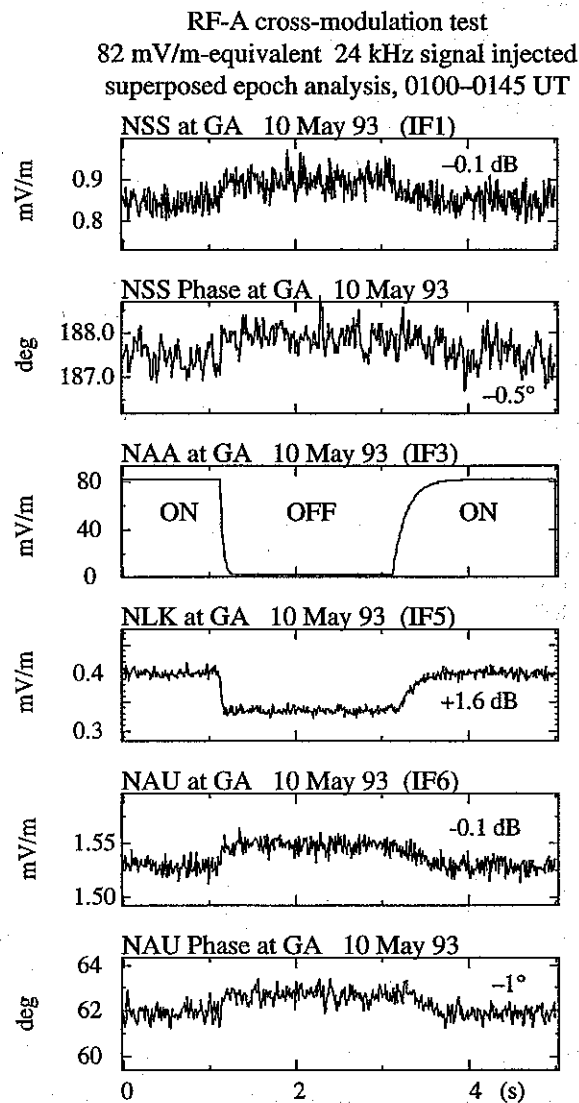
Figure A.8. Cross-modulation test of RF-A channel in VLF receiver, Gander, May 10, 1993, 0100–0145 UT. Each panel represents 45 min of data superposed in 5-s segments. Shown are the NSS phase and amplitude, NLK amplitude, and NAU phase and amplitude received from antenna A, along with the equivalent field strength of the 24 kHz signal injected into the terminals of antenna A.

perturbations observed during NAA OFF/ON episodes and interpreted to be ionospheric cross-modulation.

B

Aeronomic Rates and Reactions

This appendix documents the sources of the aeronomic rates and coefficients used in this dissertation. The aeronomic processes are divided into two categories: those that determine the temperature of electrons in response to an externally imposed electromagnetic wave, effective on millisecond time scales, and those that determine the chemistry of free electrons and ions in a weakly ionized plasma dominated by the neutral molecules N_2 and O_2, with time constants of order 1–100 s.

For consistency throughout this dissertation, all quantities are given in SI units, though historically most of the research on ionospheric chemistry has used the centimeter-gram-second (cgs) unit system along with the electron volt (eV). All expressions for cooling rates in this appendix have units $J \ m^{-3} \ s^{-1}$.

B.1   ELECTRON COOLING RATES FOR A MAXWELLIAN DISTRIBUTION

Following *Barr and Stubbe* [1992] we use the heating model of *Rietveld et al.* [1986], which takes into account elastic collisions, and inelastic collisions involving rotational and vibrational excitation of N_2 and O_2 using the cooling rates summarized by *Schunk and Nagy* [1978].

175

B.1.1 Elastic Collisions

Although the contribution of elastic collisions to electron cooling is relatively small, it is included here for completeness. Assuming the electrons and neutrals obey a Maxwellian velocity distribution, the exact form of the electron cooling rate for elastic collisions is [*Banks*, 1966]

$$L_{\text{elast}}(e, n) = 3N_e \frac{m_e m_n}{(m_e + m_n)^2} k(T_e - T_n)\nu_{\text{av}} \tag{B.1}$$

where N_e is the number density of electrons, m_e and T_e are the mass and temperature of the electrons, m_n and T_n are the mass and temperature of the neutral molecules, and k is Boltzmann's constant. The average momentum transfer collision frequency ν_{av} is given by [*Banks*, 1966]

$$\nu_{\text{av}} = \frac{4}{3}N_n\bar{g}\left[2k\left(\frac{T_e}{m_e} + \frac{T_n}{m_n}\right)\right]^{-3}\int_0^\infty g^5 q_D(g)\exp\left(\left[2k\left(\frac{T_e}{m_e} + \frac{T_n}{m_n}\right)\right]^{-1}g^2\right)dg \tag{B.2}$$

where N_n is the neutral species number density, g is the relative velocity of the particles, and $q_D(g)$ is the velocity-dependent momentum transfer (or diffusion) cross section:

$$q_D(g) = 2\pi\int_0^\pi (1 - \cos\theta)\sigma_{1,2}(g, \theta)\sin\theta d\theta \tag{B.3}$$

where $\sigma_{1,2}(g, \theta)$ is the differential scattering cross section and θ is the angle through which the electron is scattered by the collision [*Banks*, 1966; *Rees*, 1989, p. 76]. Note that the Maxwellian average of g is

$$\bar{g} = \left(\frac{8k}{\pi}\right)^{\frac{1}{2}}\left[\frac{T_e}{m_e} + \frac{T_n}{m_n}\right]^{\frac{1}{2}} \tag{B.4}.$$

By comparing (B.1) to equation (2.36) it can be seen that $G = 2m_e/m_n$ since $m_e \ll m_n$. Using experimental momentum-transfer cross sections $q_D(g)$ *Banks* [1966] integrated equation (B.2) to derive the following expressions:

$$\nu_{\text{av}}(e, N_2) = 2.33 \times 10^{-17}N_{N_2}(1 - 1.21 \times 10^{-4}T_e)T_e \tag{B.5}$$

$$\nu_{\text{av}}(e, O_2) = 1.82 \times 10^{-16}N_{O_2}(1 + 3.6 \times 10^{-2}T_e^{\frac{1}{2}})T_e^{\frac{1}{2}} \tag{B.6}$$

where the temperatures are in degrees Kelvin, the neutral densities are in m^{-3}, and the collision frequencies are in s^{-1}. Hence, by equation (B.1) the electron cooling rates for elastic collisions are:

$$L_{elast}(e, N_2) = 1.89 \times 10^{-44} N_e N_{N_2} (1 - 1.21 \times 10^{-4} T_e) T_e (T_e - T_n) \qquad (B.7)$$

$$L_{elast}(e, O_2) = 1.29 \times 10^{-43} N_e N_{O_2} (1 + 3.6 \times 10^{-2} T_e^{\frac{1}{2}}) T_e^{\frac{1}{2}} (T_e - T_n) \qquad (B.8)$$

valid for $T_e < 4500K$. As in the expressions for ν_{av}, the temperatures are in degrees Kelvin and the neutral densities are in m^{-3}.*

B.1.2 Rotational Excitation

Using the Born approximation of quantum mechanics and assuming a Maxwellian distribution for both electrons and neutrals, *Mentzoni and Row* [1963] derive the following expression for the energy transfer rate for rotational excitation of N_2 by electrons:

$$L_{rot}(e, N_2) = 4.65 \times 10^{-39} N_e N_{N_2} \left(\frac{T_e - T_n}{T_e^{\frac{1}{2}}} \right) \qquad (B.9).$$

Using the theory of *Mentzoni and Row* [1963], *Dalgarno et al.* [1968] derive a formula for the cooling rate due to rotational excitation of O_2 by electrons:

$$L_{rot}(e, O_2) = 1.11 \times 10^{-38} N_e N_{O_2} \left(\frac{T_e - T_n}{T_e^{\frac{1}{2}}} \right) \qquad (B.10).$$

The results of different measurements indicate that $L_{rot}(e, O_2)$ could be more than an order of magnitude smaller than given here [*Mentzoni*, 1977], in which case the cooling would be due essentially only to rotational excitation of N_2. The lower cooling rate would result in a larger heated T_e under equilibrium conditions.

---

* The values of L_{elast} actually given by *Banks* [1966] and frequently quoted in the literature [e.g., *Rees and Roble*, 1975; *Schunk and Nagy*, 1978; *Rees*, 1989, p. 284] are too large by a factor of 1.5, as mentioned in the note by *Rees and Roble* [1975] calling attention to this error.

B.1.3 Vibrational Excitation

Stubbe and Varnum [1972] give the following expression for the total cooling rate by vibrational excitation of N_2 for $T_e < 10^4$ K:

$$L_{\text{vib}}(e, N_2) = 4.79 \times 10^{-37} N_e N_{N_2} \exp\left(f\frac{T_e - 2000}{2000 T_e}\right)\left[\exp\left(-g\frac{T_e - T_n}{T_n T_e}\right) - 1\right] \quad \text{(B.11)}$$

where

$$f = 1.06 \times 10^4 + 7.51 \times 10^3 \tanh\left[0.0011\left(T_e - 1800\right)\right]$$

and

$$g = 3300 + 1.233\left(T_e - 1000\right) - 2.056 \times 10^{-4}\left(T_e - 1000\right)\left(T_e - 4000\right).$$

The total cooling rate by vibrational excitation of O_2 is given by *Prasad and Furman* [1973]:

$$L_{\text{vib}}(e, O_2) = 8.32 \times 10^{-38} N_e N_{O_2} \exp\left(f\frac{T_e - 700}{700 T_e}\right)\left[\exp\left(-2770\frac{T_e - T_n}{T_n T_e}\right) - 1\right]$$
$$\text{(B.12)}$$

where

$$f = 3300 - 839 \sin\left[0.000191\left(T_e - 2700\right)\right].$$

The normalized cooling rates

$$R(e, N_2) = \frac{L(e, N_2)}{N_e N_{N_2}}$$
$$R(e, O_2) = \frac{L(e, O_2)}{N_e N_{O_2}} \qquad \text{(B.13)}$$

for elastic collisions, rotational excitation, and vibrational excitation are shown in Figure B.1 as functions of $T_e \geq T_n$ for $T_n = 200$ K.
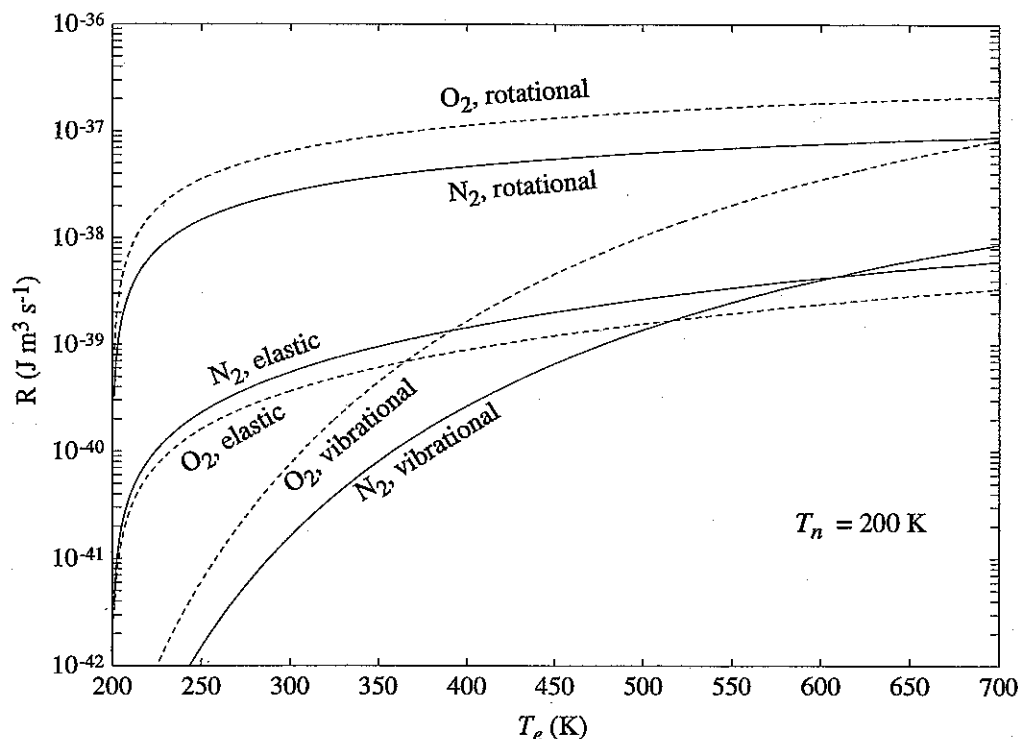
Figure B.1. Normalized rates of electron cooling through elastic and inelastic collisions with N_2 and O_2. Normalized electron cooling rates $R(e, N_2) = L(e, N_2) \left(N_e N_{N_2} \right)^{-1}$ and $R(e, O_2) = L(e, O_2) \left(N_e N_{O_2} \right)^{-1}$ due to collisions with molecular nitrogen (N_2) and oxygen (O_2). Rate curves are shown as a function of T_n for elastic collisions and for inelastic collisions resulting in rotational and vibrational excitation of N_2 and O_2, assuming $T_n = 200$ K.

B.2 CHEMISTRY OF THE NIGHTTIME D REGION

The four-species model of *Glukhov et al.* [1992] has been used in this work (Figure 6.1a), with the inclusion of the effect of different electron and neutral temperatures. This relatively simple model is appropriate since the interest here is primarily in the response of electron number density (N_e) to heating. Before water cluster ions (N_x^+) were discovered in the mesosphere [*Narcisi and Bailey*, 1965], similar three-species models were in use, that is, equations (6.1), (6.2), and (6.3) without the terms involving water cluster ions [e.g., *Bailey*, 1959; *Watt*, 1967, p. 658]. The six-species model of *Mitra and Rowe* [1972], used subsequently by, among others, *Rowe et al.* [1974] and *Tomko et al.* [1980], replaces the lumped primary positive ions N^+ with the individual species NO^+, O_2^+, and O_4^+ and separates O_2^- from the lumped negative ions N^-.

B.2.1   Three-Body Electron Attachment to O_2

At electron energies below 1 eV, electron attachment to O_2 is a three-body process represented overall by the reaction

$$e + O_2 + M \rightarrow O_2^- + M \qquad (B.14)$$

where in the Earth's atmosphere M is most likely to be either O_2 or N_2 [*Chanin et al.*, 1962]. The two-body dissociative attachment process

$$e + O_2 \rightarrow O^- + O \qquad (B.15)$$

occurs at higher electron energies, with a resonance in its cross section at 6.7 eV [*Schulz*, 1962]. It is important only for ionospheric heating at much higher power levels than those considered in this dissertation [e.g., *Taranenko et al.*, 1993a] and therefore will not be discussed further.

Attachment of electrons to O_2 was recognized as an important reaction in ionospheric chemistry as early as 1937 [*Bates*, 1993].† A common form of the three-body attachment coefficient k_{O_2}, based on the laboratory work of *Chanin et al.* [1962], is

$$k_{O_2} = 1.4 \times 10^{-41} \left(\frac{300}{T_n} \right) \exp \left(-\frac{600}{T_n} \right) \quad (m^6 \ s^{-1}) \qquad (B.16)$$

where $T_e = T_n$. This form has been used in many studies [e.g. *Rowe et al.*, 1974; *Gurevich*, 1978, p. 114; *Glukhov et al.*, 1992]. Another form of this coefficient was given by *Truby* [1972], valid for $100 \le T_n \le 600$ K:

$$k_{O_2} = 4 \times 10^{-42} \exp \left(-\frac{196}{T_n} \right) \quad (m^6 \ s^{-1}) \qquad (B.17).$$

Using data of *Chanin et al.* [1962], *Tomko et al.* [1980] modified equation (B.15) to hold for nonequilibrium conditions ($T_e > T_n$, $195 \le T_n \le 600$ K):

$$k_{O_2} = 1.4 \times 10^{-41} \left(\frac{300}{T_e} \right) \exp \left(-\frac{600}{T_n} \right) \exp \left(\frac{700}{T_n} - \frac{700}{T_e} \right) \quad (m^6 \ s^{-1}) \qquad (B.18).$$

---

† This paper gives a fascinating history of the early work on ionospheric chemistry, in which Bates played a prominent role.

The more complicated expression used in this dissertation (Table 6.1) was derived by Tomko [1981, p. 163] based on the measurements of Chanin et al. [1962], Truby [1972], and Spence and Schulz [1972]. These curves for k_{O_2} are plotted in Figure B.2. More recent measurements of k_{O_2} for thermal electrons ($T_e = T_n$) are consistent with the above curves for temperatures found in the mesosphere but indicate that k_{O_2} decreases by a factor of two between 100 and 150 K [Shimamori and Fessenden, 1981].
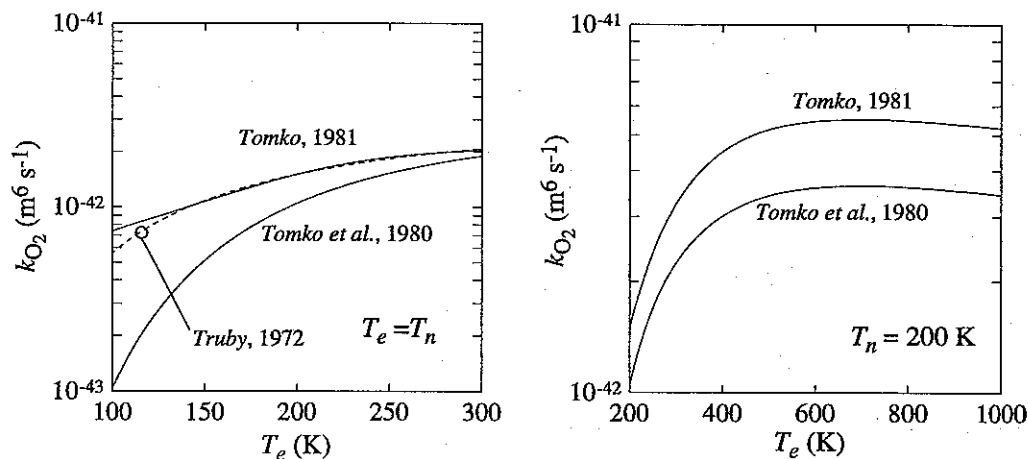
Figure B.2. Coefficient of three-body attachment of electrons to O_2. (a) k_{O_2} for $T_n = T_e$, from Tomko et al. [1980], Truby [1972], and Tomko [1981, p. 163]. (b) k_{O_2} for $T_n = 200K$ under conditions of electron heating ($T_e > T_n$), from Tomko et al. [1980] and Tomko [1981, p. 163].

The case in which the third body (M) is N_2 is less important since $k_{N_2} \gg k_{O_2}$. It has been neglected in some studies [Tomko et al., 1980; Tomko, 1981]. The value commonly used is $k_{N_2} = 10^{-43}$ m^6 s^{-1} [Rowe et al., 1974; Gurevich, 1978, p. 114; Glukhov et al., 1992]. Recent measurements of k_{N_2} for thermal electrons ($T_e = T_n$) indicate that k_{N_2}

increases from 10^{-43} m^6 s^{-1} at 300 K to 3×10^{-43} m^6 s^{-1} at 150 K [*Shimamori and Fessenden*, 1981].

B.2.2 Collisional Detachment

The production of O_2^- through the relatively well-understood process of three-body electron attachment led researchers to assume initially that the dominant negative ion is O_2^- [*Bailey*, 1959]. In the absence of photodetachment, the dominant detachment reaction, which involves collisions between negative ions and neutrals, was assumed to be

$$O_2^- + O \rightarrow O_3 + e \qquad\qquad (B.19).$$

Using a three-species model (i.e., equations (6.1), (6.2), and (6.3) without the terms involving N_x^+) *Bailey* [1959] derived a collisional detachment rate $\gamma = 2.4 \times 10^{-23} N_n$ s^{-1} that was later refined by *Bailey and Branscomb* [1960] to be $\gamma = 2 \times 10^{-23} N_n$ s^{-1}. However, the collision detachment coefficient for equation (B.18) was measured in the laboratory by *Phelps and Pack* [1961] to be 4×10^{-26} m^3 s^{-1} at 230 K, almost three orders of magnitude lower than the rate of *Bailey and Branscomb* [1960]. Subsequent research has revealed a complex chain of reactions (see the review by *Reid* [1976]). Despite these advances the uncertainties involved in a more complex model indicate that an "effective" detachment rate γ can be used in the four-species model of nighttime D region chemistry, with the realization that it is not identified with a single physical process. *Ivanov-Kholodnyi and Nikol'skii* [1972, p. 205] suggest that the rate of *Bailey* [1959] effectively represents the entire system of reactions involving collisional electron detachment from O_2^- ions. Following *Glukhov et al.* [1992] we adopt in the present work a detachment rate $\gamma = 3 \times 10^{-23} N_n$ s^{-1}.

B.2.3 Dissociative Recombination

The coefficient of dissociative recombination with cluster ions (α_d^c) is a function of T_n and the relative abundances of the different cluster ion species; however, for simplicity, we adopt a single ambient $\alpha_d^c = 3 \times 10^{-12}$ m^3 s^{-1} [*Reid*, 1977], with $\alpha_d^c \propto (T_n/T_e)^b$, where $0 \le b \le 0.08$ [*Huang et al.*, 1978; *Tomko*, 1981]. Various expressions given in the literature for α_{NO^+} and $\alpha_{O_2^+}$ (valid for thermal equilibrium conditions, $T_n = T_e$) are listed in Table B.1. In general they are consistent with the expressions of *Tomko et al.* [1980] that are used in this dissertation (Table 6.1).

Table B.1
Dissociative recombination with primary ions

$$\alpha_{NO^+} = a \left(300/T_e \right)^b \quad m^6 \ s^{-1} \quad (B.)$$

a	b	References
5×10^{-13}	1.0	*Rowe et al.,* 1974
5×10^{-13}	1.2	*Gurevich,* 1978, p. 98
4.2×10^{-13}	0.85	*Rees,* 1989, Table A.5.1
4.2×10^{-13}	0.75	*Dulaney et al.,* 1987
4.3×10^{-13}	0.7	*Davidson and Hobson,* 1987

$$\alpha_{O_2^+} = a \left(300/T_e \right)^b \quad m^6 \ s^{-1} \quad (B.)$$

a	b	References
2.2×10^{-13}	0.7	*Rowe et al.,* 1974; *Gurevich,* 1978, p. 98
1.9×10^{-13}	0.5	*Rees,* 1989, Table A.5.1
1.6×10^{-13}	0.55	*Bates,* 1990

Bibliography

Antenna Standards Committee of the IEEE Antennas and Propagation Group, *IEEE Standard Definitions of Terms for Antennas*, IEEE Std 145-1983, The Institute of Electrical and Electronics Engineers, New York, 1983.

Appleton, E. V., The existence of more than one ionised layer in the upper atmosphere, *Nature, 130*, 330, 1927.

Appleton, E. V., On some measurements of the equivalent height of the atmospheric ionised layer, *Proc. R. Soc. Lond. A, 126*, 542–569, 1930.

Appleton, E. V., Wireless studies of the ionosphere, *J. I. E. E., 71*, 642–650, 1932.

Armstrong, W. C., Recent advances from studies of the Trimpi effect, *Antarctic J., 18*, 281–283, 1983.

Bailey, D. K., Abnormal ionization in the lower ionosphere associated with cosmic-ray flux enhancements, *Proc. I.R.E., 47*, 255–266, 1959.

Bailey, D. K., and L. M. Branscomb, Rate coefficient for O_2^- collisional detachment, *Bull. Am. Phys. Soc., 5*, 123, 1960.

Bailey, V. A., and D. F. Martyn, The influence of electric waves on the ionosphere, *Phil. Mag., 18*, 369–386, 1934.

Banks, P., Collision frequencies and energy transfer: electrons, *Planet. Space Sci., 14*, 1085–1103, 1966.

Barr, R., and P. Stubbe, VLF heating of the lower ionosphere: variation with magnetic latitude and electron density profile, *Geophys. Res. Lett., 19*, 1747–1750, 1992.

Barr, R., and P. Stubbe, ELF harmonic radiation from the Tromsø heating facility, *Geophys. Res. Lett., 20*, 2243–2246, 1993.

Barr, R., M. T. Rietveld, H. Kopka, and P. Stubbe, Effect of a heated patch of auroral ionosphere on VLF radio wave propagation, *Nature, 309*, 534–536, 1984.

185

Barr, R., M. T. Rietveld, P. Stubbe, and H. Kopka, The diffraction of VLF radio waves by a patch of
        ionosphere illuminated by a powerful HF transmitter, *J. Geophys. Res., 90*, 2861–2875, 1985.

Bates, D. R., Oxygen green and red line emissions and O_2^+ dissociative recombination, *Planet. Space Sci.,*
        38, 889–902, 1990.

Bates, D. R., The ionosphere, in *Relating Geophysical Structures and Processes: the Jeffreys Volume,*
        pp. 11–18, Geophysical Monograph 76, IUGG Volume 16, 1993.

Bell, T. F., U. S. Inan, M. Danielson, and S. Cummer, VLF signatures of ionospheric heating by HIPAS,
        in *1993 Ionospheric Effects Symposium*, edited by J. M. Goodman, pp. 622–628, 1993.

Belrose, J. S., Introduction, in *ELF/VLF/LF Radio Propagation and Systems Aspects*, pp. I-1–I-12, AGARD
        Conference Proceedings No. 529, 1993.

Belrose, J. S., and M. J. Burke, Study of the lower ionosphere using partial reflection 1. Experimental
        technique and method of analysis, *J. Geophys. Res., 69*, 2799–2818, 1964.

Bickel, J. E., J. A. Ferguson, and G. V. Stanley, Experimental observation of magnetic field effects on VLF
        propagation at night, *Radio Sci., 5*, 19–25, 1970.

Booker, H. G., Developments in the theory of radio propagation, 1900–1950, *Radio Sci., 10*, 665–668,
        1975.

Bracewell, R. N., and T. W. Straker, The study of solar flares by means of very long radio waves, *Mon.*
        Not. R. Astr. Soc., 109, 28–45, 1949.

Bracewell, R. N., K. G. Budden, J. A. Ratcliffe, T. W. Straker, and K. Weekes, The ionospheric propagation
        of low- and very-low-frequency radio waves over distances less than 1000 km, *P. I. E. E., 98*, III,
        221–236, 1951.

Budden, K. G., *The Wave-Guide Mode Theory of Wave Propagation*, 325 pp., Prentice-Hall, Englewood
        Cliffs, N. J., 1961.

Budden, K. G., The influence of the earth's magnetic field on radio propagation by wave-guide modes,
        Proc. R. Soc. Lond. A, 265, 538–553, 1962.

Budden, K. G., Effect of electron collisions on the formulas of magneto-ionic theory, *Radio Sci., 69D*,
        191–211, 1965.

Budden, K. G., *The Propagation of Radio Waves: the Theory of Radio Waves of Low Power in the*
        Ionosphere and Magnetosphere, 669 pp., Cambridge University Press, Cambridge, 1985.

Burgess, W. C., and U. S. Inan, The role of ducted whistlers in the precipitation loss and equilibrium flux
        of radiation belt electrons, *J. Geophys. Res., 98*, 15,643–15,665, 1993.

Burke, W. J., Early Trimpi events from lightning-induced electric field in the ionosphere: an alternative
        explanation, *J. Atmos. Terr. Phys., 54*, 205–208, 1992.

Carter, P. S., and H. H. Beverage, Early history of the antennas and propagation field until the end of World War I, part I—antennas, *Proc. I.R.E., 50*, 679–682, 1962.

Chanin, L. M., A. V. Phelps, and M. A. Biondi, Measurements of the attachment of low-energy electrons to oxygen molecules, *Phys. Rev., 128*, 219–230, 1962.

Chapman, S., and T. G. Cowling, *The Mathematical Theory of Non-Uniform Gases*, Third Edition, 423 pp., Cambridge University Press, Cambridge, 1970.

Chilton, C. J., VLF phase perturbation associated with meteor shower ionization, *J. Geophys. Res., 66*, 379–383, 1961.

Chmyrev, V. M., V. K. Roldugin, I. A. Zhulin, M. M. Mogilevskii, V. I. Di, V. K. Koshelevskii, V. A. Bushmarin, and O. M. Raspopov, Artificial injection of very low frequency (VLF) waves into the ionosphere and the magnetosphere of the earth, *JETP Lett., 23*, 409–411, 1976.

Coffey, H. E., Geomagnetic and solar data, *J. Geophys. Res., 93*, 1028, 1988*a*.

Coffey, H. E., Geomagnetic and solar data, *J. Geophys. Res., 93*, 2016, 1988*b*.

Coffey, H. E., Geomagnetic and solar data, *J. Geophys. Res., 95*, 10,723, 1990.

Coffey, H. E., Geomagnetic and solar data, *J. Geophys. Res., 98*, 7687–7693, 1993.

Dalgarno, A., M. B. McElroy, M. H. Rees, and J. C. G. Walker, *Planet. Space Sci., 16*, The effect of oxygen cooling on ionospheric electron temperatures, 1371–1380, 1968.

Danilov, A. D., and V. K. Semenov, Relative ion composition model at midlatitudes, *J. Atmos. Terr. Phys., 40*, 1093–1102, 1978.

Davidson, D., and R. Hobson, The shock tube determination of the dissociative recombination rate of NO^+, *J. Phys. B: At. Mol. Phys., 20*, 5753–5756, 1987.

Davies, K., *Ionospheric Radio*, 580 pp., Peter Peregrinus Ltd., London, 1990.

Deeks, D. G., *D*-region electron distributions in middle latitudes deduced from the reflexion of long radio waves, *Proc. R. Soc. Lond. A, 291*, 413–437, 1966*a*.

Deeks, D. G., Generalised full wave theory for energy-dependent collision frequencies, *J. Atmos. Terr. Phys., 28*, 839–846, 1966*b*.

De Forest, L., Recent developments in the work of the Federal Telegraph Company, *Proc. I.R.E., 1*, 37–57, 1913.

Dowden, R. L., and C. D. D. Adams, Location of lightning-induced electron precipitation from measurement of VLF phase and amplitude perturbations on spaced antennas and on two frequencies, *J. Geophys. Res., 95*, 4135–4145, 1990.

Dowden, R. L., and C. D. D. Adams, VLF versus MF heating of the lower ionosphere, *J. Geophys. Res., 96*, 14,179–14,182, 1991.

Dowden, R. L., C. D. D. Adams, M. T. Rietveld, P. Stubbe, and H. Kopka, Phase and amplitude perturbations on subionospheric signals produced by a moving patch of artificially heated ionosphere, *J. Geophys. Res., 96*, 239–248, 1991.

Druyvesteyn, J., Bemerkungen zu zwei früheren Arbeiten über die Elektronendiffusion, *Physica, 1*, 1003–1006, 1934.

Dulaney, J., M. Biondi, and R. Johnsen, Electron temperature dependence of the recombination of electrons with NO$^+$ ions, *Phys. Rev. A, 36*, 1342–1350, 1987.

Eather, R. H., *Majestic Lights: The Aurora in Science, History, and the Arts*, 323 pp., American Geophysical Union, Washington, D.C., 1980.

Fejer, J. A., Radio wave probing of the lower ionosphere by cross-modulation techniques, *J. Atmos. Terr. Phys., 32*, 597–607, 1970.

Ferguson, J. A., F. P. Snyder, D. G. Morfitt, and C. H. Shellman, Long-wave propagation capability and documentation, *Tech. Doc. 1518*, Naval Ocean Systems Center, San Diego, 1989.

Fishman, G. J., and U. S. Inan, Observation of an ionospheric disturbance caused by a gamma-ray burst, *Nature, 331*, 418–420, 1988.

Forbes, J. M., LTCS: the lower thermosphere coupling study of the CEDAR and WITS programs, an attempt to better understand the "ignorosphere," *Eos Trans. AGU, 70*, 905, 1989.

Fraser-Smith, A. C., Effects of man on geomagnetic activity and pulsations, *Adv. Space Res., 1*, 455–466, 1981.

Fuller, L. F., Continuous waves in long distance radio telegraphy, *Proc. A.I.E.E., 34*, 567–585, 1915; abstract in *The Electrician, 75*, 154–157, 1915.

Fuller, L. F., The design of Poulsen arc converters for radio telegraphy, *Proc. I.R.E., 7*, 449–497, 1919.

Galejs, J., *Terrestrial Propagation of Long Electromagnetic Waves*, 362 pp., Pergamon Press, Oxford, 1972a.

Galejs, J., Ionospheric interaction of VLF radio waves, *J. Atmos. Terr. Phys., 34*, 421–436, 1972b.

Glukhov, V. S., V. P. Pasko, and U. S. Inan, Relaxation of transient lower ionospheric disturbances caused by lightning-whistler-induced electron precipitation bursts, *J. Geophys. Res., 97*, 16,971–16,979, 1992.

Goldberg, R. A., Electrodynamics of the high-latitude mesosphere, *J. Geophys. Res., 94*, 14,661–14,672, 1989.

Gordon, W. E., and H. C. Carlson, Arecibo heating experiments, *Radio Sci., 9*, 1041–1047, 1974.

Green, A. L., Early history of the ionosphere, *A. W. A. Tech. Rev., 7*, 175–228, 1946; excerpts, *J. Atmos. Terr. Phys., 36*, 2159–2166, 1974.

Gurevich, A. V., *Nonlinear Phenomena in the Ionosphere*, 372 pp., Springer-Verlag, New York, 1978.

Hara, E. H., Approximations to the semiconductor integrals $C_p(x)$ and $D_p(x)$ for use with the generalized Appleton-Hartree magnetoionic formulas, *J. Geophys. Res.*, *68*, 4388–4389, 1963.

Harwood, J., Spaced-receiver experiments on radio waves of 19-km wavelength, *Proc. I.E.E.*, *101*, IV, 183–186, 1954.

Hauser, J. P., W. E. Garner, and F. J. Rhoads, A VLF effective ground conductivity map of Canada and Greenland with revisions derived from propagation data, *NRL Report 6893*, 1969.

Hedin, A. E., MSIS-86 thermospheric model, *J. Geophys. Res.*, *92*, 4649–4662, 1987.

Helliwell, R. A., J. P. Katsufrakis, and M. L. Trimpi, Whistler-induced amplitude perturbation in VLF propagation, *J. Geophys. Res.*, *78*, 4679–4688, 1973.

Huang, C-M., M. Whitaker, M. A. Biondi, and R. Johnsen, Electron-temperature dependence of recombination of electrons with $H_3O^+ \cdot (H_2O)_n$ - series ions, *Phys. Rev. A*, *18*, 64–67, 1978.

Huxley, L. G. H., Experimental and theoretical studies of the behaviour of slow electrons in air. II. Ionospheric and other applications, *Proc. R. Soc. Lond. A*, *196*, 427–435, 1949.

Huxley, L. G. H., A discussion of the motion in nitrogen of free electrons with small energies with reference to the ionosphere, *J. Atmos. Terr. Phys.*, *16*, 46–58, 1959.

Huxley, L. G. H., and J. A. Ratcliffe, A survey of ionospheric cross-modulation (wave-interaction or Luxembourg effect), *Proc. I. E. E.*, *96*, III, 433–440, 1949.

Huxley, L. G. H., and A. A. Zaazou, Experimental and theoretical studies of the behaviour of slow electrons in air. I, *Proc. R. Soc. Lond. A*, *196*, 402–426, 1949.

Imhof, W. L., J. B. Reagan, H. D. Voss, E. E. Gaines, D. W. Datlowe, J. Mobilia, R. A. Helliwell, U. S. Inan, J. Katsufrakis, and R. G. Joiner, Direct observation of radiation belt electrons precipitated by the controlled injection of VLF signals from a ground-based transmitter, *Geophys. Res. Lett.*, *10*, 361–364, 1983*a*.

Imhof, W. L., J. B. Reagan, H. D. Voss, E. E. Gaines, D. W. Datlowe, J. Mobilia, R. A. Helliwell, U. S. Inan, J. Katsufrakis, and R. G. Joiner, The modulated precipitation of radiation belt electrons by controlled signals from VLF transmitters, *Geophys. Res. Lett.*, *10*, 615–618, 1983*b*.

Inan, U. S., VLF heating of the lower ionosphere, *Geophys. Res. Lett.*, *17*, 729–732, 1990*a*.

Inan, U. S., Modification of the lower ionosphere in lightning-induced electron precipitation events and through VLF heating, in *Ionospheric Modification and its Potential to Enhance or Degrade the Performance of Military Systems*, pp. 29-1–29-12, AGARD Conference Proceedings No. 485, 1990*b*.

Inan, U. S., and J. V. Rodriguez, Lightning-induced effects on VLF/LF radio propagation, in *ELF/VLF/LF Radio Propagation and Systems Aspects*, pp. 9-1–9-10, AGARD Conference Proceedings No. 529, 1993.

Inan, U. S., H. C. Chang, and R. A. Helliwell, Electron precipitation zones around major ground-based VLF signal sources, *J. Geophys. Res.*, *89*, 2891–2906, 1984.

Inan, U. S., H. C. Chang, R. A. Helliwell, W. L. Imhof, J. B. Reagan, and M. Walt, Precipitation of radiation belt electrons by man-made waves: a comparison between theory and measurement, *J. Geophys. Res., 90*, 359–369, 1985.

Inan, U. S., D. C. Shafer, W. Y. Yip, and R. E. Orville, Subionospheric VLF signatures of nighttime *D* region perturbations in the vicinity of lightning discharges, *J. Geophys. Res., 93*, 11,455–11,472, 1988.

Inan, U. S., F. A. Knifsend, and J. Oh, Subionospheric VLF "imaging" of lightning-induced electron precipitation from the magnetosphere, *J. Geophys. Res., 95*, 17,217–17,231, 1990.

Inan, U. S., T. F. Bell, and J. V. Rodriguez, Heating and ionization of the lower ionosphere by lightning, *Geophys. Res. Lett., 18*, 705–708, 1991.

Inan, U. S., J. V. Rodriguez, S. Lev-Tov, and J. Oh, Ionospheric modification with a VLF transmitter, *Geophys. Res. Lett., 19*, 2071–2074, 1992.

Inan, U. S., J. V. Rodriguez, and V. P. Idone, VLF signatures of lightning-induced heating and ionization of the nighttime *D* region, *Geophys. Res. Lett., 20*, 2355–2358, 1993.

Ivanov-Kholodnyi, G. S., and G. M. Nikol'skii, *The Sun and the Ionosphere*, 366 pp., Israel Program for Scientific Translations, Jerusalem, 1972.

Jordan, E. C., and K. G. Balmain, *Electromagnetic Waves and Radiating Systems*, Second Edition, 753 pp., 1968.

Jones, T. B., The physics of ground based heating, in *Ionospheric Modification and its Potential to Enhance or Degrade the Performance of Military Systems*, pp. 1A1–1A9, AGARD Conference Proceedings No. 485, 1990.

Jones, T. B., K. Davies, and B. Wieder, Observations of D-region modifications at low and very low frequencies, *Nature, 238*, 33–34, 1972.

Kane, J. A., Re-evaluation of ionospheric electron densities and collision frequencies derived from rocket measurements of refractive index and attenuation, *J. Atmos. Terr. Phys., 23*, 338–347, 1962.

Kikuchi, T., and D. S. Evans, Quantitative study of substorm-associated VLF phase anomalies and precipitating energetic electrons on November 13, 1979, *J. Geophys. Res., 88*, 871–880, 1983.

Kopytenko, Yu. A., O. A. Molchanov, M. M. Mogilevskii, V. A. Bushmarin, V. G. Eremeev, A. A. Ivanov, V. V. Lizunov, Yu. M. Markeeva, A. Yu. Shchekotov, and M. M. Pogrebnikov, Demodulation of high-power low-frequency waves in the subauroral ionosphere in the range of geomagnetic pulsations, *JETP Lett., 25*, 218–221, 1977.

Kossey, P. A., J. P. Turtle, R. P. Pagliarulo, W. I. Klemetti, and J. E. Rasmussen, VLF reflection properties of the normal and disturbed polar ionosphere in northern Greenland, *Radio Sci., 18*, 907–916, 1983.

Kraus, J. D., *Antennas*, Second Edition, 892 pp., McGraw-Hill, New York, 1988.

Langel, R. A., IGRF, 1991 revision, *Eos Trans. AGU, 73*, 182, 1992.

Lauber, W. R., and J. M. Bertrand, VLF propagation measurements in the Canadian Arctic, in *ELF/VLF/LF Radio Propagation and Systems Aspects*, pp. 5-1–5-12, AGARD Conference Proceedings No. 529, 1993.

Lodge, O., Mr. Marconi's results in day and night wireless telegraphy, *Nature, 66*, 222, 1902.

Lohrey, B., and A. B. Kaiser, Whistler-induced anomalies in VLF propagation, *J. Geophys. Res., 84*, 5122–5130, 1979.

Love, A. E. H., The transmission of electric waves over the surface of the Earth, *Phil. Trans. R. Soc. Lond. A., 215*, 105–131, 1915.

Maslin, N. M., Theory of energy flux and polarization changes of a radio wave with two magnetoionic components undergoing self demodulation in the ionosphere, *Proc. R. Soc. Lond. A, 341*, 361–381, 1974.

Maslin, N. M., Theory of the modifications imposed on the ionospheric plasma by a powerful radio wave reflected in the D or E region, *Proc. R. Soc. Lond. A, 343*, 109–131, 1975.

Mayaud, P. N., *Derivation, Meaning, and Use of Geomagnetic Indices*, Geophysical Monograph 22, 154 pp., American Geophysical Union, Washington, D.C., 1980.

Mentzoni, M., Ionospheric G factor, *J. Geophys. Res., 73*, 4444–4445, 1968.

Mentzoni, M., Thermal electron collisions and energy transter in atmospheric gases, in *Dynamical and Chemical Coupling*, edited by B. Grandal and J. A. Holtet, pp. 175–183, D. Reidel, Dordrecht, 1977.

Mentzoni, M. H., and R. V. Row, Rotational excitation and electron relaxation in nitrogen, *Phys. Rev., 130*, 2312–2316, 1963.

Mitra, A. P., and J. N. Rowe, Ionospheric effects of solar flares - VI. Changes in D-region ion chemistry during solar flares, *J. Atmos. Terr. Phys., 34*, 795–806, 1972.

Molchanov, O. A., A. Ye. Reznikov, and D. S. Fligel', Self-interaction of strong low-frequency waves in the Earth's ionospheric plasma, *Geomag. Aeron., 16*, 580–581, 1977.

Muller, R. S., and T. I. Kamins, *Device Electronics for Integrated Circuits*, Second Edition, 524 pp., John Wiley & Sons, New York, 1986.

Narcisi, R. S., and A. D. Bailey, Mass spectrometric measurements of positive ions at altitudes from 64 to 112 kilometers, *J. Geophys. Res., 70*, 3687–3700, 1965.

National Geographic Society (U. S.), Cartographic Division, *The World—Political*, National Geographic Society, Washington, D.C., February 1994.

National Oceanic and Atmospheric Administration, National Aeronautics and Space Administration, and the U. S. Air Force, *U. S. Standard Atmosphere 1976*, U. S. Government Printing Office, Washington, D. C., 1976.

Naval Ocean Systems Center, *Fixed VLF/LF Data Base*, Version 3.0, October 18, 1989.

Pappert, R. A., A numerical study of VLF mode structure and polarization below an anisotropic ionosphere, *Radio Sci., 3*, 219–233, 1968.

Pappert, R. A., and J. E. Bickel, Vertical and horizontal VLF fields excited by dipoles of arbitrary orientation and elevation, *Radio Sci., 5*, 1445–1452, 1970.

Pappert, R. A., and J. A. Ferguson, VLF/LF mode conversion model calculations for air to air transmissions in the earth-ionosphere waveguide, *Radio Sci., 21*, 551–558, 1986.

Pappert, R. A., and D. G. Morfitt, Theoretical and experimental sunrise mode conversion results at VLF, *Radio Sci., 10*, 537–546, 1975.

Pappert, R. A., and F. P. Snyder, Some results of a mode-conversion program for VLF, *Radio Sci., 7*, 913–923, 1972.

Pappert, R. A., E. E. Gossard, and I. J. Rothmuller, A numerical investigation of classical approximations used in VLF propagation, *Radio Sci., 2*, 387–400, 1967.

Phelps, A. V., and J. L. Pack, Electron collision frequencies in nitrogen and in the lower ionosphere, *Phys. Rev. Lett., 3*, 340–342, 1959.

Phelps, A. V., and J. L. Pack, Collisional detachment in molecular oxygen, *Phys. Rev. Lett., 6*, 111–113, 1961.

Philbrick, C. R., J. Barnett, R. Gerndt, D. Offermann, W. R. Pendleton, Jr., P. Schlyter, F. J. Schmidlin, and G. Witt, Temperature measurements during the CAMP program, *Adv. Space Res., 4*, 153–156, 1984.

Pierce, J. A., Intercontinental frequency comparison by very-low-frequency radio transmission, *Proc. I.R.E., 45*, 794–803, 1957.

Pitteway, M. L. V., The numerical calculation of wave-fields, reflexion coefficients and polarizations for long radio waes in the lower ionosphere. I., *Phil. Trans. R. Soc. Lond. A, 257*, 219–241, 1965.

Potemra, T. A., and T. J. Rosenberg, VLF propagation disturbances and electron precipitation at mid-latitudes, *J. Geophys. Res., 78*, 1572–1580, 1973.

Potemra, T. A., and A. J. Zmuda, Precipitating energetic electrons as an ionization source in the midlatitude nighttime *D* region, *J. Geophys. Res., 75*, 7161–7167, 1970.

Poulsen, W. L., Modeling of very low frequency wave propagation and scattering within the Earth-ionosphere waveguide in the presence of lower ionospheric disturbances, Ph.D. thesis, Stanford University, Stanford, Calif., 1991.

Poulsen, W. L., U. S. Inan, and T. F. Bell, Three-dimensional modeling of subionospheric VLF propagation in the presence of localized D region perturbations associated with lightning, *J. Geophys. Res., 95,* 2355–2366, 1990.

Poulsen, W. L., U. S. Inan, and T. F. Bell, A multiple-mode three-dimensional model of VLF propagation in the Earth-ionosphere waveguide in the presence of localized D region disturbances, *J. Geophys. Res., 98,* 1705–1717, 1993a.

Poulsen, W. L., T. F. Bell, and U. S. Inan, The scattering of VLF waves by localized ionospheric disturbances produced by lightning-induced electron precipitation, *J. Geophys. Res., 98,* 15,553–15,559, 1993b.

Prasad, S. S., and D. R. Furman, Electron cooling by molecular oxygen, *J. Geophys. Res., 78,* 6701–6707, 1973.

Press, W. H., B. P. Flannery, S. A. Teukolsky, and W. T. Vetterling, *Numerical Recipes in C: the Art of Scientific Computing,* 735 pp., Cambridge University Press, New York, 1988.

Ramo, S., J. R. Whinnery, and T. Van Duzer, *Fields and Waves in Communication Electronics,* 2nd ed., 817 pp., John Wiley & Sons, New York, 1984.

Rasmussen, J. E., P. A. Kossey, and E. A. Lewis, Evidence of an ionospheric reflecting layer below the classical D region, *J. Geophys. Res., 85,* 3037–3044, 1980.

Ratcliffe, J. A., *The Magneto-Ionic Theory and its Applications to the Ionosphere,* 206 pp., Cambridge University Press, Cambridge, 1959.

Ratcliffe, J. A., *An Introduction to the Ionosphere and Magnetosphere,* 256 pp., Cambridge University Press, Cambridge, 1972.

Ratcliffe, J. A., Scientists' reactions to Marconi's transatlantic radio experiment, *Proc. I.E.E., 121,* 1033–1038, 1974.

Ratcliffe, J. A., and I. J. Shaw, A study of the interaction of radio waves, *Proc. R. Soc. Lond. A, 193,* 311–343, 1948.

Rawer, K., D. Bilitza, and S. Ramakrishnan, Goals and status of the International Reference Ionosphere, *Rev. Geophys. Space. Phys., 16,* 177–181, 1978.

Reagan, J. B., R. E. Meyerott, R. C. Gunton, W. L. Imhof, E. E. Gaines, and T. R. Larsen, Modeling of the ambient and disturbed ionospheric media pertinent to ELF/VLF propagation, in *Medium, Long, and Very Long Wave Propagation (at Frequencies Less Than 3000 kHz),* edited by J. S. Belrose, pp. 33-1–33-10, AGARD Conference Proceedings No. 305, 1981.

Rees, M. H., *Physics and Chemistry of the Upper Atmosphere,* 289 pp., Cambridge University Press, 1989.

Rees, M. H., and R. G. Roble, Observations and theory of the formation of stable auroral red arcs, *Rev. Geophys. Space Phys., 13,* 201–242, 1975.

Reid, G. C., Ion chemistry in the D region, *Adv. Atom. Mol. Phys., 12,* 375–413, 1976.

Reid, G. C., The production of water-cluster positive ions in the quiet daytime D region, *Planet. Space Sci., 25*, 275–290, 1977.

Richter, J. H., Application of conformal mapping to Earth-flattening procedures in radio propagation problems, *Radio Sci., 1*, 1435–1438, 1966.

Rietveld, M. T., H. Kopka, and P. Stubbe, D-region characteristics deduced from pulsed ionospheric heating under auroral electrojet conditions, *J. Atmos. Terr. Phys., 48*, 311–326, 1986.

Robinson, T. R., Disturbing effects of radio, *Nature, 346*, 612–613, 1990.

Rodriguez, J. V., and U. S. Inan, Electron density changes in the nighttime D region due to heating by very-low-frequency transmitters, *Geophys. Res. Lett., 21*, 93–96, 1994.

Rodriguez, J. V., U. S. Inan, and T. F. Bell, D-region disturbances caused by electromagnetic pulses from lightning, *Geophys. Res. Lett., 19*, 2067–2070, 1992.

Roederer, J. G., *Dynamics of Geomagnetically Trapped Radiation*, 166 pp., Springer-Verlag, Berlin, 1970.

Rowe, J. N., A. P. Mitra, A. J. Ferraro, and H. S. Lee, An experimental and theoretical study of the D region - II. A semi-empirical model for mid-latitude D region, *J. Atmos. Terr. Phys., 36*, 755–785, 1974.

Schulz, G. J., Cross sections and electron affinity for O^- ions from O_2, CO, and CO_2 by electron impact, *Phys. Rev., 128*, 178–186, 1962.

Schunk, R. W., and A. F. Nagy, Electron temperatures in the F region of the ionosphere: Theory and observations, *Rev. Geophys. Space Phys., 16*, 355–399, 1978.

Sechrist, C. F., Comparison of techniques for measurement of D-region electron densities, *Radio Sci., 9*, 137–149, 1974.

Sen, H. K., and A. A. Wyller, On the generalisation of the Appleton-Hartree magnetoionic formulas, *J. Geophys. Res., 65*, 3931–3950, 1960.

Shimamori, H., and R. W. Fessenden, Thermal electron attachment to oxygen and van der Waals molecules containing oxygen, *J. Chem. Phys., 74*, 453–466, 1981.

Smith, P. C., C. L. Tang, J. I. MacPherson, and R. F. McKenna, Investigating the marginal ice zone on the Newfoundland shelf, *Eos Trans. AGU, 75*, 57, 1994.

Spence, D., and G. J. Schulz, Three-body attachment in O_2 using electron beams, *Phys. Rev. A, 5*, 724–732, 1972.

Staff of the Computation Laboratory, *Tables of the Modified Hankel Functions of Order One-Third and of Their Derivatives*, Harvard University Press, Cambridge, Mass., 1945.

Stix, T. H., *Waves in Plasmas*, 566 pp., American Institute of Physics, New York, 1992.

Stubbe, P., and W. S. Varnum, Electron energy transfer rates in the ionosphere, *Planet. Space Sci., 20*, 1121–1126, 1972.

Swanson, E. R., ELF-VLF applications in navigation and communications, in *ELF-VLF Radio Wave Propagation*, edited by J. Holtet, pp. 371–384, D. Reidel, Dordrecht, Holland, 1974.

Swanson, E. R., Omega, *Proc. I.E.E.E.*, *71*, 1140–1155, 1983.

Taranenko, Y. N., U. S. Inan, and T. F. Bell, VLF-HF heating of the lower ionosphere and ELF wave generation, *Geophys. Res. Lett.*, *19*, 61–64, 1992a.

Taranenko, Y. N., U. S. Inan, and T. F. Bell, Optical signatures of lightning-induced heating of the *D* region, *Geophys. Res. Lett.*, *19*, 1815–1818, 1992b.

Taranenko, Y. N., U. S. Inan, and T. F. Bell, Interaction with the lower ionosphere of electromagnetic pulses from lightning: heating, attachment, and ionization, *Geophys. Res. Lett.*, *20*, 1539–1542, 1993a.

Taranenko, Y. N., U. S. Inan, and T. F. Bell, Interaction with the lower ionosphere of electromagnetic pulses from lightning: excitation of optical emissions, *Geophys. Res. Lett.*, *20*, 2675–2678, 1993b.

Tellegen, B. D. H., Interaction between radio-waves?, *Nature*, *131*, 840, 1933.

Terman, F. E., *Radio Engineers' Handbook*, 1019 pp., McGraw-Hill Book Company, New York, 1943.

Tomko, A. A., Nonlinear phenomena arising from radio wave heating of the lower ionosphere, *Report PSU-IRL-SCI-470*, 165 pp., The Pennsylvania State University, University Park, 1981.

Tomko, A. A., A. J. Ferraro, H. S. Lee, and A. P. Mitra, A theoretical model of *D* region ion chemistry modifications during high power radio wave heating, *J. Atmos. Terr. Phys.*, *42*, 275–285, 1980.

Truby, F. K., Low temperature measurements of the three-body electron-attachment coefficient in O_2, *Phys. Rev. A*, *6*, 671–676, 1972.

U. S. Naval Observatory, *Daily Time Differences and Relative Phase Values*, Series 4, No. 1083, Washington, D.C., November 4, 1987.

Utlaut, W. F., Ionospheric modification induced by high-power HF transmitters—a potential for extended range VHF-UHF communications and plasma physics research, *Proc. I.E.E.E.*, *63*, 1022–1043, 1975.

von Zahn, U., and W. Meyer, Mesopause temperatures in polar summer, *J. Geophys. Res.*, *94*, 14,647–14,651, 1989.

Voss, H. D., and L. G. Smith, Global zones of energetic particle precipitation, *J. Atmos. Terr. Phys.*, *42*, 227–239, 1980.

Wait, J. R., *Electromagnetic Waves in Stratified Media*, 372 pp., Pergamon Press, New York, 1962.

Wait, J. R., Calculated diffraction effects at VLF from a localized ionospheric depression, *Tech. Note 208*, National Bureau of Standards, Boulder, Colo., 1964a.

Wait, J. R., On phase changes in very-low-frequency propagation induced by an ionospheric depression of finite extent, *J. Geophys. Res.*, *69*, 441–445, 1964b.

Wait, J. R., Influence of a circular ionospheric depression on VLF propagation, *Radio Sci.*, *68D*, 907–914, 1964c.

Wait, J. R., Concise theory of radio transmission in the Earth-ionosphere wave guide, *Rev. Geophys. Space Phys.*, *16*, 320–326, 1978.

Wait, J. R., and K. P. Spies, Characteristics of the Earth-ionosphere waveguide for VLF radio waves. *Tech. Note 300*, National Bureau of Standards, Boulder, Colo., Dec. 30, 1964.

Wait, J. R., and L. C. Walters, Reflection of VLF radio waves from an inhomogeneous ionosphere. Part I. Exponentially varying isotropic model, *J. Res. N.B.S.*, *67D*, 361–368, 1963.

Watson, G. N., The diffraction of electric waves by the Earth, *Proc. R. Soc. Lond. A*, *95*, 83–99, 1918.

Watson, G. N., The transmission of electric waves round the Earth, *Proc. R. Soc. Lond. A*, *95*, 546–563, 1919.

Watt, A. D., *VLF Radio Engineering*, 701 pp., Pergamon Press, Oxford, 1967.

Wave Propagation Standards Committee of the IEEE Antennas and Propagation Society, *IEEE Standard Definitions of Terms for Radio Wave Propagation*, IEEE Std 211-1987, The Institute of Electrical and Electronics Engineers, New York, 1977.

Willis, J. W., and J. R. Davis, VLF stimulation of geomagnetic pulsations, *J. Geophys. Res.*, *81*, 1420–1432, 1976.

Wolf, T. G., Remote sensing of ionospheric effects associated with lightning using very low frequency radio signals, Ph.D. thesis, Stanford University, Stanford, Calif., 1990.

Wolf, T. G., and U. S. Inan, Path-dependent properties of subionospheric VLF amplitude and phase perturbations associated with lightning, *J. Geophys. Res.*, *95*, 20,997–21,005, 1990.

Wong, A. Y., and R. G. Brandt, Ionospheric modification—an outdoor laboratory for plasma and atmospheric science, *Radio Sci.*, *6*, 1251–1267, 1990.

Zmuda, A. J., B. W. Shaw, and C. R. Haave, VLF disturbances caused by the nuclear detonation of October 26, 1962, *J. Geophys. Res.*, *68*, 4105–4114, 1963.